U.PORTO
FEUP FACULDADE DE ENGENHARIA
UNIVERSIDADE DO PORTO

Analysis of the dynamic behaviour of a stacker crane on impact against end stop

Pedro Fernandes Lima

Dissertation submitted to
Faculdade de Engenharia da Universidade do Porto
for the degree of:

Mestre em Engenharia Mecânica

Company advisors:
Eng. Marco Lima
(R&D Mechanical Engineer)
Eng. Luís Alexandre Oliveira
(Head of R&D Department)

Faculty advisor:
Prof. José Dias Rodrigues
(Associate Professor)

Departamento de Engenharia Mecânica
Faculdade de Engenharia da Universidade do Porto

Porto, 2019

The work presented in this dissertation was performed at
Consoveyo, S.A.
Rua Eng. Frederico Ulrich
4476-908 Moreira da Maia
Portugal

Pedro Fernandes Lima
E-mail: up201405500@fe.up.pt

Faculdade de Engenharia da Universidade do Porto
Departamento de Engenharia Mecânica
Rua Dr. Roberto Frias s/n
4200-465 Porto
Portugal

Abstract

Automated storage and retrieval systems (AS/RS) usually consist of stacker cranes running along a warehouse's aisles and performing functions of entry, placing and exit of goods. These systems are adequate solutions when a high volume of loads has to be moved into and out of storage. The high cost associated with these systems and the limitations of space for their installation makes it crucial for them to be as space efficient as possible. An appropriate shock absorber selection procedure, for a range of standard stacker crane specifications, has the potential to allow for substantial increases in aisle useful length and thus, a higher performance to cost ratio of the installation.

Consoveyo, S.A.'s current practice for shock absorber selection relies on the assumption that the shock absorber of the stacker crane must provide the machine with a deceleration of 6 m/s^2, independently on the height and the payload, even though current standards allow for decelerations of up to 10 m/s^2. The goal of this dissertation is thus to address the structural integrity of the current company's product range, for different values of deceleration, using the Finite Element Method (FEM), and, therefore, assess the maximum admissible deceleration magnitude for each height/payload combination.

The free bending vibration of a simple beam-mass-carriage system is addressed using the Assumed-modes Method to provide relevant insight for the subsequent FEM results. Furthermore, FEM models are developed for the study of free vibration of a single and a double mast stacker crane, using the ANSYS© Workbench Mechanical software. Using the same software, the impact against the end stops is studied and the stresses in the crane's structure for such conditions addressed. The influence of the payload's mass and position as well as the masts' height on the results are reported. In addition, an experimental procedure, aimed to pave the way for further investigations of the sort, is also presented and an in-operation stacker crane's fundamental natural frequency identified, by analysis of its acceleration response in the frequency domain.

Numerical simulation results predict increases of up to 800 mm in aisle useful length in the most optimal conditions of height/payload tested. On the other hand, reductions of up to 2500 mm are predicted for critical cases. The experimental results point towards the need for calibration of the current FEM models.

Keywords: AS/RS, Stacker crane, Shock absorber, Deceleration, Free vibration, Bending, Finite element method

Resumo

De um modo geral, os sistemas de armazenamento automático consistem em transelevadores que percorrem as alas de um armazém realizando funções de entrada, colocação e saída de mercadorias. Estes sistemas são adequados quando há necessidade de entrada e saída de um elevado volume de produtos do armazenamento. O elevado custo associado a estes sistemas e as limitações de espaço inerentes à sua instalação tornam crucial a sua eficiência. A apropriada seleção de amortecedores de impacto, para uma determinada gama de referência de especificações de transelevadores, tem o potencial de permitir aumentos no comprimento útil das alas e, por isso, uma melhor razão desempenho/custo da instalação.

A prática atual da Consoveyo, S.A., para a selecção dos amortecedores de impacto dos transelevadores, pressupõe que estes conferem uma desaceleração de 6 m/s^2 à máquina, independentemente da altura e carga a transportar, apesar das normas atuais fixarem o máximo em 10 m/s^2. O objetivo desta dissertação é o de aferir a integridade estrutural da gama de transelevadores da empresa, para diferentes valores de desaceleração, usando o Método dos Elementos Finitos (MEF), e assim aferir a magnitude máxima de desaceleração possível para cada combinação de altura/carga.

A vibração de flexão em regime livre de um sistema viga-massa-carruagem é avaliada usando o Método dos Modos Assumidos, de modo a promover a compreensão dos subsequentes resultados obtidos pelo MEF. Além disso, modelos MEF são desenvolvidos para o estudo da vibração em regime livre de um transelevador monomastro e de um bimastro, usando o *software* ANSYS© *Workbench Mechanical*. Usando o mesmo *software*, o impacto contra o batente fim de curso é estudado e as tensões na estrutura do transelevador determinadas nessas condições. É referida a influência da massa e posição da carga, bem como da altura do mastro nos resultados. Adicionalmente, um procedimento experimental, com o objetivo de ser expandido no futuro, é conduzido e é identificada a frequência fundamental de vibração de um transelevador em operação, por análise da sua resposta em aceleração no domínio da frequência.

Os resultados dos modelos prevêem aumentos de até 800 mm no comprimento útil das alas, nas condições menos severas de altura/carga testadas. Em oposição, diminuições de até 2500 mm são previstas no pior dos casos. A análise dos resultados experimentais revela a necessidade de proceder à calibração dos modelos numéricos.

Palavras-chave: Sistema de armazenamento automático, Transelevador, Amortecedor de impacto, Desaceleração, Vibração em regime livre, Flexão, Método dos Elementos Finitos

To my grandparents, whom I dearly love...

‘Who you are is defined by what you’re willing to struggle for.’

Mark Manson

Acknowledgements

I would like to express my gratitude to Eng. Luís Alexandre for providing the opportunity to develop this dissertation in an industrial environment, a long time goal of mine, as well as the necessary conditions to do so. It has been a challenging but very rewarding experience in both a personal and professional level.

Furthermore, I would like to thank Prof. José Dias Rodrigues for both his teachings throughout these years and for his constant reminders to doubt and critically analyse the results achieved during this dissertation.

I would also like to say thank you to the people I met at Consoveyo, S.A., in particular my colleagues in the R&D and Engineering Departments for welcoming me with open arms and helping me, without hesitation, in one way or another, throughout the last few months.

In particular I would like to thank Eng. Vítor Vaz, without whom, the experimental procedure presented in this work would not be possible.

My deepest gratitude to Eng. Marco Lima, who accompanied me more closely throughout this dissertation. His constant support and his eagerness to help with insights and experience were truly valuable.

To all my friends and colleagues I've met throughout this 5 year long journey at FEUP, it has been a pleasure to share some of the most memorable moments of my life with you.

Now, to the people I love the most, it's hard to express by words the feelings I have. To my girlfriend, Joana, who has been part of this journey since the beginning and I couldn't have asked for a better company; thank you for all the support, patience and love throughout these years, it has been a lot.

My sincere gratitude to my grandparents, Álvaro and Dina, who have always been a source of support, knowledge and care and to whom I owe a great part of who I am.

To Fernando, for being an example of discipline and values to whom I look up, and to my mother, Sandra, who is an example of strength, and to whom I am very grateful for all her teachings, her love and the opportunity to have an academic education, thank you for all your patience throughout these years.

My sincere gratitude to all,
Pedro Fernandes Lima

Contents

Abstract i

Resumo iii

Acknowledgements ix

1 Introduction 1
- 1.1 Company presentation . . . 1
- 1.2 Motivation . . . 1
- 1.3 Objectives . . . 2
- 1.4 Literature review . . . 2
- 1.5 Layout . . . 4

2 Stacker cranes 7
- 2.1 Palletized storage and Automated S/R Systems . . . 7
- 2.2 Main elements of a stacker crane . . . 9
  - 2.2.1 Applied standards in stacker crane design . . . 10
  - 2.2.2 Hoist unit . . . 11
  - 2.2.3 Lifting carriage and load handling devices . . . 11
  - 2.2.4 Bottom carriage and travel unit . . . 13
  - 2.2.5 Buffer . . . 15
- 2.3 Loads on the structure as per FEM 9.311 [17] . . . 17
  - 2.3.1 Main loads . . . 18
  - 2.3.2 Additional loads . . . 21
  - 2.3.3 Special loads . . . 22
- 2.4 Consoveyo's product lineup and benchmarking . . . 23
  - 2.4.1 Stacker crane product lineup . . . 23
  - 2.4.2 Product benchmarking . . . 26

3 Free vibration of a beam-mass-carriage system 29
- 3.1 Equations of motion . . . 29
- 3.2 Establishment of the semi-discrete model via the Assumed-mode method . . . 33
- 3.3 Natural frequencies and mode shapes . . . 35

4 Free vibration of stacker cranes using the FEM 43
- 4.1 Machine specifications . . . 43
  - 4.1.1 Structure . . . 43
  - 4.1.2 Additional components . . . 47
- 4.2 Analysis setup . . . 48
  - 4.2.1 Modelling concepts and geometry creation . . . 48

4.2.2 Lumped masses . . . 51
4.2.3 Boundary conditions . . . 55
4.2.4 Material model . . . 57
4.2.5 Mesh definition . . . 57
4.2.6 Analysis settings . . . 61
4.2.7 Remarks on previous practices at Consoveyo . . . 61
4.3 Results and discussion . . . 62
4.3.1 Parametric studies . . . 67
4.4 Procedure and remarks on single mast models . . . 77

5 Structural integrity of stacker cranes on impact using the FEM 93
5.1 Analysis setup . . . 93
5.1.1 Lumped Masses and Boundary Conditions . . . 94
5.1.2 Dead weight and working loads . . . 95
5.1.3 Analysis settings . . . 100
5.1.4 Failure criteria . . . 102
5.2 Results and discussion . . . 103
5.2.1 Dynamic behaviour under deceleration . . . 103
5.2.2 Reference case . . . 107
5.2.3 Parametric studies . . . 124
5.3 Summary on maximum deceleration results for STK-21-C . . . 131
5.4 Procedure and remarks on remaining models . . . 133

6 Experimental analysis 139
6.1 Experimental setup . . . 139
6.2 Results and discussion . . . 143

7 Conclusion 153
7.1 Conclusions . . . 153
7.2 Future Work . . . 156

References 157

A Proof of equations (3.14) **and** (3.18) **161**

B Finite element reference 163

C STK-21-C numerical simulation results 167
C.1 Maximum relative displacement of the upper crossbeam . . . 167
C.2 Maximum wheel loads . . . 168
C.3 Stresses . . . 168
C.3.1 Masts' height: 40 m . . . 168
C.3.2 Masts' height: 35 m . . . 170
C.3.3 Masts' height: 30 m . . . 172

D STK-25 numerical simulation results 175
D.1 Model details . . . 175
D.2 Maximum relative displacement of the upper crossbeam . . . 176
D.3 Maximum wheel loads . . . 176
D.4 Stresses . . . 177
D.4.1 Mast's height: 45 m . . . 177

D.4.2 Mast's height: 40 m 178
D.4.3 Mast's height: 35 m 179
D.4.4 Mast's height: 30 m 180

E NXP® MMA8451Q capacitive accelerometer data sheet [50] 181

List of Figures

2.1 Stacker crane on a warehouse's aisle [20]. 8
2.2 Aisle switching devices (figure gently conceded by Consoveyo, S.A.). 8
2.3 Storage types (figure gently conceded by Consoveyo, S.A.). 9
2.4 Elements of a Stacker Crane (figure gently conceded by Consoveyo, S.A.). . 10
2.5 Examples of reeving systems used in stacker cranes (figure gently conceded by Consoveyo, S.A.). 11
2.6 Lifting carriage. 12
2.7 Overspeed governor mounted on the crane's mast (figure gently conceded by Consoveyo, S.A.). 12
2.8 Telescopic Fork [23]. 13
2.9 Satellite vehicle [24]. 13
2.10 Example of bottom carriage of a double mast stacker crane (figure gently conceded by Consoveyo, S.A.). 14
2.11 End stop. 14
2.12 Anti-tipping device (figure gently conceded by Consoveyo, S.A.). 15
2.13 An hydraulic buffer [26]. 15
2.14 Typical force-stroke curves of hydraulic buffers from different manufacturers. 16
2.15 Example of inertial force distribution in a single mast stacker crane undergoing acceleration, v stands for velocity. 19
2.16 Dynamic equivalent system considered in FEM 9.311 [17]. 19
2.17 Influence of the acceleration's orientation on the wheel loads. 21
2.18 Misalignment of the S/R machine and the rail and skew angle. 22
2.19 Single and double mast stacker cranes' mast cross-sections. 23
2.20 Consoveyo's stacker crane lineup (figure gently conceded by Consoveyo, S.A.). 25
2.21 Maximum stacker crane height of selected manufacturers. 26
2.22 Maximum stacker crane payload of selected manufacturers. 27
2.23 Maximum horizontal (travel) velocity of selected manufacturers. 27
2.24 Maximum vertical (hoisting) velocity of selected manufacturers. 28

3.1 Beam-mass-carriage system studied by Park et al., adapted from [12]. . . . 30
3.2 First four non-zero potential energy mode shapes for $r_m = 0.1$ and $h/l = 1$. 36
3.3 First four mode shapes for different values of r_m with the lumped mass at the tip ($h/l = 1$). 38
3.4 First four mode shapes for different values of r_m with the lumped mass at mid-span ($h/l = 0.5$). 39
3.5 First four mode shapes for different values of h/l with $r_m = 0.1$. 40
3.6 First four mode shapes for different values of h/l with $r_m = 1$. 41
3.7 First four natural frequencies with respect to the change of the position of the lumped mass for various values of $r_m = m/M$. 42

4.1 Original STK-21-C model used in the present study (scale 1 : 200). 44
4.2 Cross-section geometry and dimensions (in mm) for the STK-21-C. 45
4.3 STK-21-C stacker crane's masts geometry and length (in mm). 45
4.4 STK-21-C stacker crane's bottom carriage geometry and wheelbase dimension (in mm). 46
4.5 STK-21-C stacker crane's upper crossbeam geometry (dimensions in mm). . 46
4.6 Wheel housings before and after geometry simplification using SpaceClaim© (scale 1 : 50). 48
4.7 Wheel housings before and after mid-surface extraction using SpaceClaim© (scale 1 : 50). 49
4.8 Stages of simplification of the geometry from the original model of Figure 4.1. 50
4.9 Lumped mass representing the lifting carriage, LHD and payload in ANSYS© WB Mechanical. 52
4.10 Lumped mass representing the hoist unit in ANSYS© WB Mechanical. . . 53
4.11 Lumped mass representing the EC assembly in ANSYS© WB Mechanical. . 54
4.12 *Remote displacement* boundary condition on wheel preventing displacements in the y-direction in ANSYS© WB Mechanical. 55
4.13 Rollers on the upper crossbeam and their corresponding *frictionless supports* in ANSYS© WB Mechanical. 56
4.14 Guide rollers in the bottom carriage, near the wheels, to prevent derailment. 56
4.15 *Remote displacements* imposed on the lower rollers' locations in ANSYS© WB Mechanical. 57
4.16 STK-21-C finite element mesh in ANSYS© WB Mechanical. 59
4.17 Detail of parallel surfaces where contact elements must be employed in ANSYS© WB Mechanical. 60
4.18 Contact elements mesh in ANSYS© WB Mechanical. 60
4.19 STK-21-C's 1st natural mode shape ($\omega_1 = 0.81$ Hz). 63
4.20 STK-21-C's 2nd natural mode shape ($\omega_2 = 1.27$ Hz). 64
4.21 STK-21-C's 3rd natural mode shape ($\omega_3 = 1.51$ Hz). 64
4.22 STK-21-C's 4th natural mode shape ($\omega_4 = 2.16$ Hz). 65
4.23 STK-21-C's 5th natural mode shape ($\omega_5 = 3.64$ Hz). 65
4.24 STK-21-C's 6th natural mode shape ($\omega_6 = 3.76$ Hz). 66
4.25 Experimental modal shapes of an 8 m high *mini-load* from reference [10]. . 66
4.26 Computed natural frequencies for different payload heights. 68
4.27 STK-21-C's 1st natural mode shape in the yz-plane for different values of h_r. 69
4.28 STK-21-C's 3rd natural mode shape in the yz-plane for different values of h_r. 70
4.29 STK-21-C's 1st natural mode shape in the xy-plane for different values of h_r. 71
4.30 STK-21-C's 3rd natural mode shape in the xy-plane for different values of h_r. 72
4.31 Computed natural frequencies for different payload mass, m_L, for a masts' height of 40 m with the payload at its highest position. 73
4.32 Computed natural frequencies for different masts' heights with the lifting carriage at its highest position and $m_L = 4000$ kg. 74
4.33 Area where the buffer is bolted onto the bottom carriage. 75
4.34 Computed natural frequencies for the modes of vibration in the yz-plane considering different boundary conditions. 76
4.35 STK-21-C's 1st natural mode shape in the yz-plane for different boundary conditions. 76
4.36 STK-21-C's 3rd natural mode shape in the yz-plane for different boundary conditions. 77

4.37 Original STK-25 model used in the present study (scale 1 : 200). 78
4.38 Beam extraction process in SpaceClaim©for the creation of a shell-beam mesh. 79
4.39 Top mast assembly of STK-25 (scale 1 : 20). 80
4.40 Last two mast levels (one for the 30 and 35 m cases) of the studied STK-25 geometries after simplification. 81
4.41 *Remote displacements* imposed on the upper rollers' locations of the STK-25 in ANSYS© WB Mechanical. 82
4.42 STK-25 finite element mesh in ANSYS© WB Mechanical. 83
4.43 STK-25's (45 m) 1st natural mode shape ($\omega_1 = 0.72$ Hz) 84
4.44 STK-25's (45 m) 2nd natural mode shape ($\omega_2 = 0.74$ Hz) 85
4.45 STK-25's (45 m) 3rd natural mode shape ($\omega_3 = 2.14$ Hz) 85
4.46 STK-25's (45 m) 4th natural mode shape ($\omega_4 = 3.41$ Hz) 86
4.47 STK-25's (45 m) 5th natural mode shape ($\omega_5 = 3.65$ Hz) 86
4.48 STK-25's (45 m) 6th natural mode shape ($\omega_6 = 5.06$ Hz) 87
4.49 Computed natural frequencies of the STK-25 for different mast's height with the lifting carriage at its highest position and $m_L = 1500$ kg. 88
4.50 STK-25's (30 m) 1st natural mode shape ($\omega_1 = 1.38$ Hz) 89
4.51 STK-25's (30 m) 2nd natural mode shape ($\omega_2 = 1.51$ Hz) 89
4.52 STK-25's (30 m) 3rd natural mode shape ($\omega_3 = 3.16$ Hz) 90
4.53 STK-25's (30 m) 4th natural mode shape ($\omega_4 = 5.30$ Hz) 90
4.54 STK-25's (30 m) 5th natural mode shape ($\omega_5 = 8.04$ Hz) 91
4.55 STK-25's (30 m) 6th natural mode shape ($\omega_6 = 8.44$ Hz) 91
4.56 Influence of the eccentricity of the lumped masses on the natural mode shapes of the STK-25 (30 m). 92
4.57 STK-25's bottom carriage 1st mode shape ($\omega_1 = 15.84$ Hz) 92

5.1 Lumped mass connected to only one mast in ANSYS© WB Mechanical. . . 94
5.2 Imposed velocity curve on the area where the buffer is bolted onto the bottom carriage. 95
5.3 Free body diagram of the lifting carriage. 96
5.4 STK-21-C sheave numbering notation. 96
5.5 Free body diagrams of the sheaves mounted on the upper crossbeam. 97
5.6 Forces exerted by the sheaves on the upper crossbeam in ANSYS© WB Mechanical. 98
5.7 Force on the HU's mounting plate due to action of the steel wire rope in ANSYS© WB Mechanical. 99
5.8 Force applied on the lifting carriage's remote point to counteract its weight in ANSYS© WB Mechanical. 99
5.9 Insertion of a *Mechanical APDL* command on the ANSYS© WB Mechanical interface. 100
5.10 Node on the upper crossbeam from which the displacement is shown. 103
5.11 Displacement of the bottom carriage and the upper crossbeam in the travel direction. 104
5.12 Position and shape of the structure at different time steps. 105
5.13 Acceleration contour plot in the travel direction ($t = 0.841$ s). 106
5.14 Relative displacement of the upper crossbeam to the base in the travel direction for $v_i = 2$ and 4 m/s. 107
5.15 Relative displacement of the upper crossbeam for the time step settings of Table 5.4. 107

5.16 Deformation of the STK-21-C (40 m) under static loading with a 4000 kg payload ($t_{\text{sim}} = 0.001$ s). 108
5.17 Upper crossbeam's relative displacement in respect to time for various values of Δt_{stop}. 109
5.18 Upper crossbeam's relative displacement in respect to time for various values of Δt_{stop}. 110
5.19 Wheel loads in respect to time for various values of Δt_{stop}. 111
5.20 Contour plot of σ_{yy} on the lower and upper regions of the stacker crane for $\Delta t_{\text{stop}} = 0.7$ s at $t = 0.8475$ s. 113
5.21 Contour plot of σ_{yy} on the mast on the EC assembly's side for $\Delta t_{\text{stop}} = 0.7$ s at $t = 0.8475$ s. 114
5.22 Contour plot of σ_{yy} on the lower region of the mast on the EC assembly's side at the time of peak mast deflection for various values of Δt_{stop}. 115
5.23 Contour plot of σ_{yy} on the upper region of the mast on the EC assembly's side at the time of peak mast deflection for various values of Δt_{stop}. 116
5.24 Contour plot of σ_{yy} on the lower region of the mast on the HU's side at the time of peak mast deflection for various values of Δt_{stop}. 117
5.25 Contour plot of σ_{yy} on the upper region of the mast on the HU's side at the time of peak mast deflection for various values of Δt_{stop}. 118
5.26 Contour plots of σ_{yy} on the upper region of the mast at $t = 0.9788$ s for $\Delta t_{\text{stop}} = 1.14$ s for a locally refined mesh with element size 20 mm. 119
5.27 Bending of the upper crossbeam for $\Delta t_{\text{stop}} = 1.14$ s and $t = 0.9788$ s (20× deformation amplification). 120
5.28 Contour plot of σ_{zz} on the upper crossbeam at the time of peak mast deflection for various values of Δt_{stop}. 121
5.29 Contour plot of σ_{eq} on the upper crossbeam at the time of peak stress for various values of Δt_{stop}. 121
5.30 Detail of σ_{eq} on the downward face of the upper crossbeam at the time of peak stress for various values of Δt_{stop}. 122
5.31 Contour plot of σ_{zz} on the bottom carriage at the time of peak mast deflection for various values of Δt_{stop}. 122
5.32 Contour plots of σ_{eq} on the critical regions for a static simulation using $a = 5.25$ m/s^2. 124
5.33 Relative displacement of the upper crossbeam in respect to time with varying masts' height, with $m_L = 4000$ kg and $\Delta t_{\text{stop}} = 1.14$ s. 125
5.34 Wheel loads in respect to time for various values of masts' height, with $m_L = 4000$ kg and $\Delta t_{\text{stop}} = 1.14$ s. 126
5.35 Contour plots of σ_{eq} on the upper region of the mast for the 30 and 35 m masts' heights, with $m_L = 4000$ kg and $\Delta t_{\text{stop}} = 1.14$ s. 127
5.36 Contour plots of σ_{eq} on the upper crossbeam for the 30 and 35 m masts' heights, with $m_L = 4000$ kg and $\Delta t_{\text{stop}} = 1.14$ s. 127
5.37 Contour plots of acceleration in the z-directionfor varying masts' heights at the respective $t_{\max}$, with $m_L = 4000$ kg and $\Delta t_{\text{stop}} = 1.14$ s. 128
5.38 Relative displacement of the upper crossbeam in respect to time for varying payload, m_L, with 40 m masts and $\Delta t_{\text{stop}} = 1.14$ s. 129
5.39 Upper crossbeam's relative displacement in respect to time for varying payload, m_L, with 40 m masts and $\Delta t_{\text{stop}} = 1.14$ s. 130
5.40 Wheel loads in respect to time for varying payload, m_L, with 40 m masts and $\Delta t_{\text{stop}} = 1.14$ s 130

5.41 Maximum deceleration results for STK-21-C. 131
5.42 Change in aisle useful length when changing the deceleration from the previous to the newly computed values, assuming $1/\eta = 1.2$. 132
5.43 Typical deceleration-time curve of an hydraulic buffer from the manufacturer Leben. 133
5.44 Contour plots of σ_{yy} on the lower region of the 45 m STK-25 ($v_i = 4$ m/s; $\Delta t_{\text{stop}} = 0.66$ s; $t = 0.81831$ s). 134
5.45 Real and modelled connection between the mast and the bottom carriage. . 134
5.46 Contour plots of σ_{yy} (a and b) and σ_{eq} (c and d) on the lower region of the 45 m STK-25 ($v_i = 3$ m/s; $\Delta t_{\text{stop}} = 0.50$ s; $t = 0.79008$ s). 135
5.47 Maximum deceleration and change in aisle useful length ($1/\eta = 1.2$) for STK-25, $v_i = 4$ m/s except for (*) where $v_i = 3$ m/s. 136
5.48 Contour plots of σ_{eq} on the lower region of the back of the 45 m STK-25 ($v_i = 3$ m/s; $\Delta t_{\text{stop}} = 0.40$ s). 137

6.1 An MMA8451Q capacitive MEMS accelerometer [51]. 139
6.2 3D printed DAS case dimensions (in mm). 140
6.3 Data acquisition system, housing case open and closed. 140
6.4 All DAS assembled. 141
6.5 DAS placement on the STK-21-C. 142
6.6 Modem at the end of the aisle to allow communication with the DAS. . . . 142
6.7 Example of displacement and velocity versus time curves gathered from the on-board PLC, lifting carriage at Y9, 1st measurement. 143
6.8 Extracted acceleration versus time curves from the DAS for the forward motion of the stacker crane, lifting carriage at Y9, 1st measurement. 145
6.9 Extracted S3 acceleration versus time curves from the DAS, lifting carriage at Y9, 2nd, 3rd and 4th measurements. 146
6.10 Computed FFTs from the filtered S3 data, lifting carriage at Y9. 148
6.11 Filtered and unfiltered post stop-phase S3 data, lifting carriage at Y9, 1st measurement. 149
6.12 Computed FFTs from S3 data for the post-stop phase, lifting carriage at Y9. 149
6.13 Computed FFTs from S3 data for the post-stop phase, lifting carriage at Y5. 150
6.14 Computed FFTs from S3 data for the post-stop phase, lifting carriage at Y1. 150
6.15 Experimental and computed values for the first natural frequency of the tested STK-21-C as a function of the lifting carriage's position. 151

B.1 SHELL181 finite element [45]. 163
B.2 BEAM188 finite element [45]. 163
B.3 SOLID185 finite element [45]. 164
B.4 CONTA174 and TARGE170 finite elements [45]. 164
B.5 Contact elements definition [45]. 165

C.1 Maximum relative displacement of the upper crossbeam for the conditions of Figure 5.41. 167
C.2 Maximum wheel reactions for the conditions of Figure 5.41. 168
C.3 Contour plots of σ_{eq} on the upper region of the mast at $t = 1.0287$ s for $\Delta t_{\text{stop}} = 1.14$ s and $m_L = 4000$ kg. 168
C.4 Contour plots of σ_{eq} on the upper region of the mast at $t = 1.00$ s for $\Delta t_{\text{stop}} = 1.00$ s and $m_L = 2000$ kg. 169

C.5 Detail of σ_{eq} on the downward face of the upper crossbeam at $t = 1.00$ s for $\Delta t_{\text{stop}} = 1.00$ s and $m_L = 2000$ kg. 169
C.6 Contour plots of σ_{eq} on the upper region of the mast at $t = 0.855$ s for $\Delta t_{\text{stop}} = 0.88$ s and $m_L = 4000$ kg. 170
C.7 Detail of σ_{eq} on the downward face of the upper crossbeam at $t = 0.855$ s for $\Delta t_{\text{stop}} = 0.88$ s and $m_L = 4000$ kg. 170
C.8 Contour plots of σ_{eq} on the upper region of the mast at $t = 0.80$ s for $\Delta t_{\text{stop}} = 0.80$ s and $m_L = 2000$ kg. 171
C.9 Detail of σ_{eq} on the downward face of the upper crossbeam at $t = 0.80$ s for $\Delta t_{\text{stop}} = 0.80$ s and $m_L = 2000$ kg. 171
C.10 Contour plots of σ_{eq} on the upper region of the mast at $t_{\text{sim}} = 0.630$ s for $\Delta t_{\text{stop}} = 0.72$ s and $m_L = 4000$ kg. 172
C.11 Detail of σ_{eq} on the downward face of the upper crossbeam at $t = 0.630$ s for $\Delta t_{\text{stop}} = 0.72$ s and $m_L = 4000$ kg. 172
C.12 Contour plots of σ_{eq} on the upper region of the mast for $\Delta t_{\text{stop}} = 0.61$ s and $m_L = 2000$ kg. 173
C.13 Detail of σ_{eq} on the downward face of the upper crossbeam at $t_{\text{sim}} = 0.5145$ s for $\Delta t_{\text{stop}} = 0.61$ s and $m_L = 2000$ kg. 173

D.1 Maximum relative displacement of the upper crossbeam for the conditions of Figure 5.47a. 176
D.2 Maximum wheel reactions for the conditions of Figure 5.47a. 176
D.3 Contour plots of σ_{eq} on the lower region of the 45 m STK-25 ($v_i = 3$ m/s; $\Delta t_{\text{stop}} = 0.54$ s; $t = 0.85985$ s). 177
D.4 Contour plots of σ_{eq} on the lower region of the 45 m STK-25 ($v_i = 3$ m/s; $\Delta t_{\text{stop}} = 0.42$ s; $t_{\text{sim}} = 0.51094$ s). 177
D.5 Contour plots of σ_{eq} on the lower region of the 40 m STK-25 ($v_i = 4$ m/s; $\Delta t_{\text{stop}} = 0.88$ s; $t = 0.69125$ s). 178
D.6 Contour plots of σ_{eq} on the lower region of the 40 m STK-25 ($v_i = 4$ m/s; $\Delta t_{\text{stop}} = 0.80$ s; $t = 0.69125$ s). 178
D.7 Contour plots of σ_{eq} on the lower region of the 35 m STK-25 ($v_i = 4$ m/s; $\Delta t_{\text{stop}} = 0.72$ s; $t = 0.59125$ s). 179
D.8 Contour plots of σ_{eq} on the lower region of the 35 m STK-25 ($v_i = 4$ m/s; $\Delta t_{\text{stop}} = 0.61$ s; $t = 0.54125$ s). 179
D.9 Contour plots of σ_{eq} on the lower region of the 30 m STK-25 ($v_i = 4$ m/s; $\Delta t_{\text{stop}} = 0.57$ s; $t = 0.44125$ s). 180
D.10 Contour plots of σ_{eq} on the lower region of the 30 m STK-25 ($v_i = 4$ m/s; $\Delta t_{\text{stop}} = 0.50$ s; $t = 0.44125$ s). 180

List of Tables

2.1 Height range for current stacker crane models. 24

3.1 System parameters [12]. 36

4.1 Length and cross-section dimensions per mast level for the original STK-21-C. 45
4.2 Bottom carriage's tube length and cross-section dimensions for the original STK-21-C crane. 46
4.3 Upper crossbeam's tube length and cross-section dimensions for the original STK-21-C crane. 46
4.4 Mechanical properties at ambient temperature for S355JR steel [44]. 47
4.5 Mass of the original STK-21-C structural components taken from the Autodesk Inventor© CAD model. 47
4.6 Mass of the original STK-21-C additional components as measured. 47
4.7 Comparison of the initial and final mass of the main structure. 49
4.8 Material properties for *structural steel* from ANSYS© material library. . . . 57
4.9 Mesh properties used for convergence test. 62
4.10 Natural frequency results for the first six non-zero energy modes with the payload at its highest position for $m_L = 4000$ kg, using different meshes. . . 62
4.11 Computed natural frequencies for different payload heights. 67
4.12 Example of new notation adopted for the payload at highest position. . . . 67
4.13 Computed natural frequencies for different payload heights. 68
4.14 Total mass of the STK-21-C structure model per height. 74
4.15 Mesh properties of the STK-21-C models per height. 74
4.16 Total mass of the STK-25 structure model per height. 80
4.17 Mass of the STK-25 additional components. 82
4.18 Mesh properties of the STK-25 models per height. 82
4.19 Notation adopted for the STK-25 vibration modes using the 45 m mast example. 87

5.1 Sub step settings for load steps 1 and 2. 101
5.2 Values of the safety coefficient ν_E depending on the loading case [21]. 102
5.3 Step settings for the simulations considering only dynamic effects. 103
5.4 Time step settings for comparison 107
5.5 Time step settings for load steps 3 and 4. 109
5.6 Peak relative displacement and time for various Δt_{stop} with $v = 4$ m/s, $m_L = 4000$ kg. 109
5.7 Comparison of the peak relative displacement using the newly implemented analysis setup and the previous one. 123
5.8 Comparison of the wheel loads using the newly implemented analysis setup and the previous one. 123

5.9 Peak relative displacement of the upper crossbeam and instant at which it occurs for varying masts' height, with $m_L = 4000$ kg and $\Delta t_{\text{stop}} = 1.14$ s. . 124
5.10 Peak relative displacement of the upper crossbeam and instant at which it occurs for varying payload, m_L, with 40 m masts and $\Delta t_{\text{stop}} = 1.14$ s. . . . 129

6.1 Mass of the tested STK-21-C additional components. 141
6.2 Height of each DAS. 141
6.3 Height of the surface of the telescopic forks for each tested position of the lifting carriage. 143
6.4 Mesh properties of the tested STK-21-C model. 150
6.5 Computed versus experimentally identified 1st natural frequency for tested lifting carriage's positions. 151

D.1 Total mass of the STK-25 structure model per height. 175
D.2 Mesh properties of the STK-25 models per height. 175

Chapter 1

Introduction

1.1 Company presentation

The present work was proposed by Consoveyo, S.A., a system integrator of automated materials handling technology and warehousing systems with its headquarters in Porto, Portugal. The company started out as a small group within the passenger lift division of the portuguese company Efacec and, eventually, became an independent company inside the Efacec Group, under de name of "Efacec Automação e Robótica, S.A.", in 1991. Fast forward to 2015, the company, by then under the name "Efacec Handling Solutions, S.A.", was acquired by the international technology group Körber, fortifying the group's position in the logistics systems business. In 2017, it changed its name to Consoveyo, S.A. [1; 2].

The company designs and builds automated storage and handling systems, providing turnkey solutions specifically designed for the costumers' needs. In its portfolio, the company counts hundreds of projects in different industries such as beverage, paper and retailing, with its main focus being in the handling of palletized goods (up to 1500 kg) and heavy loads (up to 10 t) [1].

In order to provide solutions in automated handling systems, Consoveyo has a vast product portfolio of in-house developed equipment like stacker cranes, conveyors, automated (AGVs) and rail-guided vehicles (RGVs), as well as proprietary software for warehouse management and control of the automated equipment in a warehousing facility [1].

1.2 Motivation

The high cost associated with Automated Storage and Retrieval Systems (AS/RS) and the limitations of space for their installation makes it crucial for companies who commercialize these to make them as space efficient as possible.

One of the machines that integrate these systems to perform the storage and retrieval of goods in a warehouse is the stacker crane, an automated machine moving along the warehouse aisles on top of rails.

Consoveyo's market philosophy is based on providing customized solutions for each client. This makes it so that, in the particular case of stacker cranes, every prototype is a functional one and equipment standardization ended up taking a back seat in the company's priorities, with the decision-making tools at disposal found to not be enough to optimize the equipments for a given application.

One example is the present procedure of selecting shock absorbers for stacker cranes, a mandatory equipment by the applicable standards. This selection is based on the assumption that the shock absorber must provide the structure with a deceleration of 6 m/s^2,

without taking into account the height of the machine nor the payload it's supposed to transport, despite the fact that current standards allow for a maximum deceleration of 10 m/s^2 [3], providing the structural integrity of the machine isn't compromised. This procedure may lead to the use of oversized shock absorbers, thus reducing the useful aisle length of the warehouse.

1.3 Objectives

The main goal of this study is to perform an analysis on the structural integrity of the stacker cranes' structure, in the specific case of impact against the end stops of the aisle, in order to assess the maximum decelerations admissible, for each stacker crane type, as a function of height and payload. Ultimately, decision-making tools like tables and graphs are to be provided that present this information in a compact and accessible form.

To achieve the aforementioned objective, the following steps were defined at the beginning of this dissertation:

- the familiarization with the current stacker crane models at Consoveyo, S.A. and their operation;
- information gathering on the current limitations and applied standards on stacker crane design;
- to perform a benchmarking comparison with other stacker crane manufacturers;
- structural analysis of the stacker crane portfolio using the Finite Element Method (FEM), for the case of impact against the end stops with ANSYS© Workbench Mechanical;
- to perform a comparison between numerical simulations carried out considering a dynamic or a statically equivalent case;
- the comparison of the results of stresses and maximum decelerations for the various height/payload combinations.

Throughout the development of this dissertation, it was found the need to analyse a simplified model in order to provide greater confidence in the numerical simulation results. This dissertation was also further complemented with an experimental analysis, intended as a first step towards further implementation of experimental procedures in the analysis of the crane's dynamic behaviour.

1.4 Literature review

An extensive literature review found no reports of previous attempts to characterize the dynamic behaviour of stacker cranes, using the FEM or any other method, to assess the structural integrity on impact against the end stops. Most journal publications found to mention this type of machine mostly dealt with operational research studies or the development of motion control techniques to reduce mast sway thus enabling faster and more precise load picking and handling operation.

Görges et al. [4] developed a model of a single mast storage and retrieval machine based on the *Euler-Bernoulli* beam theory. A low order model was then derived from the

infinite-dimensional model using the assumed modes method and used in order to evaluate several active vibration control strategies in order to reduce mast sway. The bottom carriage was assumed as a rigid body and the mast described as a cantilever beam with the lifting carriage, load handling mechanism and payload being represented as a lumped mass at the tip of the mast.

Hajdu and Gáspár have several publications regarding the dynamic behaviour of stacker cranes and the implementation of motion control schemes. For example, in references [5] and [6; 7] distributed parameter and multi-body models, respectively, were developed for single mast stacker crane structures, while in references [8; 9], controller design methods are presented to achieve a reduction in mast vibration of the same machines, using the developed dynamic models.

Bachmayer et al. [10] developed a simple analytical model of a single-mast stacker crane by considering an *Euler-Bernoulli* beam with a lumped mass connected via a torsional spring to a moving rigid body. Validation was conducted by comparing the natural vibration frequencies and modes to those measured experimentally on a double mast 8 m tall mini-load (a smaller machine, similar to a stacker crane) instrumented with accelerometers and excited with a hammer in the travel direction. A 100 kg payload was placed at a height of 1 m. A good correlation was found between the first, fourth and sixth modal forms and frequencies of the experimental model to the first three modal forms and frequencies of the analytical one. The corresponding modes of vibration consisted in the vibration of the crane's mast in the frame's plane, the second and fifth mode of the experimental model consisted in out-of-plane movement and as such, weren't modelled. Bachmayer et al. claim that the torsional rigidity of the lower carriage has a substantial influence on the natural frequencies of the system.

A similar study was conducted by Loose [11] where a 2 degree of freedom (DOF) model of a single mast stacker crane was presented and an experimental model used to implement a PID-controller scheme whose aim was to reduce the mast's vibration.

Park et al. analysed the natural modes of vibration of an elastic beam fixed on a moving carriage and carrying an intermediate lumped mass in reference [12]. A unified frequency equation which can be generally applied to this kind of systems was obtained. The researchers found that the natural frequencies and corresponding mode shapes change considerably as the mass ratios and the position of the concentrated mass varies. The model is expanded to consider moving masses in reference [13], where experiments are carried out to show the validity of the proposed analytical model to study the open-loop response of the system in tracking pre-designed paths of the moving mass.

Publications regarding other hoisting machines were found that are relevant for the study at hand. Haas [14] conducted an experimental and numerical study on the interactions of an overhead crane and its supporting structure as this was not explicitly taken into account in the design codes for structures that harbour these machines. A computationally efficient FEM model, with most of the structural elements modelled as *Timoshenko beam elements*, was developed and its calibration made by comparison with experimental data.

The FEM model was then used to determine the maximum end buffer impact force when the crane collides with the end stops and compared with the results from the computation methods provided in standards. Acceptable predictions (within 10% of error) were achieved by the FEM model when computing the maximum impact forces, however,

significant differences between the numerical and experimental responses were found on the subsequent impacts caused by the oscillation of the hoisted payload.

Feau et al. [15] studied the earthquake response of overhead crane bridges. To this end, both numerical tests, using FEM, and experimental tests on a scale model were performed. At first, the developed beam finite element model was found to be much stiffer than the mock-up by comparison of the experimental and the numerically computed natural frequencies of vibration. This was caused by the assumed boundary conditions on the crane bridge which had to be replaced by spring elements to account for the flexibility of the runway beams on which the crane bridge moves. Contact non-linearities arising from impact and friction for braked wheels were also taken into account in the FEM model.

Arena et al. [16] developed a three dimensional model of a container crane. Experimental investigations were carried out on a full-scale container crane using a capacitive micro-electromechanical system (MEMS) accelerometer. The analysis of the computed Fast Fourier Transform (FFT) of the gathered data allowed for identification of the crane's natural frequencies of vibration and validation of the numerical model.

1.5 Layout

This dissertation is divided into seven different chapters. These do not represent the chronological order of events but instead an order that was found to be logical for the understanding of the studied topic. Each remaining chapters' contents are summarized below.

Chapter 2 - Stacker cranes

Principles of stacker crane operation and its components are presented as well as an overview of the applied standards. Particular importance is given to the case of impact of the crane against the end stops.

The chapter ends with the presentation of Consoveyo's stacker crane portfolio as well as a benchmarking with other manufacturers.

Chapter 3 - Free vibration of a beam-mass-carriage system

The free vibration of a beam-mass-carriage system is studied. The equations of motion are derived via Hamilton's principle and a semi-discrete model is established using the Assumed-mode method. The system's natural modes of vibration relating to bending in the plane of travel are presented as is their dependence to the lumped mass' magnitude and its position.

Chapter 4 - Free vibration of stacker cranes using the FEM

FEM models are established to study the free vibration of Consoveyo's stacker cranes. The model creation process in ANSYS© Workbench (WB) Mechanical is presented in detail as well as the underlying modelling assumptions. Free vibration modes of the stacker cranes are presented for varying parameters in accordance with the companies' established practices.

Chapter 5 - Structural integrity of stacker cranes on impact using the FEM

The maximum decelerations of the stacker crane's are assessed using the *Transient Structural* module of ANSYS© WB Mechanical. The effect of the structure's weight and working loads are also accounted for in the numerical simulations. Influences of the crane's specifications in the displacements, stresses and wheel loads are explored and the model limitations outlined.

Chapter 6 - Experimental analysis

An initial experimental study is performed which aims to pave the way for further experimental investigation and validation of the developed numerical models. Acceleration data is retrieved from in-house developed data acquisition systems and manipulated in order to achieve conclusions on the frequency response of the system. Ultimately, the experimental results are compared with the numerical ones.

Chapter 7 - Conclusion

In this chapter, the main conclusions from this study are summarised and are given suggestions for future studies and improvements.

Chapter 2

Stacker cranes

The present chapter aims to provide a comprehensible introduction to the machine to be analysed in subsequent chapters, the stacker crane.

An overview of Automated Storage and Retrieval Systems is given in section 2.1 which explains the function of a stacker crane in such installations.

Moreover, in section 2.2, the main elements of a stacker crane are presented and important nomenclature is established which will be used throughout this dissertation. In particular, the shock absorber selection process is presented in accordance to industry practices.

On section 2.3, specifications of current applied standards to the design of stacker cranes, in particular FEM 9.311 [17], are discussed.

The chapter concludes with an overview of Consoveyo's stacker crane line up as well as a benchmarking study against other manufacturers.

2.1 Palletized storage and Automated S/R Systems

The wooden pallet is the most common unit load used in warehouses as it allows for standard storage and handling equipment to be used, irrespective of the goods being handled. The effective storage of goods in a warehouse normally involves the stacking of pallets, either one pallet on top of another or, more commonly, the placing of pallets into some form of racking [18].

An automated storage and retrieval system (AS/RS) is a storage system operated by computer control. It usually consists of stacker cranes (Figure 2.1) that run along the aisles of the warehouse, putting away and extracting pallets. These cranes travel on top of rails and due to their height, another rail placed above the top rack helps with guidance [18].

The structure of the crane can be composed by one or two tall masts, depending on the height and lifting capacity requirements of the system. Along the mast (or masts) travels a lifting carriage which houses a handling device responsible for loading and unloading the goods on to the racks of the warehouse. When the stored goods are palletized, the handling mechanism consists of forks that extend from the sides of the crane to pick up pallets, however, other handling mechanisms can be utilized [18; 19].

In fast-moving operations, there may be one crane per aisle, with both in-feed and out-feed of goods typically taking place at the same end of the aisle. In slower-moving operations, there may be fewer cranes than aisles in which case, cranes may be moved between aisles at the far end by means of a transfer car. Alternatively, the rails can be curved at the end of the aisle so that the cranes can run down a transverse aisle and, with the aid of suitable mechanisms (Figure 2.2), be redirected to the correct rack aisle [18].



Figure 2.1: Stacker crane on a warehouse's aisle [20].



Figure 2.2: Aisle switching devices (figure gently conceded by Consoveyo, S.A.).

AS/RS systems may be classified as single deep, double deep and high-density (triple deep or higher) systems according to the way the goods are stored in the pallet racking, which consequently modifies the way the stacker cranes access the pallets (Figure 2.3).

In this sense, single deep systems have two rows of pallet racking back to back between the aisles with the stacker crane accessing only one pallet deep on either side of the rack. Double deep systems on the other hand have four rows of pallet racking between the aisles, and the stacker cranes are designed to reach two deep into the racks. In high density-systems, multiple rows of pallet racking are installed together which leads to the need for systems like satellite vehicles that can move away from the crane onto rails placed underneath the pallet lanes [18].

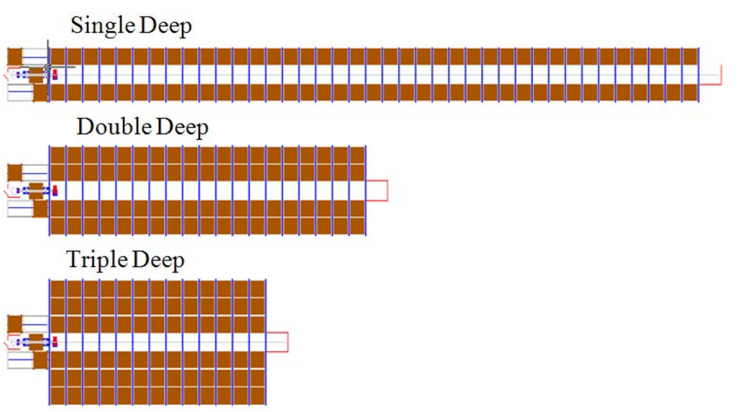


Figure 2.3: Storage types (figure gently conceded by Consoveyo, S.A.).

AS/RSs tend to make very good use of land area because of their height and narrow aisles, about 1.5 m in width, however, they have a high capital cost and are therefore suited for large installations that need to operate for most hours of the day [18].

2.2 Main elements of a stacker crane

The main elements of a stacker crane are:

- bottom carriage;
- travel unit;
- hoist unit;
- electrical cabinet;
- lifting carriage;
- mast;
- mast's top.

Other elements are added for maintenance purposes. Figure 2.4 shows a typical arrangement of a stacker crane.

Before further explanation on these elements' functions, Section 2.2.1 provides an overview of the applied standards in stacker crane design as these contain specific requirements for the elements that make up the machine.

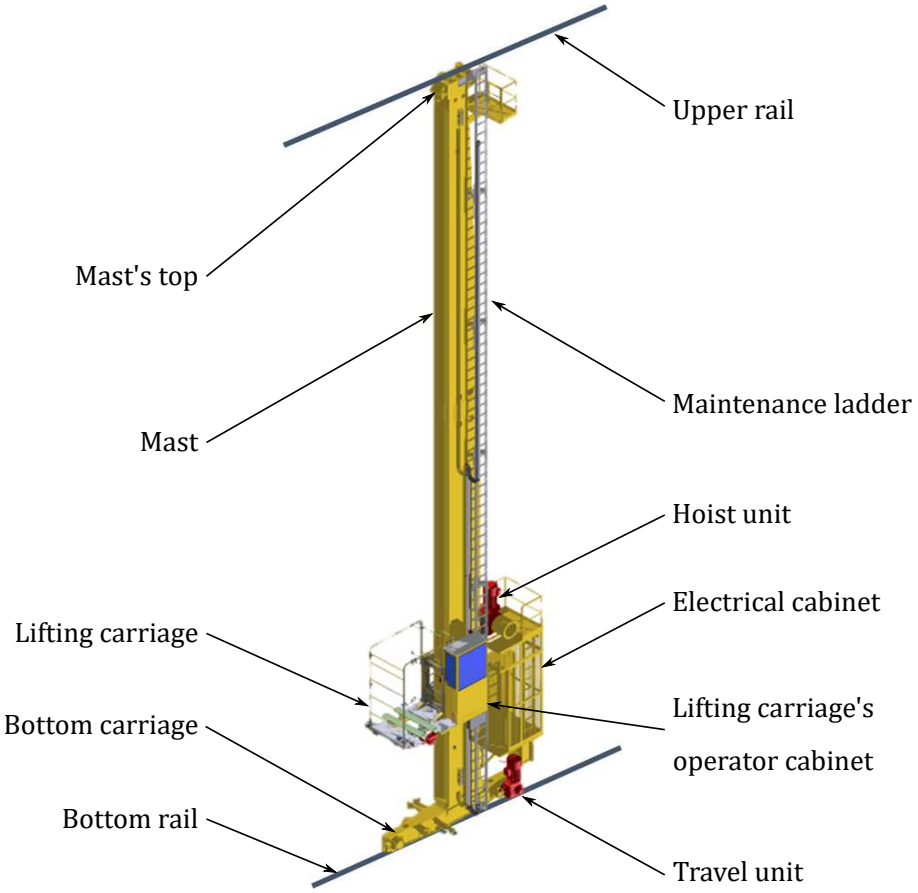


Figure 2.4: Elements of a Stacker Crane (figure gently conceded by Consoveyo, S.A.).

2.2.1 Applied standards in stacker crane design

Due to the inherent responsibility in the design of AS/R systems and the potential hazards of the equipment to warehouse operators, standards are in place in order to regulate the design of such systems.

EN 528:2008 [3] provides safety requirements on *"Rail dependent storage and retrieval equipment"*. A list of significant and relevant hazards in these applications is exposed and safety requirements in both mechanical and electrical equipment are provided, a special section is reserved for machines which provide the possibility of manual operation.

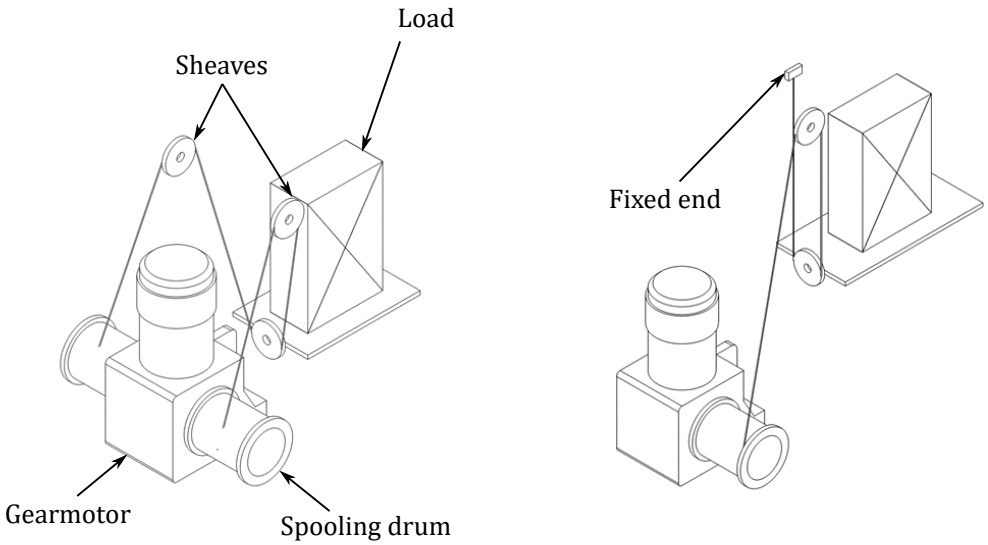
The *European Materials Handling Federation* (FEM) provides technical guides on the structural design of storage and retrieval machines, namely FEM 9.311 [17] on the *"Rules for the design of storage and retrieval equipment - Structures"*.

Even though these machines are specifically excluded from the scope of FEM 1.001 [21] - *"Rules for the design of hoisting appliances"*, this standard is used by Consoveyo as a complement to the very brief FEM 9.311. It comprises 8 booklets with contents ranging from the loadings on structures and mechanisms to stress and fatigue calculations.

2.2.2 Hoist unit

The hoist unit is a device used for lifting or lowering the load by means of a spooling drum around which a steel wire rope wraps. Sheaves located throughout the structure of the stacker crane guide the wire rope from the spooling drums to the lifting platform. The power needed to lift the load is provided by an electrical gearmotor.

There are several reeving systems to choose from, according to the application. One of the most important decisions in this regard is the choice between a direct or differential system. In a direct system (Figure 2.5a), the wire rope departs from the hoisting drum, goes through the sheave system onto the supporting structure and returns to the drum, making it so the gearmotor supports all the load provided by the lifted weights. However, in a differential system (Figure 2.5b), while one end of the rope is wrapped around the spooling drum, the other end is fixed to the mast, making it so half of the load is supported by the structure and a lower torque is required from the gearmotor.



(a) Direct reeving system. (b) Differential reeving system.

Figure 2.5: Examples of reeving systems used in stacker cranes (figure gently conceded by Consoveyo, S.A.).

2.2.3 Lifting carriage and load handling devices

The lifting carriage's (Figure 2.6) purpose is to move the load and the operator cabin vertically along rails bolted onto the mast [22].

If the carriage's speed exceeds a certain limit, an overspeed governor (Figure 2.7) locks and causes the safety catch devices in the carriage to act on the vertical rails, stopping it. The EN 528:2008 standard imposes the velocity of actuation of these devices at 1.4 times the rated velocity, or 0.7 m/s, whichever is greatest [3].

The devices contained in the lifting carriage that handle the transfer of the load from the stacker crane to the warehouse racking are the *load handling devices*. According to EN 528:2008, these devices *"shall be constructed in such a way that every part of the specified load will remain in a stable position during normal operation"*. These are selected based on the storage type of the system and on the weight and shape of the load.

The most common load handling devices are telescopic forks (Figure 2.8). These are made up of two arms joined by an articulated shaft, each one having a fixed body and a

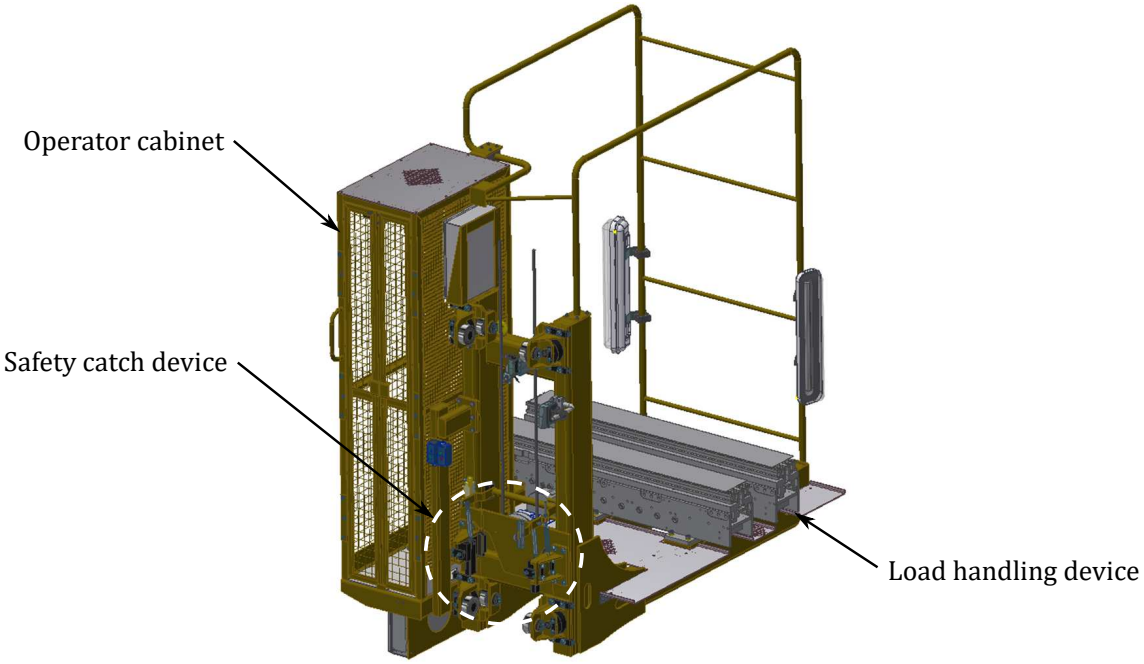


Figure 2.6: Lifting carriage.

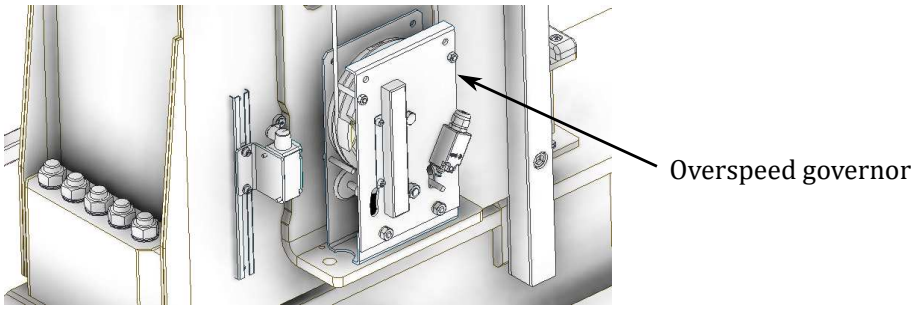


Figure 2.7: Overspeed governor mounted on the crane's mast (figure gently conceded by Consoveyo, S.A.).

variable number of moving bodies that slide on top of each other [22]. These mechanisms are classified in accordance to their storage type as single, double or triple deep. The higher the reach of the fork into the pallet rack, the higher the number of mobile parts, for example: single deep forks are comprised of two moving parts and one fixed body while double deep forks have an additional moving part [23].

When the number of racking rows is higher than three, forks are no longer a viable solution and must be replaced with satellite vehicles (Figure 2.9), for example. The storage lanes are fitted with rails on which the satellites can run. Satellite and S/R machine therefore form one logistical unit: the satellite runs on the rails to the allotted storage position where it sets down or picks up a pallet, and the S/R machine transports the satellite to the correct storage or retrieval point in the warehouse [24].

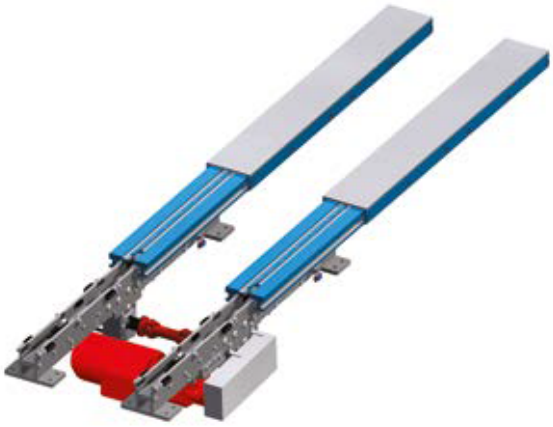


Figure 2.8: Telescopic Fork [23].



Figure 2.9: Satellite vehicle [24].

2.2.4 Bottom carriage and travel unit

The bottom carriage is a box-shaped welded steel construction that houses one or two travel units and upon which the mast (or masts) is bolted. The wheels are thermally fitted onto an axle whose bearing housings are bolted onto the welded plates of the carriage. Other safety related equipment like shock absorbers and speed reduction magnetic sensors as well as communication and positioning devices are incorporated in the bottom carriage [22].

Figure 2.10 is a schematic representation of the bottom carriage of a double mast stacker crane.

The travel unit is comprised of the parts that provide the movement to the wheels of the stacker crane, allowing it to move along the aisle. A gearmotor transmits torque to the drive shafts which in turn cause the wheels to roll on the rail. Depending on the size of the stacker crane, travel units can be applied to one wheel or both. In accordance to EN 528:2008, *"the machine shall be capable of being decelerated and stopped safely from the rated speed*[1] *with the rated load*[2] *plus operator(s) without undue shock..."*. For normal operation, this is done via an electrical or mechanical braking system, which is normally included in the gearmotor. In the event of power failure, however, an additional mechanical

[1] According to EN 528:2008 it's the *"maximum speed of the machine for which it has been designed and for which normal operation is guaranteed by the vendor."*

[2] According to EN 528:2008 it's the *"maximum load which the machine has been designed to carry, excluding the mass of operator(s) and any part of the machine"*

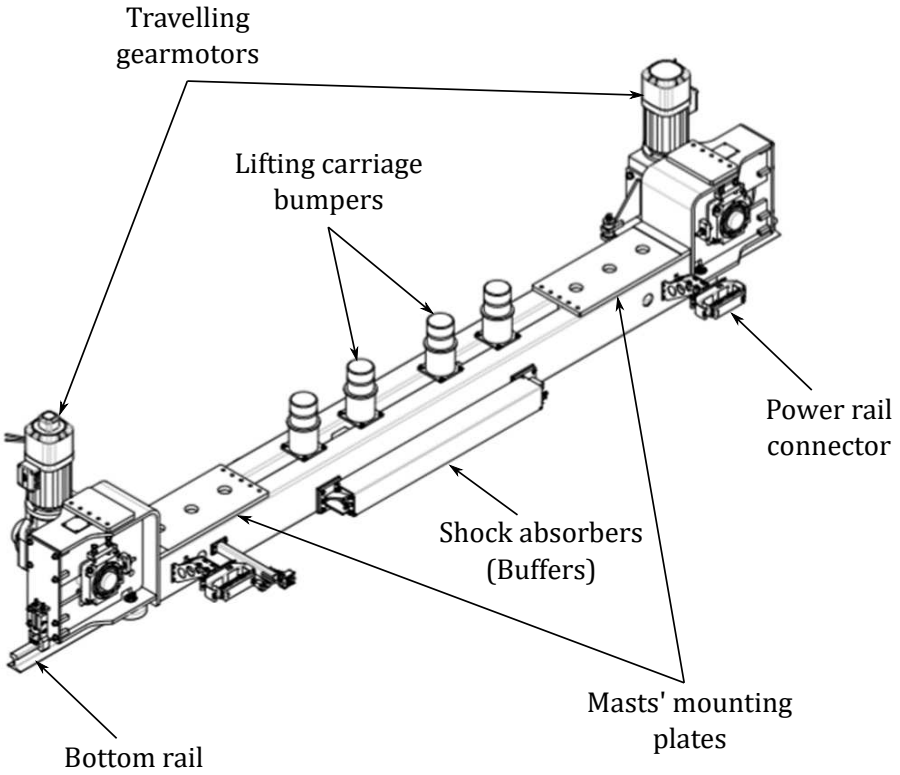


Figure 2.10: Example of bottom carriage of a double mast stacker crane (figure gently conceded by Consoveyo, S.A.).

braking system shall be operated.

In the event of the machine surpassing the travel limits imposed for normal operation (e.g., as a result of failure in the control system), means shall be provided to stop the machine safely at the limit of travel. *Shock absorbers* or *buffers*, as they are mentioned in the applied standards, shall be installed to absorb the energy of the travel movement. These can be installed either on the end of the aisle or by attaching it to the bottom carriage, as seen in Figure 2.10. In the last case, end stops like the one in Figure 2.11 are placed at the ends of the aisle.

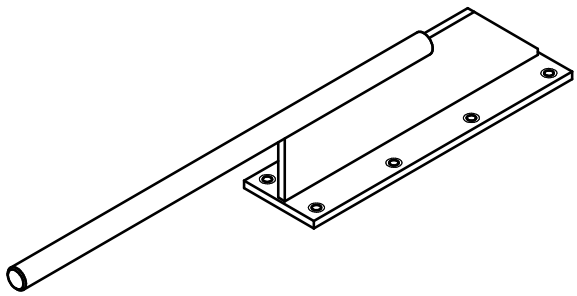


Figure 2.11: End stop.

Before the machine contacts the end stops, however, an ultimate limit switch with direct mechanical actuation shall be provided, initiating an emergency stop function and cutting power to the wheels [3].

A device to prevent tipping shall also be fitted on the bottom carriage [3]. A claw-shaped profile plate around the head of the rail, like the one seen in Figure 2.12, is an

example of such device.

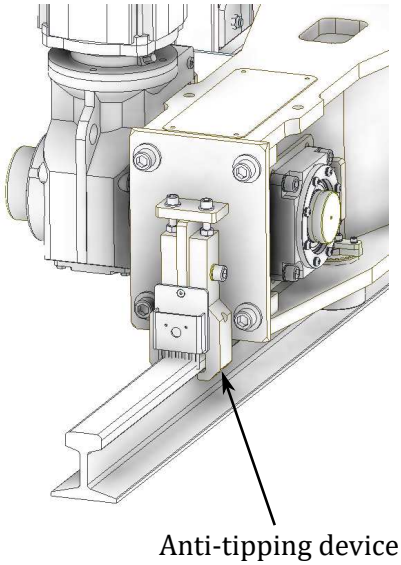


Figure 2.12: Anti-tipping device (figure gently conceded by Consoveyo, S.A.).

A limitation on the deceleration is imposed by the EN 528:2008 standard: it shall not exceed 10 m/s^2. This is of upmost importance to the study at hand as will be discussed in the next section regarding buffers.

2.2.5 Buffer

The purpose of a buffer is to dissipate the kinetic energy of the crane when it collides with the end stops. Since the rated speed of a stacker crane is in the range of 4 m/s and these machines have considerable mass, hydraulic buffers are used [25].

Hydraulic buffers are comprised of a hollow cylinder inside which moves a piston that separates the hollow section of the cylinder into two volumes. The oil inside is forced through holes that connect the two chambers when its pressure raises due to the load applied at the piston which, in this case, comes from the impact with the end stops [25]. Figure 2.13 shows an hydraulic buffer (named *Heavy-Duty Shock Absorber* in the respective catalogue [26]) from the manufacturer Weforma.

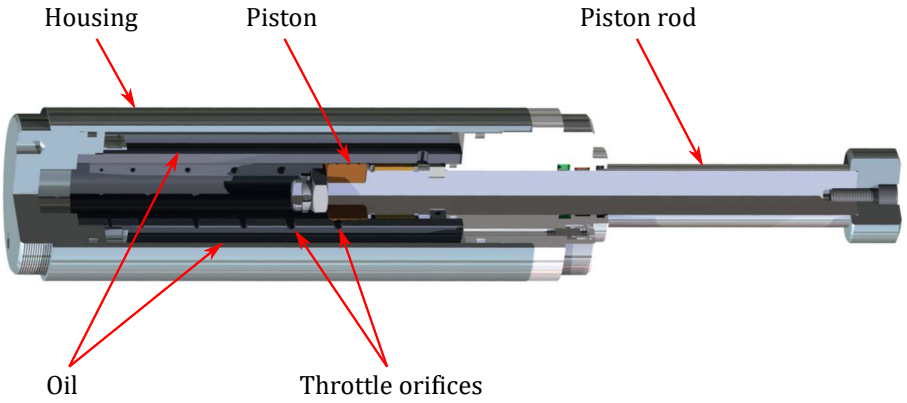
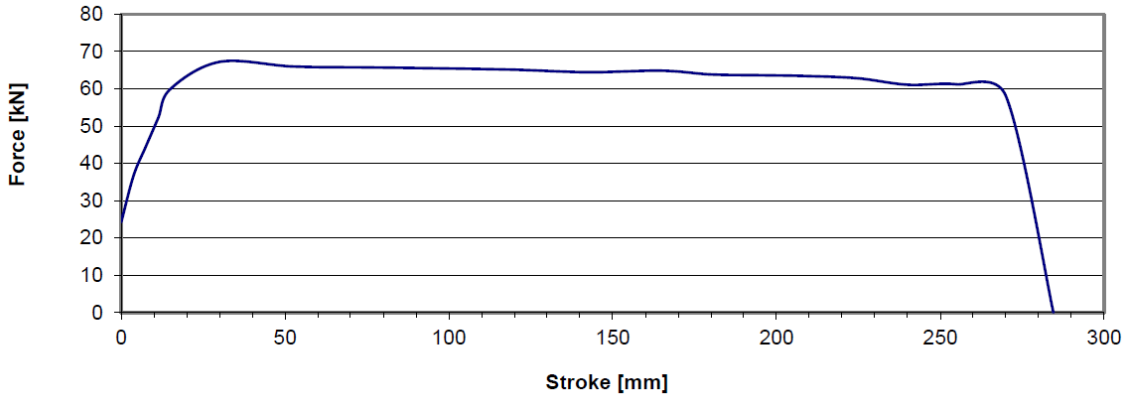


Figure 2.13: An hydraulic buffer [26].

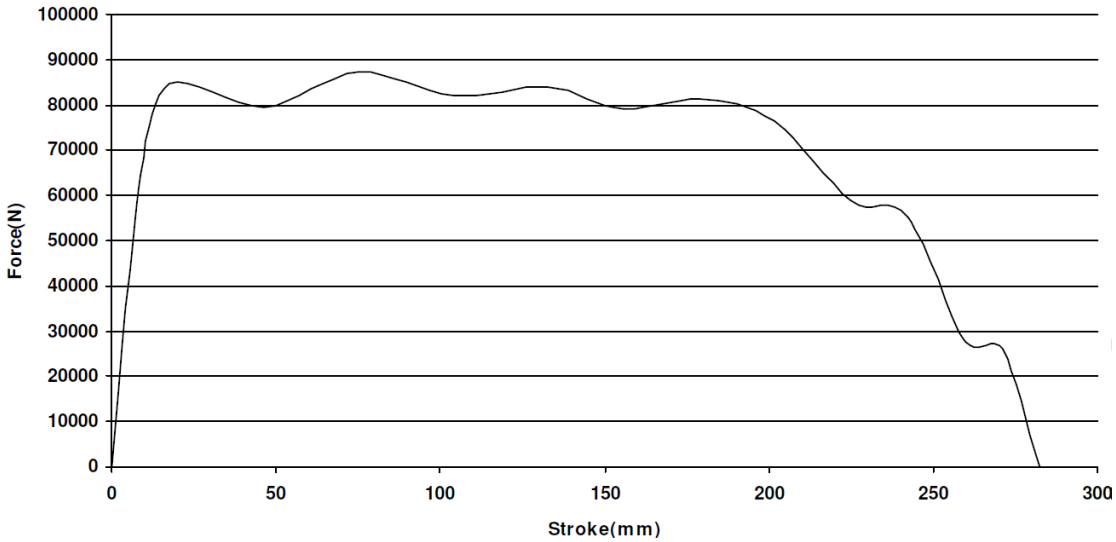
A rubber pad and a spring which cushion the initial impact between the machine and

the piston aswell as a light spring to recover the piston to its initial position are also part of the buffer [25]. Another possibility is the use of a nytrogen accumulator which compensates the displaced oil caused by the moving piston and returns the piston rod to its original position when the buffer is unloaded. The one in Figure 2.13 is one of such cases [26].

The force-stroke curve of the buffers depends on the design choice done by the manufacturer. If, like in Figure 2.13, there's an inner wall in the cylinder and the two chambers are connected via holes of varying size in that same wall, larger near the beginning position of the piston and smaller towards the end of its course, the force peak will be levelled throughout most of the stroke of the piston [25]. Figure 2.14 shows force-stroke curves, available by request, for hydraulic buffers from different manufacturers, evidencing the levelled force peak throughout most of the stroke.



(a) Force-stroke curve from the manufacturer Leben [27].



(b) Force-stroke curve from the manufacturer Weforma [28].

Figure 2.14: Typical force-stroke curves of hydraulic buffers from different manufacturers.

Manufacturers' catalogues like the one from reference [26] provide means to choose the appropriate buffer based on the impact situation: the impact of a stacker crane with an attached buffer against an end stop can be thought of as a moving mass moving towards a fixed shock absorber. Assuming the worst case, where the crane of mass m is travelling at

the rated speed v, the kinetic energy, W_{kin}, of the system an instant before impact is [17],

$$W_{kin} = \frac{m \cdot v^2}{2} \ . \tag{2.1}$$

The kinetic energy of the machine is turned into the work necessary to move the piston on the buffer so, considering the counterforce F_G, i.e., the force that acts opposite to the movement of the crane, constant throughout the stroke, S, of the piston, the equilibrium of energy can be written as,

$$F_G \cdot S \cdot \eta = W_{kin} \ , \tag{2.2}$$

with η being an efficiency coefficient provided by the manufacturer to account for the real force-displacement behaviour of the buffer. For reference [26], $1/\eta = 1.2$.

Assuming constant counterforce, the deceleration, a, will also be constant so,

$$F_G = m \cdot a \ , \tag{2.3}$$

which substituting in (2.2) makes it so the stroke of the piston in order to stop the crane must be at least [26],

$$S = \frac{v^2}{2 \cdot a} \cdot \frac{1}{\eta} \ , \tag{2.4}$$

for a given deceleration a.

Equation (2.4) provides an intuitive conclusion: if one wants to minimize the piston stroke, it will be necessary to make the machine go through larger magnitudes of deceleration.

2.3 Loads on the structure as per FEM 9.311 [17]

The FEM 9.311 standard specifies three load categories:

- main loads;
- additional loads;
- special loads.

Main loads comprise the weight of all the mechanical and electrical equipment of the S/R machine as well as the weight of the goods. However, these are separated into lifted loads and dead loads, with the first ones being those coming from the weight of the lifting carriage, load handling devices and the stored goods and the second ones being the weight of the remaining parts of the machine. The inertial forces produced by the travel units during operation and the stabilising forces that prevent the machine from tipping are also categorized as main loads.

Additional loads comprise the forces resulting from the machine running askew, the effects of temperature and the loads on walkways, handrails and such.

Finally, special loads are the ones that aren't present during the normal operation of the S/R machine like buffer forces - when the equipped buffer impacts with the ends stops - , emergency catch loads - for when the lifting platform descends with excessive speed - and test loads to be applied in mandatory tests after the on-site installation of the machine as per EN 528:2008.

Considering these loads acting on the machine, the structure must be designed in order to take into consideration the following causes of failure:

- overstraining of the material beyond the elastic limit;
- overstraining of structures beyond the critical buckling stresses;
- overstraining of materials beyond the fatigue strength.

The following sections go into detail on the loads that were deemed to be the most relevant for the study at hand.

2.3.1 Main loads

Dead loads and lifted loads

Dead loads are the forces due to weight of all fixed and moving parts, with the exception of the lifted loads.

The lifted loads comprise the effect of the payload and the dead weight of the assemblies that handle it i.e., the weight of the vertically moving parts of the machine.

The weight of the load supporting means i.e., steel wire ropes, chains or belts, is proportionately shared between these two categories.

To account for vertical forces of inertia due to the lifting or travel motions, the loads above mentioned must be multiplied by dynamic coefficients dependant on the rated travel velocity and the rated lifting velocity and acceleration of the lifting platform.

Horizontal forces of inertia

The dynamic effects of the masses resulting from structure flexibility during the acceleration and deceleration of regular service of the S/R machine shall be taken into account as an *oscillation coefficient*, S_W, which multiplies the forces of inertia applied to the individual centres of gravity. Figure 2.15 shows an example of the distribution of the following forces of inertia during acceleration of the crane's travel motion:

- F_1 is the force of inertia due to the acceleration of the the payload, of mass m_L, and the mass of the lifting carriage, m_H;
- F_2 is the force of inertia due to the acceleration of the mast (m_S);
- F_3 is the force of inertia due to the acceleration of the bottom carriage (m_B) and attachments (m_A) e.g., travel unit, hoist unit, electrical cabinet, etc.

The forces of inertia in the example described can be computed, considering a mean acceleration of a_m, as,

$$F_1 = (m_L + m_H) \cdot a_m \cdot S_W \ , \tag{2.5a}$$

$$F_2 = m_S \cdot a_m \cdot S_W \ , \tag{2.5b}$$

$$F_3 = (m_B + m_A) \cdot a_m \ . \tag{2.5c}$$

Note that, because of the dynamic effects being much more pronounced on the top of the mast than at the bottom carriage, the coefficient is taken to be "1" in the computation of F_3.

The maximum value of S_W is $S_W^{\max} = 2$ and is deducted from the approximation of the structure to the one-degree of freedom dynamic equivalent system of Figure 2.16, from where it follows that the *dynamic displacement*, $y(t)$, is given by [17],

$$y(t) = \frac{m_{\text{dyn}} \cdot a_m}{c} \cdot (\cos(\omega t) - 1) \ , \tag{2.6}$$

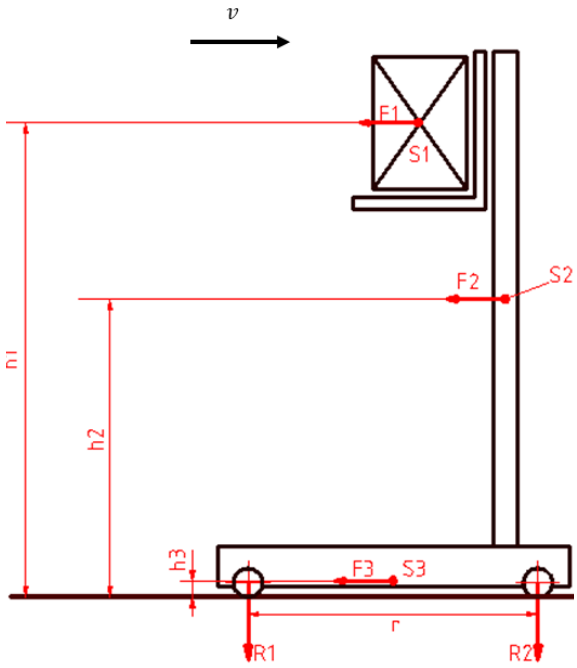


Figure 2.15: Example of inertial force distribution in a single mast stacker crane undergoing acceleration, v stands for velocity.

where m_{dyn} is the *dynamic equivalent mass of the flexible masses*, c is the rigidity of the mast, a_m is the mean acceleration of the horizontal motion and ω is the natural frequency of the system. The oscillation coefficient S_W is defined as being $S_W = |\cos(\omega t) - 1|$, therefore $S_W^{\max} = 2$.

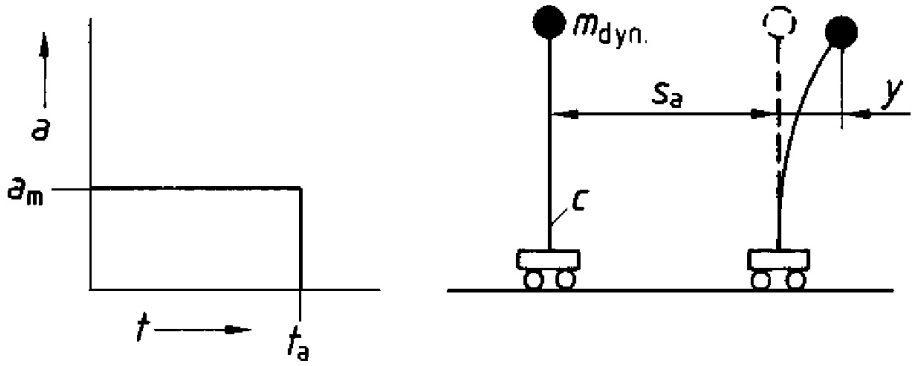


Figure 2.16: Dynamic equivalent system considered in FEM 9.311 [17].

Wheel loads and Stability

Considering the equilibrium of forces and moments on each wheel at constant travel speed, the wheel loads (R_1 and R_2 in Figure 2.15), may be computed. Only the dead loads and lifted loads multiplied by their respective dynamic coefficients shall be accounted for in this case.

However, when the machine accelerates or decelerates, it is clear that the horizontal forces of inertia considered will increase or decrease the wheel loads, depending on their direction. Both cases are schematically shown in Figure 2.17, a red coloured wheel represents a load increase for that particular wheel while a blue one represents the opposite effect.

For the first case, where the acceleration has the same sign as the velocity, the wheel loads are

$$R_{max} = R_1 = R_1^{stat} + \frac{F_1 \cdot h_1 + F_2 \cdot h_2 + F_3 \cdot h_3}{r} \ , \tag{2.7a}$$

$$R_{min} = R_2 = R_2^{stat} - \frac{F_1 \cdot h_1 + F_2 \cdot h_2 + F_3 \cdot h_3}{r} \ , \tag{2.7b}$$

where R_i^{stat} $i = 1, 2$ are the wheel loads for the static (constant velocity) case, without considering the respective dynamic coefficients, and r is the wheelbase. For the second case, where the acceleration and velocity have different signs, the subscripts 1 and 2 have their places traded in expressions (2.7a) and (2.7b).

EN 528:2008 states that *"the machine and the rails shall be designed and built in such a way that the machine will not overturn during operation of the safety devices"*. Both the EN 528:2008 and FEM 9.311 standards define a *stability factor*, ν_s, as,

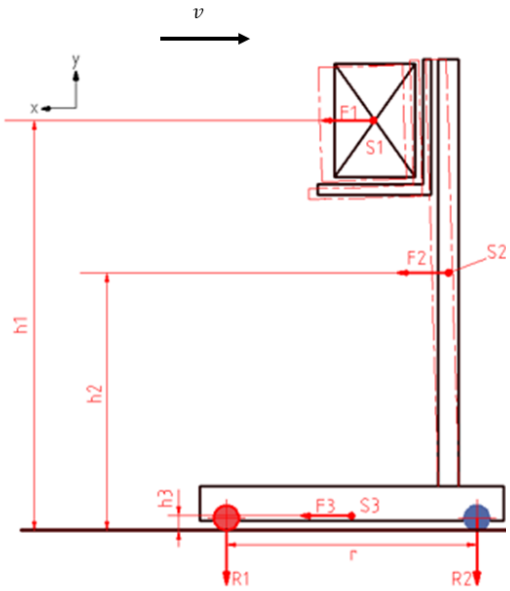
$$\nu_s = \frac{\sum \text{stabilising moments}}{\sum \text{overturning moments}} \ . \tag{2.8}$$

The *stabilising moments* are the ones resulting from the weight of the machine itself and the rated load while the *overturning moments* are caused by the horizontal forces due to the mass and wind load, which isn't applicable in the studied case.

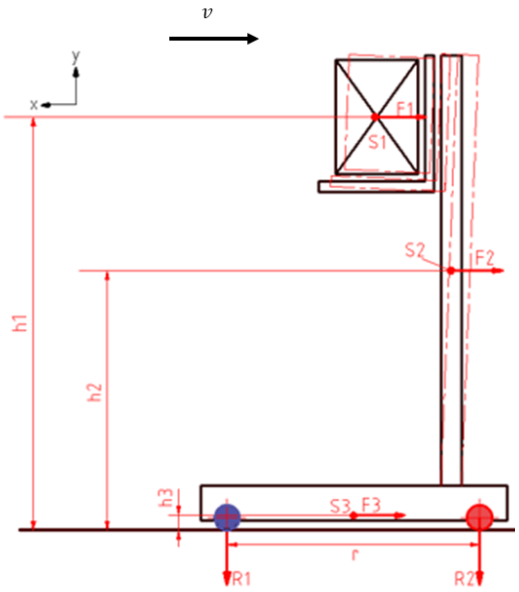
So, for example, in the case of Figure 2.17a, the stability factor for each wheel would be,

$$\nu_{s,i} = \frac{R_i^{stat} \cdot r}{F_1 \cdot h_1 + F_2 \cdot h_2 + F_3 \cdot h_3} \quad i = 1, 2 \ . \tag{2.9}$$

The stability must be checked for each load case under normal working conditions, for all cases it's required that $\nu_{s,i} \geq 1.5$ $i = 1, 2$. In emergency situations, like the loss of power or an emergency stop, this factor may be lower but shall be ≥ 1.1. When testing the buffer impact loading case, the effect of oscillation (coefficient S_W) isn't considered.



(a) Acceleration of the travel motion.



(b) Deceleration of the travel motion.

Figure 2.17: Influence of the acceleration's orientation on the wheel loads.

2.3.2 Additional loads

Forces due to running askew

Forces arise from contact between the rail and guiding rollers when the machine runs askew at an angle α. The *skew angle*, α, is taken as the sum of all possible misalignments transverse to the runway when the S/R machine takes up a skewed position, as shown schematically in Figure 2.18. The contributions to the skew angle may arise from the clearance between the rail and the guide members, the wear of the parts in contact, the

machine tolerances (e.g, parallelism of bearing mounting surfaces) and the rail placing tolerances. Data for the calculation of the skew angle can be obtained from FEM 9.311 and by consulting the tolerances depicted in FEM 9.831 [29].

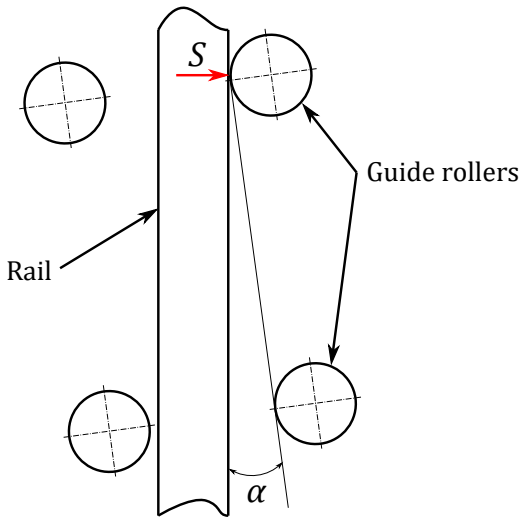


Figure 2.18: Misalignment of the S/R machine and the rail and skew angle.

The resulting force, S, on the guide roller, transverse to the runway, is given by,

$$S = f \cdot R^{stat} \ , \tag{2.10}$$

where assuming that α has units of rad $\times 10^{-1}$, f is a coefficient given by,

$$f = 0.30 \cdot \left(1 - e^{-0.25 \cdot \alpha}\right) \ . \tag{2.11}$$

2.3.3 Special loads

The FEM 9.311 standard classifies the buffer forces on the structure as "special loads" and it is assumed that, during regular service, collisions of S/R machines do not occur. It also states that *"if automatic means ensure a reduction of the travel speed"* before the impact of the buffer into the end stop, the then fastest possible travel speed may be used in equation (2.1) provided it is at least 70% of the rated speed.

In the case of a simplified analysis of the stresses in the structure, the buffer end forces shall be multiplied by an oscillation coefficient. This coefficient is dependant on the shape of the buffer characteristic (see Figure 2.14): it is taken to be 1.25 if the area below the buffer curve resembles a triangle and 1.50 if the same area resembles a rectangle.

2.4 Consoveyo's product lineup and benchmarking

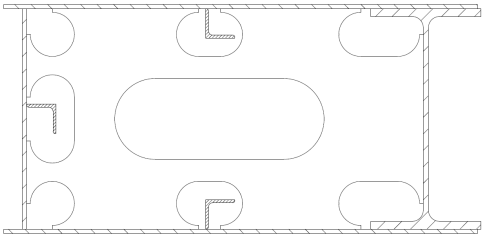
2.4.1 Stacker crane product lineup

In the particular case of stacker cranes, the following parameters help define the one to be used for a particular application:

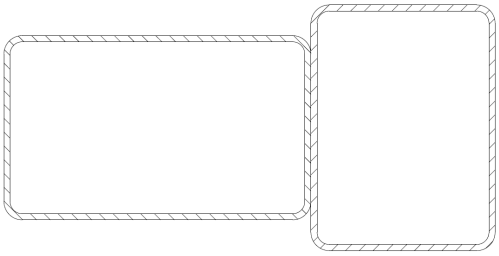
- payload weight, size and quantity per machine;
- warehouse storage type;
- total stacker crane height.

Consoveyo's product lineup comprises both single mast and double mast stacker cranes. Single mast stacker cranes are generally designed to transport unit loads of up to 1500 kg since this is the safe working load of an EPAL Euro Pallet [30] while double mast stacker cranes are considered when heavier loads are to be carried. Another situation where the need for a double mast stacker crane may arise is when more than one load is to be transferred to avoid excessive bending moments on the crane's mast, as the second load would have to be placed further from the mast.

The design of the masts in a single mast stacker crane is significantly different from the design of a double mast. In the first one (Figure 2.19a), IPE beams and sheet metal plates are welded together to form a rectangular-shaped box girder and various sheet metal plates, designated as septa, are placed throughout the structure's height, hidden inside the structure, in order to increase the flexural rigidity of the mast. On the other hand, the cross-section of the mast from double mast stacker cranes consists of either one or two (welded in a T-like fashion) rectangular tubes, as seen in Figure 2.19b.



(a) Single mast.



(b) Double mast.

Figure 2.19: Single and double mast stacker cranes' mast cross-sections.

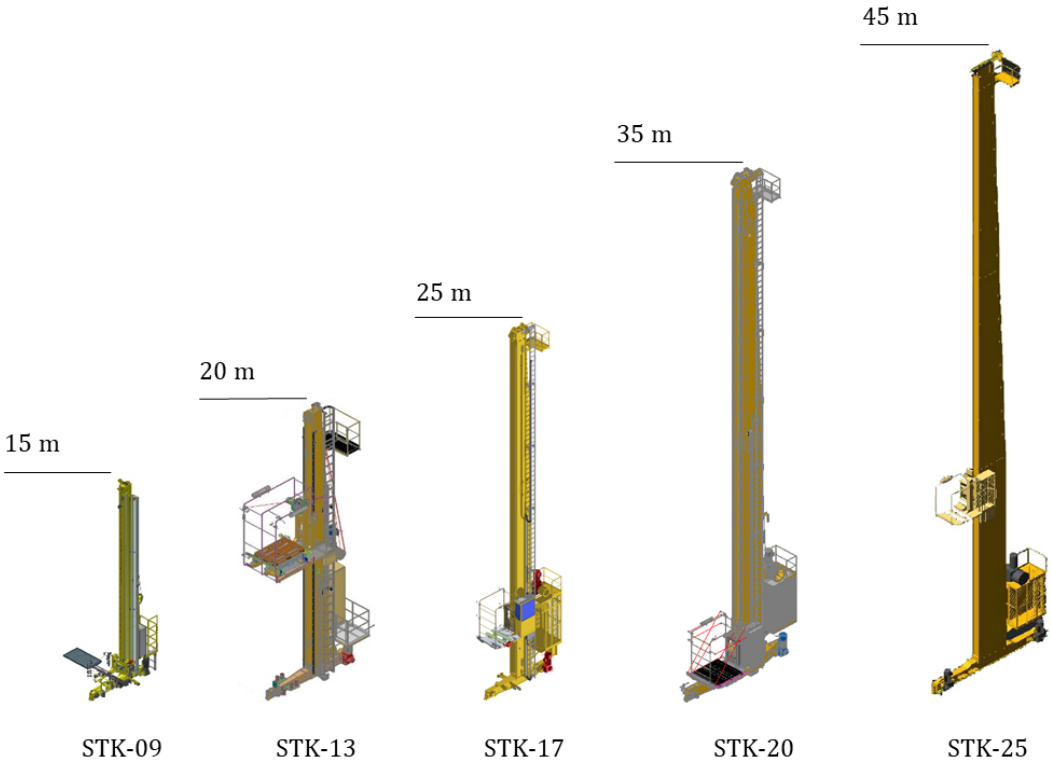
Depending on the structure's height and load, the wheelbase is selected in order to provide the necessary stability during the travel motion.

The cross-section of the mast is what differentiates the models in the company's lineup with each one's name starting with "STK-" and followed by two digits and, in some cases, a letter. A given cross-section limits the maximum height of the machine. Table 2.1 and Figure 2.20 provides an overview of the height range for each given crane model with Table 2.1 also listing the maximum admissible payload for each model. It must be taken into account that, for a given model, the maximum allowable height will lower if, for example, a double deep telescopic fork is used instead of a single deep device as it significantly increases the combined weight of the lifted bodies. The use of a double deep instead of a single deep telescopic fork provides an increase in mass between 500 kg and 1000 kg, according to previous experience at Consoveyo. It's also worthy of note that, in Table 2.1, the minimum height field is not a functional limit but merely an indication as to when the use of a particular model might be unjustified since the lower models will probably suffice.

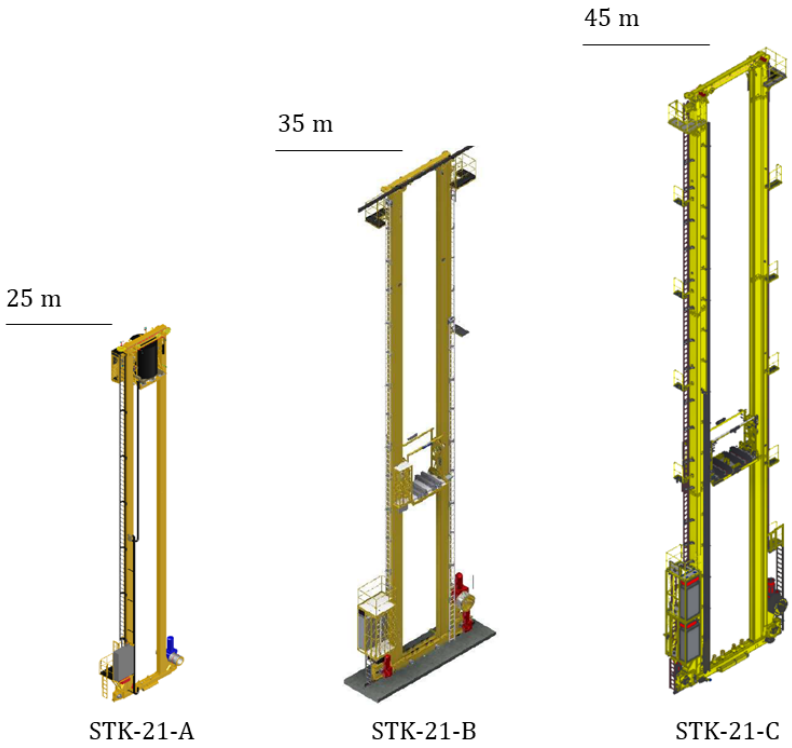
Table 2.1: Height range for current stacker crane models.

	Model	Min. height /m	Max. height /m	Max. payload /kg
Single mast	STK-09	8	15	1000
	STK-13	12	20	1500
	STK-17	15	25	1500
	STK-20	20	35	1500
	STK-25	35	45	1500
Double mast	STK-21-A	10	25	4000
	STK-21-B	25	35	6000
	STK-21-C	30	45	4000

The achievable velocities and accelerations during operation of these machines, in both travel and hoisting movements, are relevant in order to assess the performance of the warehouse. Consoveyo's stacker cranes are able to achieve a maximum travelling velocity between 4 and 5 m/s and about 1 m/s in the hoisting direction. Under normal conditions, these machines operate at travel accelerations of 1 m/s^2 and hoisting accelerations of 0.8 m/s^2 maximum.



(a) Single mast.



(b) Double mast.

Figure 2.20: Consoveyo's stacker crane lineup (figure gently conceded by Consoveyo, S.A.).

2.4.2 Product benchmarking

A brief research was conducted on more than 10 stacker crane manufacturers in order to perceive how Consoveyo stacks up against competitors in terms of performance numbers. Height, maximum payload and travel and hoisting motion kinematics were compared taking into account only the cases where the machine's payload is at least 300 kg, as below that range, Consoveyo, S.A. provides other solutions that aren't considered stacker cranes. No significant differences were found in the stacker crane structure across manufacturers.

The information presented here can be found online mostly through catalogues or data sheets easily accessible via the companies' websites [20; 22; 31–42]. The numbers presented should be considered as rough figures of the real parameters not only because they come from documents intended for commercial use but also because of the high degree of customization that these machines allow when tailoring them to a specific application, as was shown in previous sections. Moreover, being maximum values of the respective parameters, its most likely that they can't be achieved simultaneously for a given application.

Figure 2.21 shows a comparison of the maximum achievable height of various manufacturers. It can be seen that only a couple of companies are able to provide a slightly wider height range than Consoveyo, S.A.

In terms of maximum payload, from the selected companies in Figure 2.22, only LTW made a crane able to support a load higher than the 6000 kg of Consoveyo's STK-21-B (Table 2.1).

Figures 2.23 and 2.24 show, respectively, the maximum horizontal and vertical velocities of stacker cranes from various manufacturers. It's apparent that, although in terms of horizontal velocity Consoveyo's stacker cranes stack up well against the competition, there's room for improvement in terms of hoisting velocity.

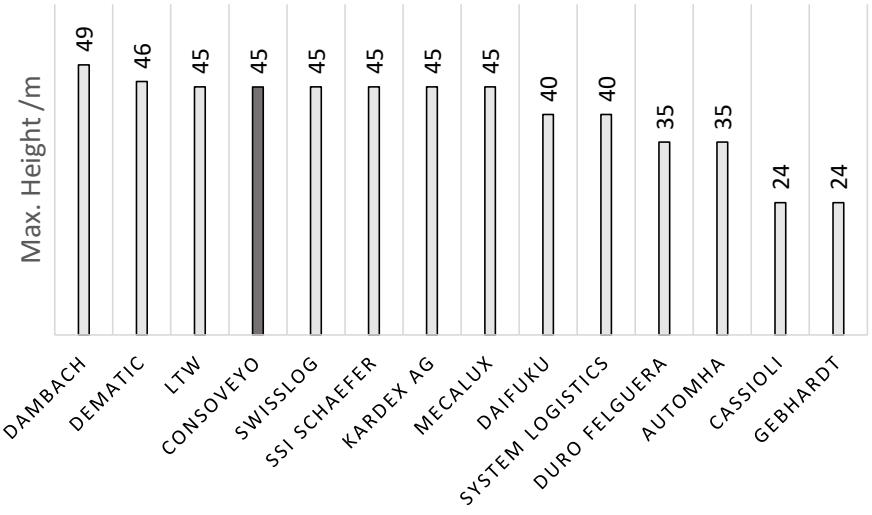


Figure 2.21: Maximum stacker crane height of selected manufacturers.

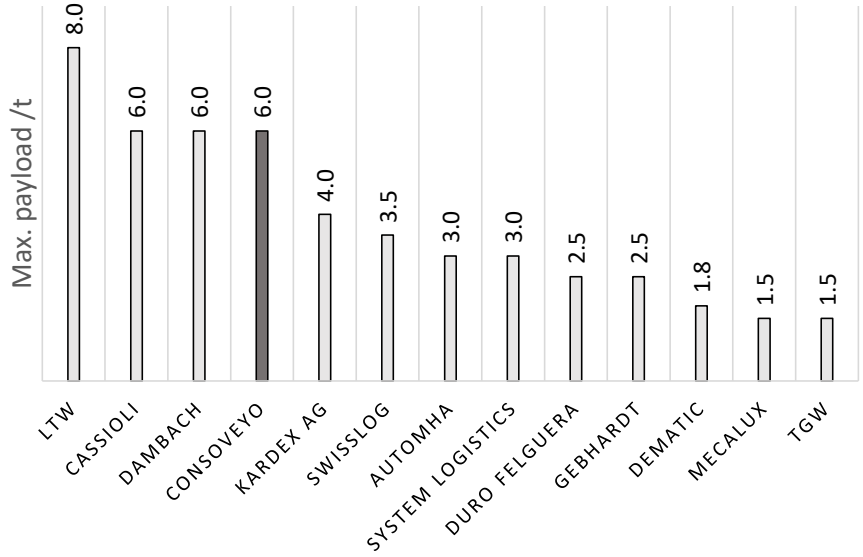


Figure 2.22: Maximum stacker crane payload of selected manufacturers.

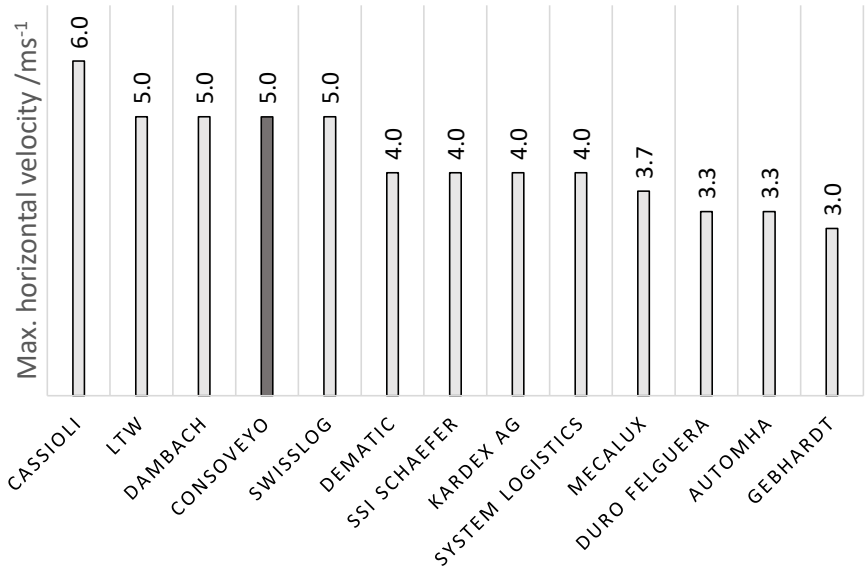


Figure 2.23: Maximum horizontal (travel) velocity of selected manufacturers.

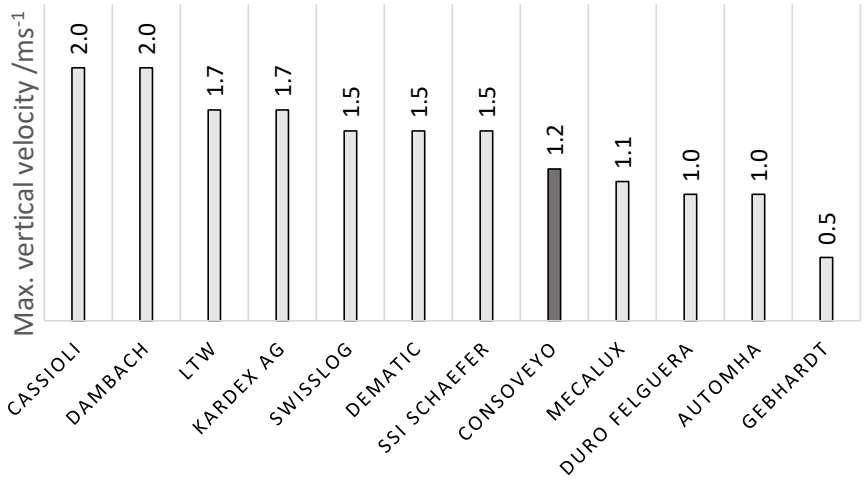


Figure 2.24: Maximum vertical (hoisting) velocity of selected manufacturers.

Chapter 3

Free vibration of a beam-mass-carriage system

The following chapter presents the vibration analysis of a beam clamped onto a moving carriage and carrying an intermediate lumped mass. Such a model reveals itself adequate in the study of the vibrational motion of stacker cranes as it depicts the vibrational motion due to the flexibility of the beam. Moreover, it allows the study of the influence of the position of the lifting carriage along the mast on the dynamic behaviour of the system.

The equations of motion are derived via Hamilton's principle and a semi-discrete model is established using the Assumed-mode method [43]. Using the derived model, the natural frequencies and mode shapes and their variation with the lumped mass' magnitude and position is presented.

While a more extensive study on the subject of the vibrational behaviour of the beam-mass-carriage system, including the exact solution for the natural frequencies and mode shapes, can be found in references [12; 13], the aim of this chapter is instead to provide a basis of comparison for the upcoming FEM models.

3.1 Equations of motion

Taking the elastic beam carrying an intermediate mass and fixed to a moving carriage of Figure 3.1 and the following assumptions:

- the beam is modeled as an Euler-Bernoulli beam;
- the rotational effect of the moving mass is neglected;
- there is no longitudinal deflection of the beam in the y-axis thus, only lateral deflection, in the x-direction, is possible;
- the lateral deflection of the beam is small compared with its length.

The mass per unit length, $\rho(y)$, of the flexible beam with a lumped mass m at height h along the beam can be represented as

$$\rho(y) = \rho_0 + m\delta\left(y - h\right) \ , \tag{3.1}$$

where ρ_0 is the mass per unit length of the flexible beam without the moving mass and $\delta\left(y - h\right)$ is the Dirac delta-function satisfying

$$\int_0^l \delta\left(y - h\right) \mathrm{d}y = 1 \ , \tag{3.2}$$

$$\delta\left(y - h\right) = 0, \forall y \neq h \ . \tag{3.3}$$

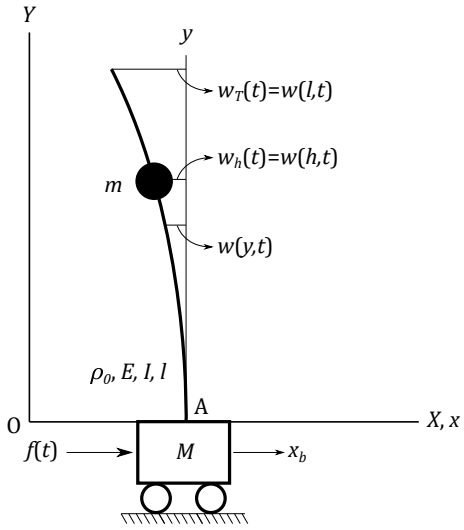


Figure 3.1: Beam-mass-carriage system studied by Park et al., adapted from [12].

In Figure 3.1, the global coordinate system (GCS), XOY, is fixed while the local coordinate system (LCS), xAy, has its x axis collinear with X and its origin point attached to the moving carriage. The relationship between the position of a given point in respect to the GCS to the position of the same point in respect to the LCS is expressed as

$$\boldsymbol{r}_G = \boldsymbol{d} + \boldsymbol{r}_L \ , \tag{3.4}$$

where $\boldsymbol{r}_G = [X, Y]^\top$, $\boldsymbol{r}_L = [x, y]^\top$ and $\boldsymbol{d} = [x_b, 0]^\top$ is the position vector of the moving carriage in respect to the GCS.

The kinetic energy, T, and the potential energy, V, of the carriage of mass M and the flexible beam are given by

$$T = T_b + \int_0^l T_{0,m}(y)\mathrm{d}y \ , \tag{3.5}$$

$$V = \int_0^l V_{0,m}(y)\mathrm{d}y \ , \tag{3.6}$$

where T_b is the kinetic energy function due to the motion of the carriage and is given by

$$T_b = \frac{1}{2} M \left(\dot{x}_b(t)\right)^2 \ . \tag{3.7}$$

The energy density functionals due to the flexibility of the beam, $T_{0,m}$ and $V_{0,m}$, can be expressed as

$$T_{0,m} = \frac{1}{2}\rho(y)\left[\dot{x}_b(t) + \dot{w}(y,t)\right]^2 \ , \tag{3.8}$$

$$V_{0,m} = \frac{1}{2} EI \left[w''(y,t)\right]^2 \ , \tag{3.9}$$

where E is the Young's Modulus and I is the second moment of area of the beam's cross-section. In the previous equation, the following notation was adopted:

$$(\bullet)' = \frac{\partial\,(\bullet)}{\partial y} \text{ and } \dot{(\bullet)} = \frac{\partial\,(\bullet)}{\partial t} \ .$$

The equations of motion can be obtained from Hamilton's principle [43] which is stated as follows:

$$\int_{t_1}^{t_2} \delta\left(T - V\right) \mathrm{d}t + \int_{t_1}^{t_2} \delta W_{nc} \mathrm{d}t = 0 \ , \tag{3.10}$$

with W_{nc} being the work done by non-conservative forces.

Taking into consideration the commutative properties of variation and differentiation, the variation of kinetic energy, δT, can be written as

$$\delta T = M\dot{x}_b(t)\delta\left[\dot{x}_b(t)\right] + \int_0^l \rho(y)\left[\dot{x}_b(t) + \dot{w}(t)\right]\delta\left[\dot{x}_b(t) + \dot{w}(t)\right]\mathrm{d}y \tag{3.11}$$

$$= M\dot{x}_b(t)\frac{\partial}{\partial t}\left(\delta x_b(t)\right) + \int_0^l \rho(y)\left[\dot{x}_b(t) + \dot{w}(t)\right]\left[\frac{\partial}{\partial t}\left(\delta x_b(t)\right) + \frac{\partial}{\partial t}\left(\delta w(y,t)\right)\right]\mathrm{d}y \ , \tag{3.12}$$

and the first term in equation (3.10) becomes

$$\begin{aligned}\int_{t_1}^{t_2} \delta T \mathrm{d}t = &\int_{t_1}^{t_2} M\dot{x}_b(t)\frac{\partial}{\partial t}\left(\delta x_b(t)\right)\mathrm{d}t \\ &+ \int_{t_1}^{t_2}\int_0^l \rho(y)\left[\dot{x}_b(t) + \dot{w}(t)\right]\frac{\partial}{\partial t}\left[\delta x_b(t) + \delta w(y,t)\right]\mathrm{d}y\mathrm{d}t \ .\end{aligned} \tag{3.13}$$

Following the procedure in Appendix A, equation (3.13) becomes

$$\begin{aligned}\int_{t_1}^{t_2} \delta T \mathrm{d}t = &-\int_{t_1}^{t_2} M\ddot{x}_b(t)\delta x_b(t)\mathrm{d}t \\ &- \int_{t_1}^{t_2}\left\{\int_0^l \rho(y)\left[\delta x_b(t) + \delta w(y,t)\right]\left[\ddot{x}_b(t) + \ddot{w}(y,t)\right]\mathrm{d}y\right\}\mathrm{d}t \ .\end{aligned} \tag{3.14}$$

Similarly, for the variation of potential energy:

$$\delta V = \int_0^l EIw''(y,t)\delta w''(y,t)\mathrm{d}y \tag{3.15}$$

$$= \int_0^l EIw''(y,t)\frac{\partial^2}{\partial y^2}\left(\delta w(y,t)\right)\mathrm{d}y \ , \tag{3.16}$$

the second term of equation (3.10) is then expressed as

$$\int_{t_1}^{t_2} \delta V \mathrm{d}t = \int_{t_1}^{t_2}\int_0^l EIw''(y,t)\frac{\partial^2}{\partial y^2}\left(\delta w(y,t)\right)\mathrm{d}y\mathrm{d}t \ , \tag{3.17}$$

which becomes, after manipulation (refer to Appendix A),

$$\begin{aligned}\int_{t_1}^{t_2} \delta V \mathrm{d}t = &\int_{t_1}^{t_2}\left\{\left[EIw''(y,t)\frac{\partial}{\partial y}\left(\delta w(y,t)\right)\right]\Big|_0^l\right. \\ &\left. - \left[\frac{\partial}{\partial y}\left(EIw''(y,t)\right)\delta w(y,t)\right]\Big|_0^l\right\}\mathrm{d}t \\ &+ \int_{t_1}^{t_2}\left\{\int_0^l \frac{\partial^2}{\partial y^2}\left[EIw''(y,t)\right]\delta w(y,t)\mathrm{d}y\right\}\mathrm{d}t \ .\end{aligned} \tag{3.18}$$

The virtual work done by the non-conservative forces is given by

$$\delta W_{nc} = f(t)\delta x_b(t) \ . \tag{3.19}$$

Substitution of equations (3.14), (3.18) and (3.19) in Hamilton's principle statement (3.10) leads to

$$\begin{aligned} -\int_{t_1}^{t_2} \Bigg\{ & \left[M\ddot{x}_b(t) + \int_0^l \rho(y) \left[\ddot{x}_b(t) + \ddot{w}(y,t) \right] \mathrm{d}y - f(t) \right] \delta x_b(t) \\ & + \int_0^l \left[\rho(y) \left[\ddot{x}_b(t) + \ddot{w}(y,t) \right] + \frac{\partial^2}{\partial y^2} \left[EIw''(y,t) \right] \right] \delta w(y,t) \mathrm{d}y \\ & + \left[EIw''(y,t) \delta \left(\frac{\partial w(y,t)}{\partial y} \right) \right] \Bigg|_0^l \\ & + \left[\frac{\partial}{\partial y} \left(EIw''(y,t) \right) \delta w(y,t) \right] \Bigg|_0^l \Bigg\} \mathrm{d}t = 0 \ . \end{aligned} \tag{3.20}$$

As $\delta x_b(t)$ and $\delta w(y,t)$ are arbitrary variations, the equations of motion for the beam-mass-carriage system with a fixed mass at h are:

$$M\ddot{x}_b(t) + \int_0^l \rho(y) \left[\ddot{x}_b(t) + \ddot{w}(y,t) \right] \mathrm{d}y = f(t) \ , \tag{3.21}$$

$$\frac{\partial^2}{\partial y^2} \left[EIw''(y,t) \right] + \rho(y) \left[\ddot{x}_b(t) + \ddot{w}(y,t) \right] = 0 \ , \tag{3.22}$$

as stated in references [12; 13]. The following equations also result from equation (3.20) and are the generalized boundary conditions:

$$EIw''(y,t) \delta \left(\frac{\partial w(y,t)}{\partial y} \right) \Bigg|_0^l = 0 \ , \tag{3.23}$$

$$\frac{\partial}{\partial y} \left(EIw''(y,t) \right) \delta w(y,t) \Bigg|_0^l = 0 \ . \tag{3.24}$$

Due to the rigid attachment of the elastic beam to the rigid moving carriage, it follows that the boundary conditions at $y = 0$ are

$$w(0,t) = 0 \ , \tag{3.25}$$

$$\left. \frac{\partial w(y,t)}{\partial y} \right|_{y=0} = 0 \ , \tag{3.26}$$

and at the other end, for $y = l$, since no moments or transverse forces are applied at the tip of the beam it follows that

$$\left. EI \frac{\partial^2 w(y,t)}{\partial y^2} \right|_{y=l} = 0 \ , \tag{3.27}$$

$$\left. \frac{\partial}{\partial y} \left(EI \frac{\partial^2 w(y,t)}{\partial y^2} \right) \right|_{y=l} = 0 \ . \tag{3.28}$$

Equations (3.25) and (3.26) are geometric boundary conditions while equations (3.27) and (3.28) translate the natural boundary conditions of the problem at hand.

It's noteworthy that if the lumped mass is located at the tip of the beam, this effect is included in the boundary conditions, therefore, equation (3.28) is replaced by

$$\left. \frac{\partial}{\partial y} \left(EI \frac{\partial^2 w(y,t)}{\partial y^2} \right) \right|_{y=l} = m \left(\ddot{x} + \ddot{w}(l,t) \right) \ . \tag{3.29}$$

3.2 Establishment of the semi-discrete model via the Assumed-mode method

Considering the mast deflection to be approximated by a series of admissible functions, $\psi_i(y)$ $i = 1, \ldots, n$, multiplied by the generalized time-dependent coordinates $q_i(t)$ $i = 1, \ldots, n$ [43], i.e.,

$$w(y,t) = \sum_{i=1}^{n} \psi_i(x) q_i(t) \ , \tag{3.30}$$

and from equations (3.5) and (3.8) the kinetic energy is given by

$$\begin{aligned} T(t) &= \frac{1}{2} M \left(\dot{x}_b(t)\right)^2 + \frac{1}{2} \int_0^l \rho(y) \left[\left(\dot{x}_b(t)\right)^2 + 2\dot{x}_b(t) \sum_{i=1}^{n} \psi_i(y) \dot{q}_i(t) \right. \\ &\left. + \sum_{j=1}^{n} \psi_j(y) \dot{q}_j(t) \sum_{k=1}^{n} \psi_k(y) \dot{q}_k(t) \right] \mathrm{d}y \\ &= \frac{1}{2} \left\{ \left(\dot{x}_b(t)\right)^2 \left[\int_0^l \rho(y) \mathrm{d}y + M \right] + 2\dot{x}_b(t) \sum_{i=1}^{n} \dot{q}_i(t) \int_0^l \rho(y) \psi_i(y) \mathrm{d}y \right. \\ &\left. + \sum_{j=1}^{n} \sum_{k=1}^{n} \dot{q}_j(t) \dot{q}_k(t) \int_0^l \rho(y) \psi_j(y) \psi_k(y) \mathrm{d}y \right\} \ , \end{aligned} \tag{3.31}$$

and following the same line of thought with equations (3.6) and (3.9), the potential energy is

$$\begin{aligned} V(t) &= \frac{1}{2} \int_0^l EI(y) \sum_{i=1}^{n} \frac{\mathrm{d}^2 \psi_i(y)}{\mathrm{d}y^2} q_i(t) \sum_{j=1}^{n} \frac{\mathrm{d}^2 \psi_j(y)}{\mathrm{d}y^2} q_j(t) \mathrm{d}y \\ &= \frac{1}{2} \sum_{i=1}^{n} \sum_{j=1}^{n} q_i(t) q_j(t) \left(\int_0^l EI(y) \frac{\mathrm{d}^2 \psi_i(y)}{\mathrm{d}y^2} \frac{\mathrm{d}^2 \psi_j(y)}{\mathrm{d}y^2} \mathrm{d}y \right) \ . \end{aligned} \tag{3.32}$$

Considering the following notation:

$$q_1^*(t) = x_b(t) \ , \tag{3.33}$$

$$q_{i+1}^*(t) = q_i(t) \quad i = 1, \ldots, n \ . \tag{3.34}$$

The space-discrete model is established by the use of the Lagrange equations [43]:

$$\frac{\mathrm{d}}{\mathrm{d}t} \left(\frac{\partial T}{\partial \dot{q}_s^*} \right) - \frac{\partial T}{\partial q_s^*} + \frac{\partial V}{\partial q_s^*} = Q_s \quad s = 1, \ldots, n+1 \ , \tag{3.35}$$

where Q_s $s = 1, \ldots, n+1$ are the generalized forces associated with the $q_s^*(t)$ $s = 1, \ldots, n+1$ generalized coordinates.

Substituting equations (3.31) and (3.32) in (3.35), the equations of motion of the discrete system are obtained as follows:

$$\sum_{p=1}^{n+1} m_{sp} \ddot{q}_s^*(t) + \sum_{p=1}^{n+1} k_{sp} q_s^*(t) = Q_s \quad s = 1, \ldots, n+1 \ , \tag{3.36}$$

or in matrix form,

$$\boldsymbol{M}\ddot{\boldsymbol{q}} + \boldsymbol{K}\boldsymbol{q} = \boldsymbol{Q} \ , \tag{3.37}$$

where $\boldsymbol{M}$ and $\boldsymbol{K}$ represent, respectively, the mass and rigidity coefficients matrix. The generalized coordinate vector, $\boldsymbol{q}$, the generalized acceleration vector, $\ddot{\boldsymbol{q}}$, and the generalized force vector, $\boldsymbol{Q}$, are

$$\boldsymbol{q} = \begin{Bmatrix} x_b(t) \\ q_1(t) \\ q_2(t) \\ \vdots \\ q_n(t) \end{Bmatrix} \ , \ \ddot{\boldsymbol{q}} = \begin{Bmatrix} \ddot{x}_b \\ \ddot{q}_1 \\ \ddot{q}_2 \\ \vdots \\ \ddot{q}_n \end{Bmatrix} \ , \ \boldsymbol{Q} = \begin{Bmatrix} f(t) \\ 0 \\ 0 \\ \vdots \\ 0 \end{Bmatrix} \ . \tag{3.38}$$

The mass coefficients, m_{sp} $s, p = 1, \ldots, n+1$ are given by

$$m_{sp} = \begin{cases} \displaystyle\int_0^l \rho(y)\mathrm{d}y + M & , s = 1 \wedge p = 1 \\ \displaystyle\int_0^l \rho(y)\psi_{p-1}(y)\mathrm{d}y & , s = 1 \wedge p \neq 1 \\ \displaystyle\int_0^l \rho(y)\psi_{s-1}(y)\mathrm{d}y & , s \neq 1 \wedge p = 1 \\ \displaystyle\int_0^l \rho(y)\psi_{s-1}(y)\psi_{p-1}(y)\mathrm{d}y & , \text{otherwise} \end{cases} , \tag{3.39}$$

while the rigidity coefficients, k_{sp} $s, p = 1, \ldots, n+1$ are

$$k_{sp} = \begin{cases} 0 & , s = 1 \vee p = 1 \\ \displaystyle\int_0^l EI(y)\frac{\mathrm{d}^2\psi_{s-1}(y)}{\mathrm{d}y^2}\frac{\mathrm{d}^2\psi_{p-1}(y)}{\mathrm{d}y^2}\mathrm{d}y & , \text{otherwise} \end{cases} . \tag{3.40}$$

Approximation functions

A family of functions that proves particularly adequate for the application of the assumed-mode method in this problem comes from the study of the free vibration of a constant-section cantilever beam of length l. The exact solution of the corresponding eigenvalue problem leads to the following mode shapes [43]:

$$\phi_i^{CB} = C_i \left\{\cosh(\beta_i y) - \cos(\beta_i y) - \gamma_i \left[\sinh(\beta_i y) - \sin(\beta_i y)\right]\right\} \quad i = 1, \ldots, \infty \ , \tag{3.41}$$

where

$$\gamma_i = \frac{\sinh(\beta_i l) - \sin(\beta_i l)}{\cosh(\beta_i l) + \cos(\beta_i l)} \quad i = 1, \ldots, \infty \ , \tag{3.42}$$

$$\beta_i = \frac{2i-1}{2}\frac{\pi}{l} \quad i = 1, \ldots, \infty \ , \tag{3.43}$$

and C_i $i = 1, \ldots, \infty$ are constants. The natural frequencies of the cantilever beam, ω_i^{CB} $i = 1, \ldots, n$ are derived from equation (3.43) as follows

$$\omega_i^{CB} = (\beta_i l)\sqrt{\frac{EI}{\rho_0 l^4}} \quad i = 1, \ldots, \infty \ , \tag{3.44}$$

Therefore, adopting the following family of approximation functions,

$$\psi_i(y) = \cosh(\beta_i y) - \cos(\beta_i y) - \gamma_i \left[\sinh(\beta_i y) - \sin(\beta_i y)\right] \quad i = 1, \ldots, n \ , \tag{3.45}$$

that admit 2nd derivative in respect to y and are compatible with the geometric boundary conditions of equations (3.25) and (3.26) and are, therefore, admissible. The first and second derivatives are, respectively:

$$\frac{\mathrm{d}\psi_i(y)}{\mathrm{d}y} = \beta_i \left\{\sinh(\beta_i y) + \sin(\beta_i y) - \gamma_i \left[\cosh(\beta_i y) - \cos(\beta_i y)\right]\right\} \ , \tag{3.46}$$

$$\frac{\mathrm{d}^2\psi_i(y)}{\mathrm{d}y^2} = \beta_i^2 \left\{\cosh(\beta_i y) + \cos(\beta_i y) - \gamma_i \left[\sinh(\beta_i y) + \sin(\beta_i y)\right]\right\} \ . \tag{3.47}$$

Substitution of equations (3.45) and (3.47) in (3.39) and (3.40) leads to the computation of the mass and rigidity coefficients.

3.3 Natural frequencies and mode shapes

For $f(t) = 0$ in equation (3.37), the equations of motion of the semi-discrete model become

$$\boldsymbol{M}\ddot{\boldsymbol{q}} + \boldsymbol{K}\boldsymbol{q} = \boldsymbol{0} \ , \tag{3.48}$$

which represent the free vibration of the system. In this case, the generalized coordinates variation in time is known to be harmonic and thus of the form

$$q_s^*(t) = u_s^* \cos(\omega t) \quad s = 1, \ldots, n+1 \ , \tag{3.49}$$

where u_s^* $s = 1, \ldots, n+1$ represents the amplitude of $q_s^*(t)$ and ω the frequency of the harmonic movement.

The substitution of the previous equation in (3.48) leads to the generalized eigenvalue and eigenvector problem associated with the discrete system:

$$\boldsymbol{K}\boldsymbol{u} = \omega^2 \boldsymbol{M}\boldsymbol{u} \ , \tag{3.50}$$

whose solution are the $n+1$ eigenvalue-eigenvector pairs, $(\omega_r^2;\ \boldsymbol{u}_r)$ $r = 1, \ldots, n+1$, where the eigenvalues are the approximations of the natural frequencies of vibration of the associated continuous system and, the eigenvectors, the generalized coordinate amplitude vectors associated with each mode of vibration. The corresponding approximation for the $n+1$ mode shapes of the continuous system of Figure 3.1 will thus be obtained by

$$\bar{\phi}_r(y) = \alpha_r + \sum_{i=1}^{n} \psi_i(y) u_{i+1,r} \quad r = 1, \ldots, n \ , \tag{3.51}$$

Where the scalar α_r is the amplitude of the harmonic movement of the carriage for the rth mode of vibration, given by

$$\alpha_r = u_{1r} \ . \tag{3.52}$$

Results and discussion

For the application of the presented model, the system parameters shown in Table 3.1 were considered and four approximation functions ($n = 4$) were used. The beam's cross-section was assumed to be the same throughout its length.

Table 3.1: System parameters [12].

Parameter	Value
M	10.0 kg
l	1.0 m
ρ_0	0.788 kg/m
E	2.07×10^{11} Pa
I	5.208×10^{-11} m^4

One of the solutions of the eigenvalue problem of equation (3.50) will naturally correspond to the rigid-body motion of the system as it doesn't have any connections to the exterior. Due to its non-oscillatory nature, this mode is disregarded in the following discussion and $(\omega_i; \bar{\phi}_i(y))$ $i = 1, \ldots, n$ taken to be the natural frequency-mode shape pairs associated with the non-zero potential energy modes.

The remaining four natural mode shapes, i.e., the non-zero potential energy mode shapes, predicted by the assumed-mode method using $n = 4$ can be observed in Figure 3.2. The lumped mass was assumed to be placed at the tip of the beam ($h/l = 1$) and its value, m, is such that $r_m = m/M = 0.1$.

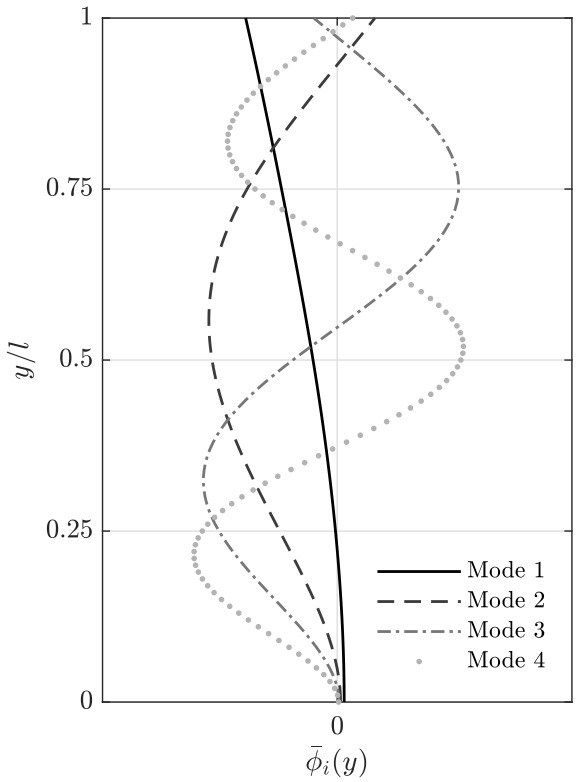


Figure 3.2: First four non-zero potential energy mode shapes for $r_m = 0.1$ and $h/l = 1$.

On Figures 3.3 and 3.4 the first four mode shapes are shown for different values of r_m,

with the lumped mass positioned at $y = l$ and $y = 0.5l$ respectively. It can be seen that, in general, the mode shapes are largely affected by the change of r_m, especially as $r_m \to 0$. However, the third mode shape reveals largely unaffected by the lumped mass when it is placed at the mid-span of the beam. This is explained by the proximity of the lumped mass to a node of vibration of this particular mode shape.

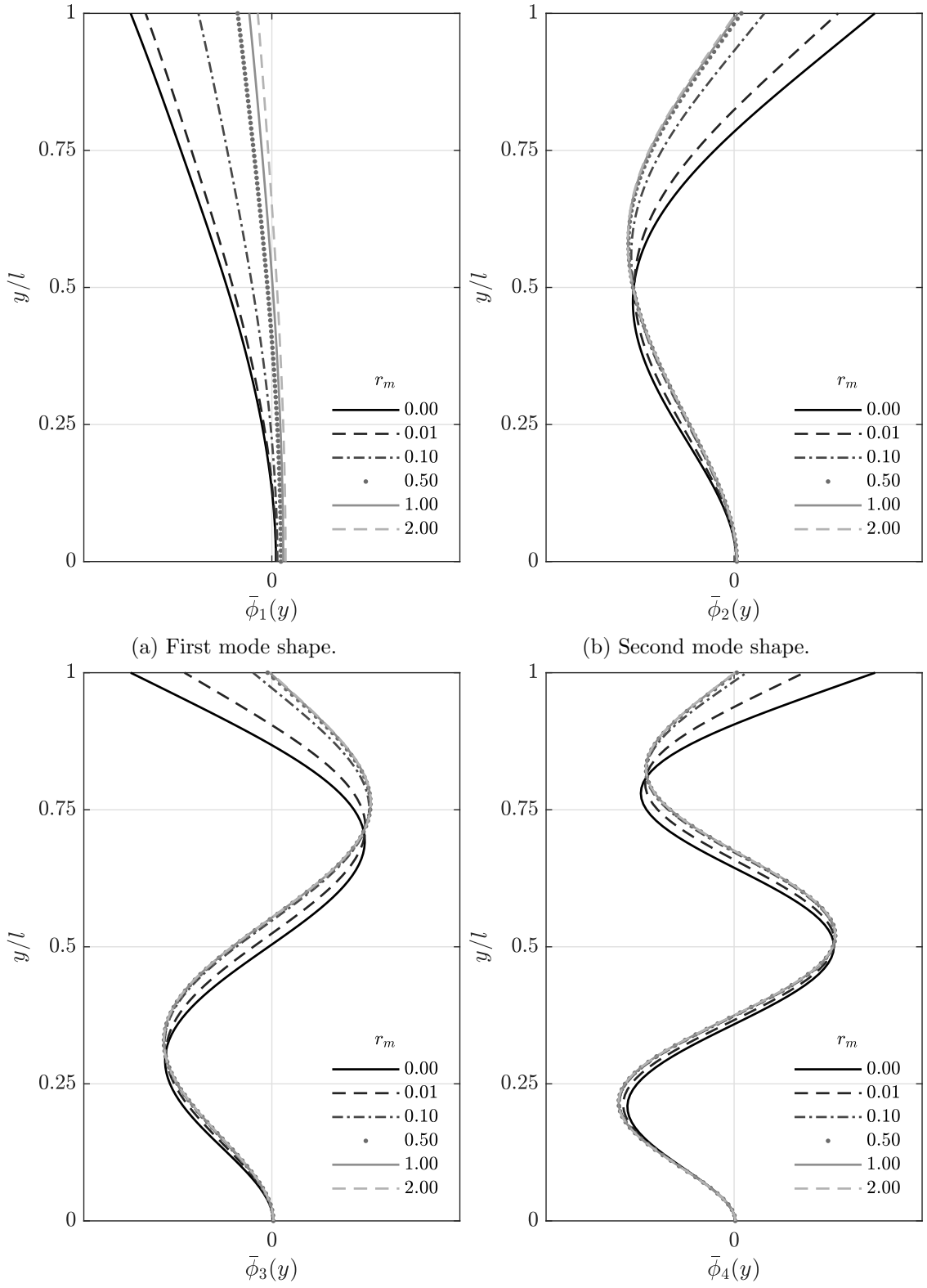
Also, in general, the increase in the ratio r_m provoked a displacement of the vibration nodes in the direction that shortens their distance to the position of the lumped mass.

As regards the dependency of the mode shapes with the lumped mass position, Figures 3.5 and 3.6 shows the first four mode shapes for different values of h/l, considering $r_m = 0.1$ and $r_m = 1$, respectively. For the first vibration mode, it's noticeable an upward displacement of the node with the increase in h. The remaining mode shapes' variation is easier to explain with the help of Figure 3.7 where the first four natural frequencies are shown as a function of the lumped mass' position, for different values of r_m. The frequency results are shown adimensionalized according to

$$\bar{\omega}_i = \sqrt[4]{\omega_i^2 \frac{\rho_0 l^4}{EI}} \quad i = 1, \ldots, n \ . \tag{3.53}$$

Returning to Figures 3.5 and 3.6, one can see that, as the lumped mass' position approaches the vibration nodes of the $r_m = 0$ curve, the mode shapes become independent of r_m and the corresponding mode's natural frequency approaches the maximum value, corresponding to the $r_m = 0$ case.

It can be seen from Figure 3.7 that the maximum possible natural frequencies are found for the case of $r_m = 0$ while maintaining all the remaining parameters constant. Even if $r_m > 0$, the natural frequencies will achieve their maximum value when the payload is positioned at the vibration nodes of the corresponding $r_m = 0$ mode shapes, at which point they become independent of r_m. Moreover, for a given r_m, the minimum value of the first natural frequency is found when $h/l = 1$. Finally, the increase of the lumped mass magnitude provokes a decrease in the natural frequencies of the system which is more noticeable at lower values of r_m.



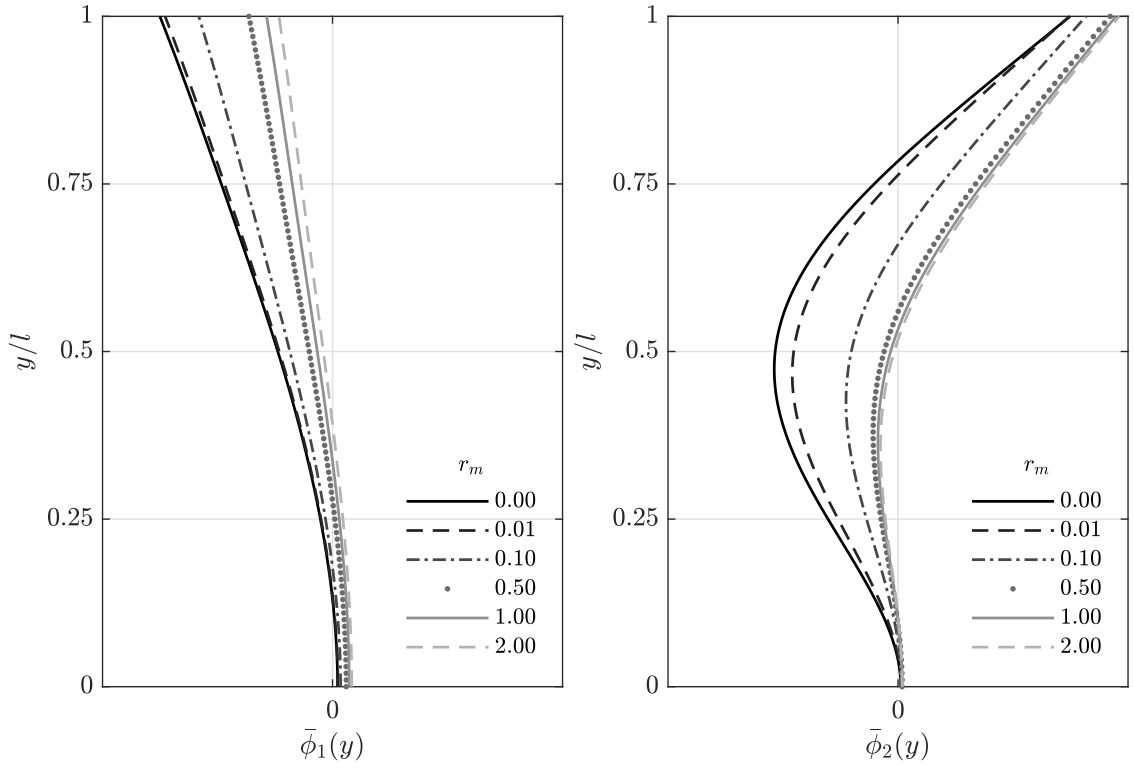
(a) First mode shape.

(b) Second mode shape.

(c) Third mode shape.

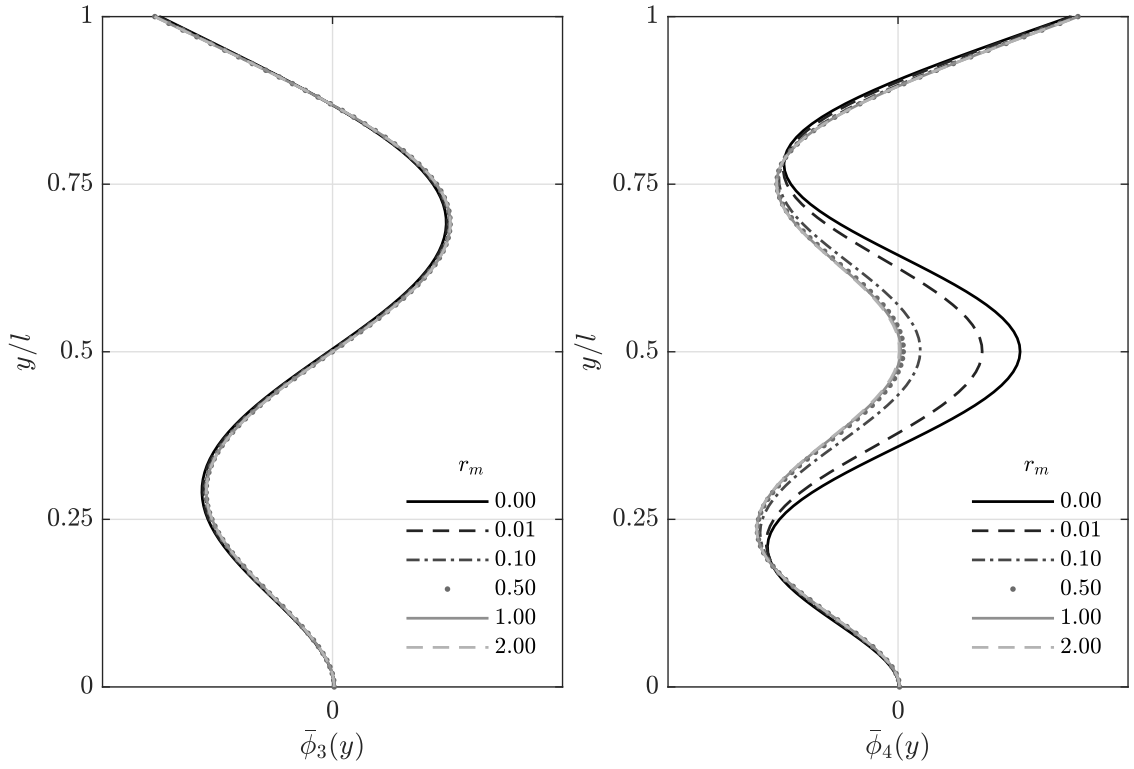
(d) Fourth mode shape.

Figure 3.3: First four mode shapes for different values of r_m with the lumped mass at the tip ($h/l = 1$).



(a) First mode shape.

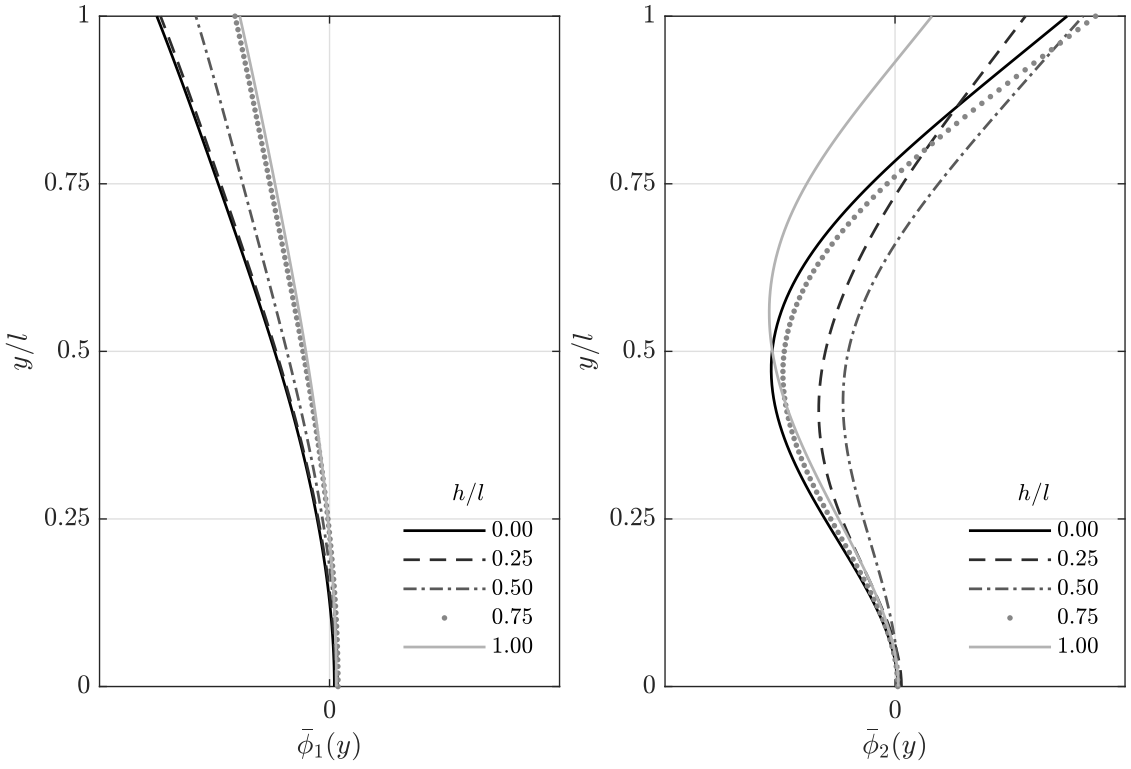
(b) Second mode shape.



(c) Third mode shape.

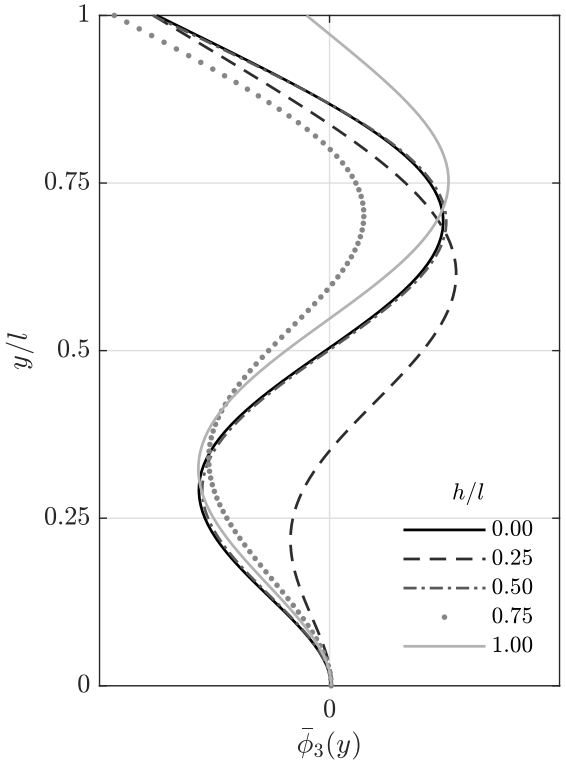
(d) Fourth mode shape.

Figure 3.4: First four mode shapes for different values of r_m with the lumped mass at mid-span ($h/l = 0.5$).

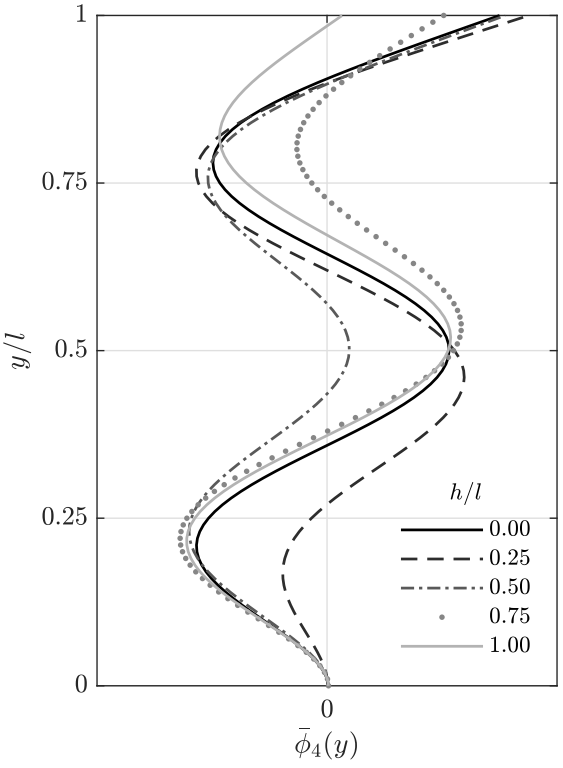


(a) First mode shape.

(b) Second mode shape.

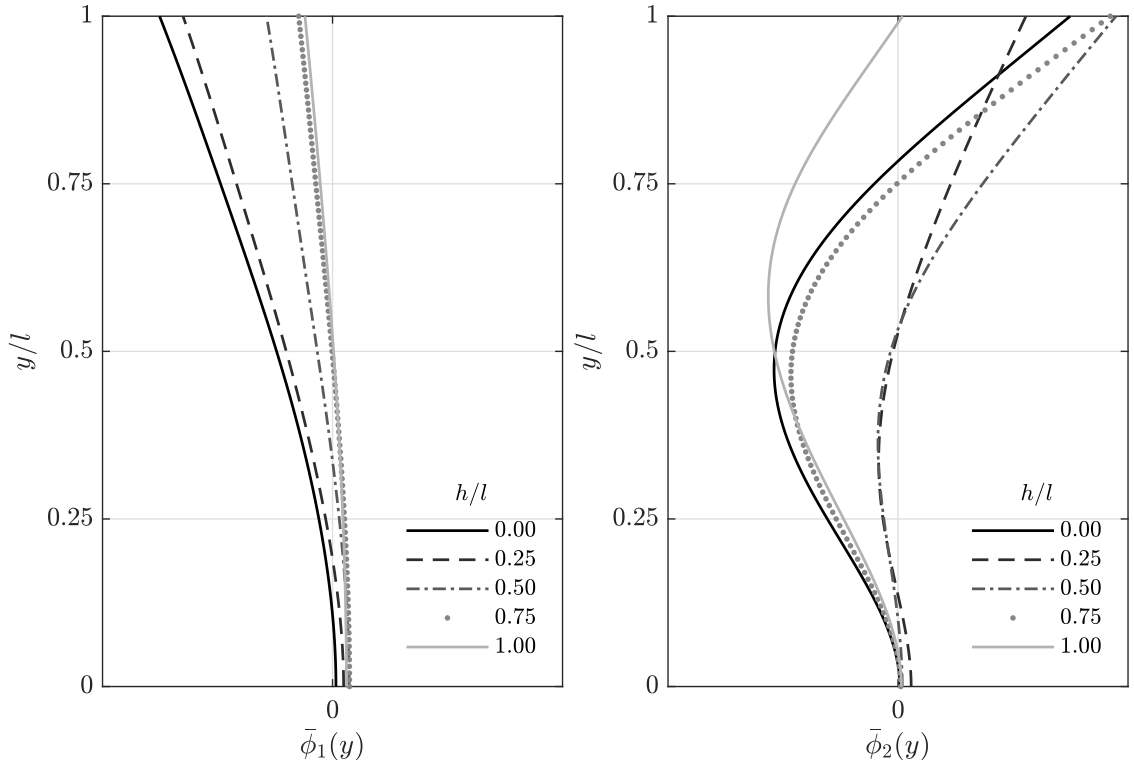


(c) Third mode shape.



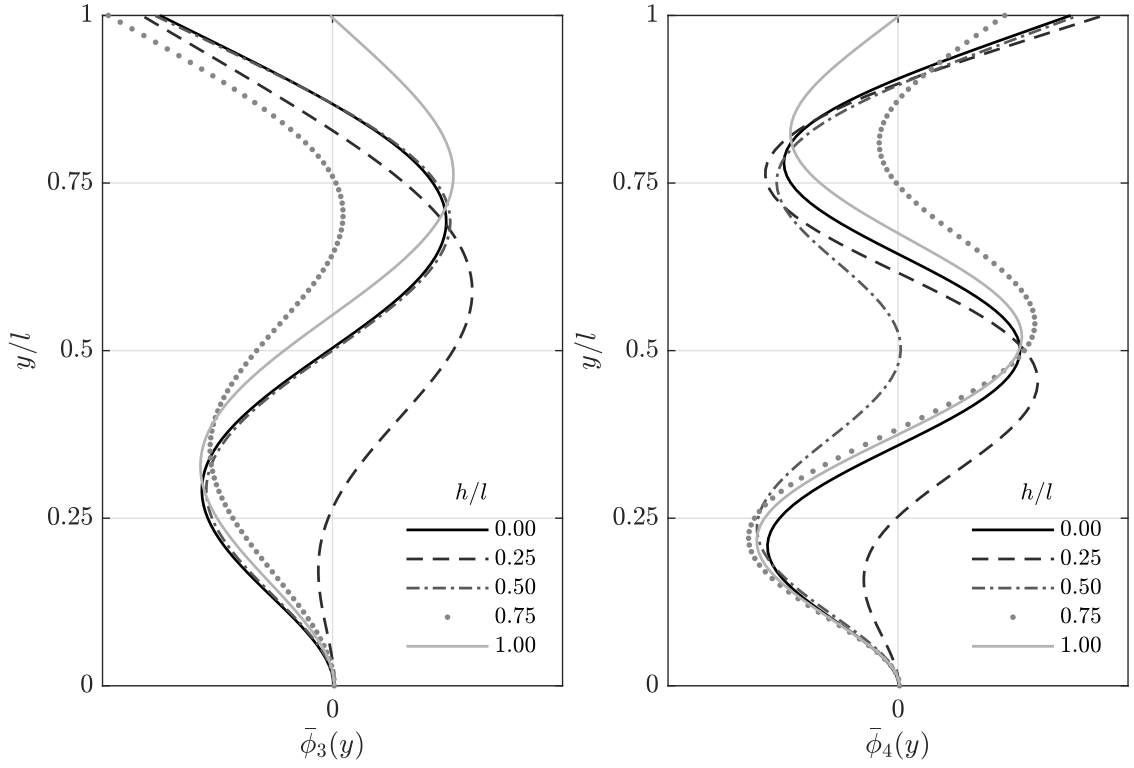
(d) Fourth mode shape.

Figure 3.5: First four mode shapes for different values of h/l with $r_m = 0.1$.



(a) First mode shape.

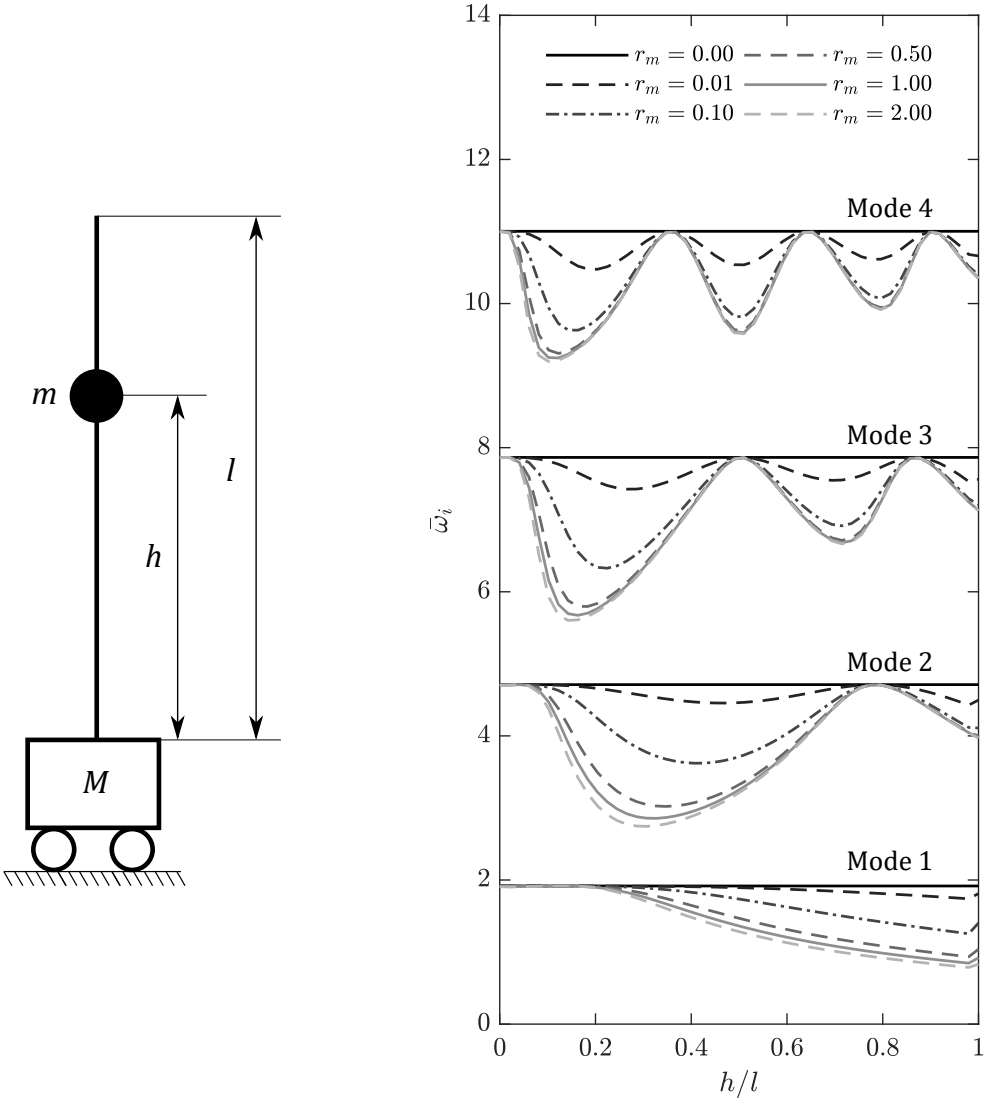
(b) Second mode shape.



(c) Third mode shape.

(d) Fourth mode shape.

Figure 3.6: First four mode shapes for different values of h/l with $r_m = 1$.



(a) Notation used.

(b) Computed natural frequencies.

Figure 3.7: First four natural frequencies with respect to the change of the position of the lumped mass for various values of $r_m = m/M$.

Chapter 4

Free vibration of stacker cranes using the FEM

The following chapter presents the modal analysis of the stacker cranes from Consoveyo's product range. A STK-21-C double mast stacker crane was chosen for an initial study due to its simpler mast geometry when compared to single mast stacker cranes as was previously discussed in section 2.4.1. Details on this machine can be found in section 4.1.

On section 4.2, FEM models are developed using the commercial software ANSYS© Workbench (WB) Mechanical.

Moreover, the natural vibration modes and frequencies are investigated in section 4.3 as these provide great insight into the crane structure's behaviour under dynamic loading, which will prove useful in Chapter 5. Also, parametric studies are presented with varying payload's height, mass and masts' height and its results analysed to assess the influence of these parameters on the crane's natural frequencies and mode shapes.

The chapter concludes with remarks regarding the application of the same procedure to a single mast stacker crane model in section 4.4.

Although the full range wasn't studied, the procedure henceforth described can be applied to the remaining models.

4.1 Machine specifications

The machine to be studied is a model STK-21-C double mast stacker crane from a previous Consoveyo project. The original crane has a total height of nearly 41 m from its lowest to its highest point, a wheelbase of 6.6 m and weights about 40.9 t.

A schematic figure of the crane indicating its structural components and zoomed in details of other additional components can be found in Figure 4.1.

4.1.1 Structure

The main structural elements of the STK-21-C are:

- two masts;
- bottom carriage;
- upper crossbeam.

The mast assemblies, on both the electrical cabinet (EC) and hoist unit (HU) sides, are comprised of four levels of rectangular tubes welded in a T-like shape as shown in Figure 4.2. The tube thickness is reduced gradually along the mast's height from the lowest to the highest level as to reduce the overall structure's weight without compromising it's

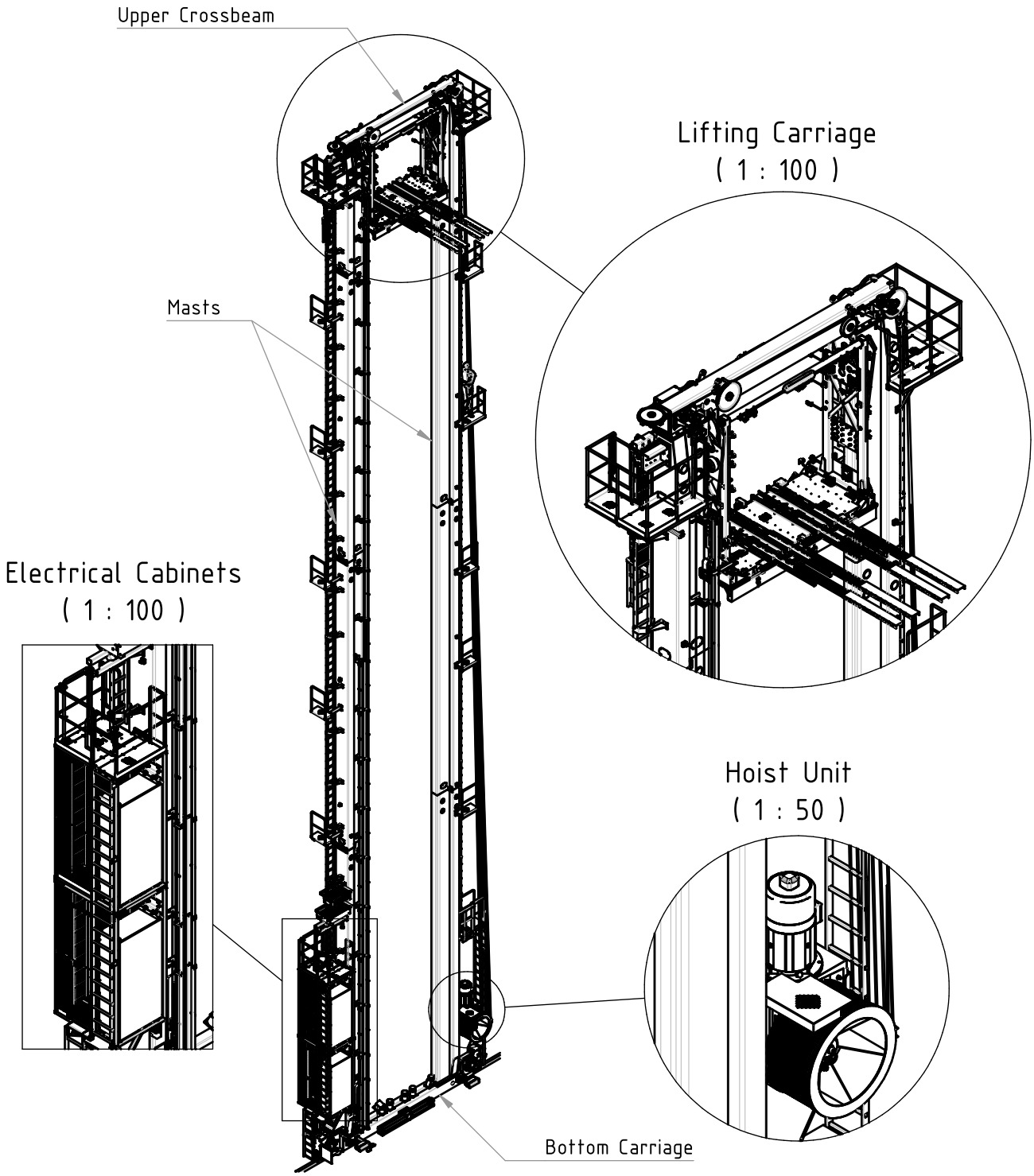


Figure 4.1: Original STK-21-C model used in the present study (scale 1 : 200).

strength in the lower regions of the mast. Due to transportation limitations, the length of each tube piece is capped at 11.7 m with that being the reason why, despite having the same cross-section, the 3rd and 4th level of each mast aren't made out of a single part. Length and cross-section dimensions per mast level, attending to the nomenclature of Figure 4.2 can be found in Table 4.1.

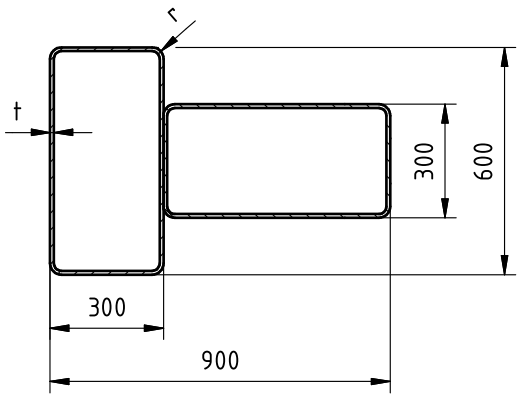


Figure 4.2: Cross-section geometry and dimensions (in mm) for the STK-21-C.

Table 4.1: Length and cross-section dimensions per mast level for the original STK-21-C.

Level	Length /mm	Thickness t /mm	Outer fillet radius r /mm
1st	11700	12.5	32.5
2nd	11700	10	30
3rd	11700	8	28
4th	4704	8	28

Two steel sheet plates are welded to the 1st and 4th level tube construction. Additionally, for the 1st level, sheet metal plates are added to support the EC and HU assemblies, inherently reinforcing the mast in those zones. The final mast assemblies considering all columns bolted together and the welded end plates have a total length of 39.9 m and can be seen in Figure 4.3. Note that both masts are identical except for the 1st level.

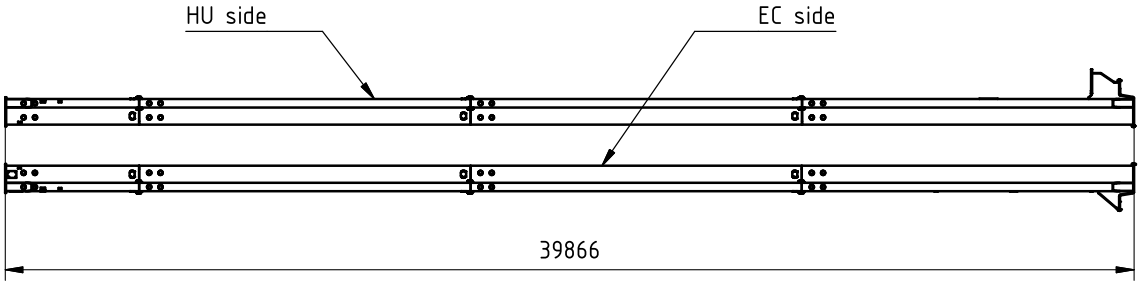


Figure 4.3: STK-21-C stacker crane's masts geometry and length (in mm).

The bottom carriage is comprised of two hot rolled rectangular tubes with their axes aligned with the machine's direction of travel that connect the wheel housings. Four short tubular elements join both tubes together. Figure 4.4 shows the bottom carriage assembly while Table 4.2 presents the dimensions of the rectangular tubular elements, following a

similar notation to Table 4.1.

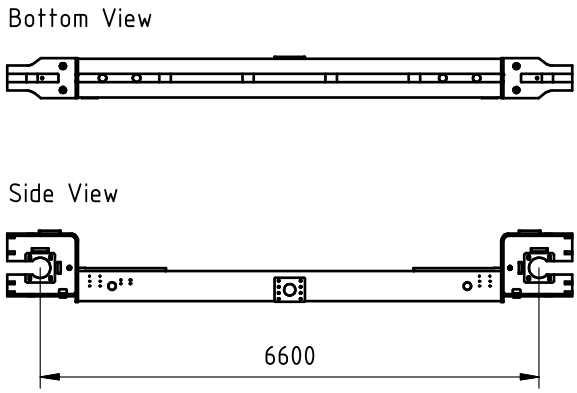


Figure 4.4: STK-21-C stacker crane's bottom carriage geometry and wheelbase dimension (in mm).

Table 4.2: Bottom carriage's tube length and cross-section dimensions for the original STK-21-C crane.

	Quantity	Cross-section /mm × mm	Length /mm	Thickness /mm	Outer fillet radius /mm
Long tubes	2	400 × 200	5600	12.5	18.5
Short tubes	4	250 × 150	110	8	14

The upper crossbeam (Figure 4.5), a tubular structure with two steel plates welded at each end is bolted to the top of the two masts, completing the frame structure. Several shafts are placed along holes made in the crossbeam to assemble the pulleys that guide the steel wire rope that hoists the lifting carriage. Following the reasoning of Tables 4.1 and 4.2, Table 4.3 shows the dimensions of the upper crossbeam tubular element.

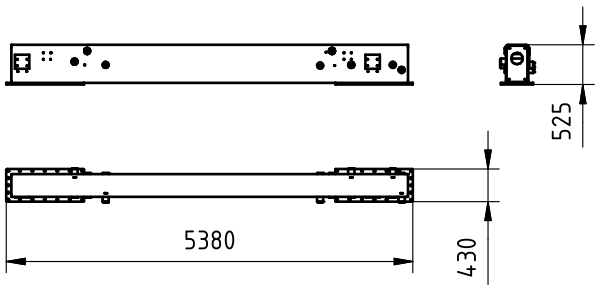


Figure 4.5: STK-21-C stacker crane's upper crossbeam geometry (dimensions in mm).

Table 4.3: Upper crossbeam's tube length and cross-section dimensions for the original STK-21-C crane.

Cross-section /mm × mm	Length /mm	Thickness /mm	Outer fillet radius /mm
500 × 300	5250	12.5	32.5

The whole crane's structure is made of S355JR grade structural steel whose mechanical properties are presented in Table 4.4.

Table 4.4: Mechanical properties at ambient temperature for S355JR steel [44].

Designation	Min. yield strength σ_y /MPa	Min. tensile strength σ_R /MPa
S355JR	355	470

Because of the importance of the inertial effects when the crane impacts the end stops, it's necessary to make sure that the developed models respect the machine's mass distribution. As such, Table 4.5 shows the mass of the structural components of the stacker crane mentioned above, this information was taken from the crane's 3D Computer-Aided Design (CAD) model in Autodesk Inventor© considering the density of steel to be 7850 kg/m^3.

Table 4.5: Mass of the original STK-21-C structural components taken from the Autodesk Inventor© CAD model.

Component	Mass /kg
1st Column (EC side)	4438
1st Column (HM side)	4732
2nd Column	3382
3rd Column	2774
4th Column	1260
Bottom carriage	2811
Crossbeam	1033

4.1.2 Additional components

From Figure 4.1 it can be seen that the reference machine for this study has two electrical cabinets placed on top of each other, with the heavier one being on top. A hoist unit placed on the opposite mast of the electrical cabinets, provides the vertical motion to the lifting carriage. The lifting carriage is equipped with a double deep telescopic fork as the LHD. Two travel units, one coupled to each wheel, provide the travel motion to the crane.

The weight of these assemblies, as measured[1], can be seen in Table 4.6.

Table 4.6: Mass of the original STK-21-C additional components as measured.

Component	Mass /kg
EC assembly	1500
Lifting carriage w/ LHD	4340
HU	2397
Travel unit	470

Other components like access ladders with a total weight of 640 kg (1.6% of total

[1]The *EC assembly* value was taken from summing the mass of the structure holding the electrical cabinets taken from the CAD model with both ECs' masses (275 and 355 kg).

mass) and maintenance platforms, 712 kg total (1.7% of total mass), are also present in the machine but these will be disregarded from the analysis as will be explained.

4.2 Analysis setup

4.2.1 Modelling concepts and geometry creation

The original stacker crane geometry was provided by Consoveyo as modelled with the Autodesk Inventor© 3D CAD package (Figure 4.1).

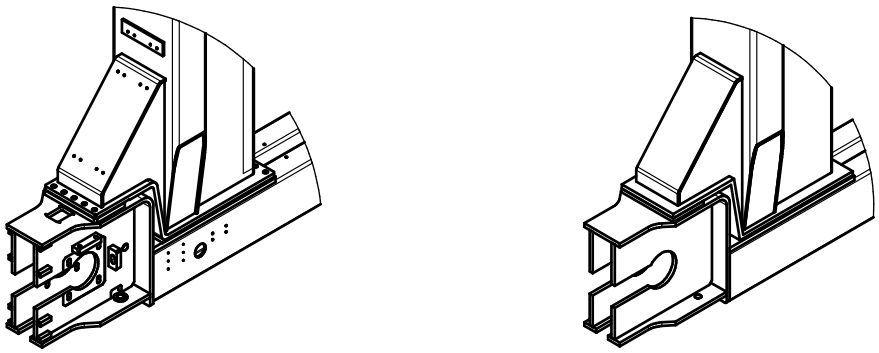
Because of the immense detail, this model wasn't suited for analysis using the FEM. As such, a simpler, lighter geometry model was created in order to run the simulations.

A new 3D geometry was created using Autodesk Inventor© where components such as maintenance platforms, safety rails and access ladders along the mast were disregarded due to being evenly distributed and having relatively low dimensions and mass when compared to the main structural components.

Assemblies with considerable mass and relatively small dimensions when compared with the crane's frame were also eliminated from the 3D geometry as they will later be implemented as lumped masses in the model.

The wheels and wheel shafts were also disregarded from the 3D geometry and replaced with adequate boundary conditions as will be explained in section 4.2.3.

Using ANSYS© SpaceClaim© application, functional features of the geometry like holes for bolted connections or excess material to allow for welding operations were removed. The reason being that the local stresses in these regions wouldn't change the stress distribution in the critical regions and, also, their removal would be favourable towards obtaining a structured finite element mesh. Figure 4.6 shows the wheel housings before and after the geometry simplification as an example of the mentioned procedure.



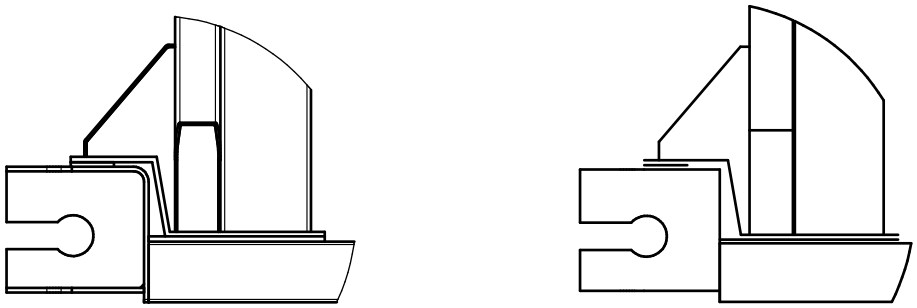
(a) Solid model (Autodesk Inventor©).

(b) Solid model (SpaceClaim©).

Figure 4.6: Wheel housings before and after geometry simplification using SpaceClaim© (scale 1 : 50).

As will be explained in section 4.2.5, shell finite elements will be used so it is necessary to prepare the CAD geometry for such analysis by extracting the mid surfaces of the structure, a process done inside SpaceClaim©'s environment. A before and after comparison can be seen in Figure 4.7 using the wheel housing example.

It must be noted that, in order to obtain a smaller number of elements in the mesh, the rounded corners of the masts tubular cross-section were replaced by 90° angles as a finer



(a) Solid model (SpaceClaim©).

(b) Surface model (SpaceClaim©).

Figure 4.7: Wheel housings before and after mid-surface extraction using SpaceClaim© (scale 1 : 50).

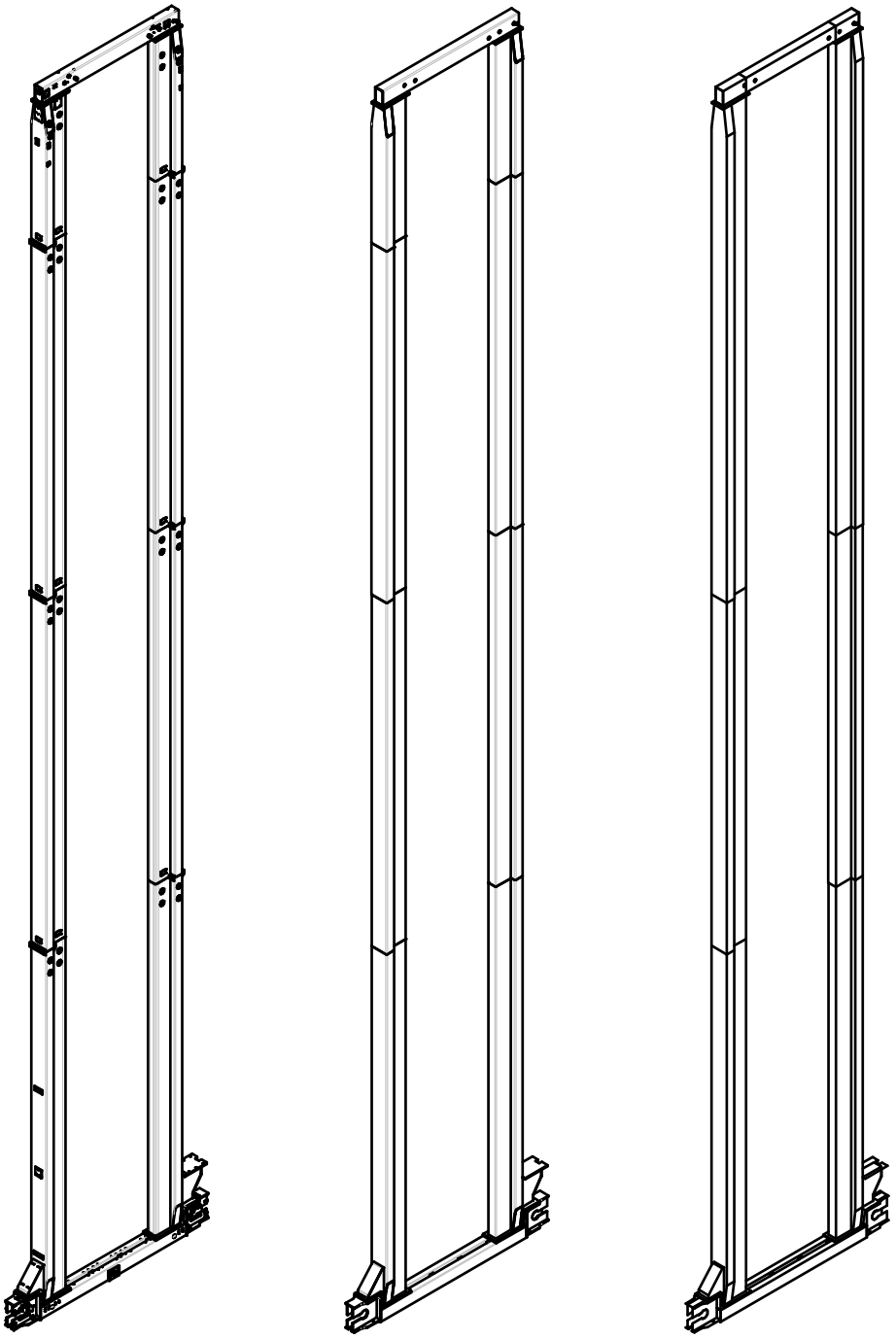
mesh would be necessary to capture this curvature. Figure 4.8 presents the aforementioned stages of model simplification from the original CAD model of Figure 4.1.

The changes in the structure's geometry inevitably led to changes in its mass distribution which may in turn produce erroneous results in subsequent analysis where inertial effects play an important role.

As such, Table 4.7 presents a comparison between the mass of the structural components taking into account the initial geometry and their final geometry counterparts following the nomenclature adopted in Table 4.5. The field "total" refers to the overall structure's mass as the sum of its components. Given this comparison, the final model was considered an acceptable approximation of the initial structure in terms of mass distribution.

Table 4.7: Comparison of the initial and final mass of the main structure.

Component	Mass /kg		Error /%
	Real	Model	
1st Column (EC side)	4438	4410	0.64
1st Column (HM side)	4732	4689	0.91
2nd Column	3382	3233	4.41
3rd Column	2774	2600	6.34
4th Column	1260	1146	9.02
Bottom carriage	2811	2810	0.04
Crossbeam	1033	1007	2.48
Total	27846	26871	3.50



(a) Solid model (Autodesk Inventor©).

(b) Solid model (SpaceClaim©).

(c) Surface model (SpaceClaim©).

Figure 4.8: Stages of simplification of the geometry from the original model of Figure 4.1.

4.2.2 Lumped masses

As stated in the previous section, components not part of the main structure but with significant mass and small dimensions were taken into account as lumped masses, which are by themselves a form of boundary conditions. Such components were:

- lifting carriage;
- load handling device;
- payload;
- hoist unit;
- electrical cabinet assembly.

Lifting carriage with LHD and payload

A single lumped mass was considered to represent the inertial effects of the lifting carriage with the LHD and the payload on the structure. Figure 4.9 shows its representation in the ANSYS© WB Mechanical environment. The lumped mass value, m_{LH}, is thus the sum of the masses of these elements (see Table 4.6),

$$m_{LH} = 4340 + m_L \ , \tag{4.1}$$

with m_L being the payload's mass.

The lumped mass properties are defined via the *point mass* feature in ANSYS© WB Mechanical. It's necessary to firstly define the lumped mass' location via the creation of a *remote point* as well as its *slave geometry*. The centre of gravity (COG) of the carriage, LHD and payload set was placed such as its y-position was taken to be in the middle of the two rollers sets that contact each mast and at the centre of the carriage's platform in the xz-plane (considering Figure 4.9's xyz-triad). This, as one can see from Figure 4.9c, is displaced slightly, by 100 mm, in relation to the masts symmetry plane.

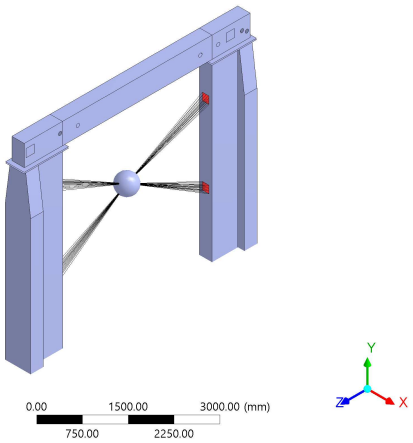
On the other hand, the slave geometry designates the points, edges or surfaces onto which the point mass transfers its inertial effects. Therefore, four surfaces placed where the rollers of the lifting carriage contact the mast in the real crane were chosen as the slave geometries. The lines seen in Figure 4.9 represent the equations the software establishes between the point mass and the finite element nodes.

It is important to note that ANSYS© WB Mechanical provides different options for the behaviour of the slave geometry of a remote type boundary condition such as a point mass [45]:

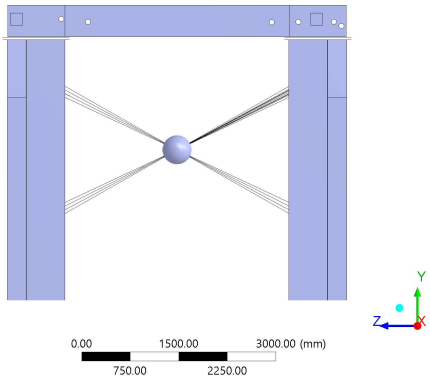
- *Deformable*: the *slave geometry* is free to deform and the displacements applied to the pilot node are distributed to the slave nodes through shape functions. As such, constraint equations are created such that the motion of the master is the average of the slaves;
- *Rigid*: the geometry will maintain its initial shape. This option is useful if the "abstracted" object (the lifting carriage) stiffens the model significantly at the attachment point;
- *Coupled*: the geometry has the same degree of freedom (DOF) solution on its underlying nodes as the remote point location;

– *Beam*: connects the *remote point* to the *slave geometry* using linear massless beam elements.

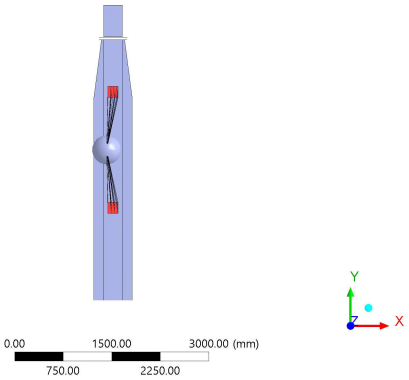
From the above information provided in the ANSYS© Help system [45] and tests carried out, the *deformable* behaviour option in ANSYS© WB Mechanical was chosen for the connection of the lumped mass and the structure as to only consider the mass increase in the model, leaving a possible local rigidity increase unaccounted for as it was deemed irrelevant when compared to the masts' rigidity.



(a) Isoparametric view.



(b) As seen from the x-axis.



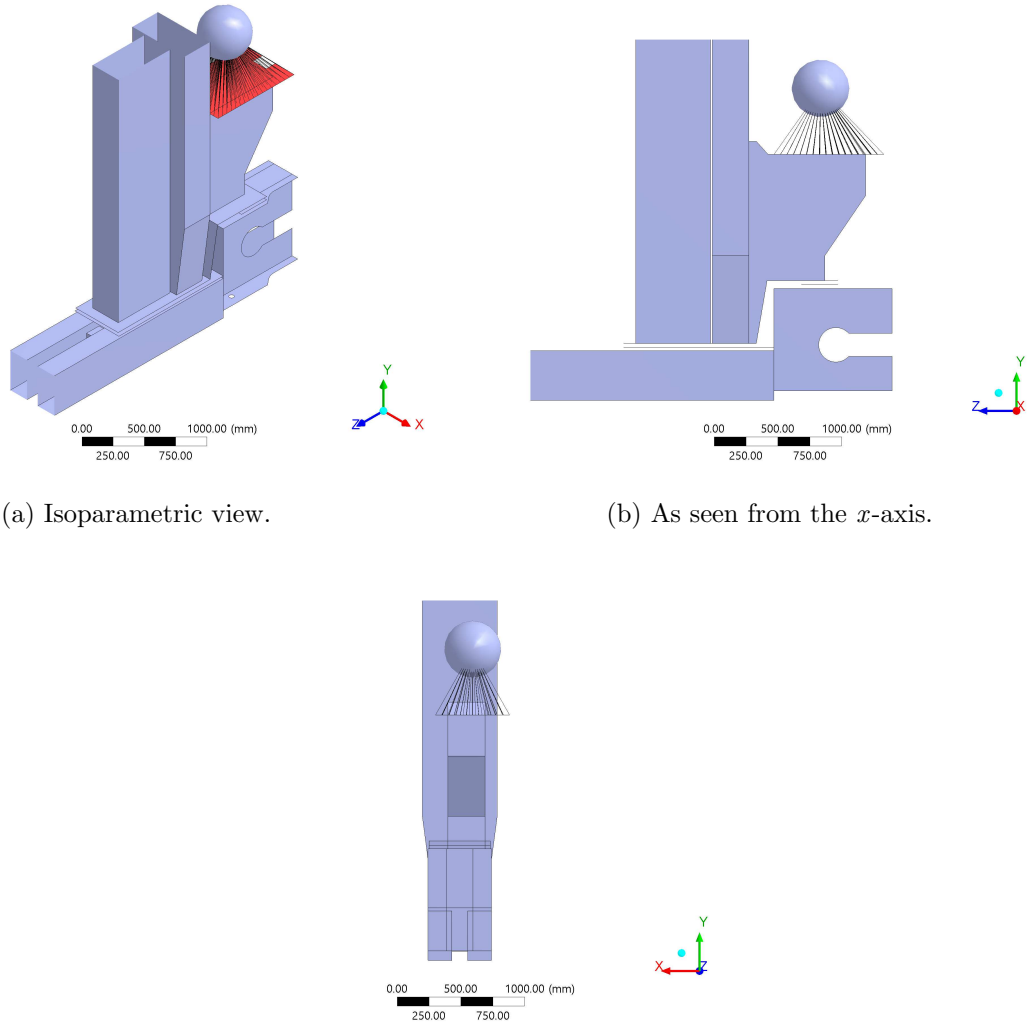
(c) As seen from the z-axis.

Figure 4.9: Lumped mass representing the lifting carriage, LHD and payload in ANSYS© WB Mechanical.

Hoist unit

The mass of the hoist unit was also considered as a lumped mass (Figure 4.10) of value $m_{HM} = 2397$ kg, taken from Table 4.6.

Position information for the COG of the gearmotor drive wasn't available in the manufacturer's catalogue. It was considered however that, in the x-direction, it lied on the plane of symmetry of the HU's mounting plate, parallel to the yz-plane. Moreover, in the z-direction, the COG was taken to be in-line with the spooling drums' axis. Meanwhile, in the y-direction, the COG was taken to be slightly above the same axis, by 200 mm. Although the placement of the lumped mass wasn't rigorous, it's not expected to influence the results, specially for higher cranes.



(a) Isoparametric view.

(b) As seen from the x-axis.

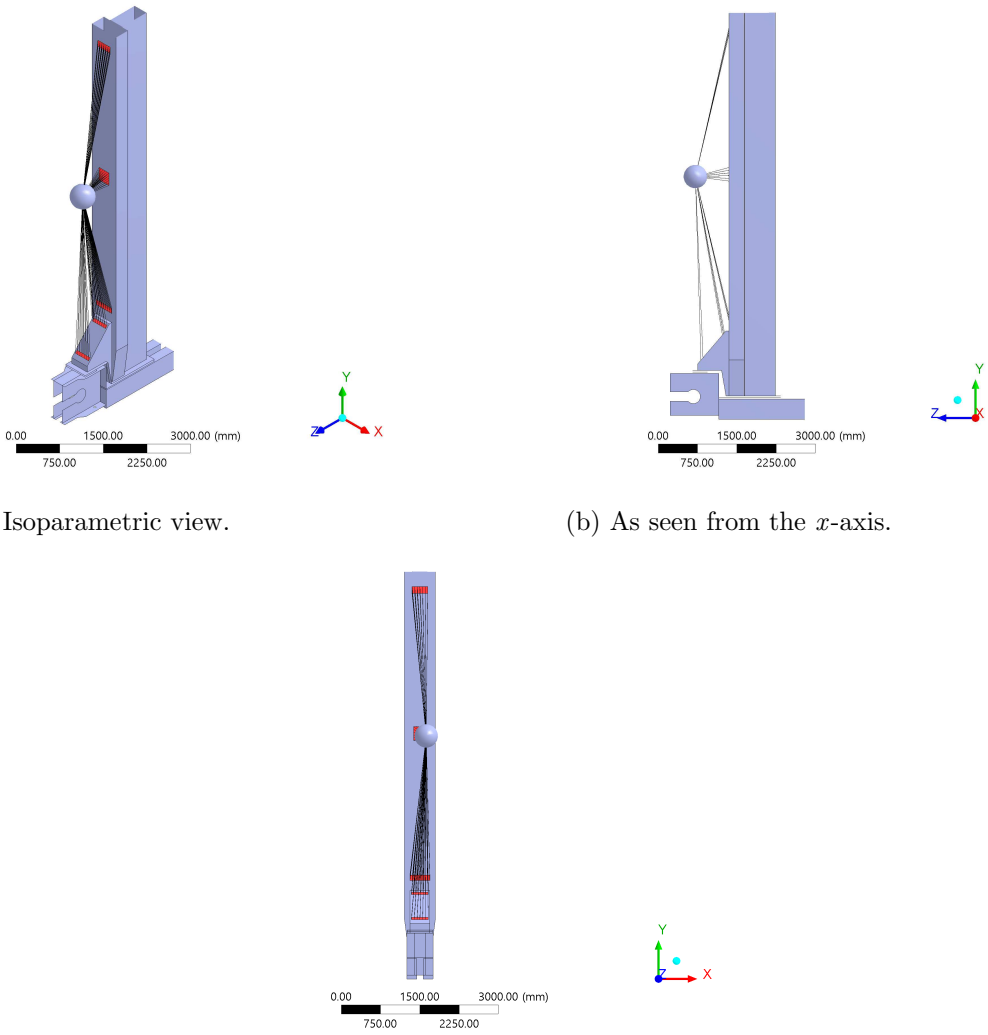
(c) As seen from the z-axis.

Figure 4.10: Lumped mass representing the hoist unit in ANSYS© WB Mechanical.

Electrical cabinet assembly

The EC assembly's COG was taken from its Autodesk Inventor© CAD model. The interior components of the electrical cabinets weren't fully modelled so computation of the exact location of it COG wasn't possible, however, again, small changes in the centre of mass location weren't found to significantly impact the results.

Figure 4.11 illustrates the lumped mass location in the ANSYS© WB Mechanical model. Its value is taken to be $m_{EC} = 1500$ kg from Table 4.6.



(a) Isoparametric view.

(b) As seen from the x-axis.

(c) As seen from the z-axis.

Figure 4.11: Lumped mass representing the EC assembly in ANSYS© WB Mechanical.

4.2.3 Boundary conditions

Wheels' shafts

By choosing to not model the wheels and wheel shafts, adequate boundary conditions must be placed to replace the influence of these components in the structure. As the wheel shafts are supported by two bearings mounted on steel plates that are subsequently bolted onto the bottom carriage's structure, the structure is thus capable of rotating locally around the wheels' axes.

Although the shafts won't resist the local rotations of the structure, they will transfer the vertical (y-direction) load from the structure to the wheels and consequently to the ground. As such, using a *remote displacement* boundary condition in ANSYS© WB Mechanical, zero displacement was imposed in the y-direction on points placed on the centre of the circular arcs, thus representing the wheel shafts in the surface model. Figure 4.12 illustrates this, the straight black lines represent, again, the equations established by the software. The *rigid* behaviour was selected for the arc *slave geometry*.

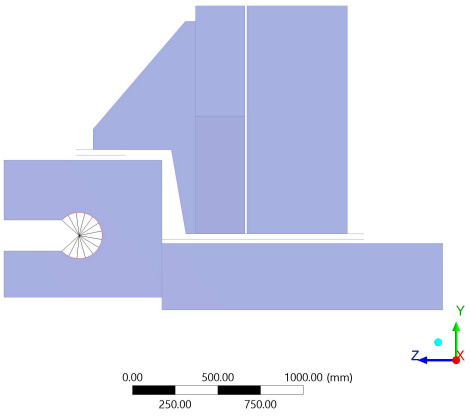


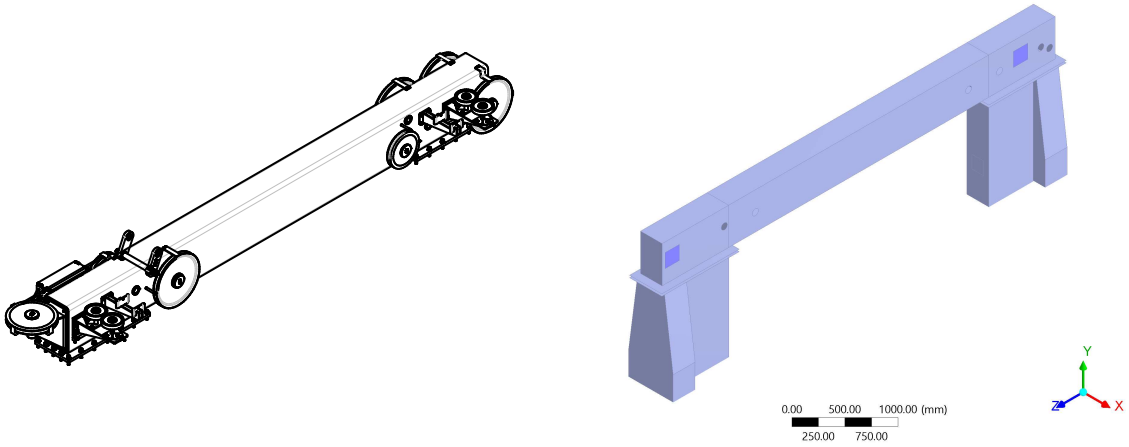
Figure 4.12: *Remote displacement* boundary condition on wheel preventing displacements in the y-direction in ANSYS© WB Mechanical.

It's worthy of note that, in reality, the wheel shafts are flexible bodies and, as such, when loaded by the structure's weight and by interaction with the wheels, they will deform, lowering the structure. However, considering the objective of this analysis, this behaviour isn't relevant.

Upper rail

Assembled near both ends of the upper crossbeam are two sets of rollers that travel along a rail as shown in Figure 4.13a. These help guide the crane and prevent mast sway at the tip in the perpendicular direction to the aisle.

To simulate this behaviour, two *frictionless supports* were placed in the upper crossbeam on the two surfaces, shown in blue in Figure 4.13b, where the rollers are assembled, thus preventing displacements and rotations of the finite element nodes in the normal direction to those surfaces [45].



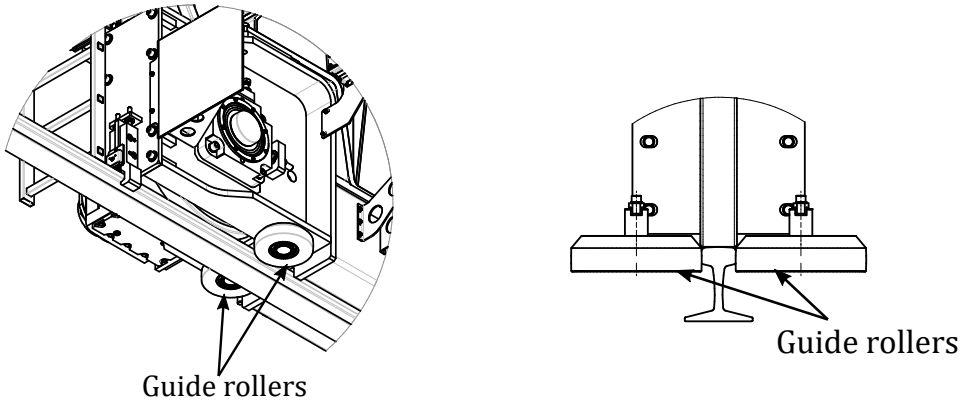
(a) Actual rollers. (Autodesk Inventor©)

(b) *Frictionless supports*. (ANSYS© WB Mechanical)

Figure 4.13: Rollers on the upper crossbeam and their corresponding *frictionless supports* in ANSYS© WB Mechanical.

Lower rail

On each end of the bottom carriage, two guide rollers, placed near the wheels, prevent the crane from derailing (Figure 4.14).



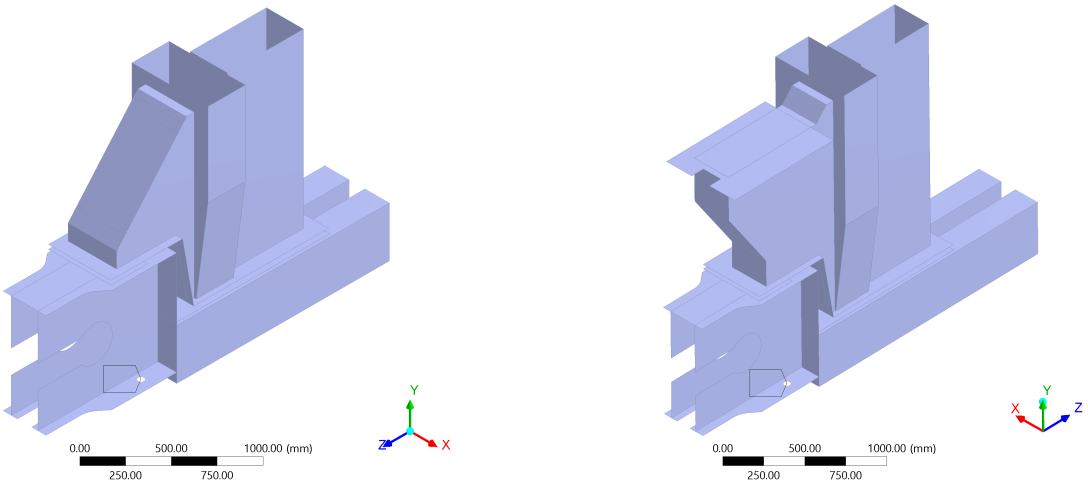
(a) Position of the rollers.

(b) Front view.

Figure 4.14: Guide rollers in the bottom carriage, near the wheels, to prevent derailment.

Similarly to what was done with the wheel shafts, two *remote displacement* boundary conditions were placed having the circular edges shown in Figure 4.15 as *slave geometries* with their behaviour set to *rigid*. At these points, the displacement in the x-direction was prevented to represent the action of the rail.

Although there are four rollers destined to guide the machine on the lower rail, two at each end of the bottom carriage, only one on each end was selected to apply the above mentioned boundary conditions. The reason being that, at all times, only one roller in each end is in contact with the rail.



(a) EC side.

(b) HU side.

Figure 4.15: *Remote displacements* imposed on the lower rollers' locations in ANSYS© WB Mechanical.

4.2.4 Material model

Due to the linear nature of the modal analyses here carried out, any non-linearities in material behaviour are ignored [45]. As stated in section 4.1, the structure is made out of S355JR grade steel. As so, the *structural steel* properties from ANSYS© material library were selected for the whole structure. The elastic properties i.e. Young's modulus and Poisson's ratio and the density for this material are stated in Table 4.8.

Table 4.8: Material properties for *structural steel* from ANSYS© material library.

Young's modulus /GPa	Poisson's ratio	Density /kgm^{-3}
200	0.3	7850

4.2.5 Mesh definition

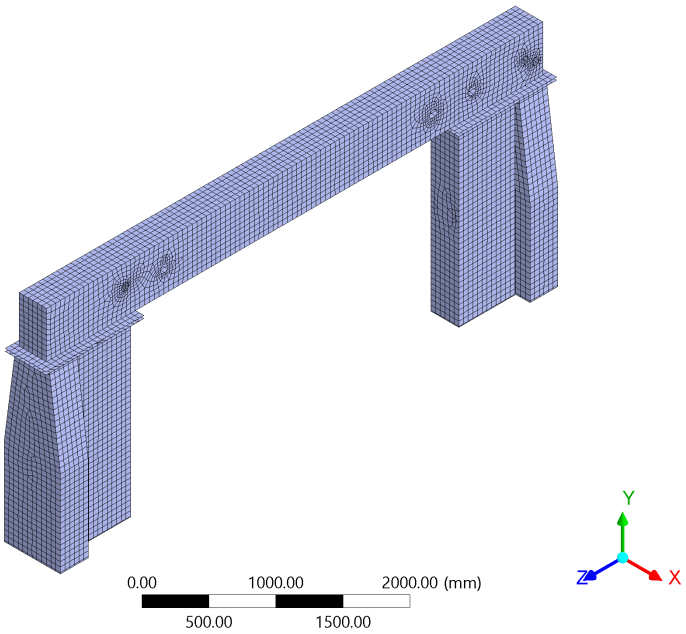
A finite element mesh comprised mainly of *shell* type elements was chosen for the simulations. It was seen in section 4.1 that the thickness of the tube beams is three orders of magnitude lower than their length and, as such, a mesh comprised of 3D *solid* type elements would require a very large number of elements in order to achieve an undistorted mesh with sufficient elements across the thickness direction. Normally, three or four elements across each direction are considered the minimum to achieve meaningful results. The used *shell* type finite element is the SHELL181 whose information can be found on Appendix B.

While the possibility of modelling the structure with *beam* type elements was also equated, it was decided against as it would be insufficient to provide the required representation of local stress phenomena in the upcoming transient analyses.

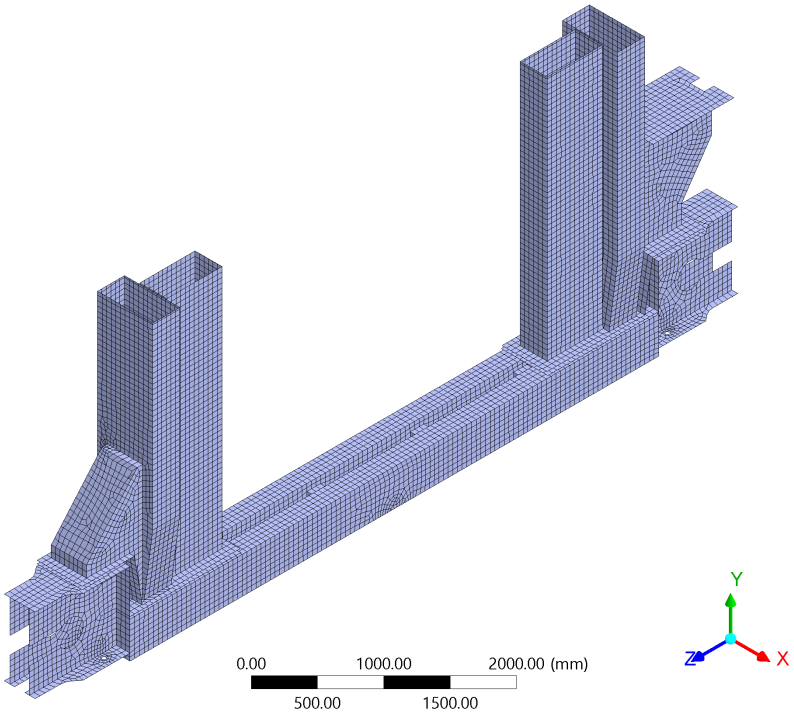
In the ANSYS© WB Mechanical environment, a *quadrilateral dominant* meshing method [45] was applied on the whole geometry in order to obtain a uniform mesh mostly comprised of quadrilateral elements. These elements are known to perform better than

triangular ones, especially where bodies undergo significant bending, as the last ones tend to become too stiff [46]. The resultant mesh contained some triangular filler elements that were created where the software wasn't able to create a quad-only mesh due to the geometry, however, these were few and sparse and should not impact the results.

The mesh size was controlled via the *element size* parameter. It was found that a minimum mesh size of 50 mm was necessary to capture the geometry's small features and to provide a structured mesh. Figure 4.16 shows the resulting mesh for an element size of 50 mm in the upper and lower regions of the structure.



(a) Upper region.



(b) Lower region.

Figure 4.16: STK-21-C finite element mesh in ANSYS© WB Mechanical.

Contact definition

The use of shell elements to discretize the structure implies that in locations of the machine where two plates contact each other by a common face, the model will have two unconnected surfaces (Figure 4.17).

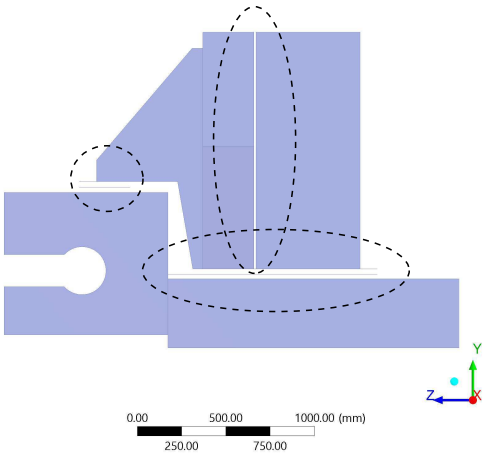


Figure 4.17: Detail of parallel surfaces where contact elements must be employed in ANSYS© WB Mechanical.

In order to correctly model the contact between the two faces, the *contact* functionality of ANSYS© WB Mechanical must be employed. This way, by introducing additional elements, CONTA174 and TARGE170 in this case, the software establishes equations between the two surfaces' nodes to prevent them from intersecting each other [45]. The result is a mesh of contact elements (Figure 4.18) overlaying the existant surface elements. An overview on the specifics of CONTA174 and TARGE170 elements can be found in Appendix B.

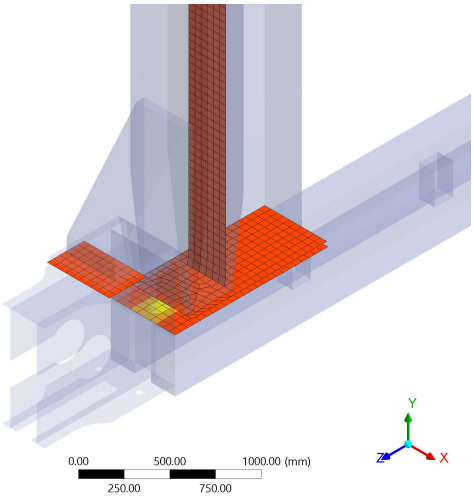


Figure 4.18: Contact elements mesh in ANSYS© WB Mechanical.

The different *contact* types available in ANSYS© are [45]:

– *Bonded*: no sliding or seperation between faces or edges is allowed. This type of contact allows for a linear solution since the contact area will not change during the

application of the load;

- *No separation*: similar to *bonded* but with sliding allowed between the contacting regions;
- *Frictionless*: this setting models unilateral contact; that is, normal pressure equals zero if separation occurs. As such, gaps can form in the model between adjacent bodies, depending on the loading;
- *Rough*: this setting models perfectly rough frictional contacts where there is no sliding, corresponding to an infinite friction coefficient between the contacting bodies. Separation between adjacent bodies is allowed;
- *Frictional*: similar to *rough* but with a finite coefficient of friction. With this setting, the two contacting geometries can carry shear stresses up to a certain magnitude across their interface before they start sliding relative to each other.

However, since the performed modal analysis is purely linear, only *bonded* and *no separation* contact types behave as described above. The rest of the *contact* behaviours resort to their linear counterparts.

In reality, the plates shown above are bolted together which might, in theory, allow for gaps to occur. It is expected however that during operation, the structure's own weight ensures that minimal changes to the contact area are ensued. The *bonded* contact type was thus chosen for the analysis.

The *shell thickness effect* on the contact settings must be turned on so that contact is detected a distance of half the thickness away from the modelled middle surface thus correctly accounting for the thickness of the shells [45].

4.2.6 Analysis settings

As can be noted in section 4.2.3, no boundary conditions constraining rigid body motion in the travel direction were placed so a zero energy mode can be found by running the analysis starting at 0 Hz. Doing so was found to considerably lengthen the simulation time required with no added benefit. Therefore, for the conducted analysis, a frequency search range from 0.7 to 4 Hz was selected since preliminary analyses found the first six natural frequencies associated with non-zero energy modes to lie inside this range.

The *Block Lanczos* direct solver was selected for the analysis as it is a robust solver for most applications, in particular, for models combining shell and solid elements [45].

4.2.7 Remarks on previous practices at Consoveyo

Previous practices at Consoveyo for the modal analysis of stacker cranes differed in particular from the aforementioned procedure in a mostly important factor, the mesh. It was common to use 3D solid elements to discretize the geometry leading to an exponential increase in computational expense if a structured mesh is to be achieved. Commonly, a more distorted mesh ended up being used in order to lower the simulation time.

By spending more effort in the geometry related steps, like simplification and mid-surface extraction, the use of shell elements becomes possible and obtaining a structured mesh becomes easier and requires less user defined controls in ANSYS© WB Mechanical.

4.3 Results and discussion

Firstly, the first six non-zero natural mode shapes were computed for a payload m_L = 4000 kg, the maximum of the STK-21-C range, with the lifting carriage considered to be at its highest position. The convergence of the resulting natural frequencies was also analysed for different meshes obtained by varying the *element size* parameter from 50 to 20 mm. The resultant mesh properties, namely in terms of element, node and DOF count can be found in Table 4.9. A consistent mass matrix formulation was adopted.

Table 4.9: Mesh properties used for convergence test.

Element size /mm	Num. elements	Num. nodes	Num. DOFs
50	201722	130686	783526
40	308613	199725	1197666
30	550916	356314	2137914
20	1243439	804443	4825370

The natural frequencies for the first six non-zero energy modes, ω_i $i = 1, \ldots, 6$, are listed in Table 4.10 for the different analysed meshes. Table 4.10 also shows the elapsed simulation time with each mesh. Bear in mind that the simulations were performed on a desktop computer equipped with an Intel® Xeon® W-2133 3.60 GHz CPU without an HPC (High Performance Computing) license so only a maximum of 4 out of 6 available cores were used.

Table 4.10: Natural frequency results for the first six non-zero energy modes with the payload at its highest position for $m_L = 4000$ kg, using different meshes.

Element size /mm	Natural frequencies /Hz						Elapsed time /s
	ω_1	ω_2	ω_3	ω_4	ω_5	ω_6	
50	0.809	1.274	1.507	2.157	3.643	3.766	36
40	0.809	1.275	1.507	2.150	3.640	3.767	55
30	0.809	1.270	1.503	2.152	3.638	3.759	1829
20	0.809	1.268	1.503	2.145	3.635	3.755	6045

Notice that the first natural frequency lies on the expected 0.5 to 2 Hz range reported in reference [11]. Moreover, the error between consequent iterations is always inferior to 1% which indicates solution convergence. The 50 mm element size mesh was thus found to give accurate results at little computational expense and further refinement is found to increase the simulation time drastically with no significant accuracy gain.

On Figures 4.19 to 4.24, the natural mode shapes of the stacker crane corresponding to the frequencies listed in Table 4.10 can be observed using the mesh corresponding to the 50 mm element size. The contour plot values refer to the components of the eigenvectors resulting from the solution of the eigenvalue problem and ANSYS© WB Mechanical displays such results normalized to the mass matrix by default. The contour bands help differentiate the regions where nodes suffer little to no excitation (blue regions) from highly excitable degrees of freedom of the model (red regions) at the given frequencies. For comparison, in each figure, the undeformed model is shown faded.

The 1st natural mode shape (Figure 4.19) corresponds to the structure's oscillation in the travel direction. A vibration nodal section is found midway through the mast. It's

also worthy of note that the frame effect of the structure leads to an high bending rigidity at the top of the masts which locally reduces their amplitude of bending vibration.

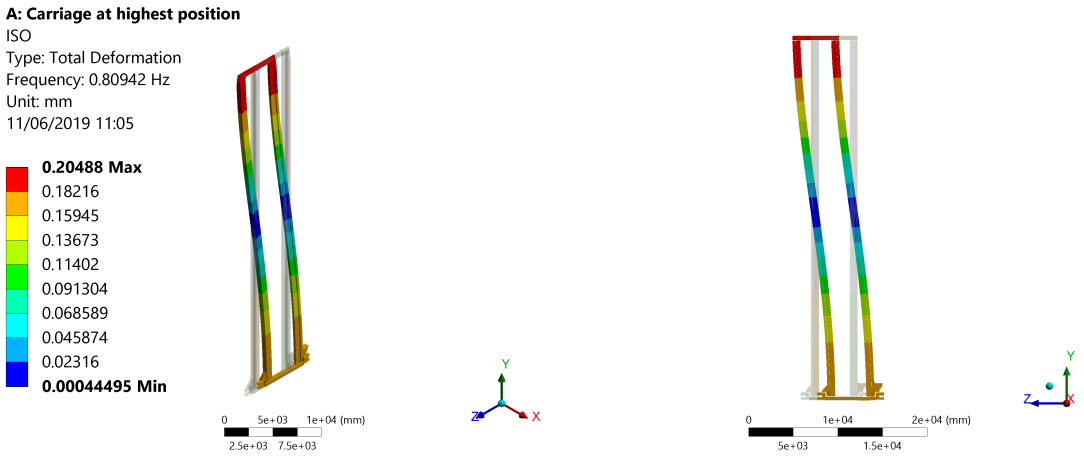
In the 2nd and 3rd natural mode shapes, the masts bend in a plane perpendicular to the travel direction resembling a fixed-simply supported beam. In these modes they adopt, respectively, an in-phase (Figure 4.20) or opposite-phase configuration (Figure 4.21).

Meanwhile, the 4th natural mode shape (Figure 4.22) has the masts bending in the frame's plane in opposite phase. A closer examination of the crane's bottom carriage show that, as intended, the structure is free to pivot around the wheels' axes. Also, considerable bending of the bottom carriage can be observed in this mode.

The 5th natural mode shape (Figure 4.23) occurs primarily in the frame's plane as did the 1st and 4th modes. This time, however, two nodal sections instead of one can be found throughout each mast. Also, the maximum displacements are found to be in the middle of the mast.

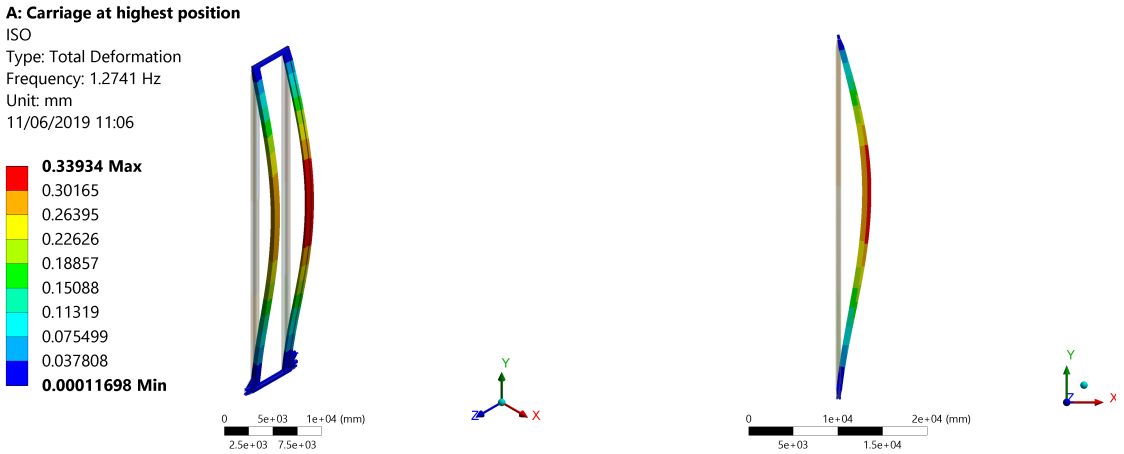
Finally, for the 6th natural mode shape (Figure 4.24) which, like modes 2 and 3, is characterized by bending in the direction perpendicular to the frame's plane, an additional vibration nodal section can be found halfway through each mast.

Comparison of the presented results with the experimental mode shapes from reference [10], which can be found in Figure 4.25, show an agreement between the frame's plane bending modes, i.e., the first, fourth and fifth natural vibration mode shapes here presented and the first, second and fourth experimental mode shapes from the study of Bachmayer et al. Bear in mind that the machine in the referenced study is, however, much different than the STK-21-C presented, being only 8 m high.



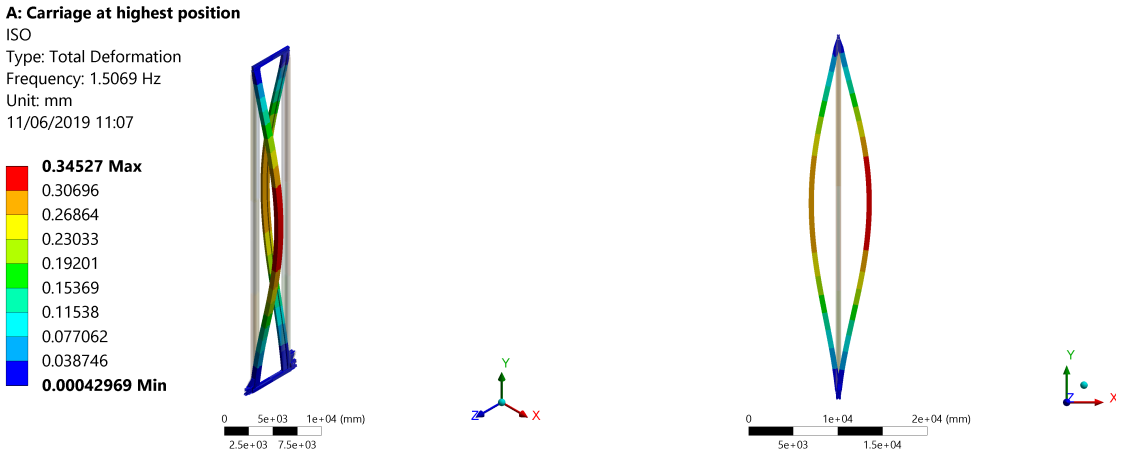
(a) Isoparametric view. (b) In the yz-plane.

Figure 4.19: STK-21-C's 1st natural mode shape ($\omega_1 = 0.81$ Hz).



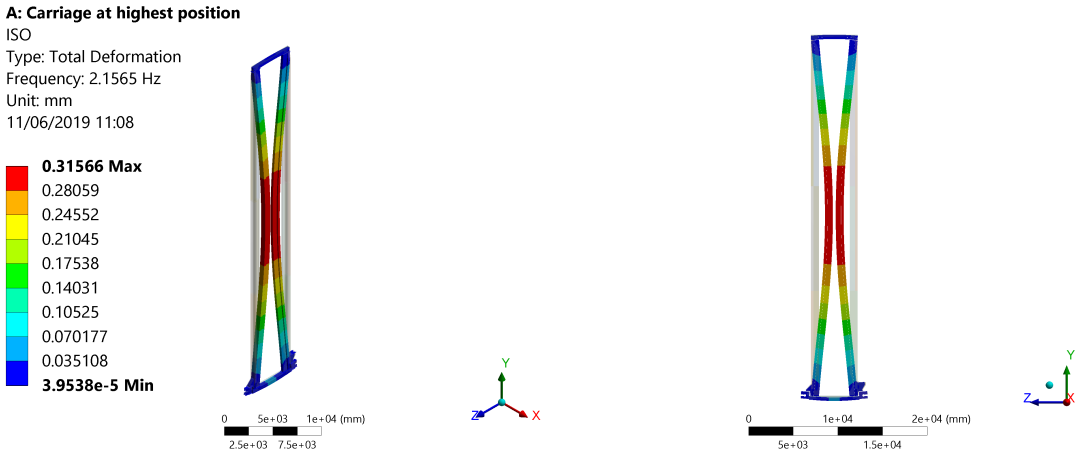
(a) Isoparametric view. (b) In the xy-plane.

Figure 4.20: STK-21-C's 2nd natural mode shape ($\omega_2 = 1.27$ Hz).



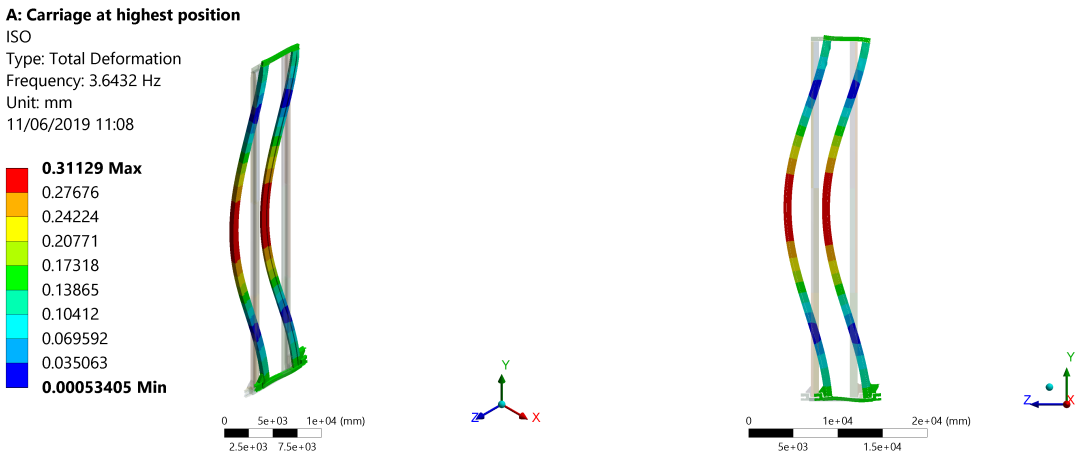
(a) Isoparametric view. (b) In the xy-plane.

Figure 4.21: STK-21-C's 3rd natural mode shape ($\omega_3 = 1.51$ Hz).



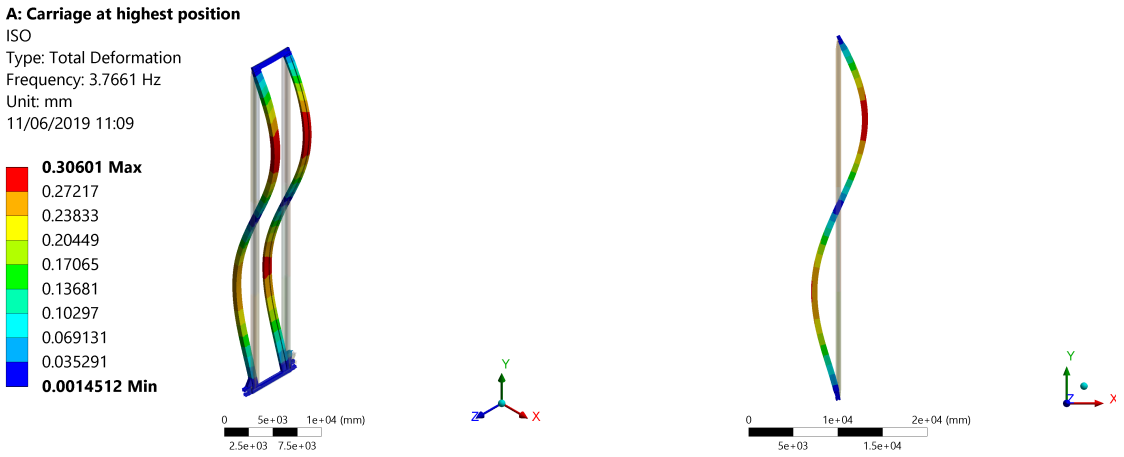
(a) Isoparametric view. (b) In the yz-plane.

Figure 4.22: STK-21-C's 4th natural mode shape ($\omega_4 = 2.16$ Hz).



(a) Isoparametric view. (b) In the yz-plane.

Figure 4.23: STK-21-C's 5th natural mode shape ($\omega_5 = 3.64$ Hz).



(a) Isoparametric view. (b) In the xy-plane.

Figure 4.24: STK-21-C's 6th natural mode shape ($\omega_6 = 3.76$ Hz).

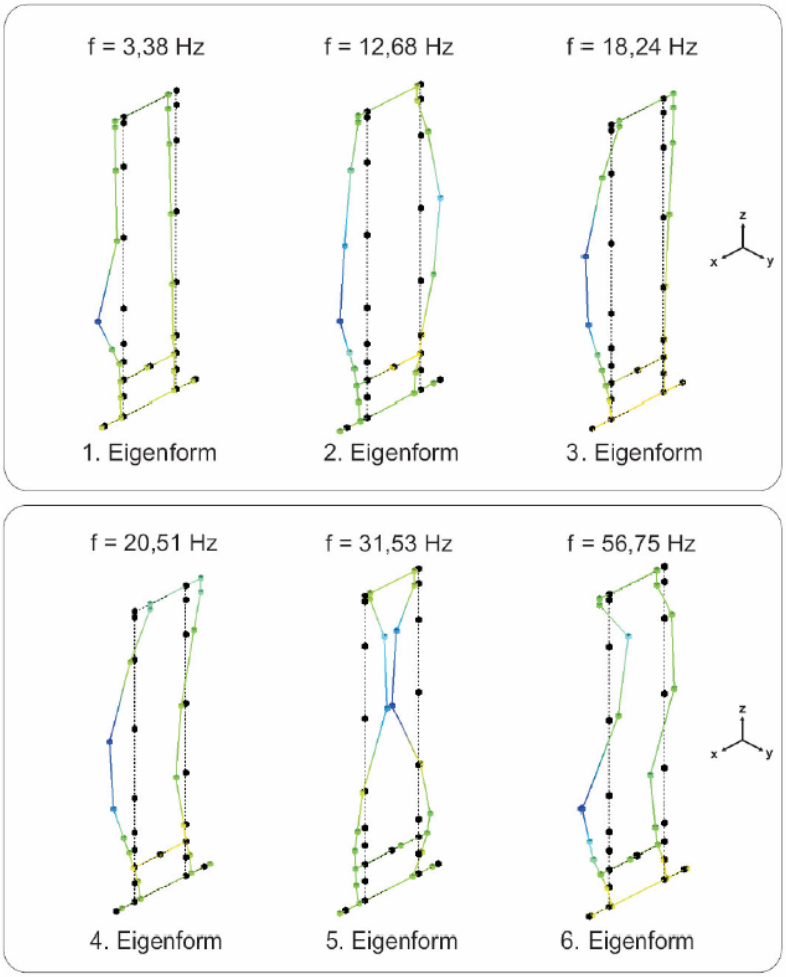


Figure 4.25: Experimental modal shapes of an 8 m high *mini-load* from reference [10].

4.3.1 Parametric studies

Influence of payload's height

For this comparison, four different heights of the payload were selected: the lowest and highest possible position (seen previously) and in between positions at 1/4, 1/2 and 3/4 of the lifting carriage's course. For the highest possible position of the lifting carriage, its corresponding lumped mass is placed at a height of 38120 mm counting from the base of the mast assembly (Figure 4.3) while its lowest position is at the 1520 mm mark. Therefore, the total course of the lifting carriage is $l_c = 36600$ mm. Let h_r be the relative position of the lifting carriage throughout its course, i.e.,

$$h_r = \frac{h}{l_c} \tag{4.2}$$

with h being the height of the lifting carriage relative to the base of the mast assembly.

Table 4.11 shows the natural frequencies computed for the four different situations. The 50 mm element size mesh from Table 4.9 was used in all cases.

Table 4.11: Computed natural frequencies for different payload heights.

Payload height h_r /%	Natural frequencies /Hz					
	ω_1	ω_2	ω_3	ω_4	ω_5	ω_6
100	0.809	1.274	1.507	2.157	3.643	3.766
75	0.913	1.002	1.506	2.157	3.193	4.057
50	0.954	1.038	1.505	2.154	3.305	3.942
25	1.027	1.130	1.506	2.151	3.190	3.899
0	0.968	1.288	1.507	2.151	3.896	3.956

The information on Table 4.11 is however incomplete without the corresponding mode shapes. For example, the first vibration mode shape for the payload at 1/2 the course isn't similar to the mode shape for the payload at highest position shown in Figure 4.19, instead corresponding to the bending in the xy-plane similar to the one found in Figure 4.20.

To allow for a more meaningful comparison, results will be grouped according to the plane of bending of the masts in each vibration mode. As such, the natural frequencies of the modes corresponding to bending on the frame's plane, the yz-plane, will be referenced as ω_i^{yz} $i = 1, \ldots, 3$ and the ones where the masts bend in the xy-plane will be ω_i^{xy} $i = 1, \ldots, 3$. Table 4.12 provides correspondence from the old to the new notation for the previously shown case where the payload is placed at its highest position ($h_r = 100\%$).

Table 4.12: Example of new notation adopted for the payload at highest position.

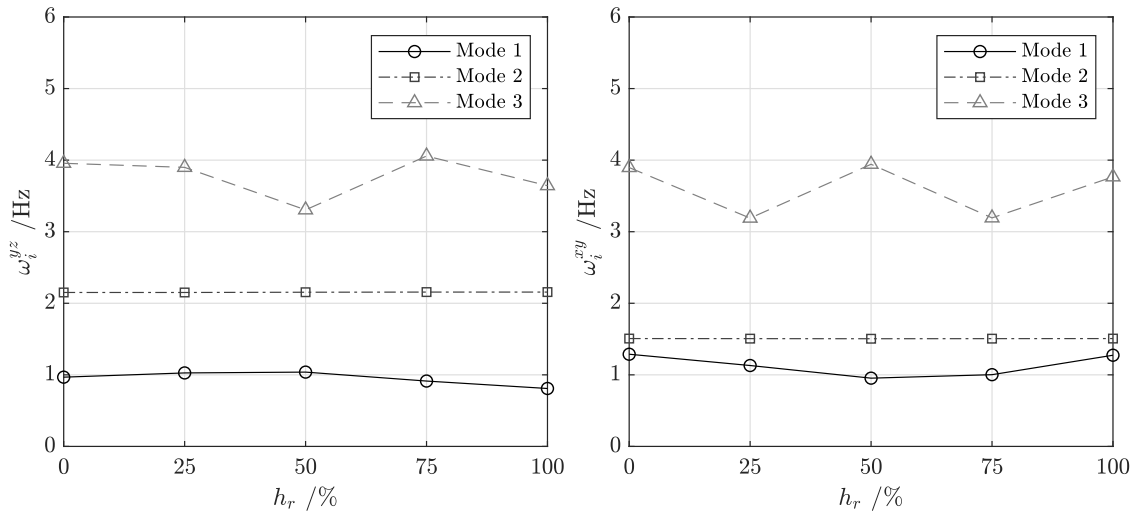
Old	ω_1	ω_2	ω_3	ω_4	ω_5	ω_6
New	ω_1^{yz}	ω_1^{xy}	ω_2^{xy}	ω_2^{yz}	ω_3^{yz}	ω_3^{xy}

The information present in Table 4.11 is repeated in Table 4.13 adopting the new notation and shown graphically in Figure 4.26.

The 2nd natural frequencies for both xy and yz-planes vibration which correspond, in all cases, to the 3rd and 4th overall natural frequencies respectively, are almost insensible to the payload's height change with their mode shapes also unaffected. However, in both cases, their minimum occurs when the payload is in the middle of the course.

Table 4.13: Computed natural frequencies for different payload heights.

Payload height h_r /%	Natural frequencies /Hz					
	ω_1^{yz}	ω_2^{yz}	ω_3^{yz}	ω_1^{xy}	ω_2^{xy}	ω_3^{xy}
100	0.809	2.157	3.643	1.274	1.507	3.766
75	0.913	2.157	4.057	1.002	1.506	3.193
50	1.038	2.154	3.305	0.954	1.505	3.942
25	1.027	2.151	3.899	1.130	1.506	3.190
0	0.968	2.151	3.956	1.288	1.507	3.896



(a) In the yz-plane.

(b) In the xy-plane.

Figure 4.26: Computed natural frequencies for different payload heights.

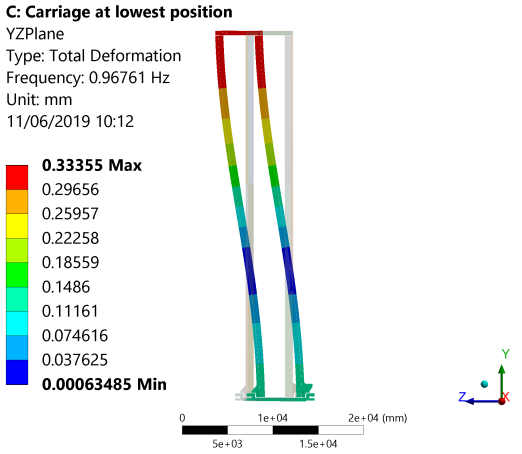
The same cannot be said for the remaining natural modes. As the payload approaches its mid-course position, the frequencies for the first yz-plane vibration mode, ω_1^{yz}, increase, the same happens for ω_3^{yz} as the payload approaches its 1/4 and 3/4 positions since these are the ones closer to the nodal sections of the corresponding mode shapes. A similar behaviour to the one reported by Park et al. [12] and to the one presented in Chapter 3.

Inspection of the first yz-plane vibration natural mode shapes in Figure 4.27 reveals an upward shift in the nodal section with increasing h_r which tends to equalize the amplitude of vibration at the highest and lowest points of the crane. The mode shapes associated with the 3rd yz-plane mode (Figure 4.28) also vary greatly with the parameter h_r, particularly, the ratio between the amplitude of vibration of the masts' middle section and of the upper crossbeam. It can be seen that the extreme (highest and lowest) positions of the lifting carriage tend to favour the increase of this ratio while the positioning of the lifting carriage at mid-span has the opposite effect.

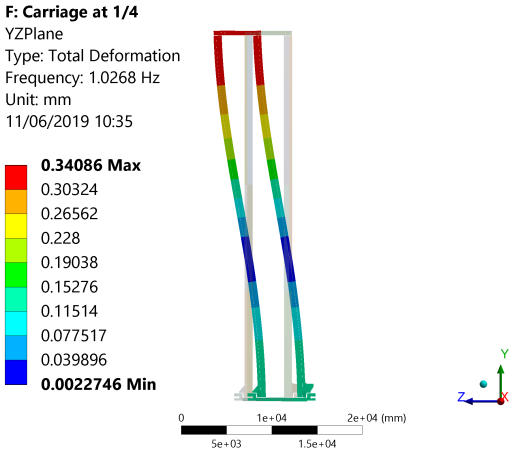
Likewise, for bending in the xy-plane, the natural frequencies decrease as the payload gets further away from the nodal sections and from the laterally fixed ends. For ω_1^{xy}, for example, the lowest value present in Table 4.13 corresponds to the payload on the mast's middle section. The corresponding mode shapes can be found in Figure 4.29.

Also, looking at Figure 4.30, one can conclude that at the extreme positions of the lifting carriage as well as for $h_r = 50\%$, the 3rd xy-plane mode shapes are such that the masts are nearly antisymmetric in relation to their middle section which, in itself, is

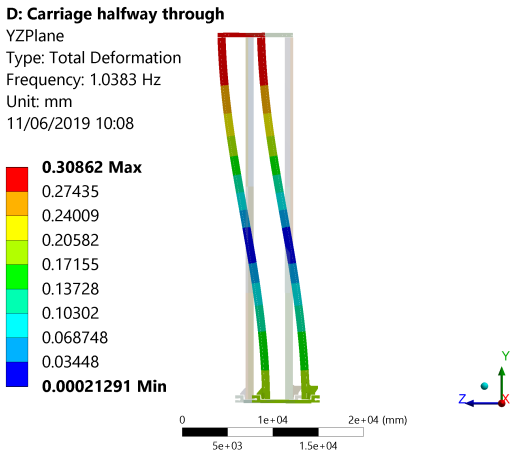
a vibration nodal section. This vibration nodal section, however, suffers a vertical shift towards the lifting carriage's position for $h_r = 25\%$ and 75%.



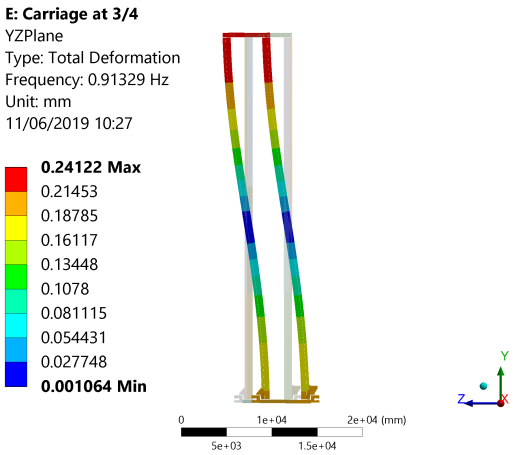
(a) $h_r = 0\%$.



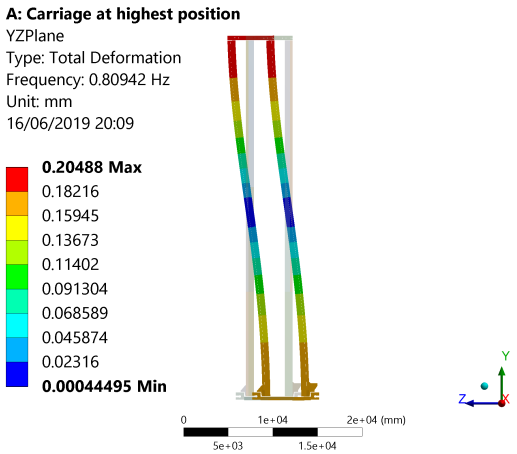
(b) $h_r = 25\%$.



(c) $h_r = 50\%$.



(d) $h_r = 75\%$.

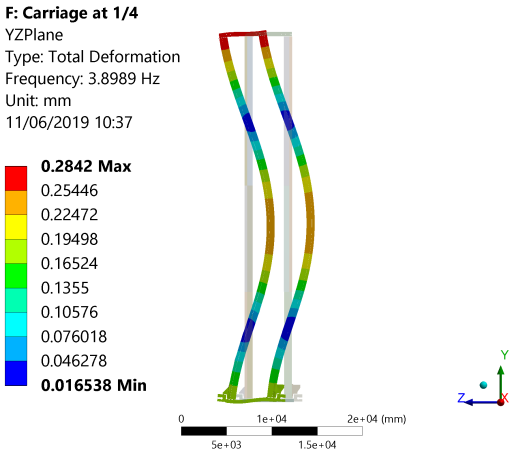


(e) $h_r = 100\%$.

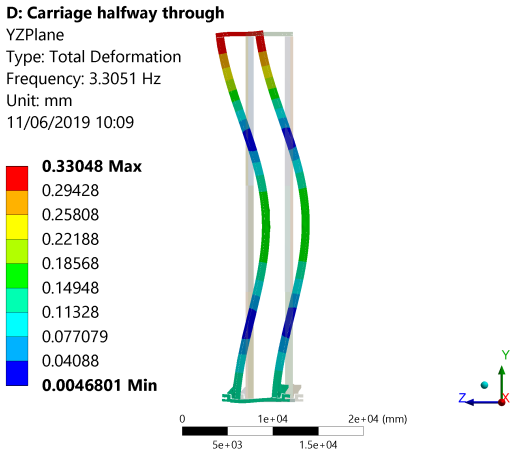
Figure 4.27: STK-21-C's 1st natural mode shape in the yz-plane for different values of h_r.



(a) $h_r = 0\%$.



(b) $h_r = 25\%$.



(c) $h_r = 50\%$.

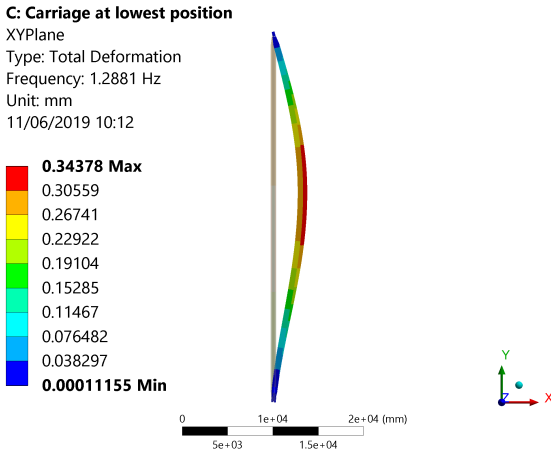


(d) $h_r = 75\%$.

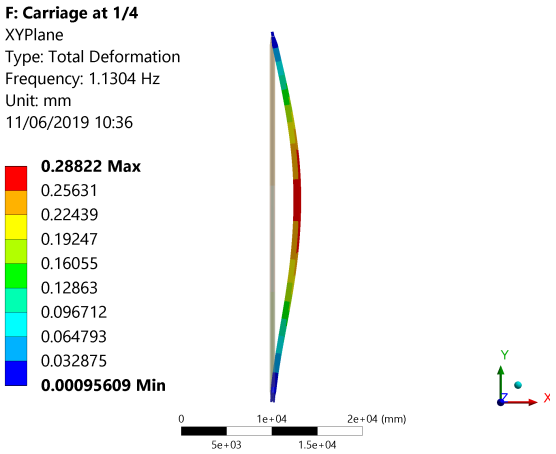


(e) $h_r = 100\%$.

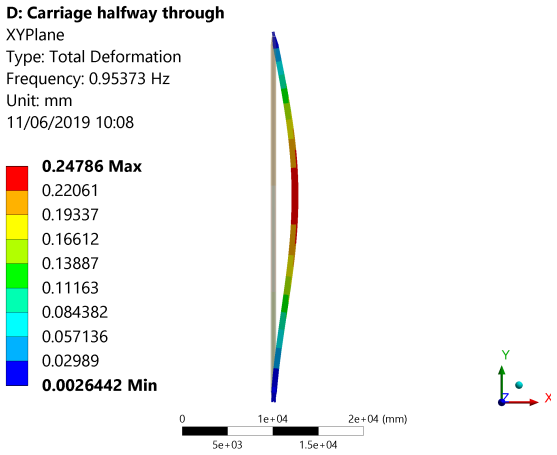
Figure 4.28: STK-21-C's 3rd natural mode shape in the yz-plane for different values of h_r.



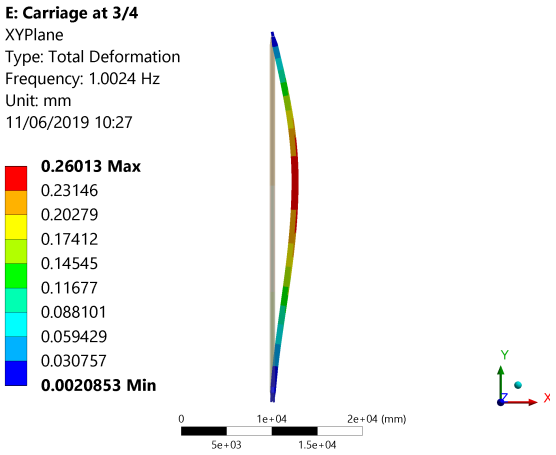
(a) $h_r = 0\%$.



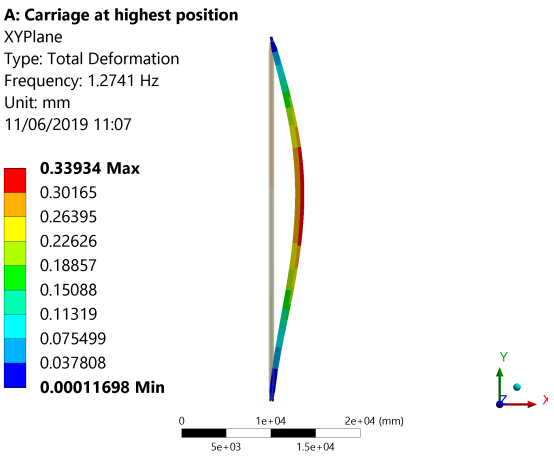
(b) $h_r = 25\%$.



(c) $h_r = 50\%$.

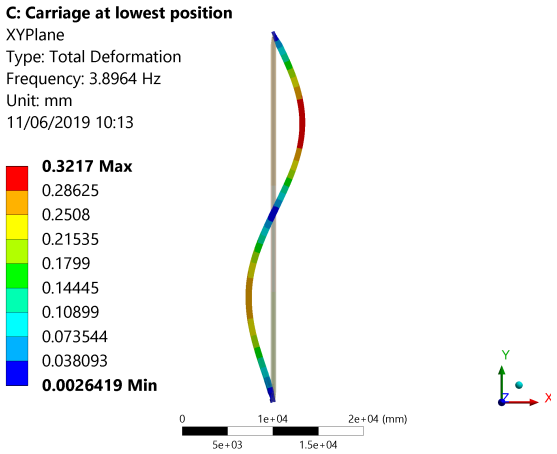


(d) $h_r = 75\%$.

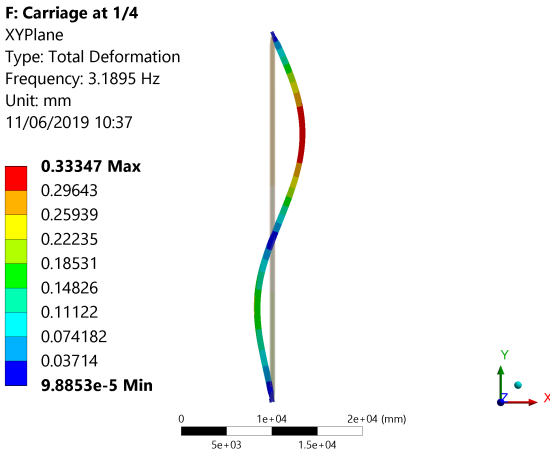


(e) $h_r = 100\%$.

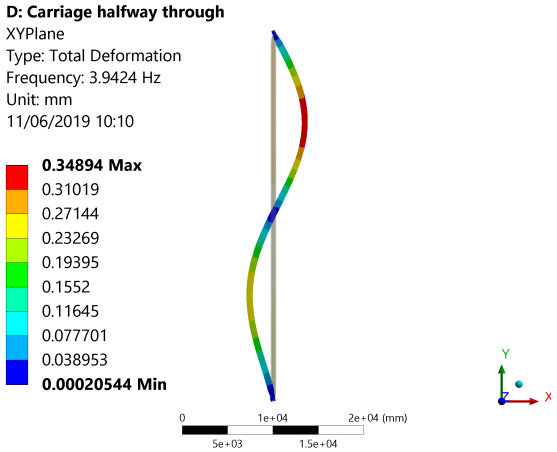
Figure 4.29: STK-21-C's 1st natural mode shape in the xy-plane for different values of h_r.



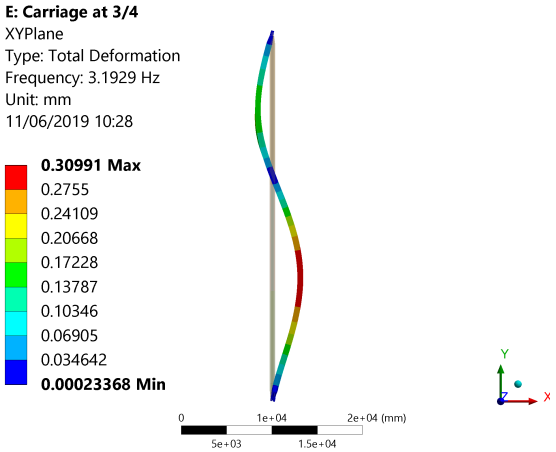
(a) $h_r = 0\%$.



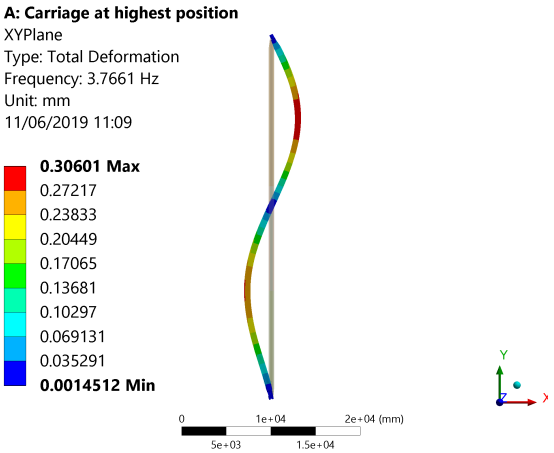
(b) $h_r = 25\%$.



(c) $h_r = 50\%$.



(d) $h_r = 75\%$.



(e) $h_r = 100\%$.

Figure 4.30: STK-21-C's 3rd natural mode shape in the xy-plane for different values of h_r.

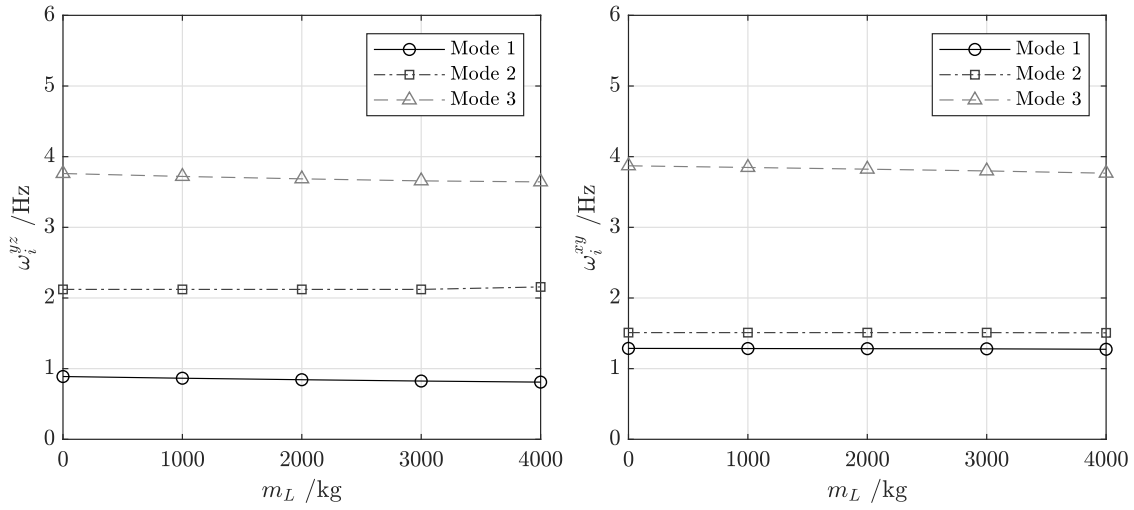
Influence of payload

As the lowest natural frequency in the plane of travel was found for the case where the payload is at its highest position and since this is expected to be the worst case scenario for the following analysis of the stacker crane's impact against the end stops, attentions were focused on this condition. Firstly, the payload's mass, m_L, was varied from 0 to 4000 kg in intervals of 1000 for the original masts' height (≈ 40 m).

From Figure 4.31 where such results are shown, it can be seen that the increase in payload's mass contributes slightly to the decrease of the natural frequency associated with the first mode of vibration in the yz-plane with even smaller effects being observed for the third modes of vibration in both the yz and xy-planes.

On Chapter 3 it was concluded that an increase in the lumped mass' value generally caused a decrease in the natural frequencies of the beam-mass-carriage system and that such decrease became less noticeable with increasing values of the mass. It might be the case that, at the studied range of m_L, a similar situation happens, one must note that even at $m_L = 0$ kg, the mass of the lifting carriage and equipped LHD are still in place because, practically, it wouldn't make sense otherwise.

The absence of effects in the remaining modes is explained by the conclusions of the previous section: the proximity of the lumped mass to the vibrational nodal sections causes it to have a neglectable effect on the natural modes of vibration of the structure.



(a) In the yz-plane.

(b) In the xy-plane.

Figure 4.31: Computed natural frequencies for different payload mass, m_L, for a masts' height of 40 m with the payload at its highest position.

Influence of masts' height

Using SpaceClaim©, models with 30 and 35 m were constructed so that the natural frequencies and mode shapes could be investigated for different masts' heights. The total mass of the structure for each height value is shown in Table 4.14 while their correspondent mesh properties are shown in Table 4.15.

Table 4.14: Total mass of the STK-21-C structure model per height.

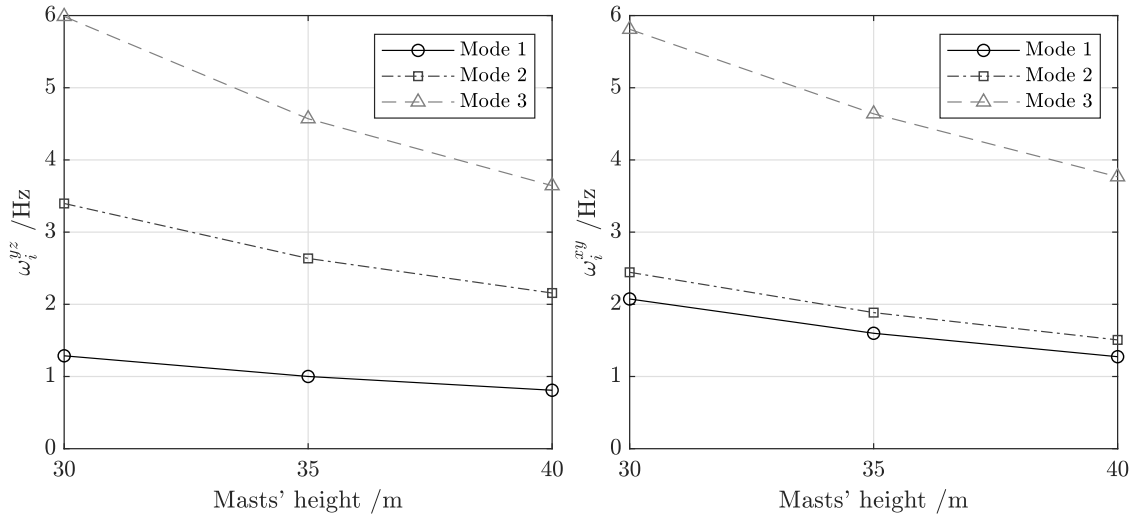
Height /m	Total mass /kg
40	26871
35	24710
30	22489

Table 4.15: Mesh properties of the STK-21-C models per height.

Height /m	Num. elements	Num. nodes	Num. DOFs
40	201722	130686	783526
35	180656	116655	699334
30	159046	102228	612772

As can be seen from Figure 4.32, the increase in masts' height, for the same $m_L = 4000$ kg causes an overall decrease of the natural frequencies, a phenomenon most noticeable in the higher frequency modes. As the masts' height increases, not only there's an increase in the structure's mass but also a reduction in the rigidity, both effects contributing to the observed reduction.

Also worthy of note is that, for a masts' height of 30 m, $\omega_3^{yz} > \omega_3^{xy}$. A situation that is reversed as the height increases.



(a) In the yz-plane. (b) In the xy-plane.

Figure 4.32: Computed natural frequencies for different masts' heights with the lifting carriage at its highest position and $m_L = 4000$ kg.

Influence of boundary conditions

Until this moment, the crane was considered to be allowed to move in the travel direction. However, if the wheels of the machine are locked by action of the gearmotor brakes, the natural frequencies are expected to change due to the change of the boundary conditions of the model.

To understand the sensitivity of the model to the applied boundary conditions, the following situations were tested:

- the movement in the travel direction was fixed at the wheel mounts on the ECs' assembly side (Figure 4.12);
- the movement in the travel direction was fixed at the wheel mounts on the HM's side;
- the movement in the travel direction was fixed at all four wheel mounts (a condition henceforth labelled "All");
- the movement in the travel direction was fixed at the area marked in Figure 4.33 where the buffer is bolted onto the bottom carriage (labelled "Buffer").

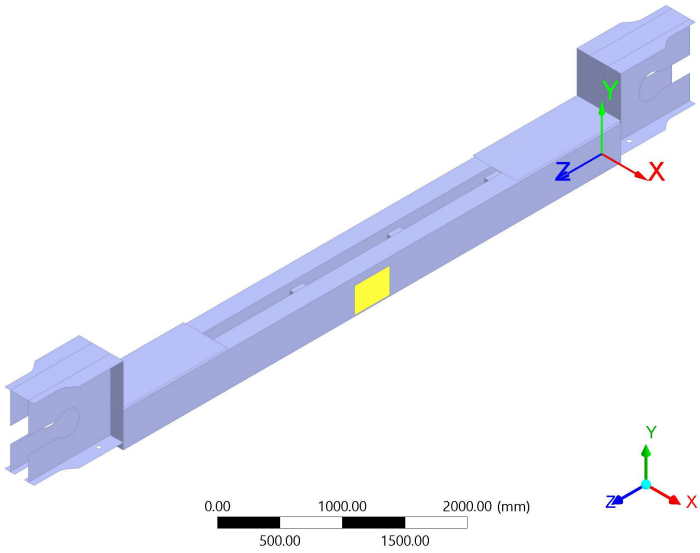


Figure 4.33: Area where the buffer is bolted onto the bottom carriage.

The previous model with 40 m masts and a 4000 kg payload at the highest position was considered and the results are shown in Figure 4.34 for the modes of vibration in the yz-plane as the ones in the xy-plane remained unchanged. Since the first two situations gave the same results, only the ones concerning the first case are presented (labelled "One side"). The previously computed results from the beginning of Section 4.3 with the crane free to move in the travel direction are labelled as "Free".

The most noticeable difference is found on the 1st and 3rd modes between the "Free" condition and the remaining ones whose corresponding mode shapes can be found in Figures 4.35 and 4.36. In both cases, fixing the bottom carriage either on the wheels or

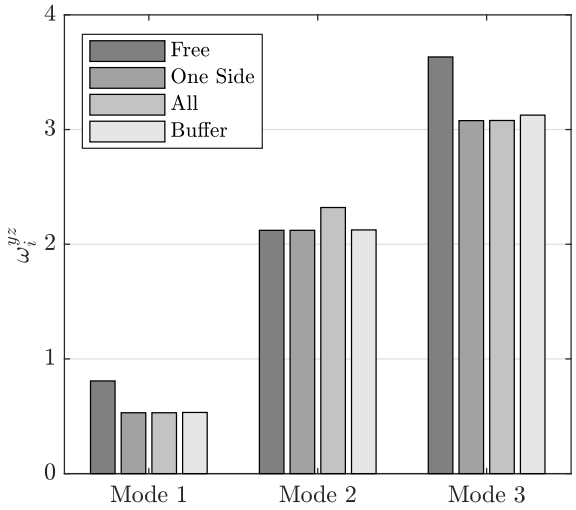
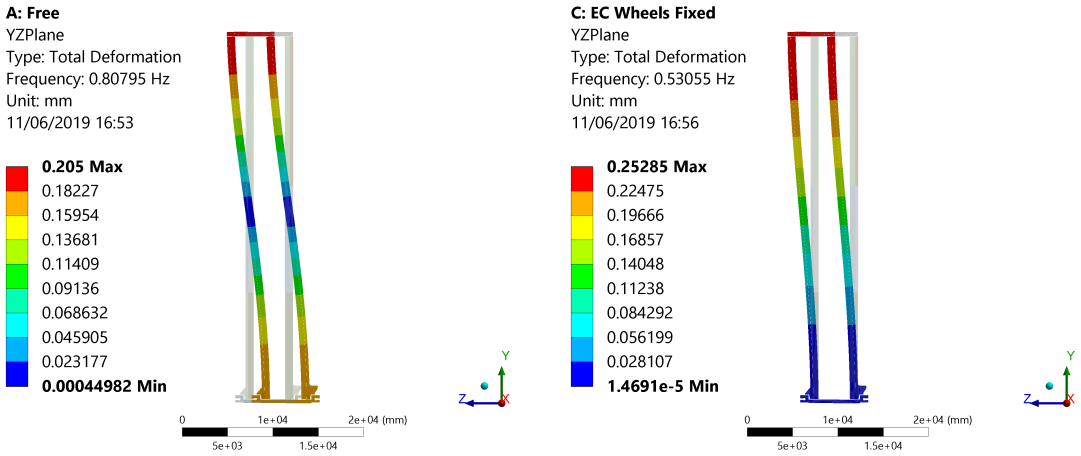


Figure 4.34: Computed natural frequencies for the modes of vibration in the yz-plane considering different boundary conditions.

at the buffer surface cause a shift of one of the nodal sections to the bottom carriage as well as a decrease in the natural frequencies. It's important to note that the nodal section near the upper crossbeam remains roughly at the same position for both free and fixed positions.

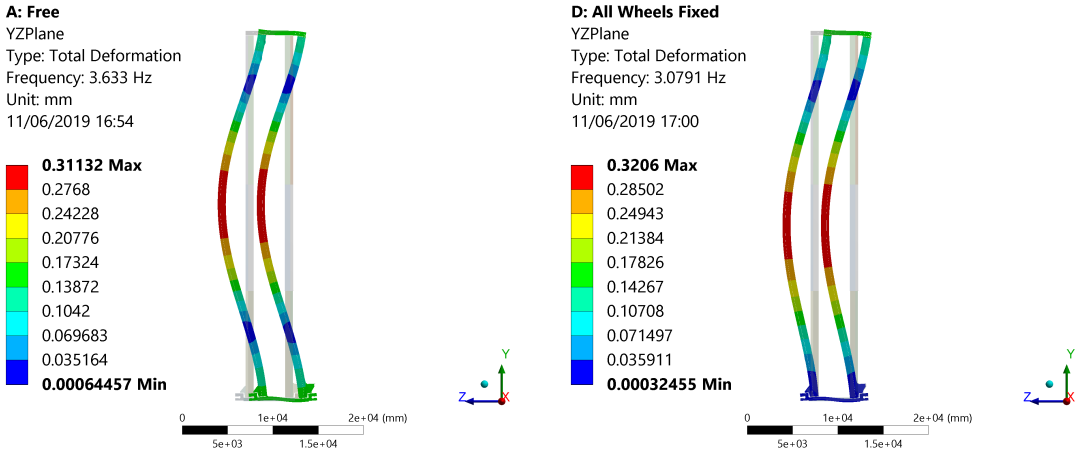
For the 2nd mode, only the "All" condition showed an influence on the natural frequency as it constrains the movement of the wheel axes relative to each other due to the bending of the bottom carriage, thus making the system more rigid and causing an increase on the corresponding natural frequency.



(a) "Free" condition.

(b) "One side" fixed condition.

Figure 4.35: STK-21-C's 1st natural mode shape in the yz-plane for different boundary conditions.



(a) "Free" condition.

(b) "One side" fixed condition.

Figure 4.36: STK-21-C's 3rd natural mode shape in the yz-plane for different boundary conditions.

4.4 Procedure and remarks on single mast models

While the aforementioned procedure can be adopted for the study of the natural vibration of the remaining double mast stacker cranes, important changes have to be made when it comes to the analysis of single mast stacker cranes. Though some principles remain the same, key points relating to the geometry preparation, mesh creation and boundary conditions undergo significant changes. These are explained using the case of a model STK-25 single mast stacker crane. The original crane, presented in Figure 4.37 has a height of 41 m, from its lowest to its highest position, and weights 27.5 t. The machine's wheelbase is 6300 mm.

Geometry creation

The most significant change starts perhaps with the geometry creation, while the process of simplification (both in Autodesk Inventor© and SpaceClaim©) follows the already explained principles, the mid-surface extraction is accompanied by the extraction of line bodies which shall later be used for the definition of *beam* elements in ANSYS© WB Mechanical. The latter combines three phases:

- the extraction itself of the beams' profiles and paths;
- the offset of the beam's paths;
- the offset of the beam's profiles.

The offset of the paths is made so that they lie on the surface geometry, thus allowing for node sharing between the beam and shell elements. In its turn, the profile offset is made so that the inertial properties of the beam are computed correctly and in accordance to their real life counterparts. Figure 4.38 shows the offset process, on Figure 4.38a, the beams are in their "as extracted" condition, on Figure 4.38b, the result of the path offset is shown and lastly, on Figure 4.38c, one can see the final result after the profile offset.

Still on the topic of geometry creation, four different geometries were created, each corresponding to a different mast height from 30 to 45 m in intervals of 5 m to cover the

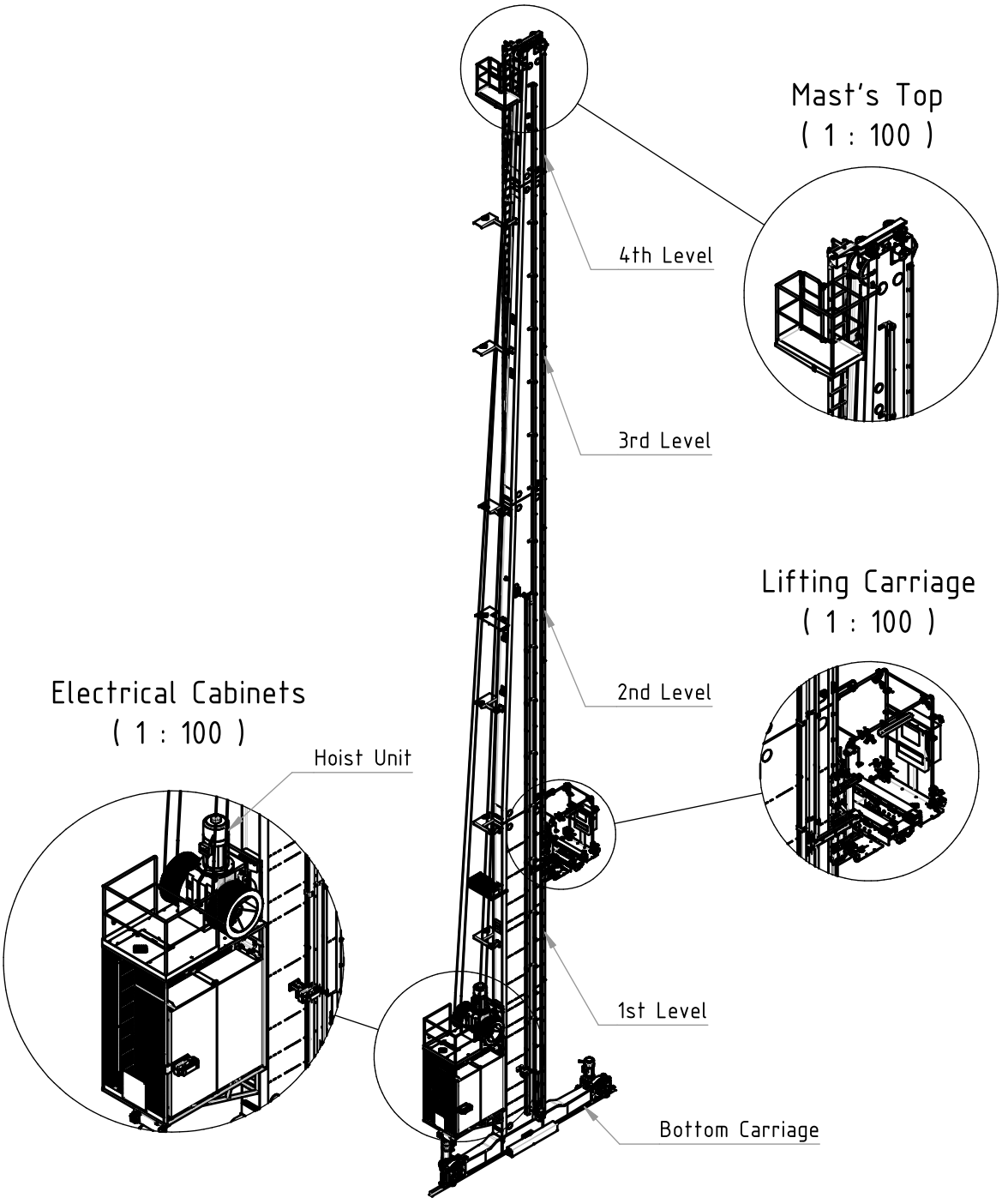
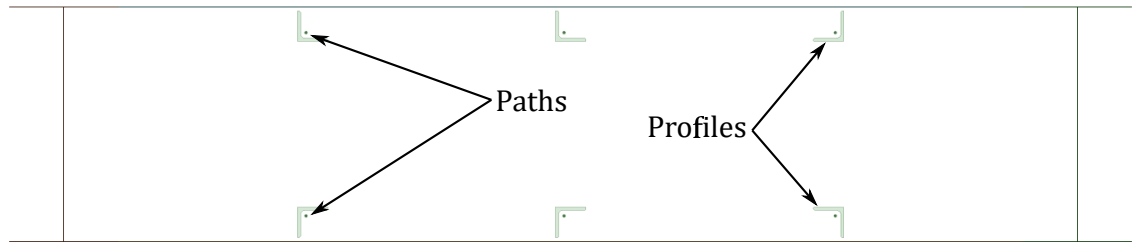
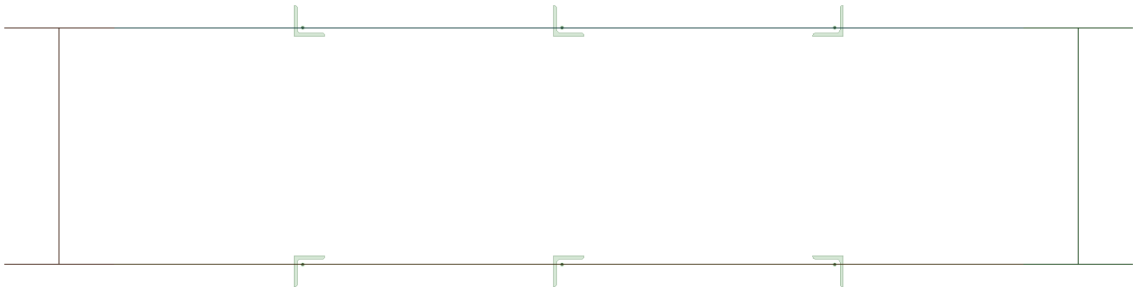


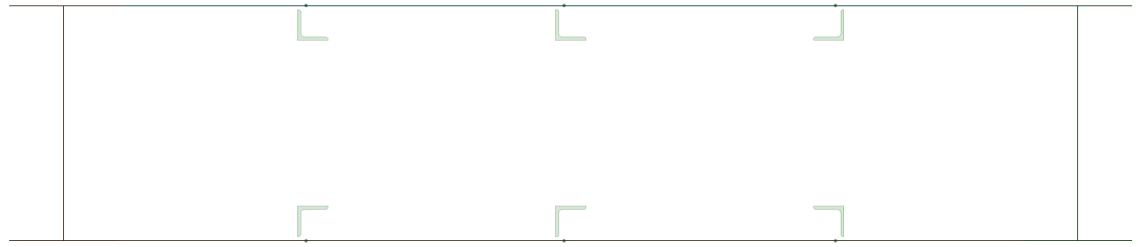
Figure 4.37: Original STK-25 model used in the present study (scale 1 : 200).



(a) As extracted.



(b) After path offset.



(c) After profile offset.

Figure 4.38: Beam extraction process in SpaceClaim©for the creation of a shell-beam mesh.

range of heights for this particular model, as mentioned in section 2.4.1. The procedure used for the creation of the different geometries must be emphasized as it was significantly more complex than for the case of the STK-21-C, though, the reduction in height is also done primarily in the last level.

Moreover, starting on the second level, the mast suffers a gradual cross-section reduction to save weight which is asymmetrical as the "front" of the crane has to remain straight to allow the movement of the lifting carriage. The beginning and end cross-sections are defined on a per level basis, being independent of the level's length. The reinforcement beam lengths are adjusted in accordance with the masts' height and go as far as they are allowed to fit. An exception is the last level which, in order to fit the top mast assembly that contains the sheaves (Figure 4.39), its upper section must be the same in order for the top to fit. The top mast assembly is always the same, no matter the crane's height.

It was already mentioned that a single mast stacker crane's mast has inner septa that reinforce the mast and force its individual parts to work together in bending. The applied rule of thumb is for these to be placed 1000 mm apart from each other.

In order to make the previous explanation more clear, Figure 4.40 shows the upper mast levels for the 30, 35, 40 and 45 m mast STK-25 geometries for model preparation. The resultant structure's mass for each height's model is shown in Table 4.16.

On a last note, the mesh creation is simplified and produces better results if the

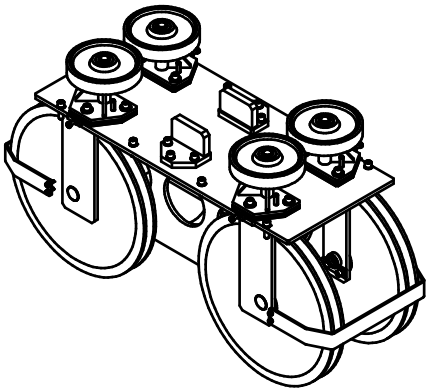
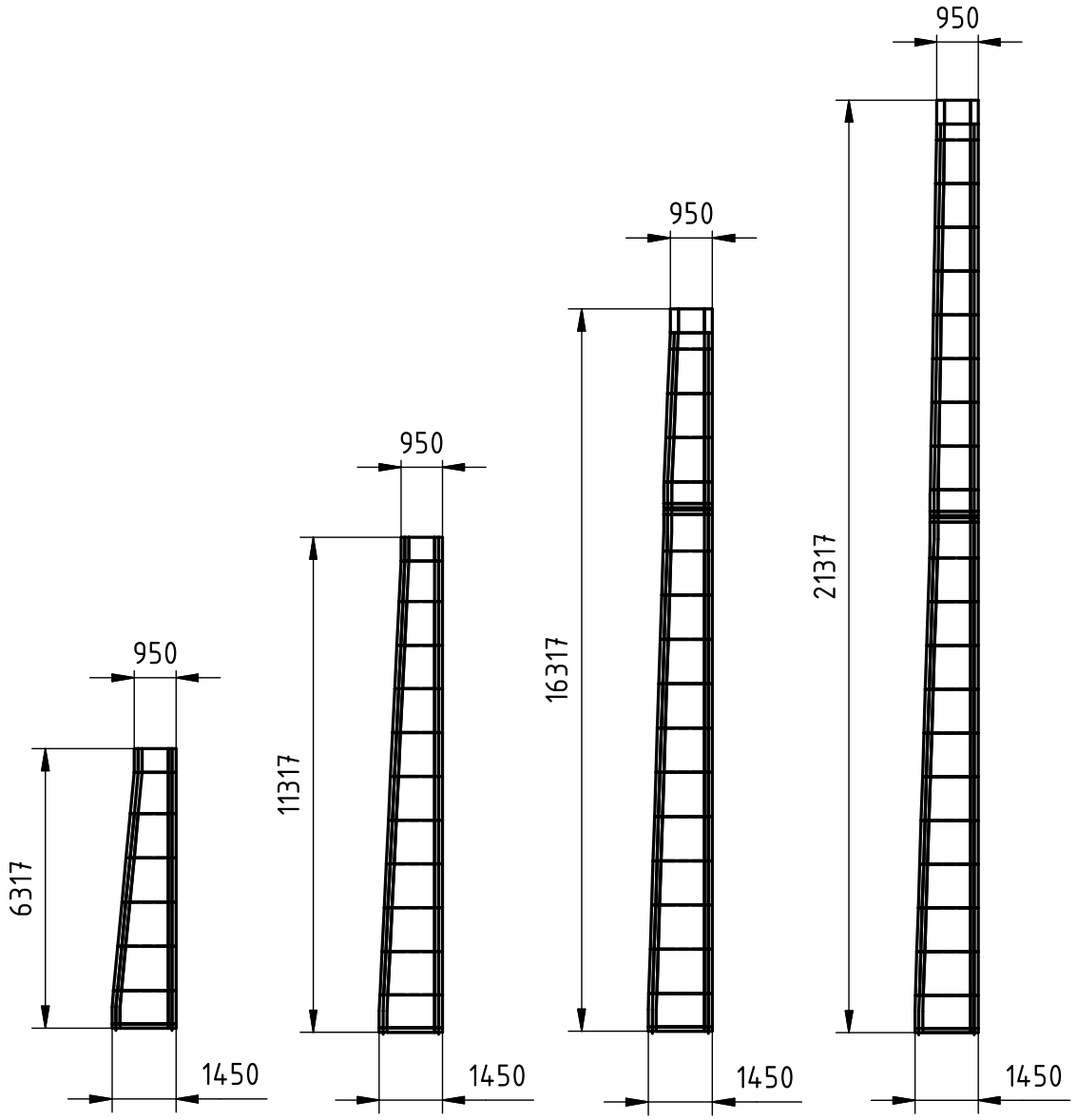


Figure 4.39: Top mast assembly of STK-25 (scale 1 : 20).

Table 4.16: Total mass of the STK-25 structure model per height.

Height /m	Total mass /kg
45	16969
40	15798
35	14391
30	13079

resulting surfaces are split where they are in contact with other surfaces, in the geometry creation phase. This allows the software to more easily define the areas where a structured mesh can be mapped, therefore, regions with intersecting surfaces end up with a less distorted mesh than the case without surface splitting.



(a) 30 m. (b) 35 m. (c) 40 m. (d) 45 m.

Figure 4.40: Last two mast levels (one for the 30 and 35 m cases) of the studied STK-25 geometries after simplification.

Model setup

Similarly to what was done before, lumped masses were placed to represent the EC assembly, hoist unit and lifting carriage. The corresponding mass values can be seen in Table 4.17.

In terms of boundary conditions, the ones from section 4.2.3 have a direct counterpart in the STK-25 and were applied accordingly. An exception occurs for the boundary condition representing the interaction with the upper rail. In reality, the rollers of the top mast (Figure 4.39) prevent the movement in the perpendicular direction to the plane of travel. Following the logic of the lower rollers, only two are expected to be in contact with the rail at a given time, therefore, *remote displacement* boundary conditions were placed preventing the aforementioned movement. The *remote points* representing the rollers were

Table 4.17: Mass of the STK-25 additional components.

Component	Mass /kg
EC assembly	800
Lifting carriage w/ LHD	1700
HU	2300

placed in the actual roller centre and for the respective *slave geometries*, the areas where the rollers are bolted onto the mast were selected. Figure 4.41 illustrates the final result in ANSYS© WB Mechanical.

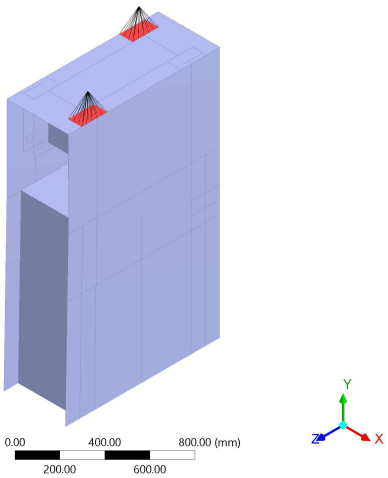


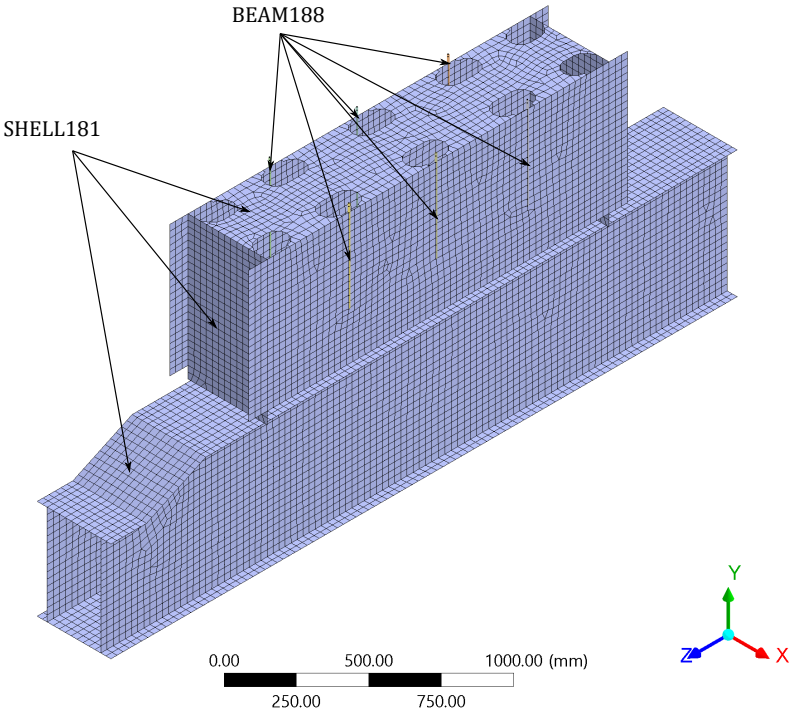
Figure 4.41: *Remote displacements* imposed on the upper rollers' locations of the STK-25 in ANSYS© WB Mechanical.

The mesh is composed of shell and beam elements, SHELL181 and BEAM188 respectively, as seen in Figure 4.42. Element description can be found in Appendix B. An element size of 30 mm was found to provide good results in terms of mesh quality.

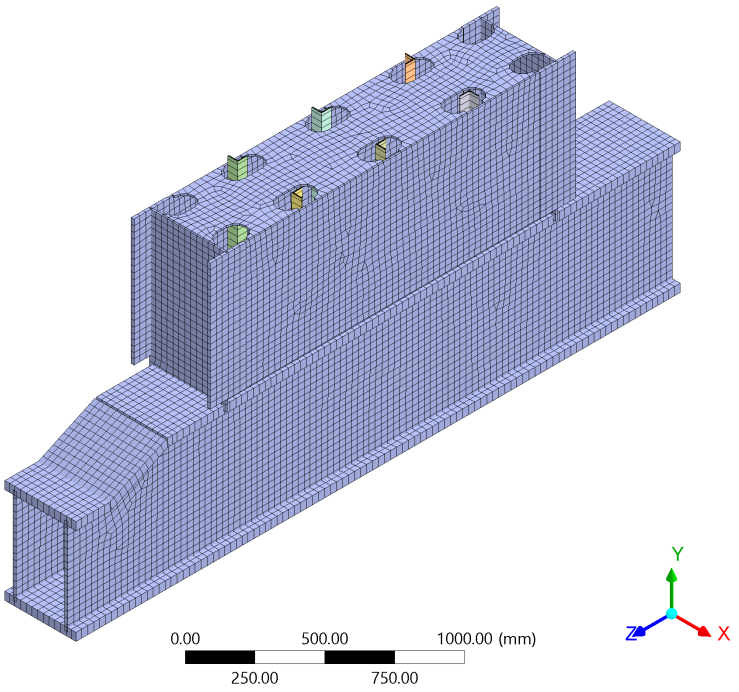
The mesh properties for the various height models can be found in Table 4.18.

Table 4.18: Mesh properties of the STK-25 models per height.

Height /m	Num. elements	Num. nodes	Num. DOFs
45	245014	244361	1465398
40	225703	225119	1349946
35	204200	203649	1221126
30	183060	182532	1094424



(a) Elements employed.



(b) "Thick shells and beams" visual option turned on.

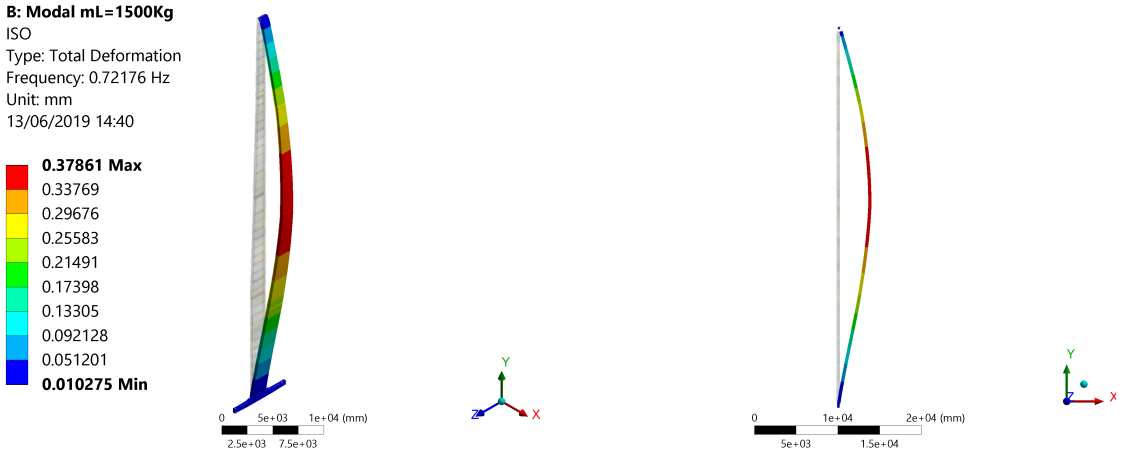
Figure 4.42: STK-25 finite element mesh in ANSYS© WB Mechanical.

Results and discussion

Figures 4.43 to 4.48 depict the first six natural mode shapes for the STK-25 with a mast height of 45 m and considering a payload of $m_L = 1500$ kg.

The 2nd and 5th modes mainly consist in bending of the mast in the travel plane. These, in comparison with Figures 4.19 and 4.23, highlight the effect of the frame structure in double mast stacker cranes. Moreover, the presented 2nd and 5th mode shapes are in agreement with the first two mode shapes of the beam-mass-carriage model in Figure 3.3 for higher values of r_m, despite the fact that a constant cross-section was considered on the simpler model. The same can be said about the general placement of the nodal sections: on Figure 4.44 one can see the nodal section at the masts mid-span on the 1st mode shape and, for the 5th mode shape of Figure 4.47, a nodal section lying very close to the mast's tip.

Remaining modes are characterized mainly by the bending of the mast in the xy-plane although, in the higher energy modes, namely the 4th and 6th modes, torsion of the mast in the y-direction can be observed and will be later explored further. The difference between the two modes has to do with the phase of the torsion of the mast and the bending of the mast and bottom carriage. While, on mode 4, a positive displacement in the z-direction of the mid-section of the bottom carriage is accompanied by torsion in the negative y-direction of the mast, mode 6 has the mast twisting in the positive y-direction.



(a) Isoparametric view.

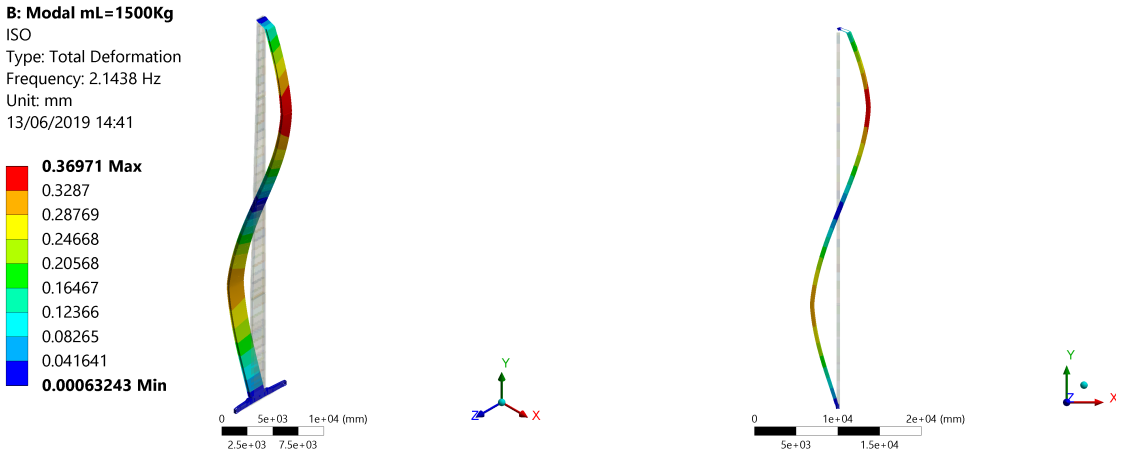
(b) In the xy-plane.

Figure 4.43: STK-25's (45 m) 1st natural mode shape ($\omega_1 = 0.72$ Hz)



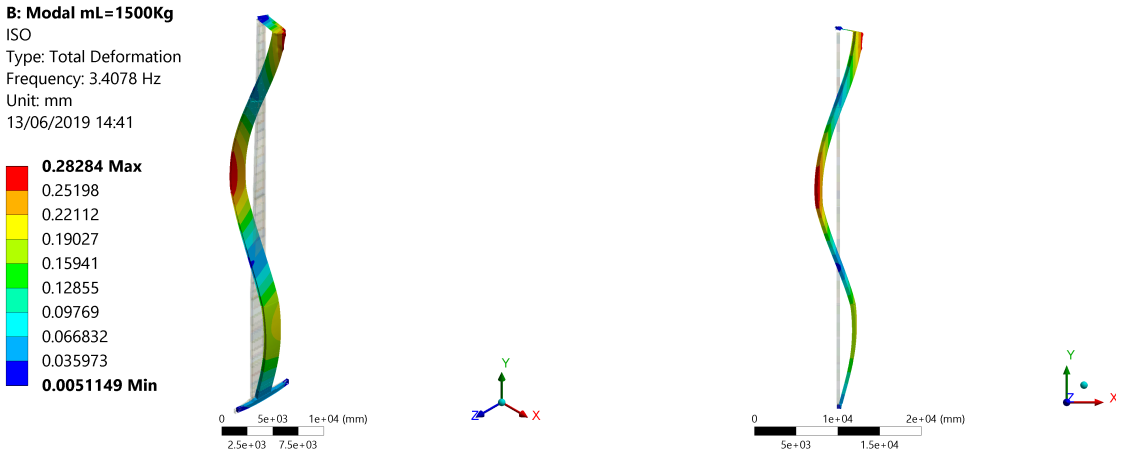
(a) Isoparametric view. (b) In the yz-plane.

Figure 4.44: STK-25's (45 m) 2nd natural mode shape ($\omega_2 = 0.74$ Hz)



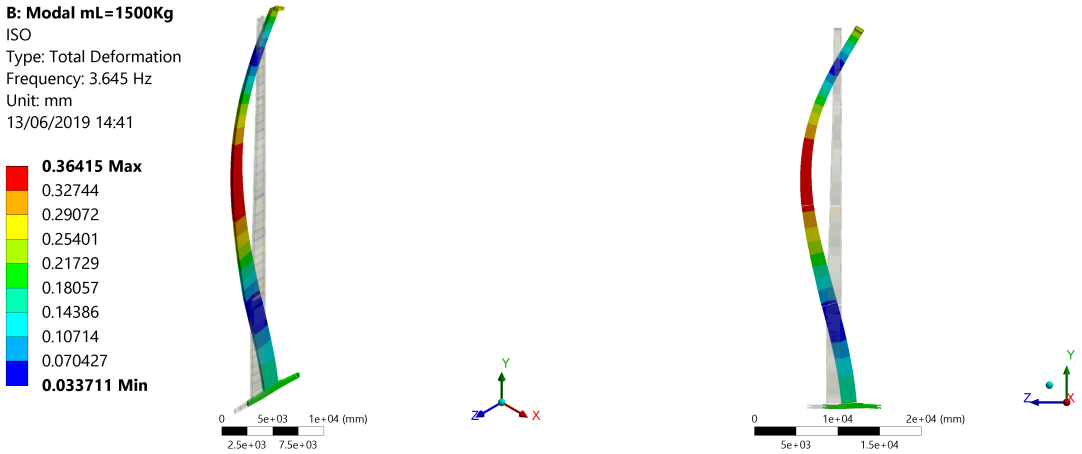
(a) Isoparametric view. (b) In the xy-plane.

Figure 4.45: STK-25's (45 m) 3rd natural mode shape ($\omega_3 = 2.14$ Hz)



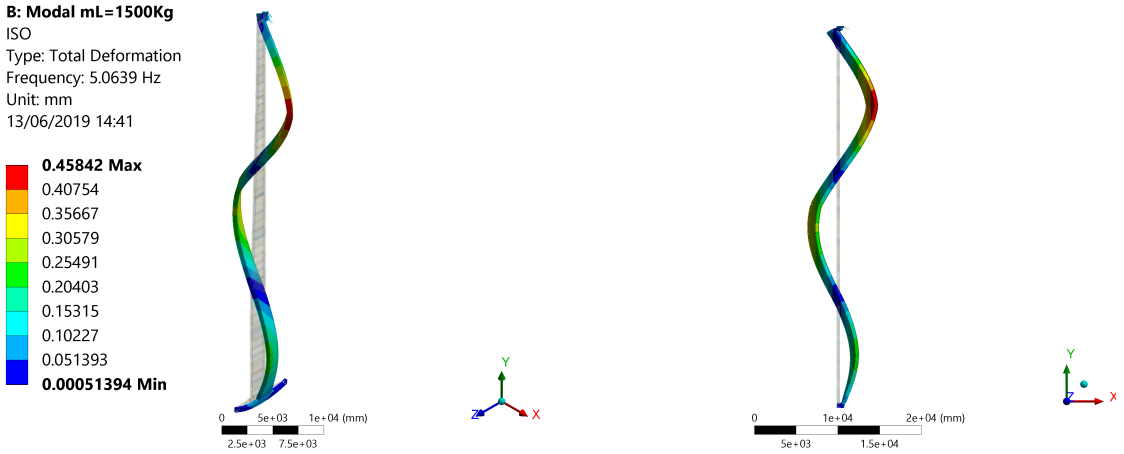
(a) Isoparametric view. (b) In the xy-plane.

Figure 4.46: STK-25's (45 m) 4th natural mode shape ($\omega_4 = 3.41$ Hz)



(a) Isoparametric view. (b) In the yz-plane.

Figure 4.47: STK-25's (45 m) 5th natural mode shape ($\omega_5 = 3.65$ Hz)



(a) Isoparametric view. (b) In the xy-plane.

Figure 4.48: STK-25's (45 m) 6th natural mode shape ($\omega_6 = 5.06$ Hz)

As with the STK-21-C, Table 4.19 shows the new notation adopted for the natural modes of vibration of the STK-25 according to the main plane of bending of the masts in the corresponding mode shapes.

Table 4.19: Notation adopted for the STK-25 vibration modes using the 45 m mast example.

Old	ω_1	ω_2	ω_3	ω_4	ω_5	ω_6
New	ω_1^{xy}	ω_1^{yz}	ω_2^{xy}	ω_3^{xy}	ω_2^{yz}	ω_4^{xy}

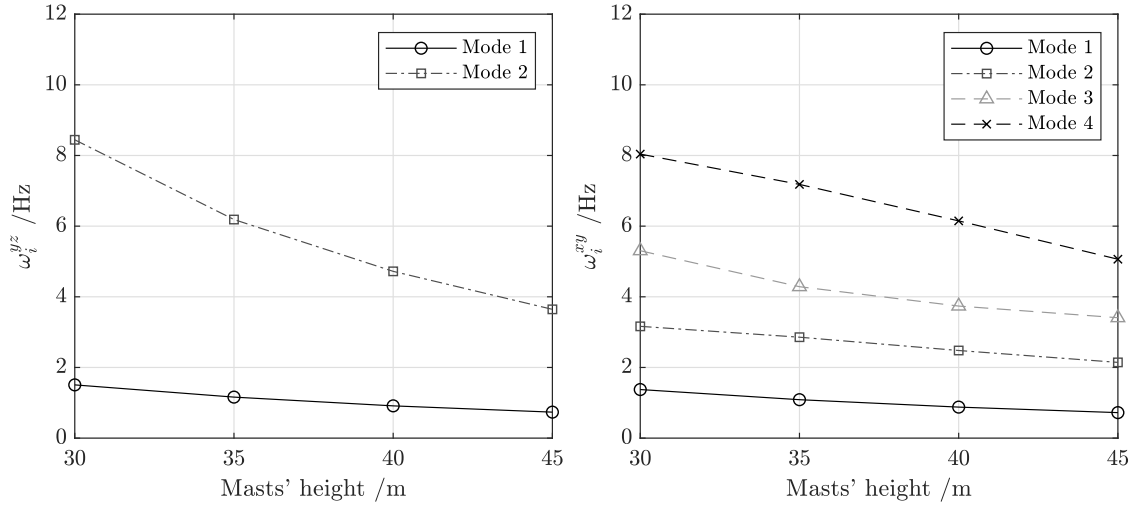
The mode shapes for heights 35 and 40 m were similar to the ones already presented for the 45 m case and are therefore not shown. Figure 4.49 shows the variation of the natural frequencies with the mast's height. Note that due to the aforementioned geometry creation procedure, interpolations between two height values should only be made for reference purposes.

For the 30 m case, the mode shape results are depicted in Figures 4.50 to 4.55 as they show noticeable differences to the remaining cases. The previously noticed torsion is now found on modes 4 to 6, which include the second mode of vibration relating to the bending of the mast in the travel plane. Moreover, the 4th mode shape, i.e., the 3rd xy-plane bending vibration mode shape, is now much more similar to the 2nd xy-plane mode shape than to the 4th xy-plane mode shape as opposed to what was found in the previous cases. In the latter, the bending of the bottom carriage can be observed.

Two possible causes were proposed and evaluated for the appearance of torsion on the 30 m mast STK-25:

- the eccentricity of the lumped masses relative to the structure's plane of symmetry parallel to the xy-plane;
- the proximity to the natural frequencies associated with the bending vibration modes of the bottom carriage in the xz-plane.

To test the first hypothesis, two new models comprising only the crane's 30 m tall mast were investigated. One of the models didn't account for the lumped masses while the other



(a) In the yz-plane.

(b) In the xy-plane.

Figure 4.49: Computed natural frequencies of the STK-25 for different mast's height with the lifting carriage at its highest position and $m_L = 1500$ kg.

did. In both cases, the nodes at the edges that previously established the connection to the bottom carriage had their translational degrees of freedom fixed.

For the model with the lumped masses, the 3rd and 4th xy-plane bending modes (Figures 4.56a and 4.56b) show the previously observed combination of torsion and bending. Removal of the lumped masses makes it so that the 3rd and 4th xy-plane modes comprise pure bending vibration as seen in Figures 4.56c and 4.56d.

However, there's not much torsion in the 2nd yz-plane mode shape when the bottom carriage isn't considered but the lumped masses are maintained, contrary to what is found in Figure 4.55, suggesting the presence of another mast torsion inducing effect. Therefore, for the second hypothesis, a model comprising only the bottom carriage was used on which the boundary conditions referred to the wheels and rollers were applied. It was found that the first natural frequency of the bottom carriage, which corresponds to the bending in the xz-plane (Figure 4.57), is in the vicinity of the computed natural frequencies for the 30 m STK-25. Although no boundary conditions were applied to account for the interaction with the mast, the previous reasoning leads to the conclusion that both the effects of the eccentricity of the lumped masses and the bending vibration of the bottom carriage contribute to the differences found on the 30 m STK-25.



(a) Isoparametric view. (b) In the xy-plane.

Figure 4.50: STK-25's (30 m) 1st natural mode shape ($\omega_1 = 1.38$ Hz)



(a) Isoparametric view. (b) In the yz-plane.

Figure 4.51: STK-25's (30 m) 2nd natural mode shape ($\omega_2 = 1.51$ Hz)



(a) Isoparametric view. (b) In the xy-plane.

Figure 4.52: STK-25's (30 m) 3rd natural mode shape ($\omega_3 = 3.16$ Hz)



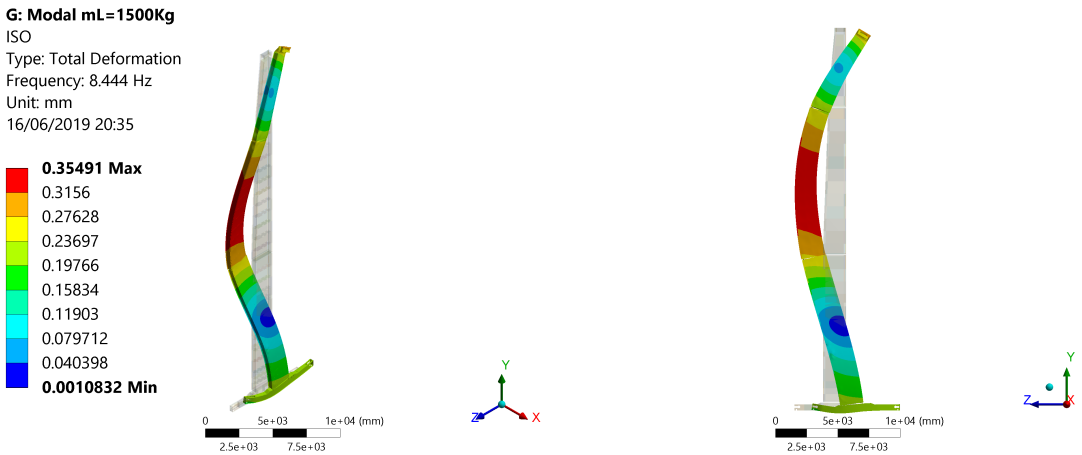
(a) Isoparametric view. (b) In the xy-plane.

Figure 4.53: STK-25's (30 m) 4th natural mode shape ($\omega_4 = 5.30$ Hz)



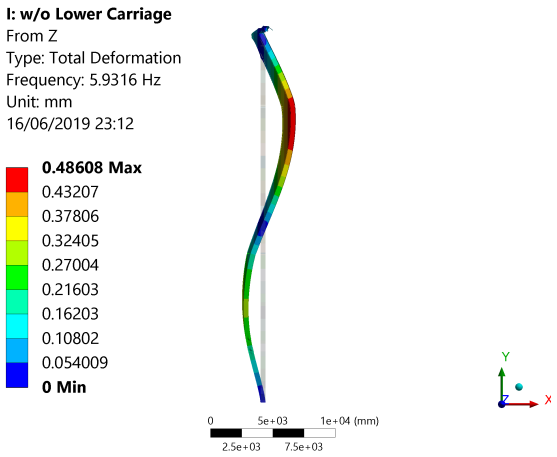
(a) Isoparametric view. (b) In the yz-plane.

Figure 4.54: STK-25's (30 m) 5th natural mode shape ($\omega_5 = 8.04$ Hz)



(a) Isoparametric view. (b) In the xy-plane.

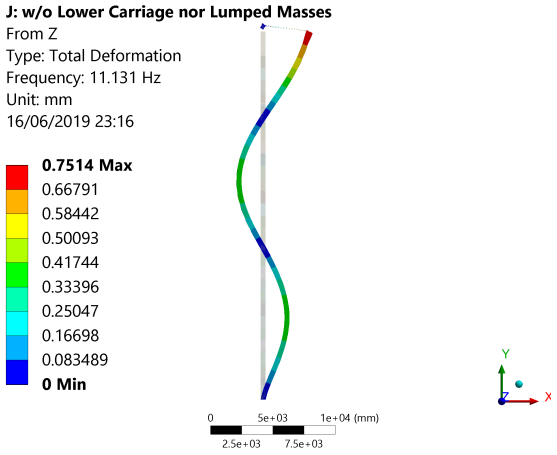
Figure 4.55: STK-25's (30 m) 6th natural mode shape ($\omega_6 = 8.44$ Hz)



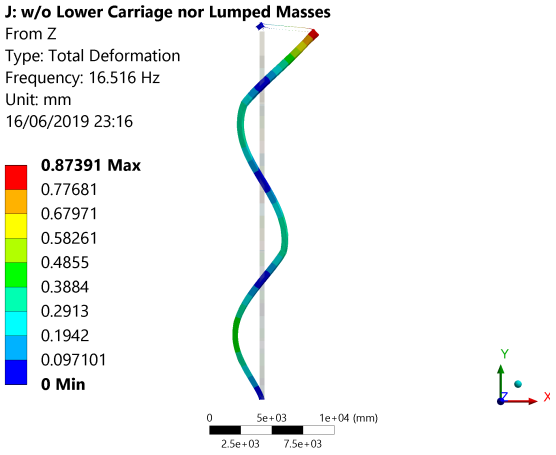
(a) with lumped masses ($\omega_3^{xy} = 5.93$ Hz)



(b) with lumped masses ($\omega_4^{xy} = 9.07$ Hz)



(c) without lumped masses ($\omega_3^{xy} = 11.13$ Hz)



(d) without lumped masses ($\omega_4^{xy} = 16.52$ Hz)

Figure 4.56: Influence of the eccentricity of the lumped masses on the natural mode shapes of the STK-25 (30 m).

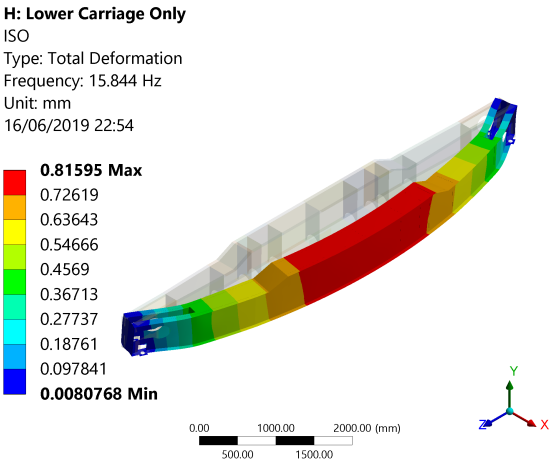


Figure 4.57: STK-25's bottom carriage 1st mode shape ($\omega_1 = 15.84$ Hz)

Chapter 5

Structural integrity of stacker cranes on impact using the FEM

The following chapter presents numerical simulations of a double mast stacker crane's behaviour on impact against the end stops as to assess the maximum stresses in the structure in this limiting condition. Though the impact itself wasn't modelled, conclusions are drawn from the behaviour of the structure when subject to extreme accelerations.

The STK-21-C double mast stacker crane from Chapter 4 is used as a reference case. In section 5.1 the assumptions made for the development of the model are explained as well as the adopted failure criteria.

Parametric studies are carried out and their results presented in section 5.2. The influence of varying acceleration, mast height and payload on the behaviour of the structure are assessed by looking at the displacement of the top of the crane relative to its bottom carriage, the resulting wheel loads and the stress distribution.

Moreover, section 5.3 presents the adopted procedure and results for the assessment of the maximum decelerations to which the stacker cranes machines can be subjected in accordance with their height and payload. These were performed on a go/no-go basis.

The chapter concludes with remarks regarding the application of the same procedure to the remaining stacker crane models.

5.1 Analysis setup

According to section 2.3 of FEM 1.001, three different cases of loading are to be considered for the purpose of the calculations [21]:

- Case I: the working case without wind;
- Case II: the working case with limiting working wind;
- Case III: the case of exceptional loadings.

The standard clearly establishes the case where the machine is "working and subjected to a buffer effect" as being a case III loading. This implies that the loads due to dead weight and due to the working load as well as the greatest buffer effect need to be included in the analysis.

5.1.1 Lumped Masses and Boundary Conditions

On section 4.3 it was seen how the lifting carriage's position along the mast affected the vibrational behaviour of the stacker crane. It is intuitive to assume that in the case of an emergency stop, the mast deflection will increase as the lifting carriage approaches its uppermost position. As such, only this case will be considered as it is the worst case scenario.

The previous assumption that the centre of gravity is placed vertically between the rollers at an equal distance from both is a conservative one as, in reality, it is expected that the platform and LHD push the centre of gravity slightly downwards.

It's important to note that, in reality, the lifting carriage transfers its inertial load to the masts via rollers that allow its vertical movement along the masts which implies that the forces exerted on the structure because of the lifting carriage are compressive by nature. To recreate this behaviour in the finite element model, the lumped mass representing the lifting carriage and payload was considered to only be connected to the mast on the side of the end stop towards which the stacker crane was considered to move, as seen in Figure 5.1.

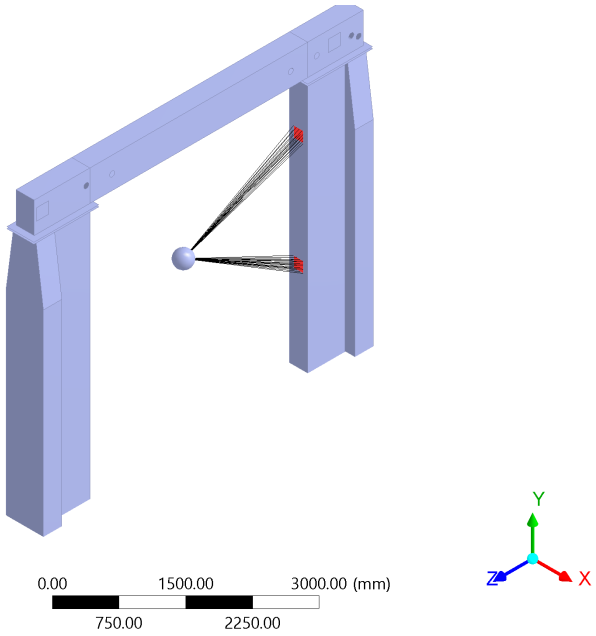


Figure 5.1: Lumped mass connected to only one mast in ANSYS© WB Mechanical.

When the stacker crane impacts the buffer at a velocity v_i, the crane is expected to decelerate as a rigid body at an approximately constant rate by the inherent construction of the equipped buffer. Therefore, the buffer effect on the stacker crane when it reaches the end stops is simulated by making use of a *velocity* boundary condition applied to the area where the buffer is bolted onto the bottom carriage (Figure 4.33). A velocity curve like the one seen in Figure 5.2, starting at the crane's initial rigid body motion velocity, v_i, and decreasing linearly over a time interval, Δt_{stop}, until it reaches zero is imposed. After the deceleration period, the velocity remains enforced null. The resulting deceleration is, therefore, constant and of magnitude, a, so that,

$$a = \frac{v_i}{\Delta t_{\text{stop}}} \ . \tag{5.1}$$

The assumption of constant deceleration is in agreement with the data provided by

the buffer manufacturers and the reasoning present in FEM 9.311.

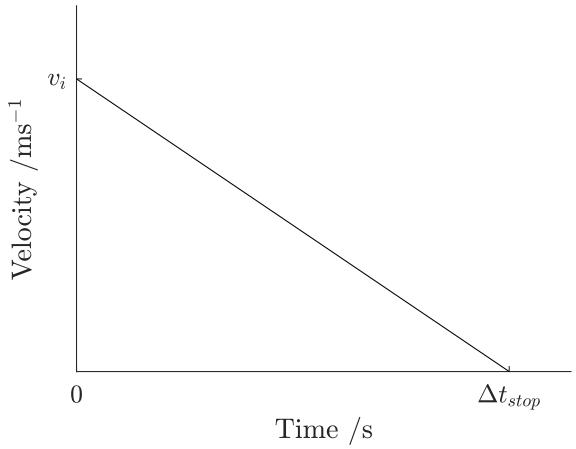


Figure 5.2: Imposed velocity curve on the area where the buffer is bolted onto the bottom carriage.

The boundary conditions relating to the interaction of the machine with the lower and upper rails, either by the wheels or the guiding rollers, remain as presented in Chapter 4. However, attention must be drawn to the fact that when the load on the structure is such that it causes one wheel to lift, it's the reaction of the rail on the anti-tipping device (Figure 2.12) that prevents the machine from derailing. The current model doesn't recreate this behaviour, the stabilising reaction is always assumed to be on the location of the wheel.

5.1.2 Dead weight and working loads

To account for the weight of the structure and its additional components, a *Standard Earth Gravity* load was applied in ANSYS© WB Mechanical to the whole structure. By default, the software considers the acceleration of gravity to have a magnitude $g = 9.8066$ m/s^2.

The weight of the lifting carriage is supported by steel wire ropes running through sheaves mounted on the upper crossbeam. Considering the free body diagram (Figure 5.3) of the vertical loads acting on the lifting carriage, the tension force, T, on the steel wire ropes can be computed as,

$$T = \frac{m_{LH}}{4} g \ . \tag{5.2}$$

Considering the sheave numbering of Figure 5.4, the free body diagram of all sheaves except sheave 7 are analogous to the one seen in Figure 5.5a for sheave 3. The free body diagram of sheave 7 can be seen in Figure 5.5b. Considering $\alpha_i = \beta_i \approx 0 \ i = 1, \ldots, 7$, the application of the basic principles of statics leads to the computation of the reaction forces at the sheave mountings:

$$R_i^z = T \quad i = 1, \ldots, 6 \ , \tag{5.3}$$

$$R_i^y = T \quad i = 1, \ldots, 6 \ , \tag{5.4}$$

$$R_7 = 2T \ . \tag{5.5}$$

The reaction forces on the upper crossbeam due to sheaves 1 to 6 were implemented in ANSYS© WB Mechanical by the use of *remote forces* placed on the centroids of the sheaves. As there was no interest in modelling the deformation of the sheaves mounting shafts, the *remote force* functionality provides an alternative to modelling the shafts as

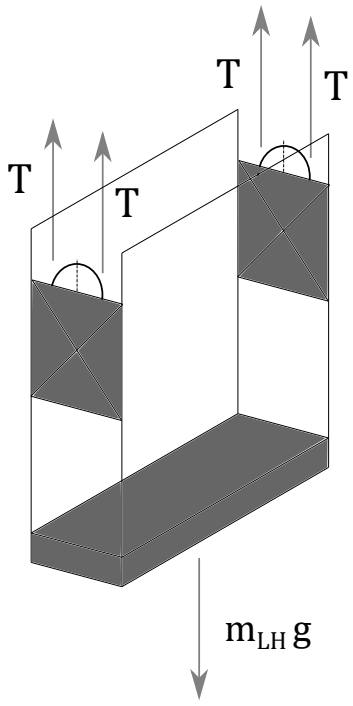


Figure 5.3: Free body diagram of the lifting carriage.

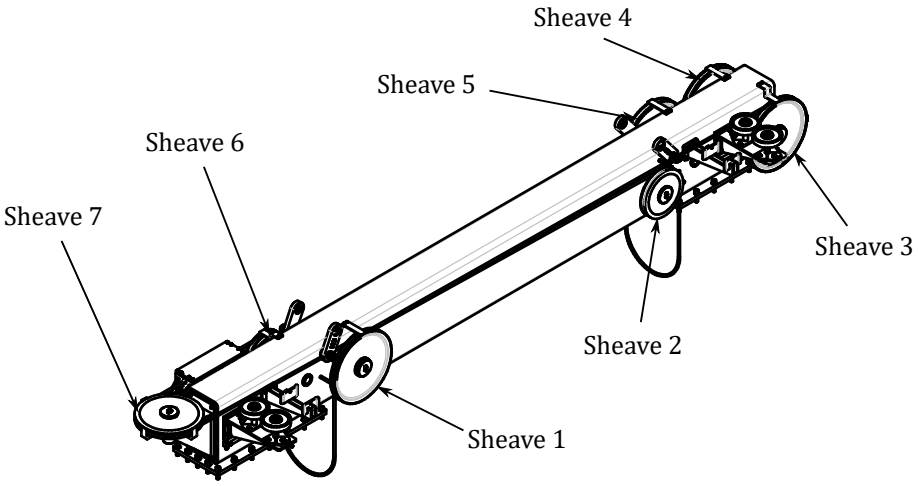
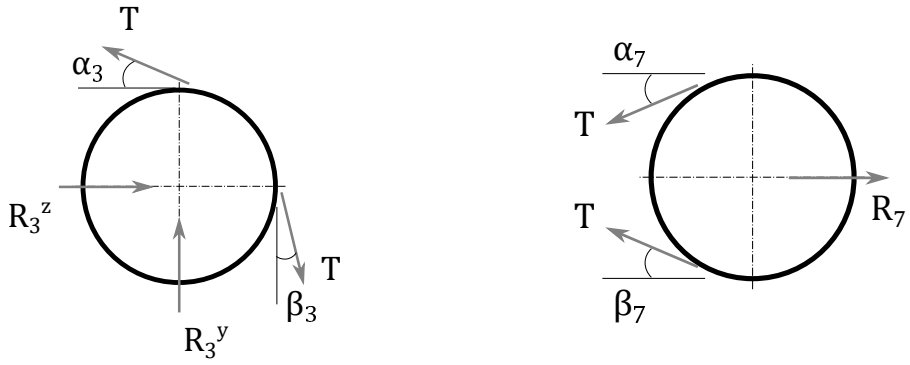


Figure 5.4: STK-21-C sheave numbering notation.

rigid body parts and applying the sheave loads on those [45]. The forces corresponding to the sheaves are depicted in ANSYS© WB Mechanical as seen in Figure 5.6.

From sheaves 3 and 4, the steel wire rope returns to the spooling drums at the hoist unit. As such, a force of magnitude $2T$ was considered to be applied on the hoist unit's mounting plate as seen in Figure 5.7.

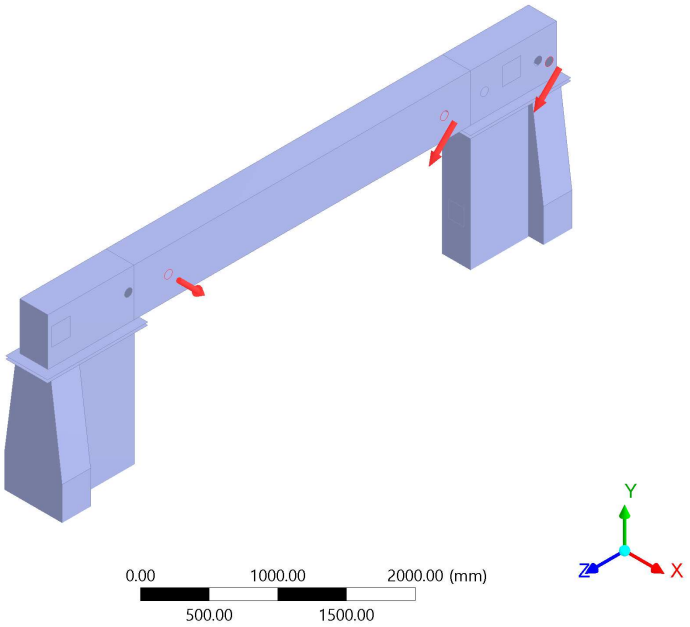
Note that, if nothing else is done, the numerical model will account for the lifting carriage's weight twice. In fact, the applied *Standard Earth Gravity* body force also affects the lumped mass representing the lifting carriage thus causing the transfer of its weight to the connected mast through its corresponding *slave geometry*. A workaround is to apply a force on the lumped mass *remote point* counteracting its weight, as can be seen in Figure 5.8.



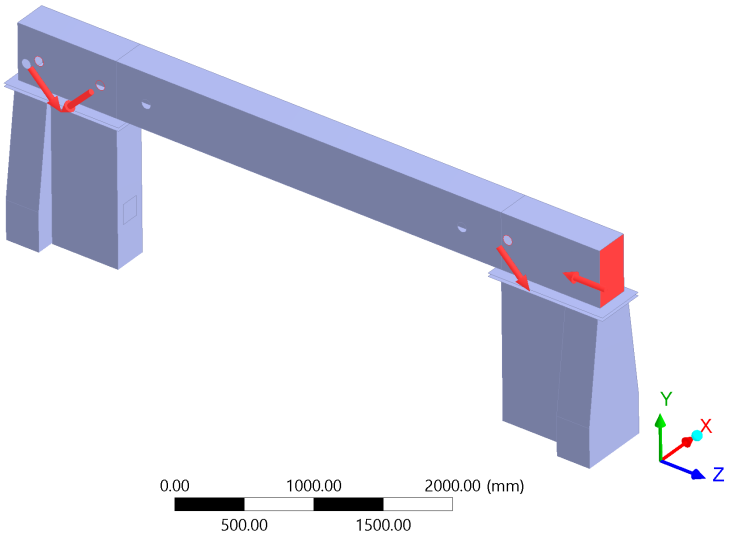
(a) Sheave 3.

(b) Sheave 7.

Figure 5.5: Free body diagrams of the sheaves mounted on the upper crossbeam.



(a) Sheaves 1 to 3, from left to right.



(b) Sheaves 4 to 7, from left to right.

Figure 5.6: Forces exerted by the sheaves on the upper crossbeam in ANSYS© WB Mechanical.

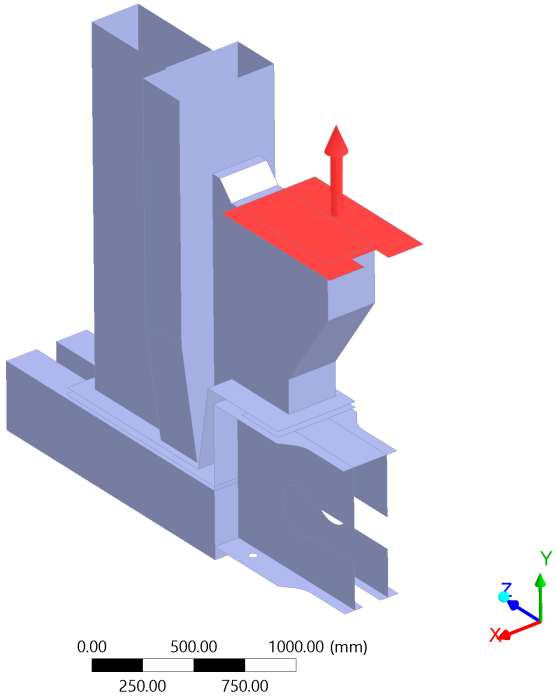


Figure 5.7: Force on the HU's mounting plate due to action of the steel wire rope in ANSYS© WB Mechanical.

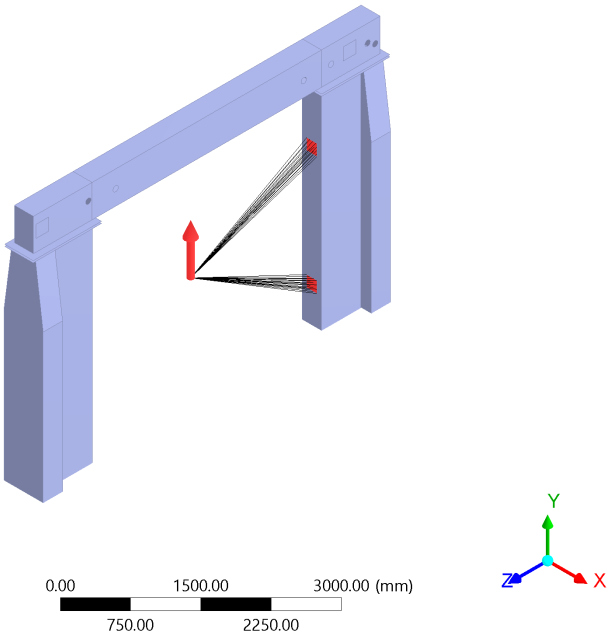


Figure 5.8: Force applied on the lifting carriage's remote point to counteract its weight in ANSYS© WB Mechanical.

5.1.3 Analysis settings

The governing equations of the finite element model take the general form:

$$\boldsymbol{M}\ddot{\boldsymbol{u}}(t) + \boldsymbol{C}\dot{\boldsymbol{u}}(t) + \boldsymbol{K}\boldsymbol{u}(t) = \boldsymbol{F}(t) \ , \tag{5.6}$$

where $\boldsymbol{M}$ is the mass matrix, $\boldsymbol{C}$ the damping matrix, $\boldsymbol{K}$ is the stiffness matrix and $\boldsymbol{F}$ is the vector of generalized nodal forces. The vector $\boldsymbol{u}$ contains the generalized nodal displacements and vectors $\dot{\boldsymbol{u}}$ and $\ddot{\boldsymbol{u}}$ are the corresponding generalized nodal velocity and acceleration vectors.

The numerical simulations were performed using the *Transient Structural* module of ANSYS© WB Mechanical which uses the Newmark time integration method to compute the nodal displacements at any given instant $t + \Delta t$ by use of the solution for instant t [43; 45].

Note that, while the buffer effect on the structure is a dynamic effect and, therefore, justifies the use of the *Transient Structural* module, the working loads on the structure are due to the weight of the crane's components and thus static in nature. The need to divide the simulation into *load steps* arises as it allows for specifying different solver options per step.

A total of four analysis steps were used. The first two steps are used to establish the initial conditions for the transient analysis which occurs on steps 3 and 4.

In step 1, the dead weight and working loads specified in section 5.1.2 are applied. The *time integration* option is turned "off" so that the solver doesn't include the structural inertia of the model. Equation (5.6) is, therefore, reduced to

$$\boldsymbol{K}\boldsymbol{u} = \boldsymbol{F} \ . \tag{5.7}$$

Step 2 is used to apply the initial velocity, v_i, on the structure. To do so, the *Time Integration* option must also be turned "off" in this step and a *Mechanical APDL* command snippet reading "`kbc,0`" must be added under the analysis setup branch as seen in Figure 5.9. This command ensures that the loads at a given load step are linearly interpolated for each substep from the values of the previous load step, thus being necessary to ensure that, at the beginning of step 3, the crane is moving as a rigid body at the imposed velocity.

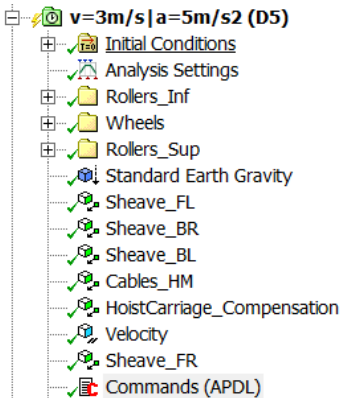


Figure 5.9: Insertion of a *Mechanical APDL* command on the ANSYS© WB Mechanical interface.

The *Time Integration* option is turned "on" for step 3 onwards. It's in this step that the deceleration of the stacker crane is conducted.

The simulation ends with step 4 where the velocity is imposed null in the area where the buffer is bolted on to the bottom carriage.

On all steps, the *Large Deflection* setting was left at its default "on" value. This way, the stiffness matrix is adjusted over multiple iterations to account for changes due to large deflections of the structure using the Newton-Rhapson method [45]. Steps 1 and 2 are divided into sub steps which allow for the incremental application of the static load, thus improving solution convergence. For the presented analyses, the minimum, maximum and initial number of sub steps were specified as seen in Table 5.1, leaving the software in charge of choosing the appropriate number of steps within these bounds according to the ease of obtaining solution convergence. In Table 5.1, the simulation instant of time at which each step ends is also depicted. These values were kept constant and don't have any physical meaning due to *Time Integration* being "off". For future reference, let t_{sim} be the simulation time step, as in the instant of time as seen by the software, and t denote an instant of time after the beginning of the deceleration phase, so that $t = 0$ is the instant at which the crane starts to decelerate.

Table 5.1: Sub step settings for load steps 1 and 2.

Step	End time /s	Num. Sub steps		
		Minimum	Maximum	Initial
1	0.001	4	30	20
2	0.002	4	30	20

The instants at which a solution for the equations of motion is obtained on steps 3 and 4 are separated by integration time steps of size Δt. This time increment between successive time points must be small enough so that it correctly describes the time-varying loads and captures the dynamic response of the system. Moreover, as the system behaviour is non-linear, the time step size also controls the accuracy and convergence of the Newton-Rhapson method [45]. As with sub steps, the minimum (Δt_{min}), maximum (Δt_{max}) and initial (Δt_i) time step size were specified, leaving the software in charge of choosing the appropriate time step size for each time increment.

An equation of current use for the selection of the initial time step is [45]:

$$\Delta t_i = \frac{1}{20\omega_n} \tag{5.8}$$

where ω_n, in Hz, is the frequency of the highest natural mode of vibration of interest. The results from the previous modal analyses of Chapter 4 prove useful for this purpose. For example, a 40 m mast STK-21-C with a 4000 kg payload has a 6th natural frequency of $\omega_6 = 3.74$ Hz whose substitution in (5.8) leads to $\Delta t_i \approx 0.01$ s.

It is possible to add damping to the simulations as Rayleigh damping which implies the damping matrix, $\boldsymbol{C}$, to be established such that [45]:

$$\boldsymbol{C} = \alpha \boldsymbol{M} + \beta \boldsymbol{K} \ . \tag{5.9}$$

However, the determination of the mass and stiffness proportionality coefficients α and β proves difficult and is outside the scope of this dissertation. Moreover, the absence of damping implies that the simulation will provide a worst case scenario condition for the structure. Therefore, in the developed model, no damping effects were considered and the damping term in equation 5.6 can be dropped.

5.1.4 Failure criteria

As the impact of the machine against the end stops is an exceptional loading case, a check with respect to the elastic limit of the material will be conducted.

According to FEM 1.001 [21], the maximum permissible stress, σ_a, is defined by dividing the yield strength of the material (refer to Table 4.4) by a coefficient ν_E dependent on the loading case.

Table 5.2: Values of the safety coefficient ν_E depending on the loading case [21].

	Case I	Case II	Case III
Values of ν_E	1.5	1.33	1.1

Considering a Case III loading and the material to be S355JR steel:

$$\sigma_a = \frac{\sigma_y}{\nu_E} = \frac{355}{1.1} \approx 323 \text{ MPa} . \tag{5.10}$$

Members subjected to simple tension or compression

For structural members subject to simple tension or compression, the computed stress must not exceed the permissible stress σ_a [21].

Members subjected to shear

The permissible stress in shear, τ_a, is defined as being [21]

$$\tau_a = \frac{\sigma_a}{\sqrt{3}} , \tag{5.11}$$

and considering (5.10),

$$\tau_a = \frac{323}{\sqrt{3}} \approx 186 \text{ MPa} . \tag{5.12}$$

Members subjected to combined loads

In situations where the structural members are subjected to combined loading, the most general case, the following checks shall be made [21]:

- each normal stress component is less than the permissible stress σ_a;
- each shear component is less than the permissible shear stress τ_a;
- the equivalent von Mises stress, σ_{eq}, is less than σ_a.

The equivalent von Mises stress, σ_{eq}, is related to the principal stresses by the equation [47]

$$\sigma_{eq} = \sqrt{\frac{(\sigma_1 - \sigma_2)^2 + (\sigma_2 - \sigma_3)^2 + (\sigma_3 - \sigma_1)^2}{2}} , \tag{5.13}$$

or in terms of the cartesian components of the stress-strain tensor as,

$$\sigma_{eq} = \sqrt{\frac{(\sigma_{xx} - \sigma_{yy})^2 + (\sigma_{yy} - \sigma_{zz})^2 + (\sigma_{zz} - \sigma_{xx})^2}{2} + 3\left(\tau_{xy}^2 + \tau_{yz}^2 + \tau_{zx}^2\right)} . \tag{5.14}$$

5.2 Results and discussion

5.2.1 Dynamic behaviour under deceleration

To understand the dynamic behaviour depicted by the model under the deceleration induced by the buffer, simulations were performed without the application of the effects of gravity and the working loads on the structure. The presented case is a 40 m stacker crane with initial velocity $v_i = 4$ m/s and carrying a 4000 kg payload. A stopping time of $\Delta t_{\text{stop}} = 0.7$ s with the crane's movement in the direction of the hoist unit was imposed. The simulation steps and its correspondent end time steps are presented in Table 5.3, note that step 1 in this case corresponds to step 2 from Table 5.1.

Table 5.3: Step settings for the simulations considering only dynamic effects.

Step	End t_{sim} /s	Description	Δt_{min} /s	Δt_{max} /s	Δt_{i} /s
1	0.001	Rigid body velocity v_i	N/A	N/A	N/A
2	0.701	Deceleration	0.005	0.01	0.005
3	3.001	Null rigid body velocity	0.005	0.05	0.01

Taking the displacement in the travel direction of a node (Figure 5.10) in the upper crossbeam, Figure 5.11 presents a comparison between the displacement in the travel direction of the upper crossbeam to that of the bottom carriage. Meanwhile, Figure 5.12 shows the position and shape of the structure at different instants without any deformation amplification.

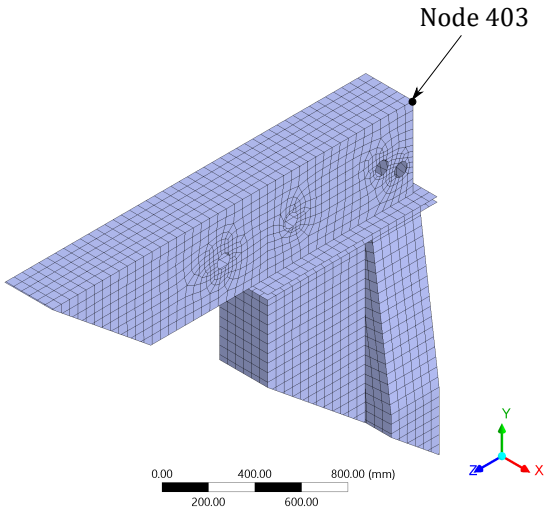
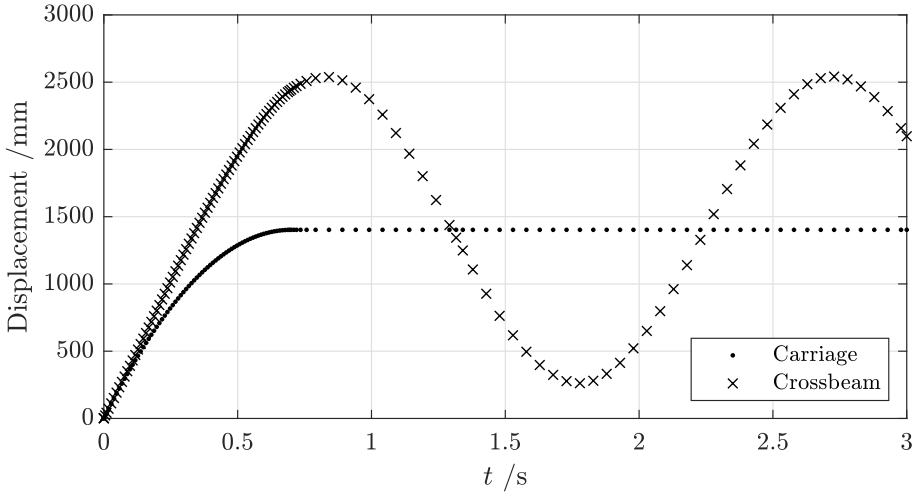


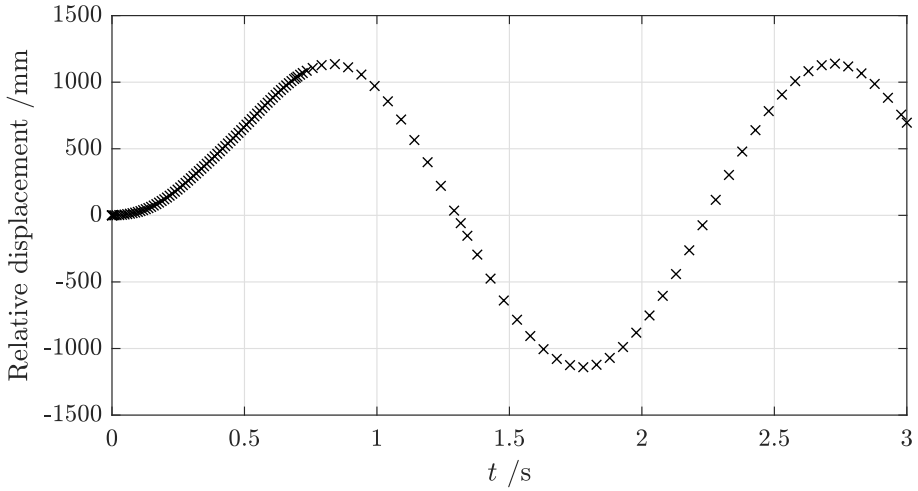
Figure 5.10: Node on the upper crossbeam from which the displacement is shown.

Inspection of Figures 5.11 and 5.12 show that the deceleration imposed to the bottom carriage provokes bending of the masts due to the inertia of the upper regions that advance in relation to the bottom carriage (Figure 5.12b).

A maximum value of 1140.4 mm for the relative displacement of the upper crossbeam in respect to the bottom carriage is achieved after the deceleration period, at $t = 0.841$ s as can be seen in Figure 5.12c. At this point, the upper regions of the crane suffer accelerations with magnitude double the imposed deceleration, as noted in Figure 5.13. Afterwards, the upper crossbeam begins its movement in the opposite direction.



(a) Absolute displacement.



(b) Displacement of the upper crossbeam relative to the bottom carriage.

Figure 5.11: Displacement of the bottom carriage and the upper crossbeam in the travel direction.

The elastic potential energy of the structure is then converted into kinetic energy as the structure returns to its undeformed shape at approximately $t = 1.291$ s. The opposite happens with the kinetic energy of the structure being converted back to elastic potential energy as the momentum of the machine causes it to bend to the other side (Figure 5.12e).

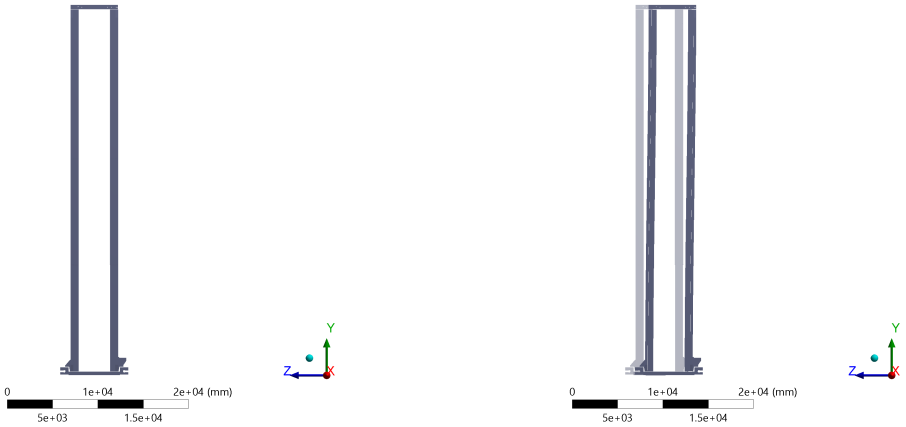
Since no damping effects are in place, a displacement peak of the same magnitude is observed later at $t = 2.729$ s. It can also be seen that since the computed response adopts the shape of a sinusoidal wave, the response of the system will be provoked integrally by one of its modes. The time interval, T, between peaks, i.e., the period of the response is, therefore, computed as,

$$T = 1.888 \text{ s} , \tag{5.15}$$

which leads to a corresponding frequency, ω, of

$$\omega = 0.530 \text{ Hz} , \tag{5.16}$$

which is the value of the first natural frequency found for this particular crane's model/ height/ payload combination in section 4.3.1 when the crane's travel motion was restrained.



(a) $t = 0$ s

(b) $t = 0.358$ s

(c) $t = 0.841$ s

(d) $t = 1.291$ s

(e) $t = 1.779$ s

Figure 5.12: Position and shape of the structure at different time steps.

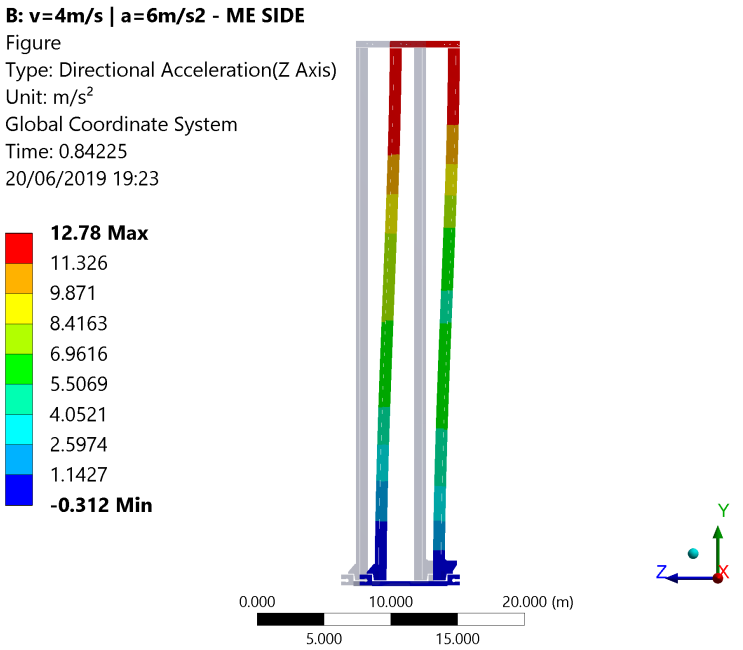


Figure 5.13: Acceleration contour plot in the travel direction ($t = 0.841$ s).

Although, for the most part, the model's behaviour is in agreement with the real phenomenon, a few comments are in order in regards to the simulation's accuracy:

- the assumption of zero velocity of the bottom carriage after the deceleration period is an extreme simplification of the behaviour of the machine. In reality, the end stop will only prevent the machine from moving to one side. However, it is also the case that in an emergency stop, the brakes of the gear motors of the travelling machines will be active, thus locking the wheels;
- the current model assumes no tipping of the machine, something that is likely to happen in emergency stops;
- as explained in section 5.1.1, the transfer of the inertial loads from the lifting carriage to the masts was extremely simplified. In reality, after reaching the first peak mast deflection, the lifting carriage should change the mast to which its inertial load is transferred. Therefore, the present assumption shall only be valid until the first peak of mast deflection is reached. This doesn't prove to be a drawback as there's no interest in the behaviour past this point for the current model.

By lowering the initial velocity to 2 m/s and changing the Δt_{stop} from 0.7 s to 0.35 s in order to maintain the same deceleration as the reference case, it can be seen in Figure 5.14 that the maximum computed relative displacement, henceforth $\Delta w_{\max}$, decreases by 40.4%.

Simulations for $v_i = 4$ m/s were repeated with the time step settings shown in Table 5.4 for steps 2 and 3, the last one ending at $t_{\text{sim}} = 1.001$ s. Figure 5.15 shows the two results, the maximum relative displacement predicted by the simulation with the larger maximum time step is within 0.1% of the same value computed with a smaller time step. Therefore, both settings are equally accurate at predicting the system's response.

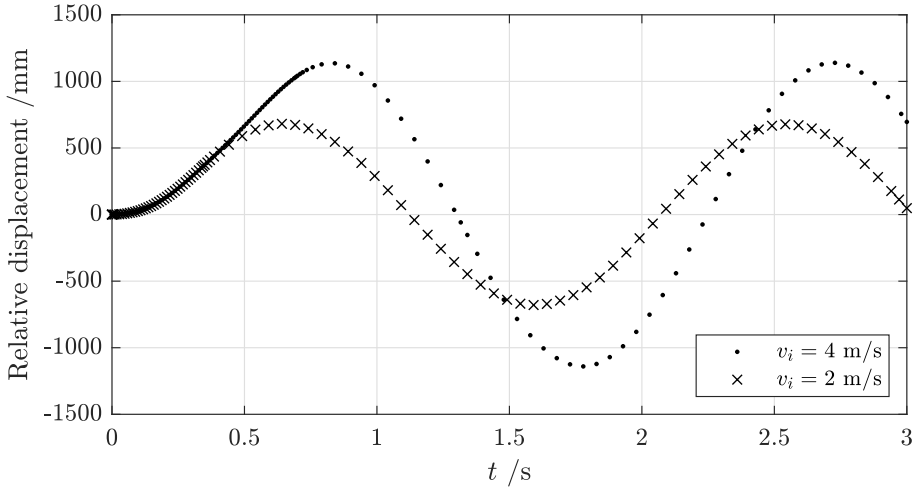


Figure 5.14: Relative displacement of the upper crossbeam to the base in the travel direction for $v_i = 2$ and 4 m/s.

Table 5.4: Time step settings for comparison

Case	$\Delta t_{\min}$ /s	$\Delta t_{\max}$ /s	Δt_{i} /s
1	0.005	0.05	0.01
2	0.005	0.01	0.005

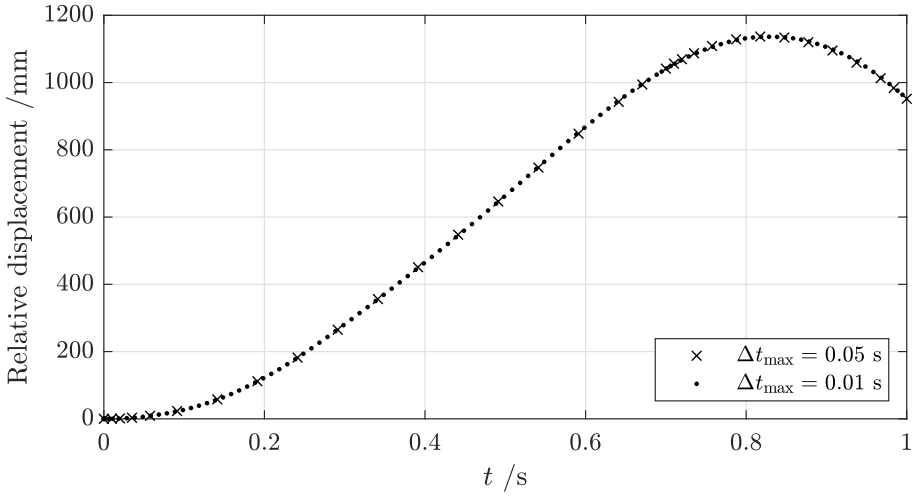


Figure 5.15: Relative displacement of the upper crossbeam for the time step settings of Table 5.4.

5.2.2 Reference case

Response under static loading

After understanding the dynamic behaviour of the presented model and how it compares with its real world counterpart, the additional step to account for the static loading of the structure was applied.

The deformed shape of the structure at the end of the static step, i.e., for $t_{\mathrm{sim}} = 0.001$ s is shown in Figure 5.16. Naturally, the applied loads will cause both masts to bend inward

as well as the bending of the bottom carriage.

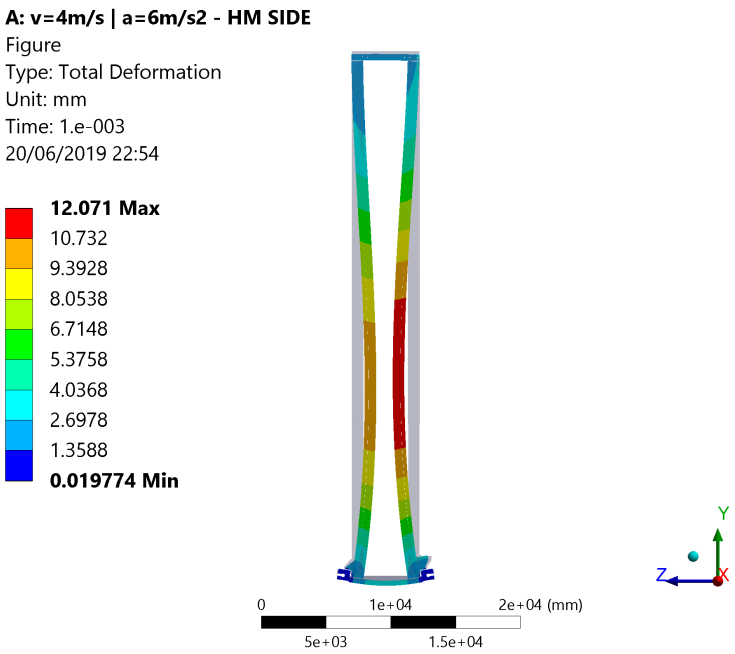


Figure 5.16: Deformation of the STK-21-C (40 m) under static loading with a 4000 kg payload ($t_{\text{sim}} = 0.001$ s).

To ensure that the weight of the lifting carriage isn't accounted twice, the wheel loads can be computed by summing the reaction forces at the nodes on the wheel housings at time step $t_{\text{sim}} = 0.001$ s:

$$R_{\text{HU}} = 191.08 \text{ KN} , \tag{5.17}$$

$$R_{\text{EC}} = 192.03 \text{ KN} . \tag{5.18}$$

A quick hand calculation ensures that the reaction forces are indeed counteracting the structure's weight,

$$m_{\text{Total}} = \frac{R_{\text{HU}} + R_{\text{EC}}}{g} = 39066 \text{ kg} \tag{5.19}$$

which is within 0.11% of the total 39108 kg mass of the model. The reason for this error is the rounding in the magnitude of the force applied on the lifting carriage's remote point.

Upper crossbeam displacement

Simulations were conducted for increasing values of stopping time, Δt_{stop}. Due to the considerations on simulation accuracy and relevance of section 5.2.1, the elapsed simulation time was chosen to be just enough so that the maximum peak deflection of the mast could be achieved. As for step settings, steps 1 and 2 followed the specifications from Table 5.1 while the time step settings for steps 3 and 4 are given in Table 5.5.

Figure 5.18 shows the relative displacement of the upper crossbeam in respect to time for the simulated values of Δt_{stop} which can be found in Table 5.6 with their corresponding values of imposed deceleration. On the same table, one can retrieve information on the values of Δw_{max} as well as the instant of time after the beginning of the deceleration when it happened, t_{max}.

Table 5.5: Time step settings for load steps 3 and 4.

Step	$\Delta t_{\min}$ /s	$\Delta t_{\max}$ /s	Δt_{i} /s
3	0.005	0.02	0.01
4	0.005	0.02	0.01

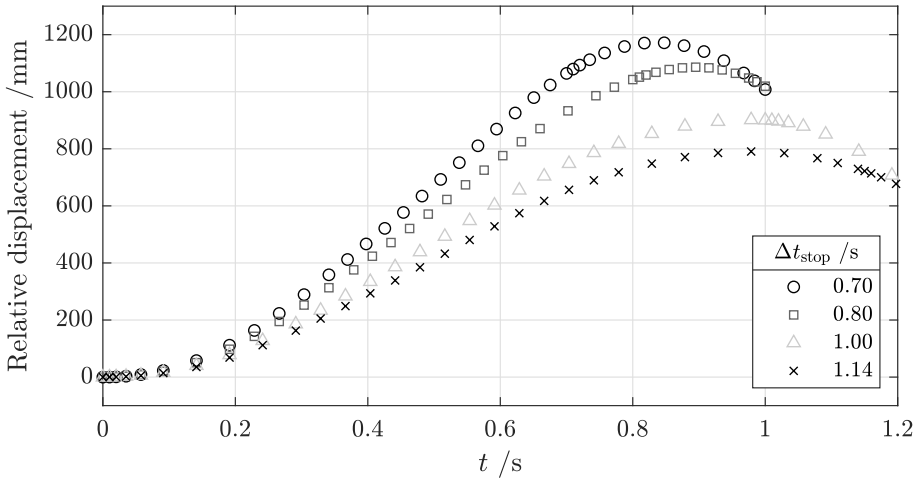


Figure 5.17: Upper crossbeam's relative displacement in respect to time for various values of Δt_{stop}.

Table 5.6: Peak relative displacement and time for various Δt_{stop} with $v = 4$ m/s, $m_L = 4000$ kg.

Δt_{stop} /s	a /ms^{-2}	$\Delta w_{\max}$ /mm	$t_{\max}$ /s
0.70	5.71	1171.5	0.8475
0.80	5.00	1086.0	0.8950
1.00	4.00	901.5	0.9788
1.14	3.51	790.6	0.9788

It becomes clear from the above that the time step at which the maximum displacement of the crossbeam is observed diminishes as the stop time increases until Δt_{stop} becomes larger than approximately half the fundamental natural period of the stacker crane, being the first mode the most predominant one. It follows from section 4.3.1 that, $T_1/2 = 0.94$ s.

From that stopping time onward, the maximum is found at this particular instant.

It can also be observed that the increase in Δt_{stop} causes a proportional decrease in the maximum relative displacement of the upper crossbeam as seen in Figure 5.18.

The maximum upper crossbeam displacement might impose a limitation on the design of the warehouse as it must be ensured that the crane's deformation doesn't cause it to collide against the surrounding elements. From the above it can be seen that these values easily exceed the 1000 mm mark which makes the masts' deformation noticeable without any kind of amplification, as seen in Figure 5.12.

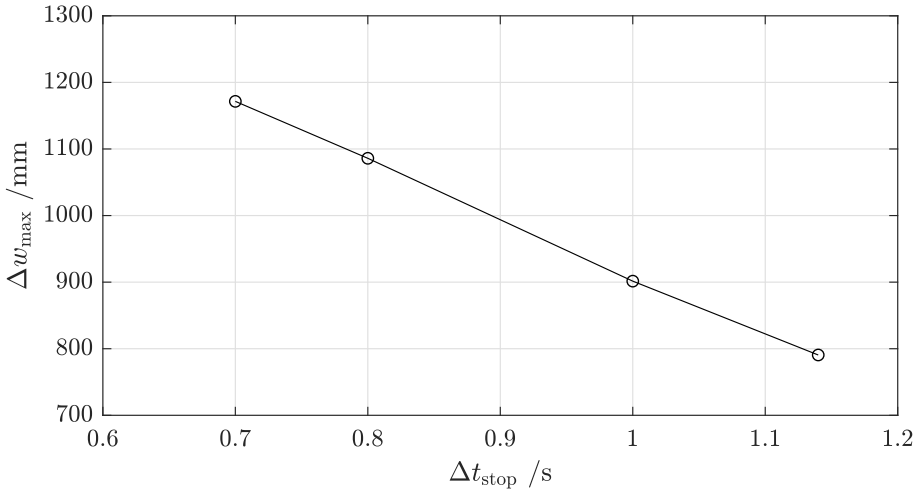
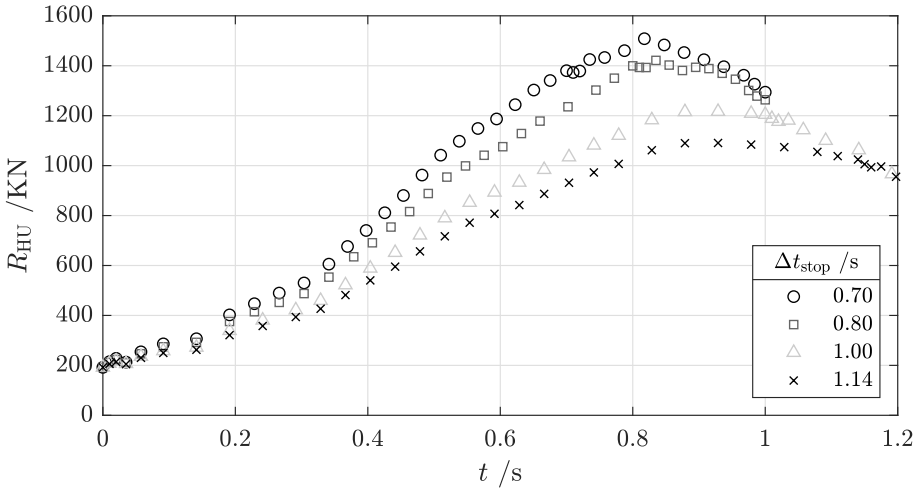


Figure 5.18: Upper crossbeam's relative displacement in respect to time for various values of Δt_{stop}.

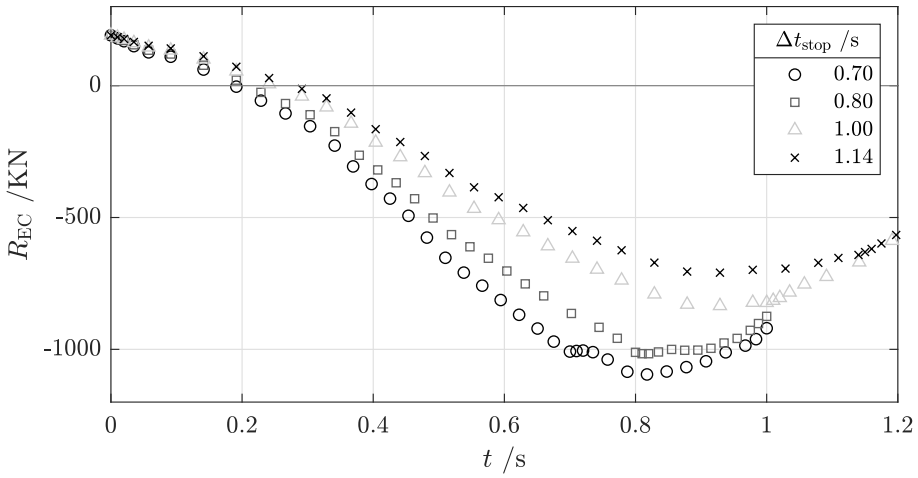
Wheel loads

As mentioned, the wheel loads can be estimated from the sum of the vertical reactions of the nodes in the wheel housings. The maximum values computed by the model can be directly compared to the computation method presented in FEM 9.311 as well as the original simulations performed at Consoveyo, S.A. and can be used as input values for the dimensioning of the drive shafts. Moreover, their variation in time can be analysed to predict the possibility of tipping of the machine, a reality when negative wheel loads take place. Note that these negative wheel loads are actually bore by the non-modelled anti-tipping devices.

The computed wheel loads are shown as a function of time in Figure 5.19 for the values of Δt_{stop} from Table 5.6. One can observe that, as already shown, the static loading contributes to the positive loading of the wheels (notation as of Figure 2.15). The inertial forces further increase the positive loading on the side of the hoist unit in contrast to the decrease in the side of the EC assembly. At a certain instant in the deceleration phase of the crane's motion, the load on the wheel on the side opposite to the travel direction becomes negative. In practice, this would correspond to the lifting of the crane from the rails.



(a) HU's side.



(b) EC assembly's side.

Figure 5.19: Wheel loads in respect to time for various values of Δt_{stop}.

Stresses in the mast

For each case of Table 5.6, the equivalent von Mises stress, σ_{eq}, and the cartesian stress components were analysed.

Figure 5.20 shows contour plots of σ_{yy} for a $\Delta t_{\mathrm{stop}} = 0.7$ s at $t = 0.8475$ s. It was noted early that, at this instant, the upper crossbeam is at its maximum distance from the bottom carriage. Before proceeding with the analysis of the results, it's important to point out that the values shown result from the computation of the stresses at the mid-planes of the shells which comprise the model. The stresses in the mid-plane instead of the outer or inner surfaces were chosen because:

- unless otherwise specified, the element nodes are geometrically placed at the mid-plane thus that's where the solver computes the stress values [45];
- the values on the outer and inner shell surfaces are extrapolated from the values at the mid-plane. Due to the small thickness to length ratio of the masts, the through thickness variation is expected to not be significant;
- if the stresses in the mid-plane are higher than the allowable stress there's a clear

indication of the possibility of plasticity across the whole thickness and further investigation is needed.

Moreover, the presented results are unaveraged, i.e., no averaging is applied to "smooth" the contour plots at the interfaces of the elements, therefore, the results are shown as interpolated inside each element.

The signs of bending in the yz-plane due to the inertia and the structure's weight can be well perceived from these plots. On the lower regions of the masts, the left faces of both masts are in tension in the normal y-directionwhile the right faces are in compression. Travelling upwards along the mast, this effect gradually changes until reaching the upper regions of the mast where the opposite happens due to the bending rigidity added by the upper crossbeam.

On Figure 5.21, the σ_{yy} values are shown on the lower and upper regions of the EC assembly's mast for the mentioned time instant and $\Delta t_{\text{stop}} = 0.7$ s. It's important to note the fact that the σ_{yy} values increase in magnitude as we travel from the middle to the extreme regions of the mast. After reaching the stiffening elements on the lower region, the stresses suffer a considerable decrease in both tension and compression due to the increase in rigidity provoked by these structural elements, restricting the rotations in the lower regions.

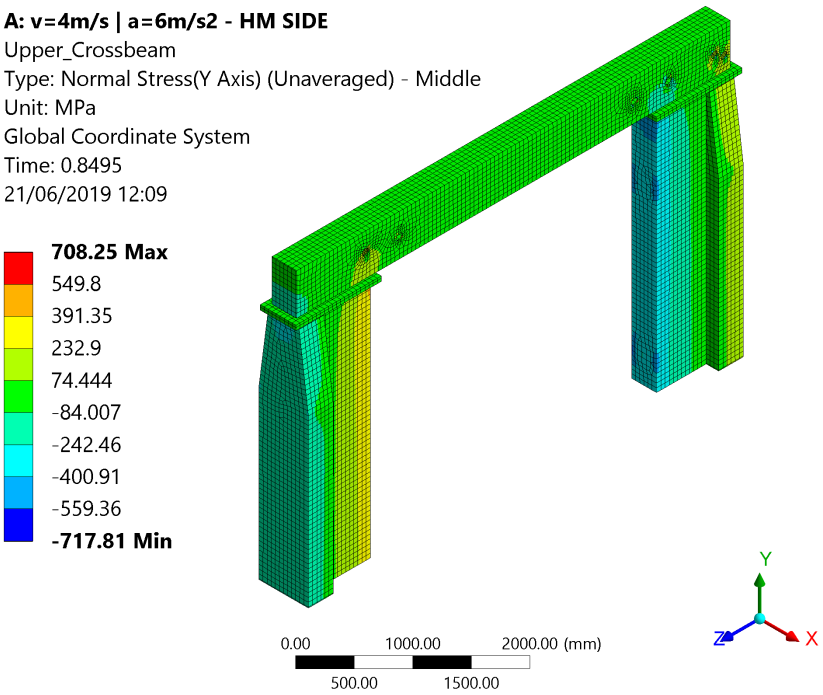
At the lower region (Figure 5.21a), the maximum positive values can be found at the nodes shared with the stiffening structural element while, at the upper region (Figure 5.21b), the highest values are found in the nodes shared between the tubular elements of the mast and the end plates. In both cases, the maximum values are located in zones where large stress gradients appear across the span of a few elements or even inside the same element, indicating a high sensitivity of the results to the particular mesh characteristics of these regions. The re-entrant corners of the geometry cause artifical stress concentrations, i.e., numerical singularities, and thus high stress gradients. Moreover, it must be noted that, by using shell elements, the elements and respective nodes lie on the middle of the plane of the original 3D solids, thus creating regions where the thickness of one shell overlaps another, effectively creating rigidity innacuracies in the model and causing the stress values in Figure 5.21b to drop slightly in the elements nearest to the upper crossbeam, except in the corners due to the aforementioned singularities.

The influence of the acceleration on the σ_{yy} stress component can be seen clearly in Figure 5.22 where contour plots are shown on the lower region of the EC assembly's mast. On this figure and the subsequent ones, the colour map is such that regions where stresses are higher than the 323 MPa are shown in the same colour, contrary to the colour map of Figure 5.21.

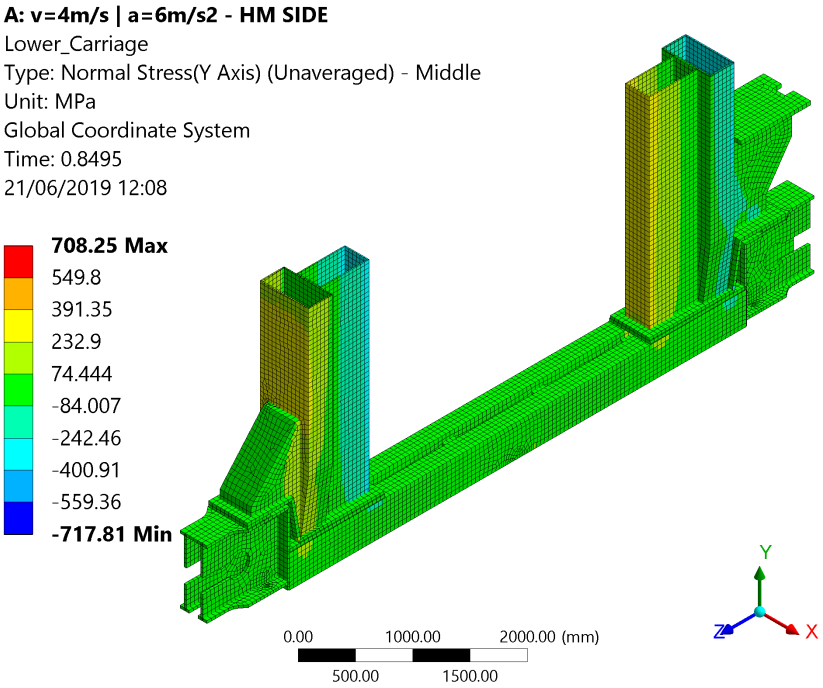
More concerning is the upper region of the same mast where a large area where the stresses surpass the 323 MPa limit can be found for values of Δt_{stop} lower than 1 s (Figure 5.23).

For the other mast, a similar situation can be found, however, here it's the compressive stresses near the hoist unit (Figure 5.24) and on the upper region of the mast (Figure 5.25) that cause the most concern. The asymmetrical stress distribution of Figure 5.24 is explained by the eccentricity of the HU's mounting to the mast. Note that due to the modelling assumptions, the stress distribution near the areas where the lumped mass was connected aren't a correct representation of the actual phenomenon but that should not impact the results in distant regions like the top of the mast.

The aforementioned discussion leads to the conclusion that the major areas of concern in terms of risk of plasticity on the masts are the upper regions, near the upper crossbeam. However, the simulations are affected by singularities which makes it difficult to establish

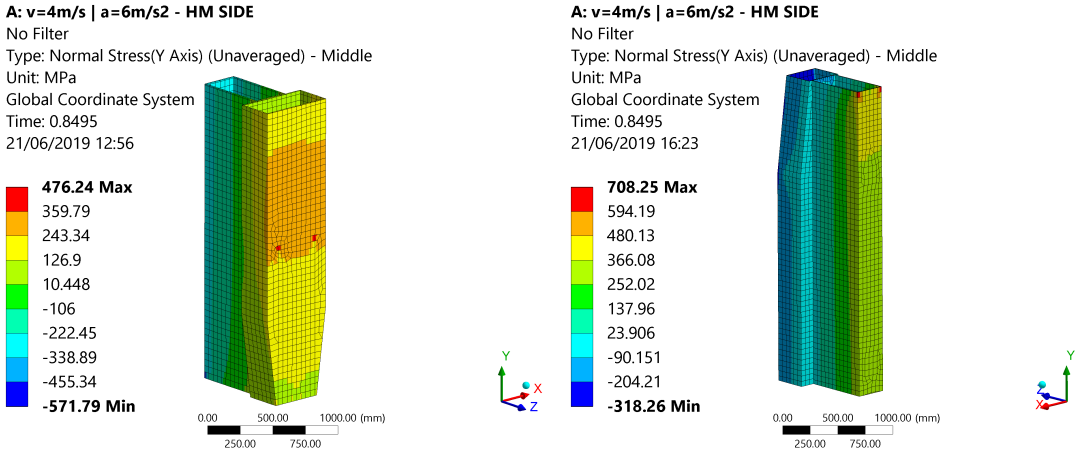


(a) Upper region.



(b) Lower region.

Figure 5.20: Contour plot of σ_{yy} on the lower and upper regions of the stacker crane for $\Delta t_{\text{stop}} = 0.7$ s at $t = 0.8475$ s.



(a) Lower region. (b) Upper region.

Figure 5.21: Contour plot of σ_{yy} on the mast on the EC assembly's side for $\Delta t_{\text{stop}} = 0.7$ s at $t = 0.8475$ s.

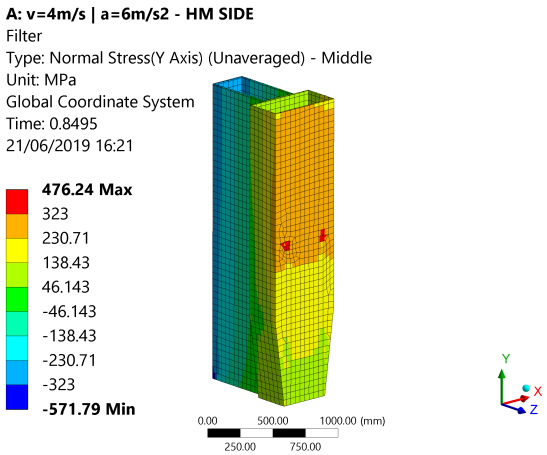
criteria for deciding if a situation is safe or not. On Figure 5.26 it's noticeable that the local refinement of the mesh increases the local stress values as a result of the divergence provoked by the local numerical singularities. In order to eliminate the singularities from the model, the following approaches were equated:

- the modelling of the welds of the reinforcements and the end plates to the masts which would provoke a stress concentration in that region but allow stress values to converge. This is, however, a highly artificial approach and would not provide meaningful results;
- an elastic-perfectly-plastic model could be employed which would imply the local yielding of the material and a stress redistribution in the surrounding region.

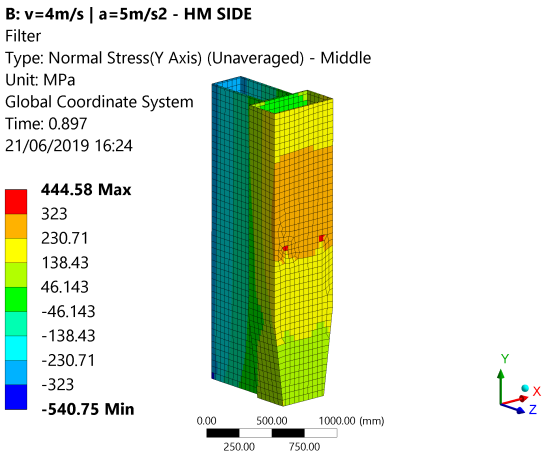
Neither of the above methods ended up being employed however as they wouldn't provide meaningful improvements in the results. Moreover, it can be argued that, while the conditions where $\Delta t_{\text{stop}} < 1.00$ s are unsafe due to the large area over which the admissible stress is exceeded, for $\Delta t_{\text{stop}} \geq 1.00$ s even if plasticity occurs, it will be very localized thus not being a possible cause of bulk failure of the material.

For consistency, it was decided that as long as the area above the admissible stress is confined to two elements length from the maximum nodal value, the condition would be considered safe.

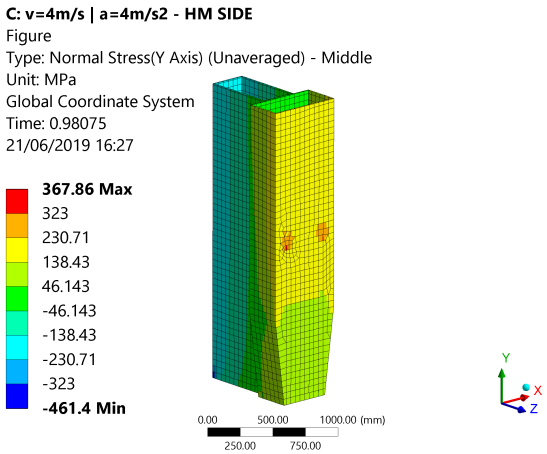
On Appendix C.3.1, Figure C.3 shows contour plots of σ_{eq} on the critical regions for the instants of time when the maximum equivalent stresses are found for $\Delta t_{\text{stop}} = 1.14$ s. These did not always corresponded to the instant of the maximum relative displacement of the upper crossbeam. A possible explanation is the fact that the higher modes of vibration have a higher contribution in the acceleration response of the system than in its displacement response being that the loading case here considered is mainly due to inertial effects.



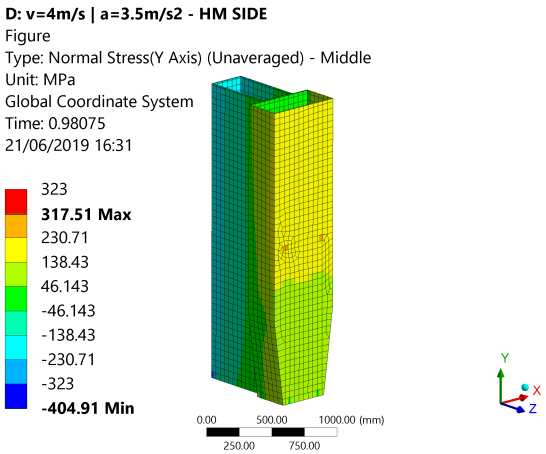
(a) $\Delta t_{\text{stop}} = 0.70$ s, $t = 0.8475$ s.



(b) $\Delta t_{\text{stop}} = 0.80$ s, $t = 0.8950$ s.

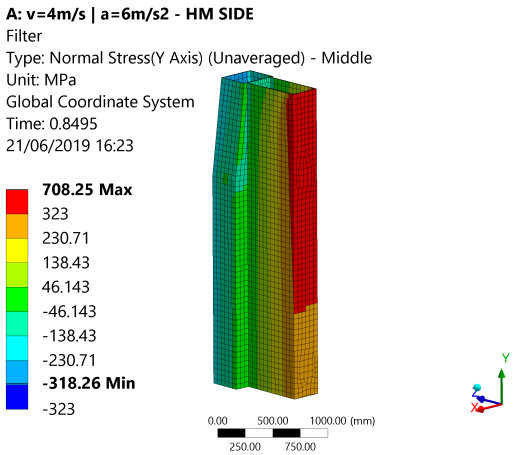


(c) $\Delta t_{\text{stop}} = 1.00$ s, $t = 0.9788$ s.

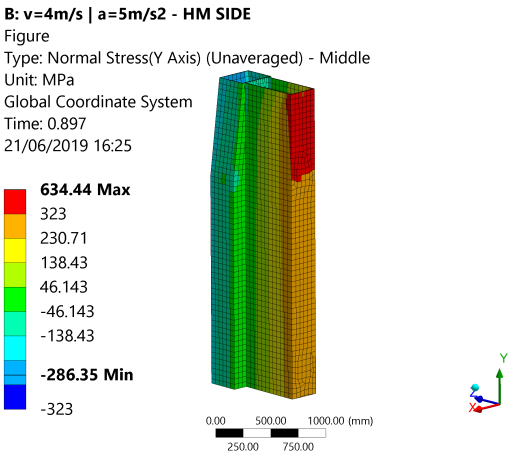


(d) $\Delta t_{\text{stop}} = 1.14$ s, $t = 0.9788$ s.

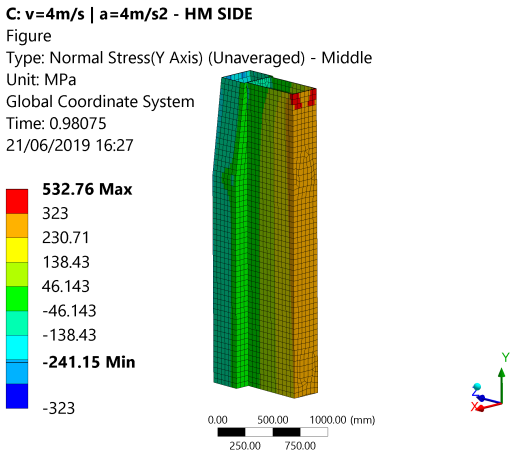
Figure 5.22: Contour plot of σ_{yy} on the lower region of the mast on the EC assembly's side at the time of peak mast deflection for various values of Δt_{stop}.



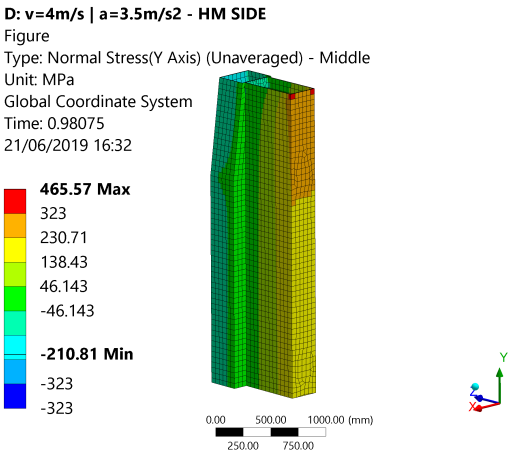
(a) $\Delta t_{\text{stop}} = 0.70$ s, $t = 0.8475$ s.



(b) $\Delta t_{\text{stop}} = 0.80$ s, $t = 0.8950$ s.

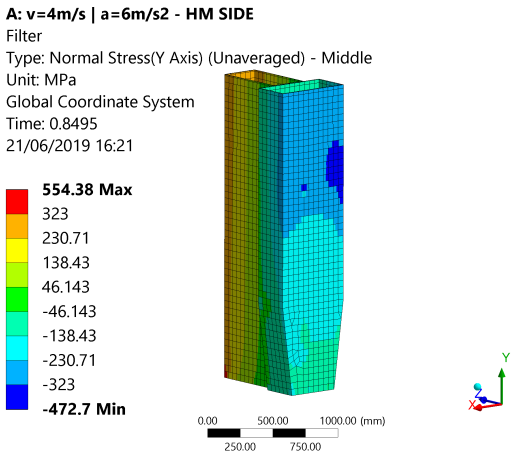


(c) $\Delta t_{\text{stop}} = 1.00$ s, $t = 0.9788$ s.

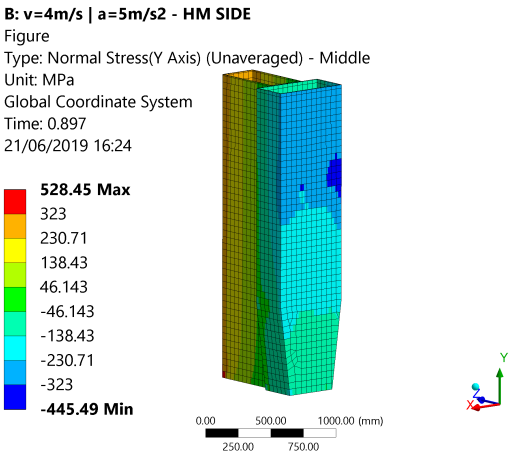


(d) $\Delta t_{\text{stop}} = 1.14$ s, $t = 0.9788$ s.

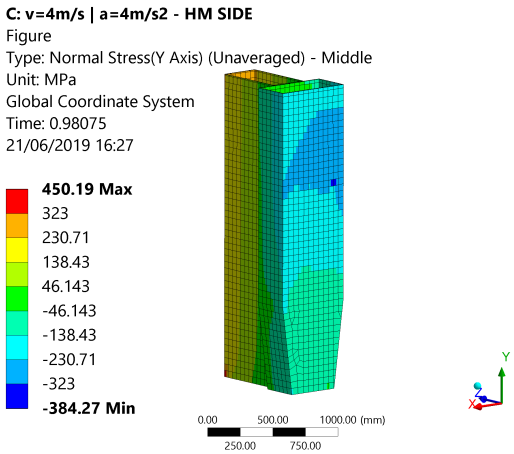
Figure 5.23: Contour plot of σ_{yy} on the upper region of the mast on the EC assembly's side at the time of peak mast deflection for various values of Δt_{stop}.



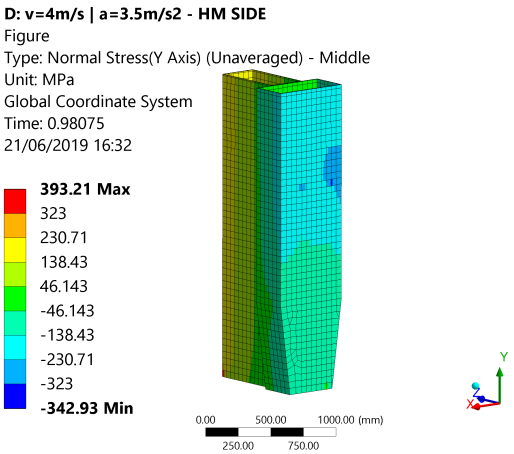
(a) $\Delta t_{\text{stop}} = 0.70$ s, $t = 0.8475$ s.



(b) $\Delta t_{\text{stop}} = 0.80$ s, $t = 0.8950$ s.

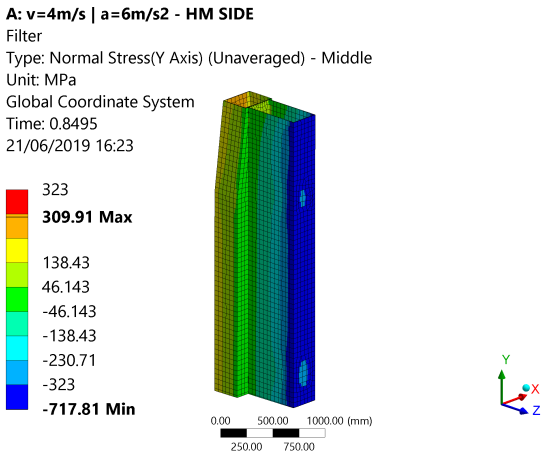


(c) $\Delta t_{\text{stop}} = 1.00$ s, $t = 0.9788$ s.

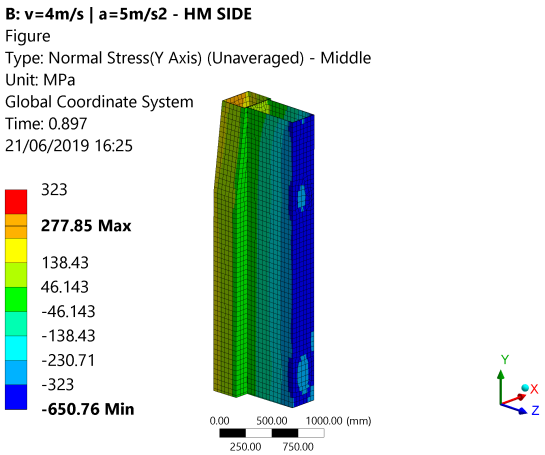


(d) $\Delta t_{\text{stop}} = 1.14$ s, $t = 0.9788$ s.

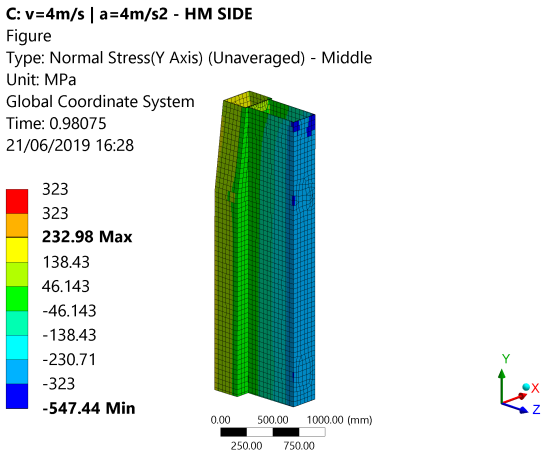
Figure 5.24: Contour plot of σ_{yy} on the lower region of the mast on the HU's side at the time of peak mast deflection for various values of Δt_{stop}.



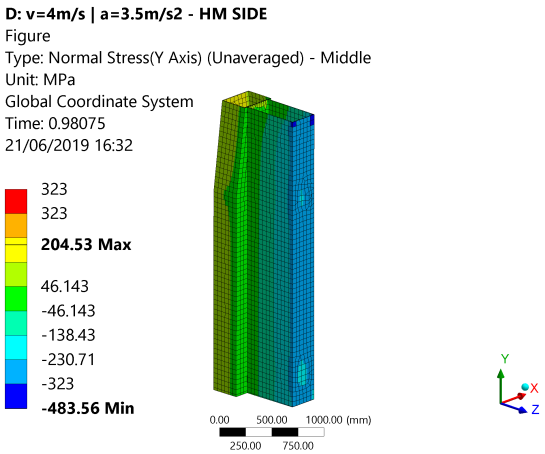
(a) $\Delta t_{\text{stop}} = 0.70$ s, $t = 0.8475$ s.



(b) $\Delta t_{\text{stop}} = 0.80$ s, $t = 0.8950$ s.

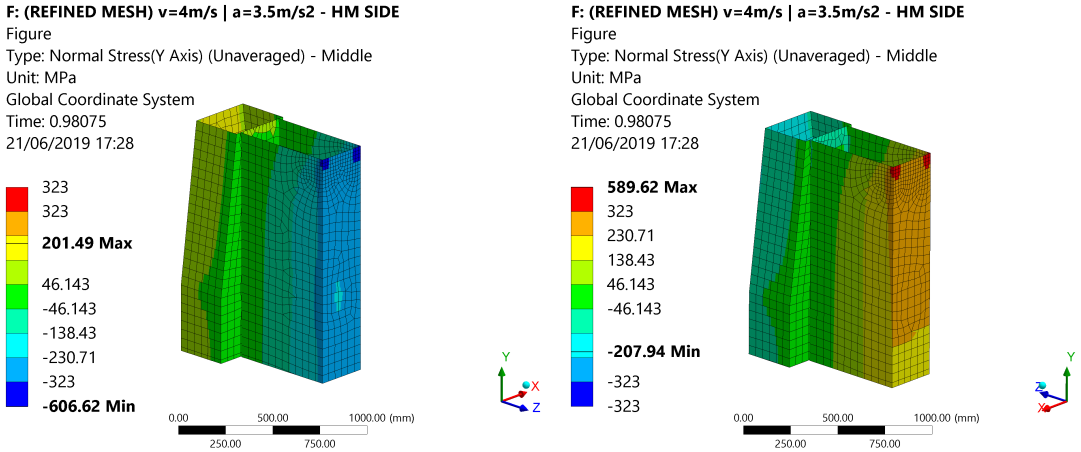


(c) $\Delta t_{\text{stop}} = 1.00$ s, $t = 0.9788$ s.



(d) $\Delta t_{\text{stop}} = 1.14$ s, $t = 0.9788$ s.

Figure 5.25: Contour plot of σ_{yy} on the upper region of the mast on the HU's side at the time of peak mast deflection for various values of Δt_{stop}.



(a) HU side.

(b) ECs' assembly side.

Figure 5.26: Contour plots of σ_{yy} on the upper region of the mast at $t = 0.9788$ s for $\Delta t_{\text{stop}} = 1.14$ s for a locally refined mesh with element size 20 mm.

Stresses in the upper crossbeam and bottom carriage

The action of the masts on the upper crossbeam will cause it to bend in the yz-plane as shown in Figure 5.27. These will induce stresses in the z-direction(Figure 5.28) that must also be taken into consideration.

On Figure 5.29, σ_{eq} contour plots are shown for two values of Δt_{stop} at the instant where the maximum value was computed. In particular, the regions near the mast on the downward face of the crossbeam are prone to surpassing the admissible stresses as shown in Figure 5.30a. The condition of Figure 5.30b was considered to be safe as only slightly higher than admissible stresses were located near the cross-section corners which, because of the geometry simplifications employed, are locations where stress concentrations are bound to occur.

Similarly, the bottom carriage will also bend in the yz-plane as a result of the "whipping" of the structure. Figure 5.31 shows a contour plot of σ_{zz} in the bottom carriage. The extreme values are found on the vicinity of the area on which the *velocity* boundary condition was imposed on the structure and should be disregarded, therefore, the bottom carriage was found to not be a region of concern.

In conclusion, a Δt_{stop} of 1.14 s, i.e., a deceleration of 3.5 m/s^2 was found to be the maximum for this particular model with a 4000 kg payload, with the limiting factor being the stresses in the upper crossbeam.

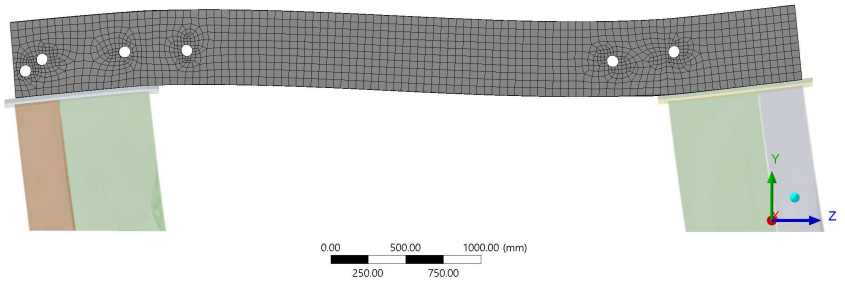
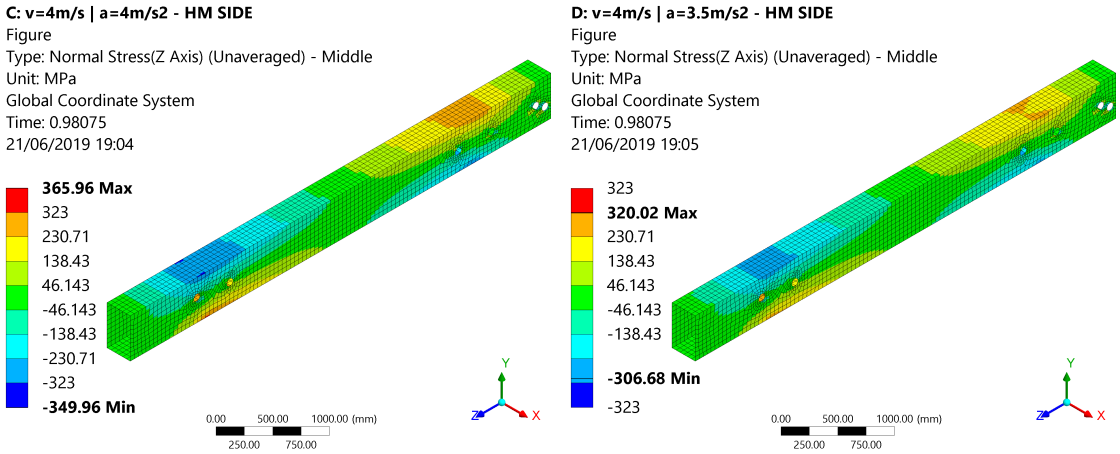
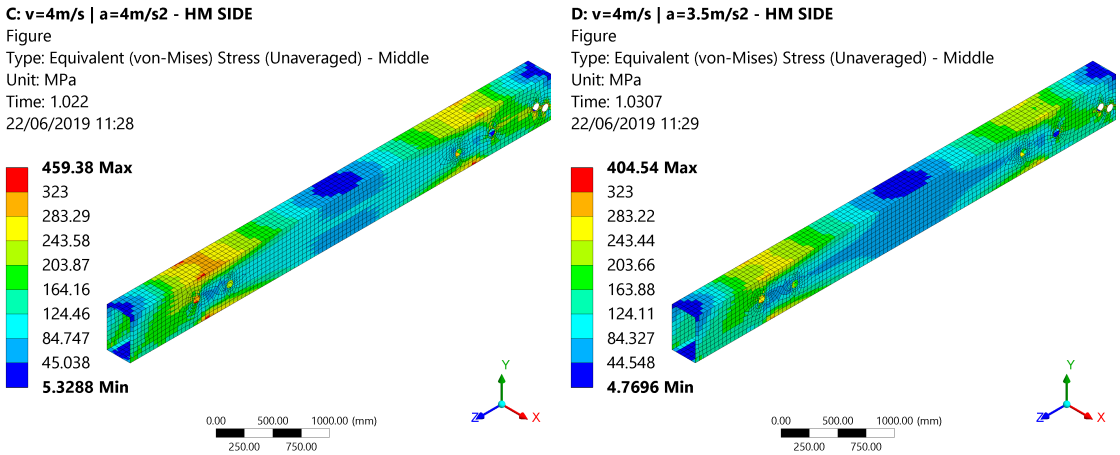


Figure 5.27: Bending of the upper crossbeam for $\Delta t_{\text{stop}} = 1.14$ s and $t = 0.9788$ s (20× deformation amplification).



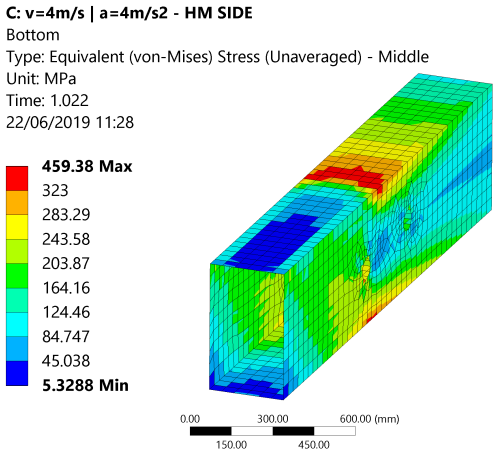
(a) $\Delta t_{\text{stop}} = 1.00$ s, $t = 0.9788$ s. (b) $\Delta t_{\text{stop}} = 1.14$ s, $t = 0.9788$ s.

Figure 5.28: Contour plot of σ_{zz} on the upper crossbeam at the time of peak mast deflection for various values of Δt_{stop}.

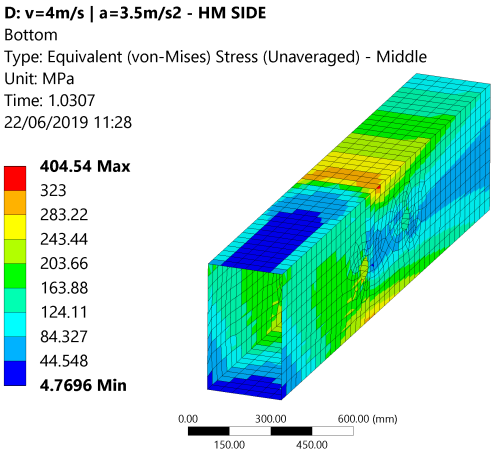


(a) $\Delta t_{\text{stop}} = 1.00$ s, $t = 1.020$ s. (b) $\Delta t_{\text{stop}} = 1.14$ s, $t = 1.0287$ s.

Figure 5.29: Contour plot of σ_{eq} on the upper crossbeam at the time of peak stress for various values of Δt_{stop}.

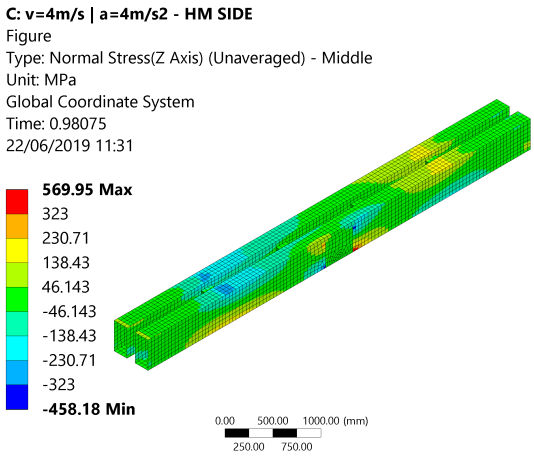


(a) $\Delta t_{\text{stop}} = 1.00$ s, $t = 1.020$ s.

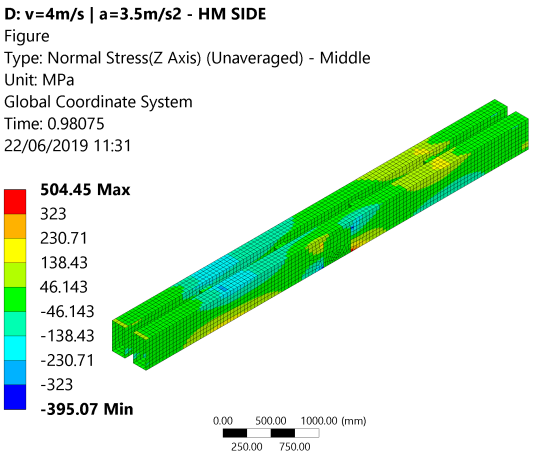


(b) $\Delta t_{\text{stop}} = 1.14$ s, $t = 1.0287$ s.

Figure 5.30: Detail of σ_{eq} on the downward face of the upper crossbeam at the time of peak stress for various values of Δt_{stop}.



(a) $\Delta t_{\text{stop}} = 1.00$ s, $t = 0.9788$ s.



(b) $\Delta t_{\text{stop}} = 1.14$ s, $t = 0.9788$ s.

Figure 5.31: Contour plot of σ_{zz} on the bottom carriage at the time of peak mast deflection for various values of Δt_{stop}.

Comparison with previous practices

The previous calculation method differed from the adopted one in the current study mainly on the fact that the impact situation was assessed via a static study using the *Static Structural* module of ANSYS© Mechanical.

An *acceleration* load [45] was considered to be applied to the whole structure with the movement being fixed in the travel motion on the area where the buffer is bolted on to the bottom carriage. This *acceleration* load translates to a body force applied to each element of a magnitude equal to the elements' mass multiplied by the imposed acceleration.

The acceleration was also multiplied by an oscillation coefficient of 1.5 to account for the buffer characteristic curve as explained in Section 2.3.3.

Considering an acceleration of 3.50 m/s^2 and of 5.25 m/s^2 the peak relative displacement are 50% and 26% less than the value for $t_{\text{stop}} = 1.14$ s found on Table 5.6. The computed values can be found on Table 5.7.

Table 5.7: Comparison of the peak relative displacement using the newly implemented analysis setup and the previous one.

a /ms^{-2}	$\Delta w_{\max}$ /mm	Error /%
3.50	392.5	50.4
5.25	589.2	25.5

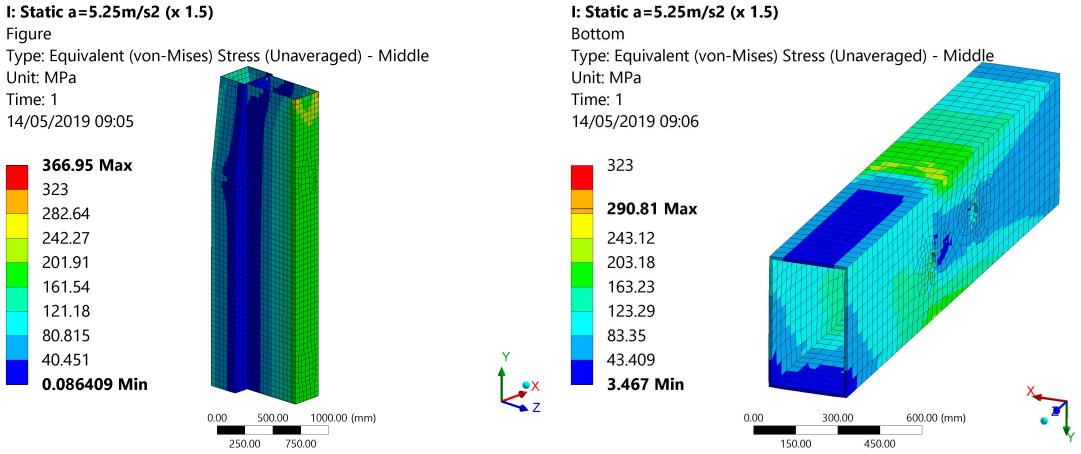
On Table 5.8 it can be seen that the wheel loads are also under predicted by the old model when compared to the new implementation.

Table 5.8: Comparison of the wheel loads using the newly implemented analysis setup and the previous one.

a_z /ms^{-2}	R_{HU}		R_{EC}	
	R_{HU} /KN	Error /%	R_{EC} /KN	Error /%
3.50	550.56	49.5	272.03	61.6
5.25	886.74	18.7	503.60	29.0

Naturally, the stresses in the critical regions show a similar pattern as seen from Figure 5.32 with the majority of these regions having $\sigma_{eq} < 200$ MPa which contrasts with the results of Figure C.3.

The differences between the values computed using the two different methods are due to the fact that, as was seen in Figure 5.13, the maximum accelerations on the structure tend to surpass twice the magnitude of the imposed deceleration. These values are also found near the top of the mast where there's significant percentage of the system's mass due to the upper crossbeam and the lifting carriage. Also of note is the fact that the previously employed static study wasn't able to account for the effect of the initial velocity whereas the new model provides means to optimize the buffer size taking into account the travel speed of the crane.



(a) Upper region of the mast on HU's side.

(b) Bottom of the upper crossbeam.

Figure 5.32: Contour plots of σ_{eq} on the critical regions for a static simulation using $a = 5.25$ m/s^2.

5.2.3 Parametric studies

Influence of masts' height

To understand the influence of the mast's height on the dynamic response of the system, simulations were carried out considering values of 30 and 35 m for the masts' height and $\Delta t_{\text{stop}} = 1.14$ s. The payload was kept at 4000 kg and the analysis time step settings of Table 5.5 were also maintained. While it may be argued that, since the natural frequencies increase with the decrease in mast height, the employed time step should be lower, it must be remembered that the current time step settings were chosen based on the 6th natural frequency of the 40 m case while the response is mainly due to the excitation of the first mode of the structure, at a much lower frequency.

On Figure 5.33, the upper crossbeam's relative displacement in respect to time is plotted for the various values of height and Table 5.9 shows the maximum values of relative displacement and instants, t_{max}, at which they occur. A reduction of 5 m in the masts' height is found to lower the peak relative displacement by 35% with this decrease achieving 60% for a reduction in height of 10 m.

Table 5.9: Peak relative displacement of the upper crossbeam and instant at which it occurs for varying masts' height, with $m_L = 4000$ kg and $\Delta t_{\text{stop}} = 1.14$ s.

Masts' height /m	Δw_{max} /mm	t_{max} /s
40	790.6	0.9788
35	512.0	0.7750
30	310.0	0.5975

The reduction in height causes a decrease of the maximum wheel loads as seen from Figure 5.34. For the EC's assembly side, this reduction reaches 39% from the 40 to the 30 m case while it's only of 29% for the opposite wheel. The difference in these percentages is due only to the contribution of the static loading which adds to the inertial effects in the HU's side while having the contrary effect in the opposite side.

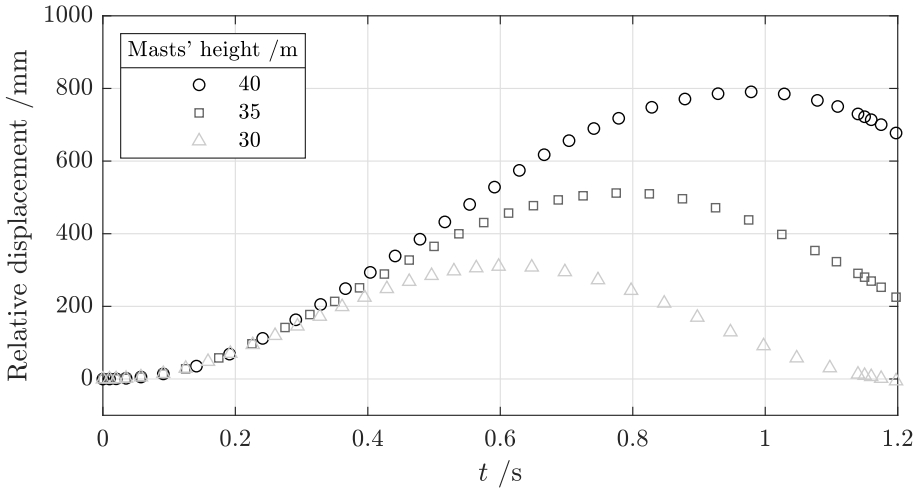
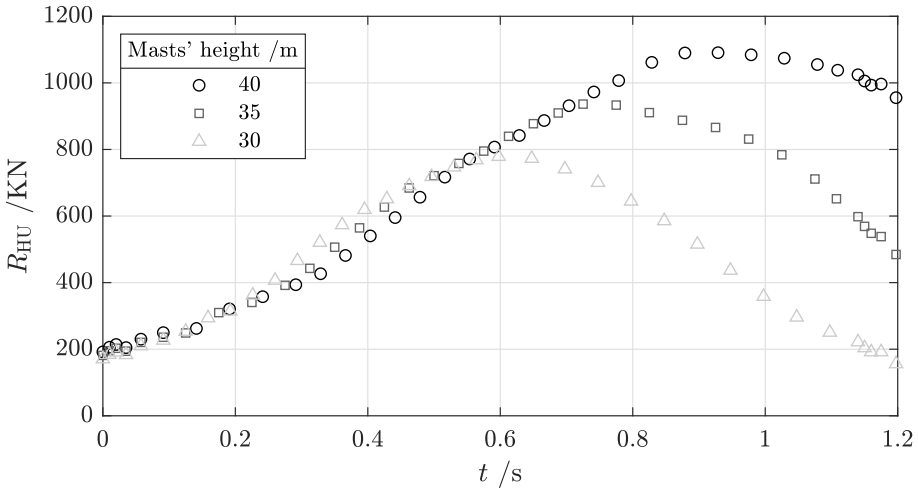


Figure 5.33: Relative displacement of the upper crossbeam in respect to time with varying masts' height, with $m_L = 4000$ kg and $\Delta t_{\text{stop}} = 1.14$ s.

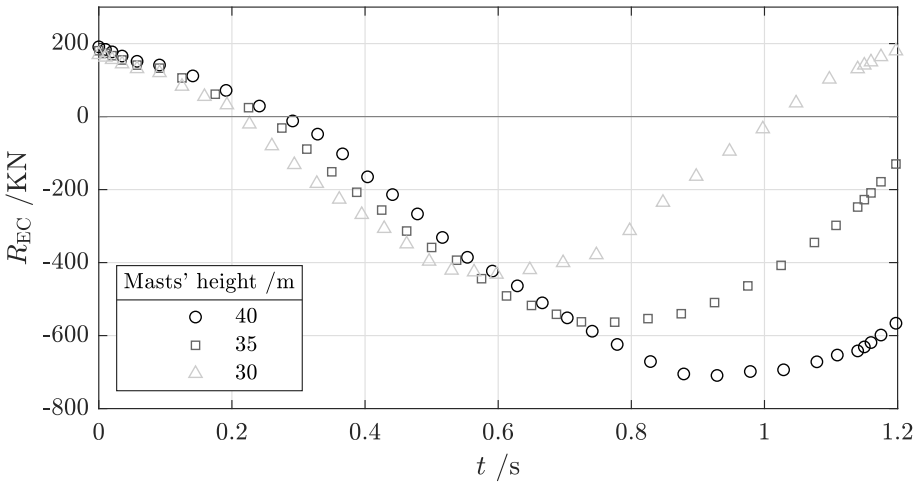
On the regions deemed critical in Section 5.2.2, namely the upper regions of the masts (Figure 5.35) and the upper crossbeam (Figure 5.36). One observes that, while for the 40 m case (Figure C.3), σ_{eq} achieves values between 240 and 300 MPa on the upper regions of the mast (excluding the singularities), these decrease to the 200-250 MPa range for the 35 m masts and are lower than 200 MPa for the 30 m case. The same thing happens in the upper crossbeam.

The significant differences in the relative displacement of the upper crossbeam, the maximum wheel loads and the stress distribution with the decrease of the masts' height are attributed to:

- the removal of a significant amount of mass of the structure. As it stands, the 10 m height decrease leads to a reduction of 11% of the model's mass (from 39108 to 34726 kg);
- the fact that the removed mass was located in the upper regions of the structure which are subject to the most significant acceleration magnitudes;
- the reduction of the maximum magnitudes of acceleration that the crane is subject to at the instant of peak mast deflection as shown in Figure 5.37;
- the lowering of the position of the lifting carriage.

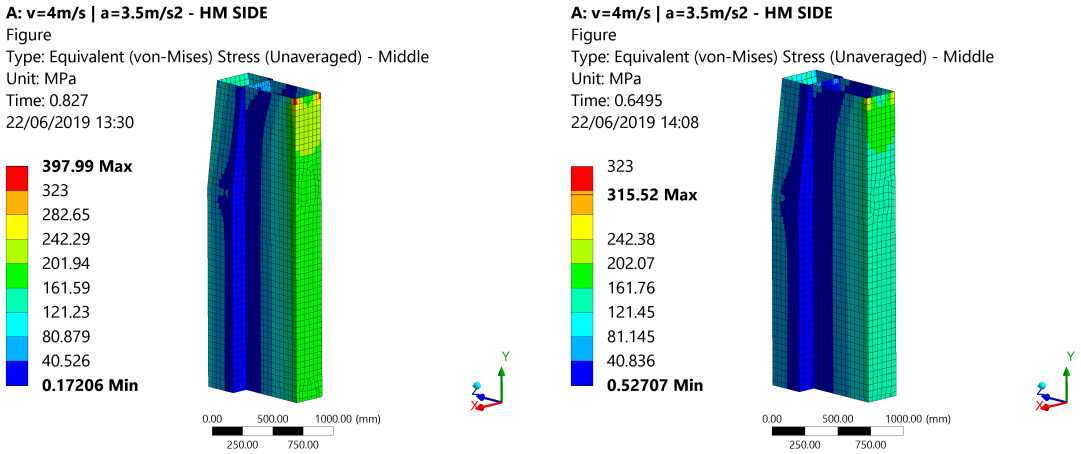


(a) HU's side.



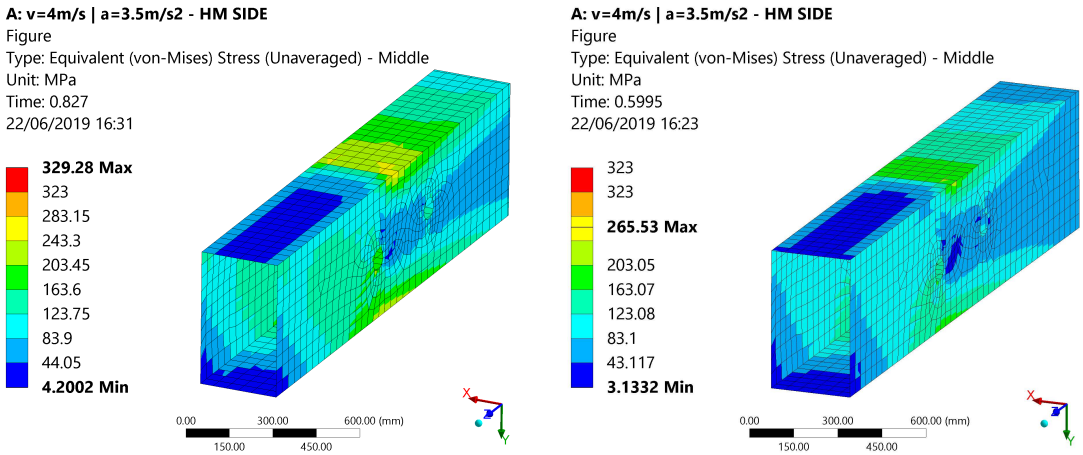
(b) EC assembly's side.

Figure 5.34: Wheel loads in respect to time for various values of masts' height, with $m_L = 4000$ kg and $\Delta t_{\mathrm{stop}} = 1.14$ s.



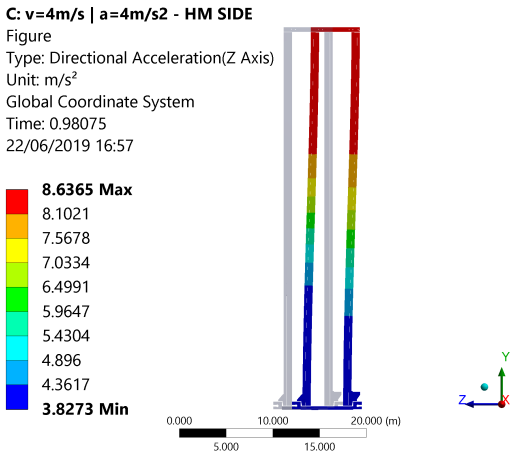
(a) 35 m, $t = 0.825$ s. (b) 30 m, $t = 0.6475$ s.

Figure 5.35: Contour plots of σ_{eq} on the upper region of the mast for the 30 and 35 m masts' heights, with $m_L = 4000$ kg and $\Delta t_{\text{stop}} = 1.14$ s.

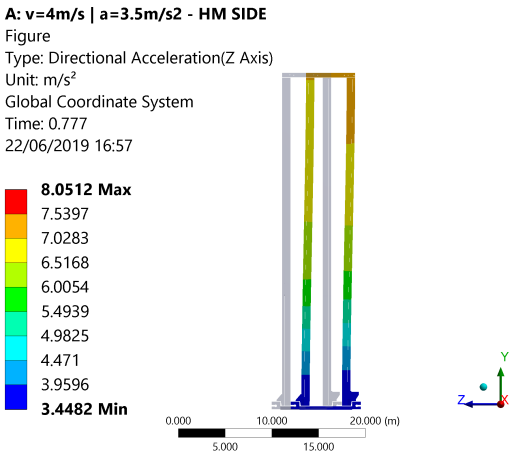


(a) 35 m, $t = 0.825$ s. (b) 30 m, $t = 0.5975$ s.

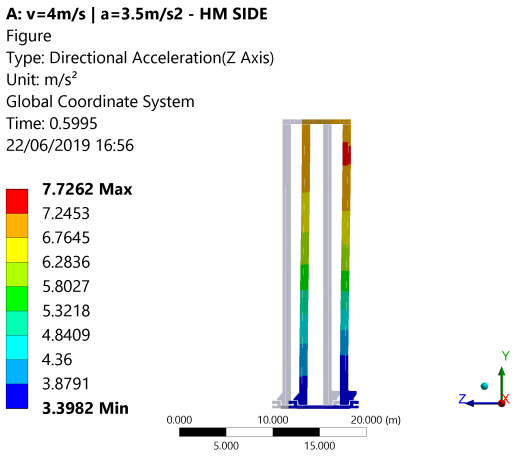
Figure 5.36: Contour plots of σ_{eq} on the upper crossbeam for the 30 and 35 m masts' heights, with $m_L = 4000$ kg and $\Delta t_{\text{stop}} = 1.14$ s.



(a) 40 m, $t = 0.9788$ s.



(b) 35 m, $t = 0.7750$ s.



(c) 30 m, $t = 0.5975$ s.

Figure 5.37: Contour plots of acceleration in the z-directionfor varying masts' heights at the respective $t_{\max}$, with $m_L = 4000$ kg and $\Delta t_{\text{stop}} = 1.14$ s.

Influence of payload

The variation of the system's response to the payload's mass, m_L, was also studied. The following comparison was carried considering $\Delta t_{\text{stop}} = 1.14$ s and the original masts' height with m_L taken to be 2000, 3000 and 4000 kg.

On Figure 5.38, the upper crossbeam's relative displacement in respect to time is plotted for the various values of m_L and Table 5.10 shows the maximum values of relative displacement and the simulation time steps at which they occur. From Figure 5.39 it can be seen that the variation of the maximum relative displacement with the payload's mass is linear. By halving the payload's mass, a decrease of only 11% in the relative displacement of the upper crossbeam was achieved.

Contrary to what happened when the payload was lowered from 4000 kg to 3000 kg, when lowered from 3000 kg to 2000 kg, t_{max} suffered a slight increase. Since the in-plane natural frequencies become higher as the payload's mass decreases, it was expected that the contrary would happen. A closer look at the 3000 kg curve shows that it's possible that the time step employed wasn't small enough to capture the peak of response occcuring between the time step corresponding to $t = 0.9287$ s and the subsequent one.

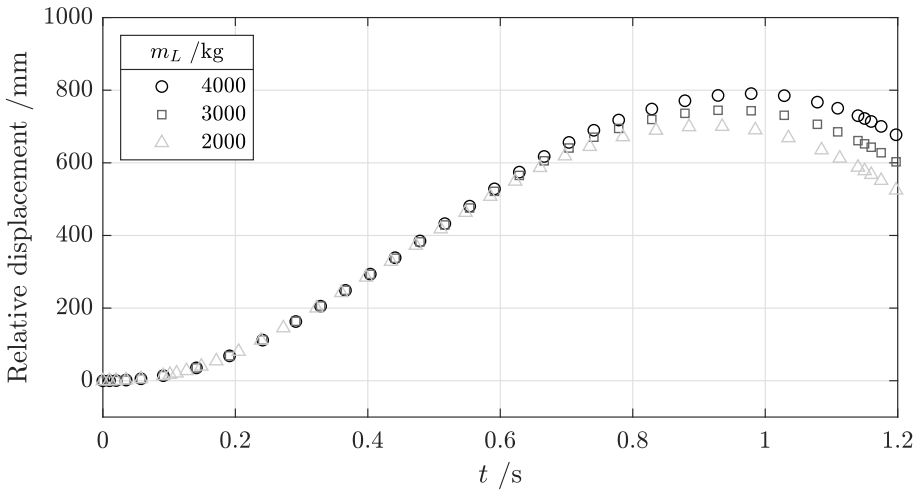


Figure 5.38: Relative displacement of the upper crossbeam in respect to time for varying payload, m_L, with 40 m masts and $\Delta t_{\text{stop}} = 1.14$ s.

Table 5.10: Peak relative displacement of the upper crossbeam and instant at which it occurs for varying payload, m_L, with 40 m masts and $\Delta t_{\text{stop}} = 1.14$ s.

m_L /kg	Δw_{max} /mm	t_{max} /s
4000	790.6	0.9788
3000	744.7	0.9287
2000	699.9	0.9350

The reduction in payload's mass causes a slight decrease of the maximum wheel loads as seen from Figure 5.40. For the EC's assembly side, this reduction reaches 11% from the 4000 to the 3000 kg case while it's only of 9% for the opposite wheel. This difference is due only to the contribution of the static loading.

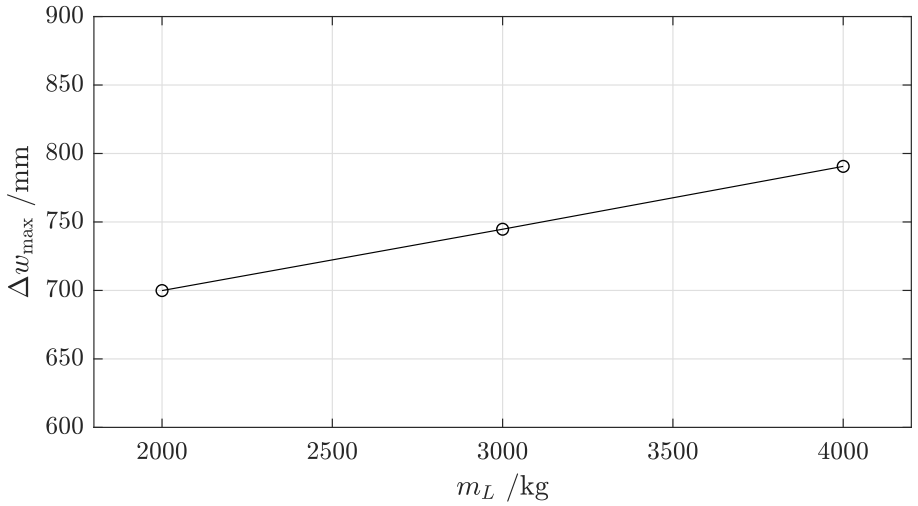
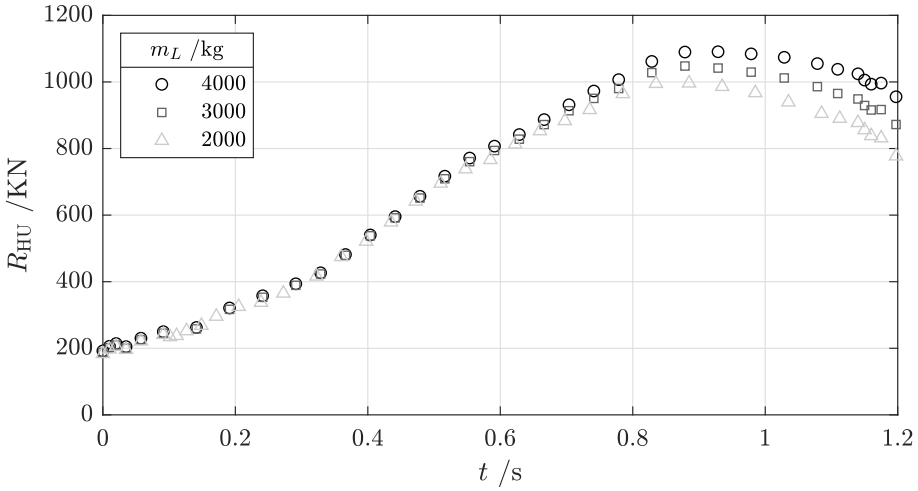
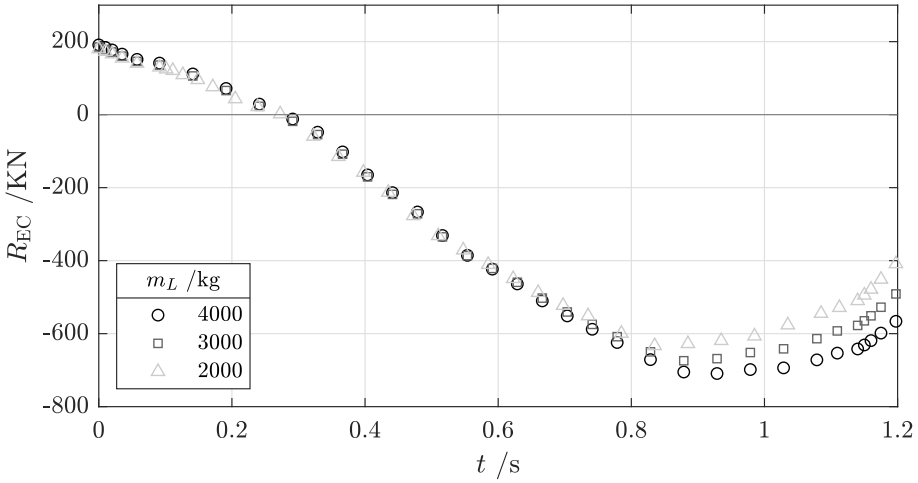


Figure 5.39: Upper crossbeam's relative displacement in respect to time for varying payload, m_L, with 40 m masts and $\Delta t_{\text{stop}} = 1.14$ s.



(a) HU's side.



(b) EC assembly's side.

Figure 5.40: Wheel loads in respect to time for varying payload, m_L, with 40 m masts and $\Delta t_{\text{stop}} = 1.14$ s

5.3 Summary on maximum deceleration results for STK-21-C

In the light of the previous discussion and to determine the maximum deceleration for each height/ payload combination, simulations were carried out in a "go-no go" fashion by varying the imposed deceleration (via the Δt_{stop} parameter) by intervals of 0.5 m/s^2 minimum and considering the rated speed of 4 m/s. The following procedure was adopted:

1. for the maximum payload's mass, $m_L = 4000$ kg, the maximum admissible deceleration was determined for each height value (30, 35 and 40 m);

2. furthermore, the payload was reduced to 2000 kg and the maximum admissible deceleration determined for each height;

3. if the difference between the two aforementioned deceleration magnitudes was considerable, as in ≥ 1 m/s^2, simulations were carried out for the 3000 kg payload; if not, the accepted value for $m_L = 4000$ kg is to be considered for $m_L = 3000$ kg as well.

The results are summarized in Figure 5.41. A dash-dotted line represents the previously used value of 6 m/s^2. In Appendix C, the σ_{eq} contour plots for the combinations of height and payload of Figure 5.41 are presented. In all cases, the stresses in the upper crossbeam were the preventing factor to further increases in deceleration. Also in Appendix C, one can find the maximum values of relative upper crossbeam displacement and wheel loads for the proposed "safe" conditions.

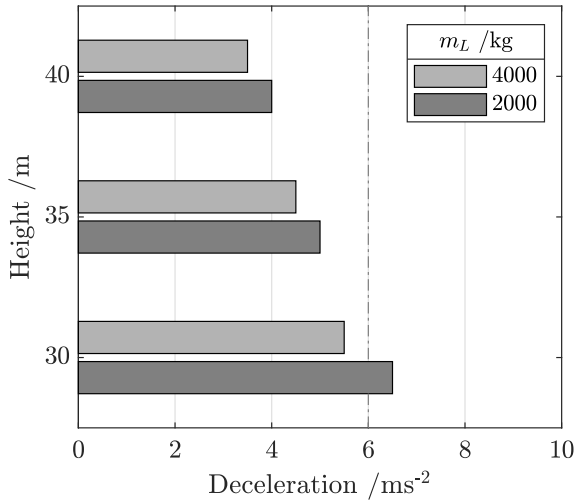


Figure 5.41: Maximum deceleration results for STK-21-C.

Interestingly, the payload's mass has a bigger impact at lower masts' heights which may be explained by the increase of the ratio of payload's mass to the total mass of the structure which translates in a bigger relative impact in the inertial loads.

To assess the impact of the previous results on the aisle occupation by the end stops, a comparison can be made using equation (2.4) between the previously calculated piston stroke, S_0, assuming $a = a_0 = 6$ m/s^2 and the new one, S_f, using the results $a = a_f$ from

Figure 5.41. The difference between the two results, ΔS, is given by

$$\begin{aligned} \Delta S &= S_f - S_0 \\ &= \frac{v^2}{2\eta}\left(\frac{1}{a_f} - \frac{1}{a_0}\right) . \end{aligned} \tag{5.20}$$

By consulting shock absorber manufacturers' data sheets [26; 48], it can be seen that the maximum available stroke doesn't exceed the 1800 mm mark. Also, introducing $v = 4$ m/s and $a = a_0 = 6$ m/s^2 in equation (2.4) gives $S_0 = 1600$ mm which is already very close to the uppermost limit and thus the recommended further increases in stroke will only be possible by mounting two shock absorbers back to back.

As there is one end stop at each end of the aisle, the change in useful aisle space will be double the symmetric of the previous value, $-2 \times \Delta S$. Figure 5.42 presents the change in aisle useful length for the different height/ payload combinations, assuming $1/\eta = 1.2$.

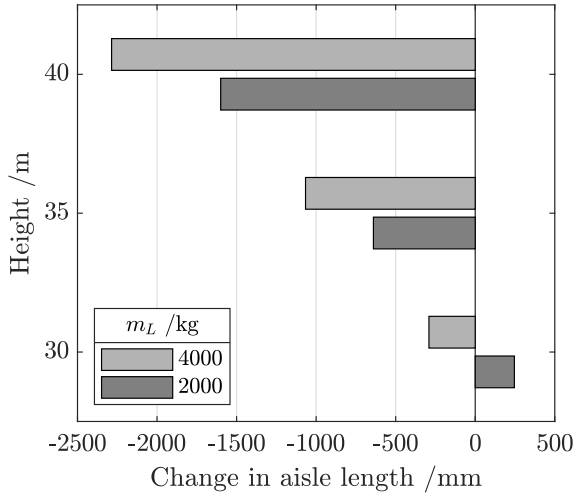


Figure 5.42: Change in aisle useful length when changing the deceleration from the previous to the newly computed values, assuming $1/\eta = 1.2$.

The results show that only the 30 m, $m_L = 500$ kg combination allows savings to be had in the warehouse's aisle, of about 240 mm. The remaining results actually point otherwise, to reductions in useful length as high as 2300 mm.

Some final notes regarding the study of the maximum decelerations for the STK-21-C double mast stacker crane are in order:

- the imposed velocity curve of Figure 5.2 is a very conservative approximation of the real deceleration phenomenon. In reality, the deceleration of the rigid body motion won't follow a step-like function but a more smoothed version of it. Figure 5.43 shows a typical deceleration versus time curve from the shock absorber manufacturer Leben, corresponding to the force versus stroke curve presented in Figure 2.14a;
- the lifting carriage's mass can vary significantly according to the payload specifications which should be taken into account when consulting the information here presented;
- same applies for the LHD's mass. While in the presented case, a double-deep telescopic fork was considered, the use of a single-deep telescopic fork instead would provide a reduction in mass of between 500 and 1000 kg, according to previous experience at Consoveyo;

– the variation of the initial velocity wasn't studied but it was made clear with section 5.2.1 that the decrease of the stacker crane's rated speed will significantly decrease the masts' deflection on the deceleration phase thus allowing for smaller-sized buffers.

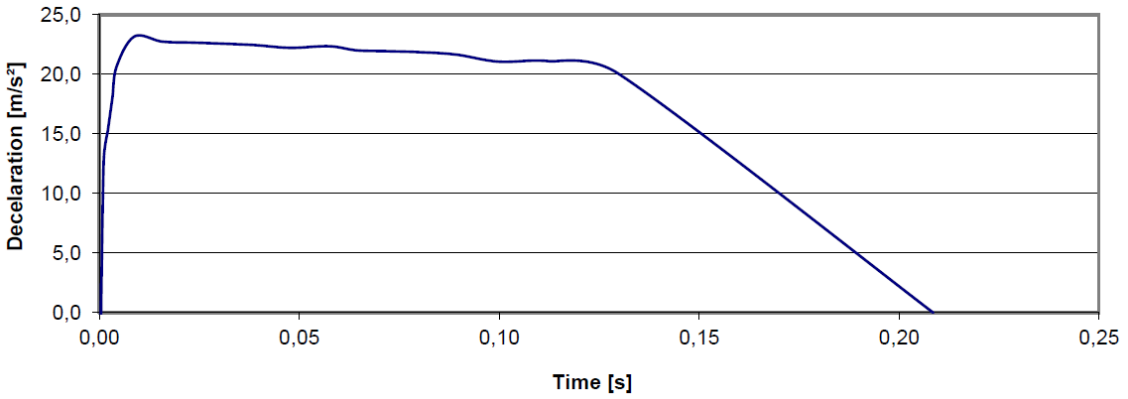


Figure 5.43: Typical deceleration-time curve of an hydraulic buffer from the manufacturer Leben.

5.4 Procedure and remarks on remaining models

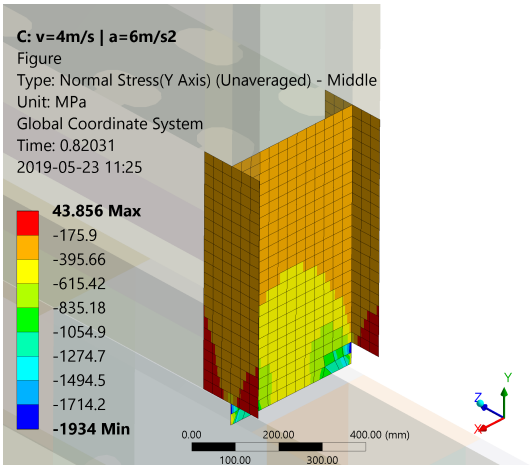
Model considerations

As with the previously conducted modal analyses, it's particularly relevant to present the study of a single mast stacker crane.

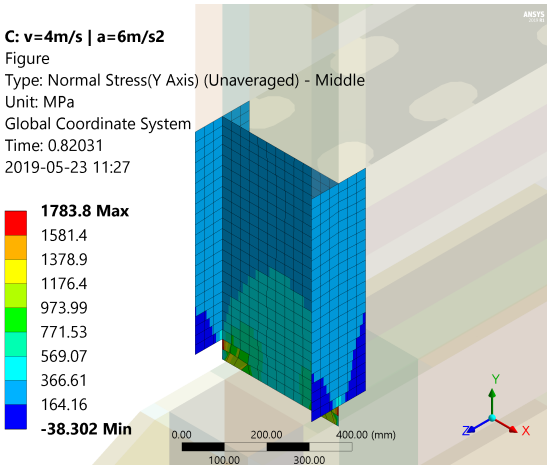
Initially, the model comprised only SHELL181 and BEAM188 elements as specified in section 4.4 which meant that the connection between the mast and bottom carriage was modelled by an extension of the I-profile beams' web to allow for a continuous mesh. This resulted in the σ_{yy} contour plots of Figure 5.44 which show the beam's web under a more severe loading condition than its flange in the lower region of the mast, the critical region. In reality, the connection between the mast and the bottom carriage is done via blocks welded to the I-beams (Figure 5.45a) and bolted onto the bottom carriage. These blocks compel the end of the I-beams' flanges to work together with the bottom carriage.

To achieve a stress distribution closer to what is expected in reality, the aforementioned blocks of the real crane were modelled using SOLD185 elements (refer to Appendix B) as seen in Figure 5.45b. CONTA174 and TARGE170 elements were used to establish the connection of the blocks to the I-beams and to the bottom carriage. As with the STK-21-C models, the connection behaviour was set to *bonded* and the *shell thickness effect* turned on. The same procedure was used for the connections between mast levels which are performed by the use of similar blocks. The resulting mass and mesh properties, respectively, due to the changes performed can be found on Appendix D.

The new modelling approach led to contour plots like the one from Figure 5.46. These show that the maximum σ_{yy} stress values appear on the I-beams' flanges. Although these maximum values appear in the expected locations, its values are inflated by the sharp internal corners caused by the modelled contact elements which create numerical singularities as can be seen from the large variations within the same element. Therefore,

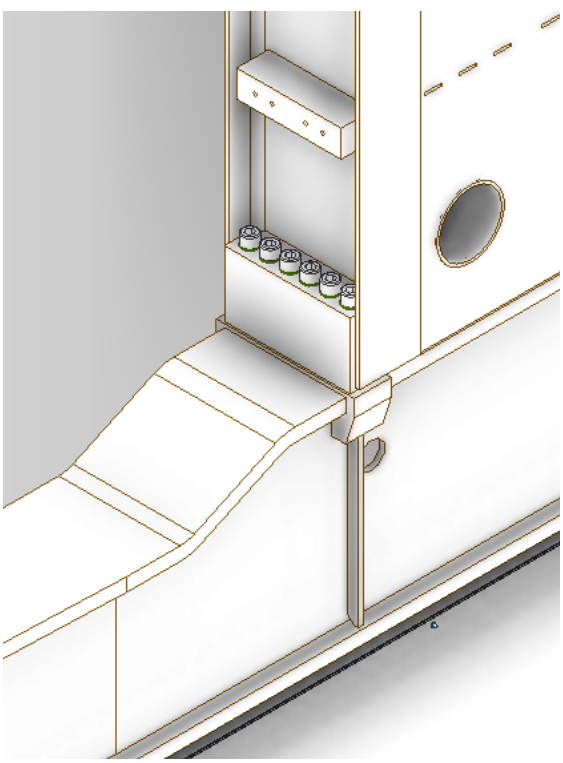


(a) Compression on the front of the mast.

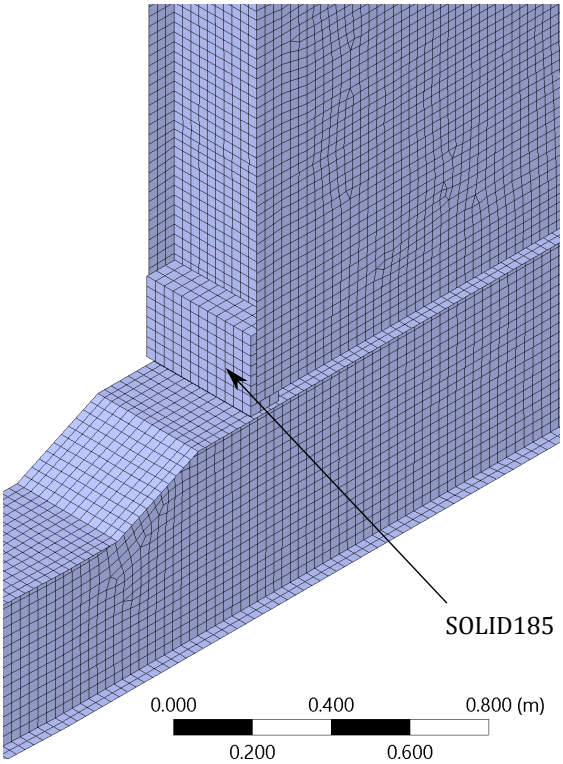


(b) Tension on the back of the mast.

Figure 5.44: Contour plots of σ_{yy} on the lower region of the 45 m STK-25 ($v_i = 4$ m/s; $\Delta t_{\text{stop}} = 0.66$ s; $t = 0.81831$ s).



(a) Original 3D model.



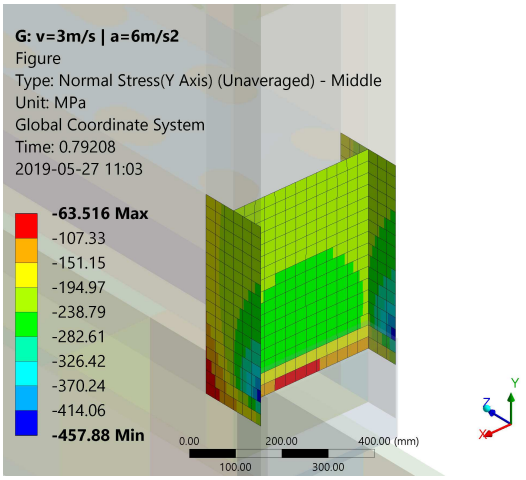
(b) FEM model counterpart.

Figure 5.45: Real and modelled connection between the mast and the bottom carriage.

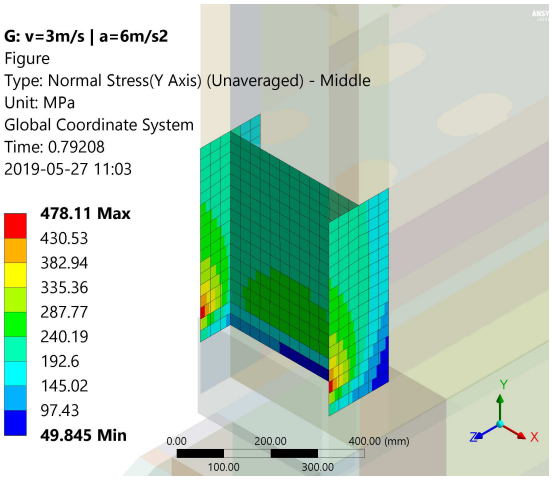
an accurate prediction of the stress values in these regions isn't possible with the current model.

As with the STK-21-C, it was decided that as long as the stress values are limited to a span of two elements in each direction counting from the maximum stress node, the condition was considered safe. Moreover, it can also be seen in Figure 5.46 that the front shows higher magnitudes of σ_{yy} and σ_{eq} on the side of the mast that is in a compressive

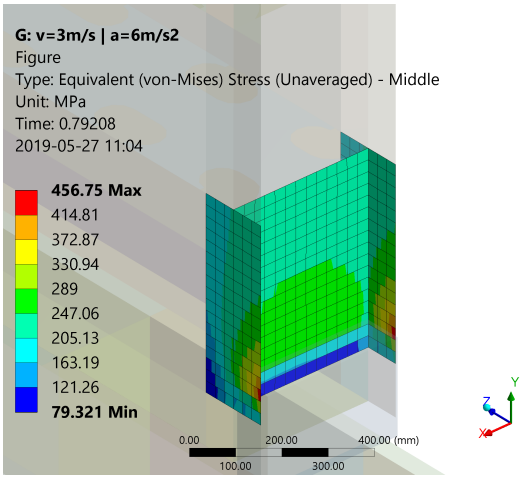
state due to the compressive axial force acting on the mast due to the structure's weight.



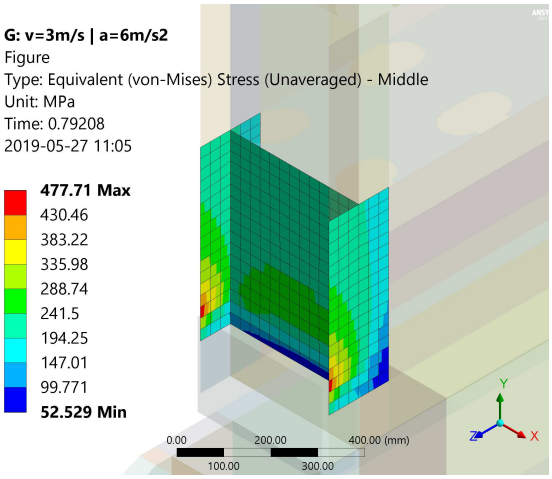
(a) σ_{yy} on the front of the mast.



(b) σ_{yy} on the back of the mast.



(c) σ_{eq} on the front of the mast.



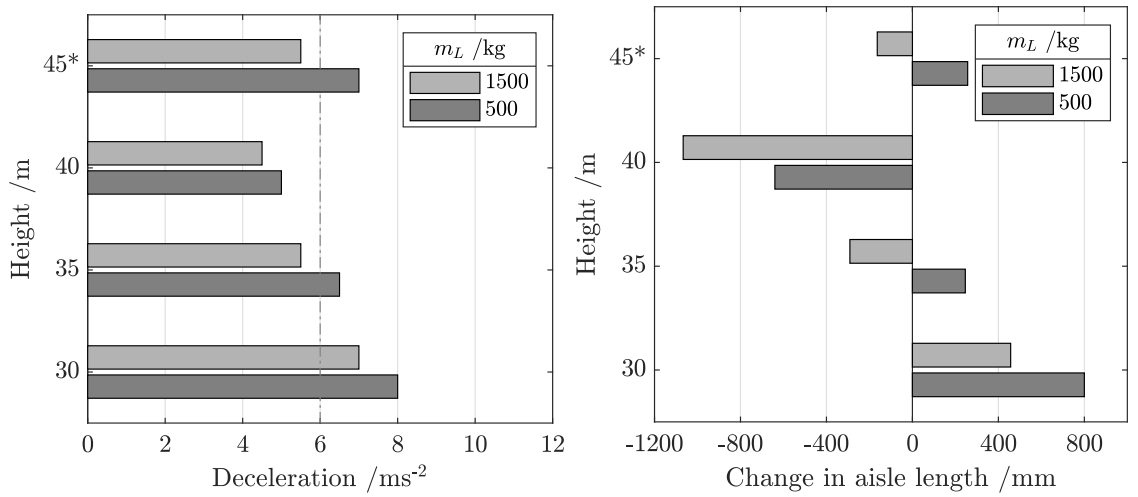
(d) σ_{eq} on the back of the mast.

Figure 5.46: Contour plots of σ_{yy} (a and b) and σ_{eq} (c and d) on the lower region of the 45 m STK-25 ($v_i = 3$ m/s; $\Delta t_{\text{stop}} = 0.50$ s; $t = 0.79008$ s).

Results and discussion

A similar procedure to the one employed for the STK-21-C in section 5.3 was used. Figure 5.47 summarizes the maximum deceleration results for the STK-25 for the tested payload's masses, $m_L = 500, 1500$ kg. The crane's movement was considered to be in the direction of the straight side of the mast, i.e., the one where the lifting carriage travels. In all cases but the 45 m the results are presented for a rated speed of 4 m/s. The 45 m case was yielding extremely low deceleration values with this speed so it was simulated considering $v_i = 3$ m/s. In Appendix D, the σ_{eq} contour plots, as well as the maximum relative displacement of the mast's top and the wheel loads are shown for the combinations of height and payload of Figure 5.47a. Note that the values for the maximum relative displacement of the top mast and the wheel loads show consistency for the same mast height across the tested payloads.

It can be seen from Figure 5.47b that the gains in aisle's useful length are possible and



(a) Maximum deceleration.

(b) Increase in piston stroke.

Figure 5.47: Maximum deceleration and change in aisle useful length ($1/\eta = 1.2$) for STK-25, $v_i = 4$ m/s except for (*) where $v_i = 3$ m/s.

can go as high as 800 m, however, the more severe inertial effects of the higher cranes and higher payloads still imply a reduction in the useful length in several cases.

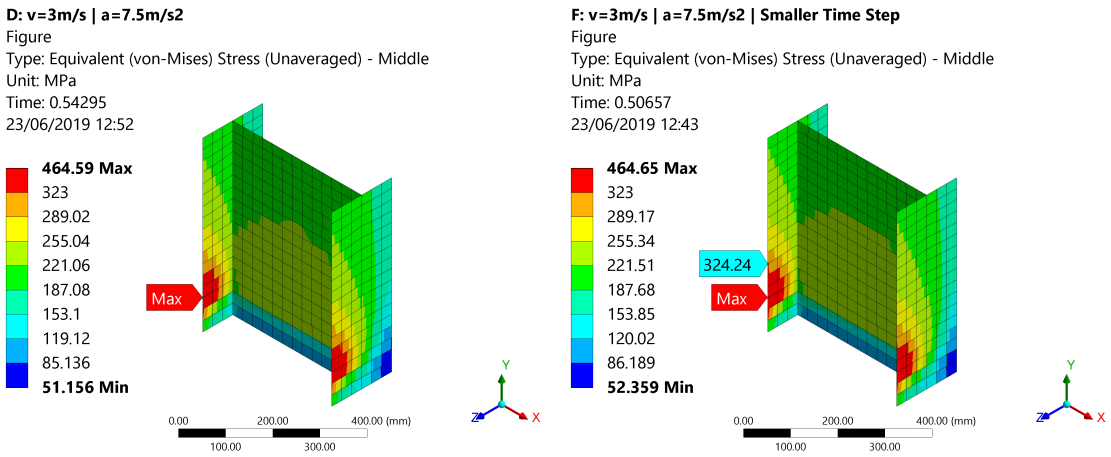
Previously, for the STK-21-C, it was argued that the increase in the ratio of the payload's mass to the total system's mass was the cause for the bigger gaps in admissible deceleration for different payload values at low heights. This argument is further reinforced by the results of the STK-25.

An exception to the previous conclusion is the fact that between the 1500 and 500 kg results for the 45 m case, the biggest gap in deceleration magnitude was found. It was noted, however, that for this height, a value of $v_i = 3$ m/s was adopted which might indicate that the payload's mass has a bigger impact at lower velocities. Further studies should be carried out to endorse this statement.

In the particular case of the 45 m and $m_L = 500$ kg, the initial time step settings aren't able to capture the peak stress value in time which would lead to setting a maximum deceleration of 7.5 m/s^2. Rerunning the simulation with smaller time step settings ($\Delta t_{\mathrm{i}} = 0.005$ s and $\Delta t_{\min} = 0.002$ s) showed a stress plot that failed the previously established criteria, even if by a small margin as seen in Figure 5.48 (regions with $\sigma_{eq} > 323$ MPa shown in red). Other cases like the 30 m, $m_L = 500$ kg model also failed the employed criteria with a 8.5 m/s^2 deceleration by a very small margin.

Some final notes regarding the study of the STK-25 are in order:

- the observations made for the STK-21-C regarding the lifting carriage's and LHD's masses and the conservative approaches of the numerical simulations still apply;
- the current model isn't capable of providing enough information about the maximum stresses in the bottom mast region due to the singularities caused by the contact element's formulation;
- the adopted criteria due to the previous item seems to be excessively conservative since, when consulting Appendix D, it can be seen that the computed σ_{eq} values in the web of the I-beam don't surpass 260 MPa, in general.



(a) Larger time step, $t = 0.54095$ s.

(b) Smaller time step, $t = 0.50457$ s.

Figure 5.48: Contour plots of σ_{eq} on the lower region of the back of the 45 m STK-25 ($v_i = 3$ m/s; $\Delta t_{\text{stop}} = 0.40$ s).

Chapter 6

Experimental analysis

In an effort to compare the developed numerical models with the actual phenomena they depict, an experimental procedure was developed and employed on a 33 m high STK-21-C.

The development of the experimental setup and the on-site procedures employed for the conducted tests are explored in section 6.1.

On section 6.2, the accelerometer data is filtered and analysed by computing the corresponding fast Fourier transforms (FFT). The corresponding results are then compared with a numerical model developed using the procedures highlighted in Chapters 4 and 5.

6.1 Experimental setup

Data acquisition system

The experimental program was to be carried out at a fully functional automated warehouse. To minimize the inconvenience caused by the stop of the warehouse, a portable, "plug and play" solution was required for carrying the measurements.

The data acquisition system (DAS) includes a 3-axes capacitive micro-electromechanical system (MEMS) accelerometer (Figure 6.1), model MMA8451Q, from NXP® [49] with 14 bits of resolution and selectable measurement ranges of $\pm 2g/\pm 4g/\pm 8g$. The output data rates, i.e., the rate at which the data is sampled can vary between 1.56 and 800 Hz. The first page of the accelerometer's data sheet can be found on Appendix E, full details can be found in reference [50].



Figure 6.1: An MMA8451Q capacitive MEMS accelerometer [51].

Capacitive MEMS accelerometers have much poorer data quality, especially on the higher frequency and amplitude when compared to piezoeletric or piezoresistive accelerom-

eters [52]. They are, however, much cheaper and are adequate for the low frequency range (< 10 Hz) that the modal results of Chapter 4 have shown.

To allow for the storage of the sampled data and its wireless retrieval and display, the accelerometer is connected to a Raspberry Pi 3 Model B+.

A case whose dimensions are presented in Figure 6.2 was 3D printed to house the DAS. Moreover, a 10400 mAh battery is also included to power the Raspberry Pi and the accelerometer, thus ensuring portability.

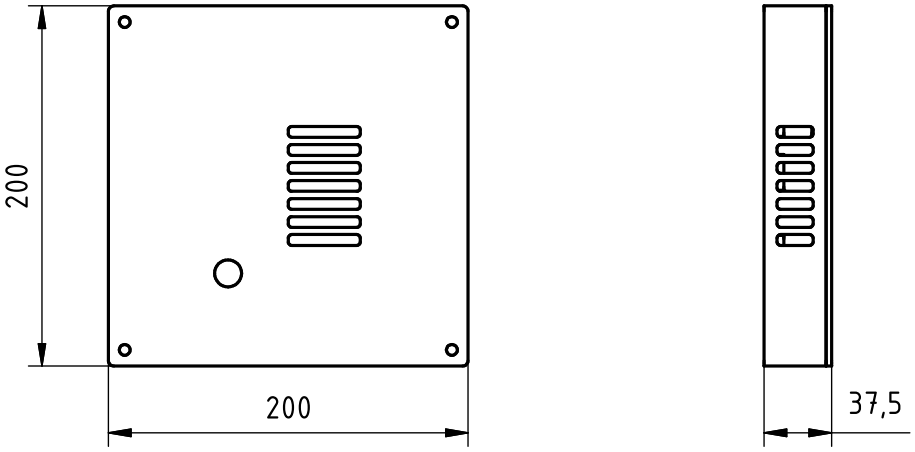
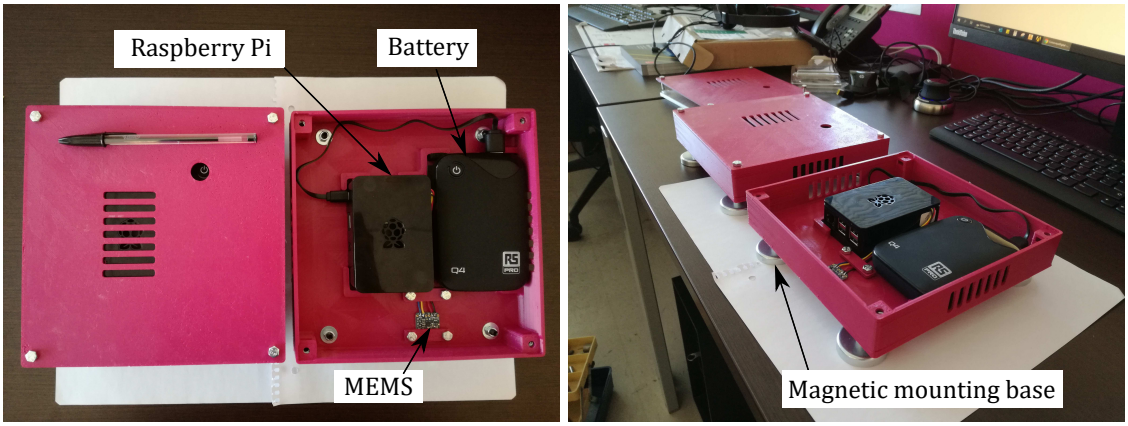


Figure 6.2: 3D printed DAS case dimensions (in mm).

The accelerometer is fixed to the case by the use of two 3D printed plates that are bolted onto the case. Also, the case's mounting to the structure is assured by four magnetic mounting bases bolted onto the case. Each magnet is rated for a pulling force of 125 N.

The case is closed via a bolted cover adjusted to prevent motion of its housed components. Foam was also used to accommodate the interior components as to prevent their movement when the machine is operating. Figure 6.3 shows the DAS in its assembled state with the case open and closed.



(a) Top view. (b) Showing the magnetic mounting bases.

Figure 6.3: Data acquisition system, housing case open and closed.

Three DAS (Figure 6.4) were used in the experimental tests. It's important to note that one of the DAS' cases was slightly different from the others as it was an earlier functional prototype with thicker walls (5 mm instead of 3 mm) and made of white PETG instead of pink PLA.

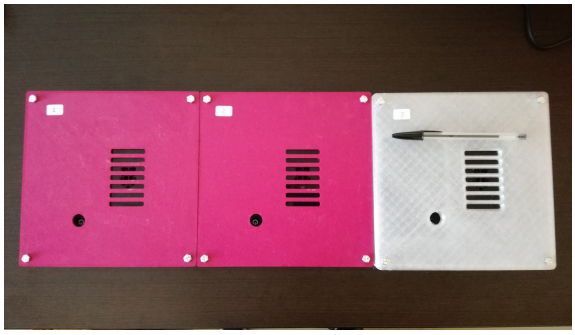


Figure 6.4: All DAS assembled.

Test procedure

The tests were carried on a 33.5 m tall stacker crane with 32.25 m tall masts and weighting approximately 34.2 t without payload. The mass of its additional components can be found in Table 6.1.

Table 6.1: Mass of the tested STK-21-C additional components.

Component	Mass /kg
EC assembly	1456
Lifting carriage w/ LHD	5560
HU	3320

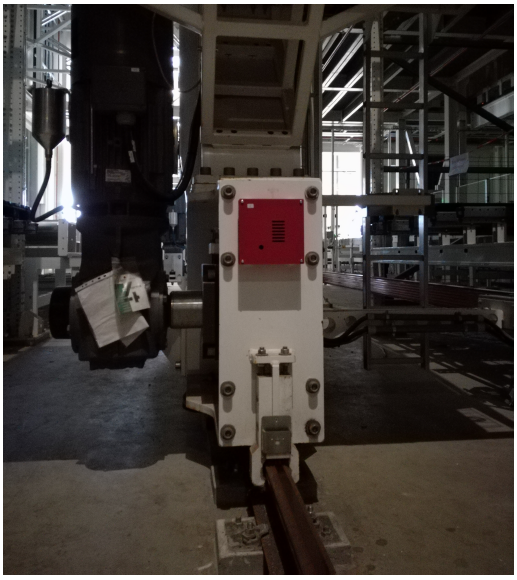
The DAS were positioned at the bottom carriage and along the mast on the ECs assembly's side facing the aisle so that the z-axis of the accelerometers (refer to Figure 6.1) is aligned with the aisle's direction and its y-axis is positive in the direction of gravity. Positioning of the DAS on the mast was done at roughly the mid-span and at the top near the maintenance platforms so that these could be taken as references to know the height of each sensor. Figure 6.5 shows the DAS placed on the structure. Henceforth the nomenclature S1, S2 and S3 is used to refer to each DAS, from the lowest to highest position. Each DAS's height, taken from the ground to their highest point, can be consulted in Table 6.2.

Table 6.2: Height of each DAS.

Designation	Height /mm
S1	929
S2	17094
S3	32029

A wireless modem was placed at the end of the aisle as seen in Figure 6.6 to allow communication with the DAS and retrieval of accelerometer data.

The testing of the impact of the crane against the end stop wasn't allowed, therefore, the crane was set to move to one of its pre-programmed storage and retrieval positions. The position was selected so that the crane would have enough time to reach the rated speed and maintain it for some time before decelerating, all using the already installed programming of the on-board PLC.



(a) S1 at the bottom carriage.



(b) S2 at the middle of the mast.



(c) S3 at the top of the mast.

Figure 6.5: DAS placement on the STK-21-C.

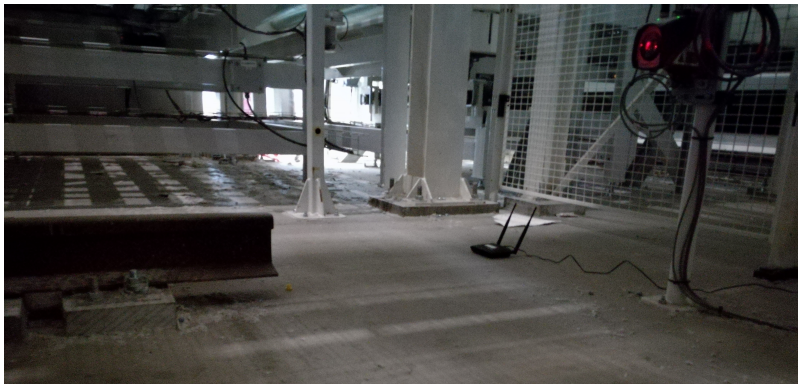
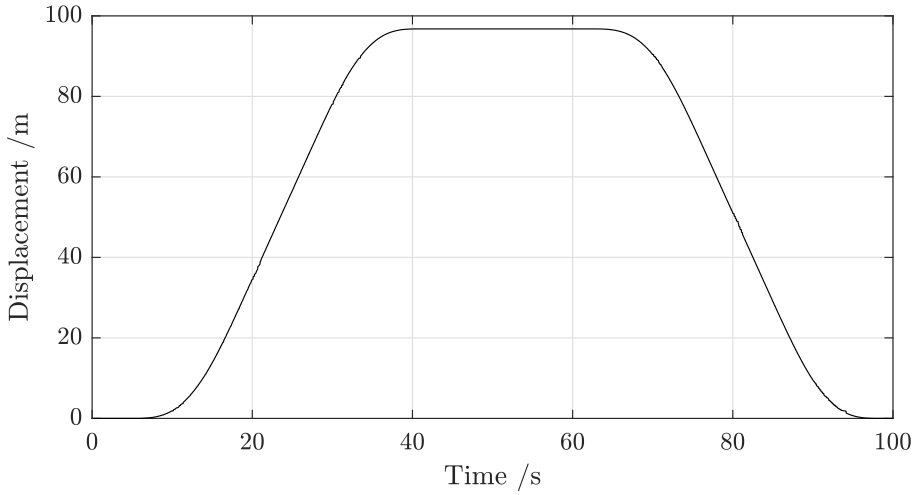


Figure 6.6: Modem at the end of the aisle to allow communication with the DAS.

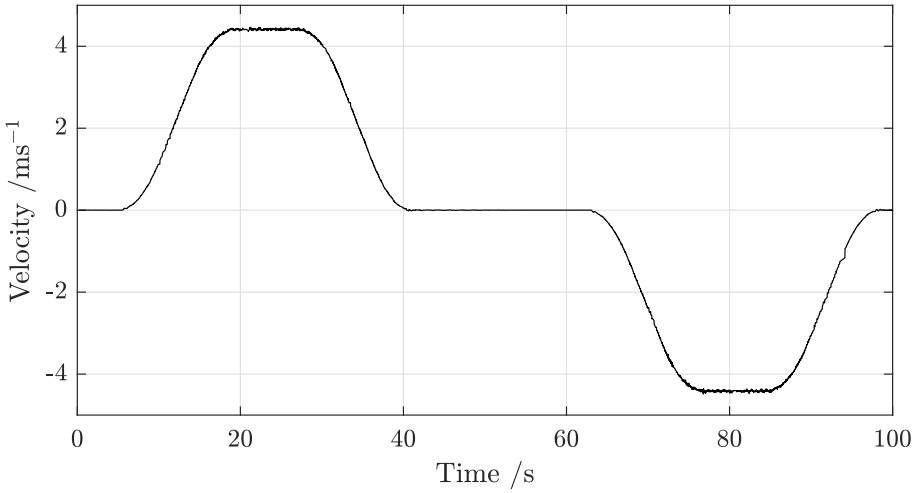
After stopping, the crane was held still for an interval of, at least, 20 s, after which it was ordered to return to its initial position. This was done to minimize the error caused in the return phase by the free vibration of the structure after coming to a stop.

On Figure 6.7 the above description becomes clearer; Figure 6.7a shows the rigid body displacement of the crane as a function of time by taking the successive positions of the encoder and Figure 6.7b shows the measured velocity versus time computed by the on-board PLC. Note that the rated speed is 4.4 m/s and the maximum travel acceleration is 0.4 m/s^2 for this particular installation.

The aforementioned procedure was repeated for three different positions of the lifting carriage, without payload, each corresponding to storage and retrieval levels. As the warehouse where the tests were carried was comprised of nine levels of storage, the tests were carried with the lifting carriage in the 1st, 5th and 9th positions, henceforth referred to as Y1, Y5 and Y9. The distance from the surface of the equipped telescopic forks to the ground for each position of the lifting carriage is presented in Table 6.3. For each position, four measurements were taken.



(a) Displacement in respect to time.



(b) Velocity in respect to time.

Figure 6.7: Example of displacement and velocity versus time curves gathered from the on-board PLC, lifting carriage at Y9, 1st measurement.

Table 6.3: Height of the surface of the telescopic forks for each tested position of the lifting carriage.

Position	Height /mm
Y1	1100
Y5	15300
Y9	29500

6.2 Results and discussion

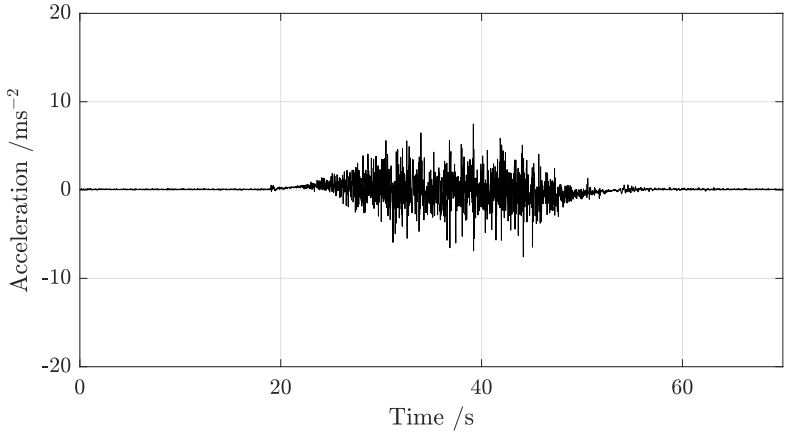
An example of the retrieved accelerometer data in the travel direction can be found in Figure 6.8 for each DAS with the lifting carriage in position Y9. Note that only the interval corresponding to the forward movement is shown and the sample frequency is $f_s = 50$ Hz. It's also important to note that the instant at which the data of the accelerometers started recording doesn't coincide with the one from the PLC, therefore, the

0 s of Figure 6.8 doesn't correspond to the one of Figure 6.7. This would be easily corrected with the recorded time stamp of both devices, however, during the experimental campaign, an unresolved software error caused the time stamp of the accelerometers to display incorrectly.

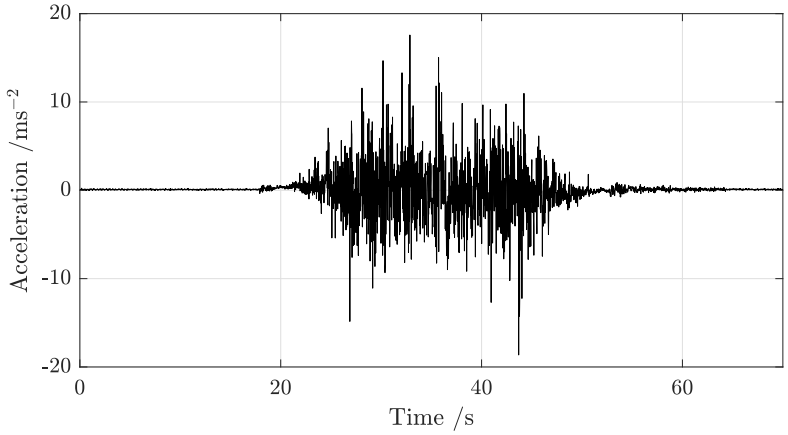
As expected, the magnitudes of acceleration are higher on the higher regions of the mast. Note that, in S3, the instant accelerations probably surpassed the upper limit of the measurement range in more than one occasion which can impact the conclusions taken from the analysis of these results, a higher measurement range should have been selected. Moreover, while for the S1 and S2 measurements the acceleration plot looks evenly distributed in terms of positive and negative values, the same can't be said about the S3 measurement. This is further noticed when analysing the other three runs on the same conditions (Figure 6.9) although it wasn't clear on why this happened.

Apart from instant acceleration magnitude peaks, no information can be retrieved from the sampled data in its raw state, further manipulation is thus needed. To do so, Tom Irvine's "Vibrationdata Signal Analysis" software package [53], henceforth called VDATA, was used with permission from the author.

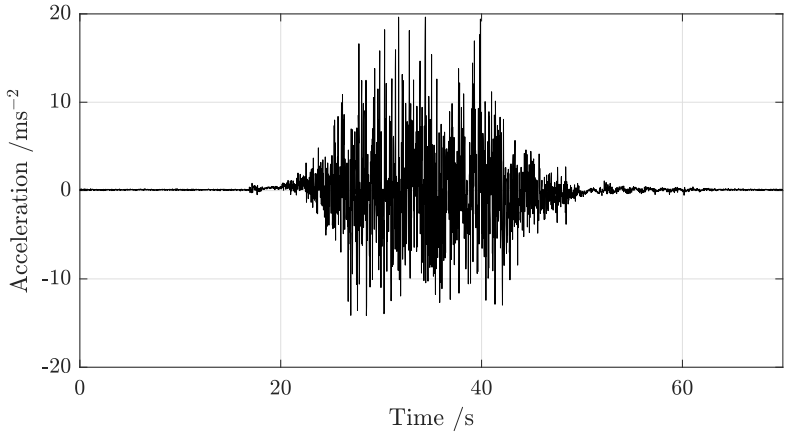
The following analysis relies on computing the Fast Fourier Transform (FFT) of the accelerometer data which allows to visualise the system's response in the frequency domain. However, proper frequency response functions (FRFs) couldn't be computed as only the output of the system was measured.



(a) Data retrieved from S1.

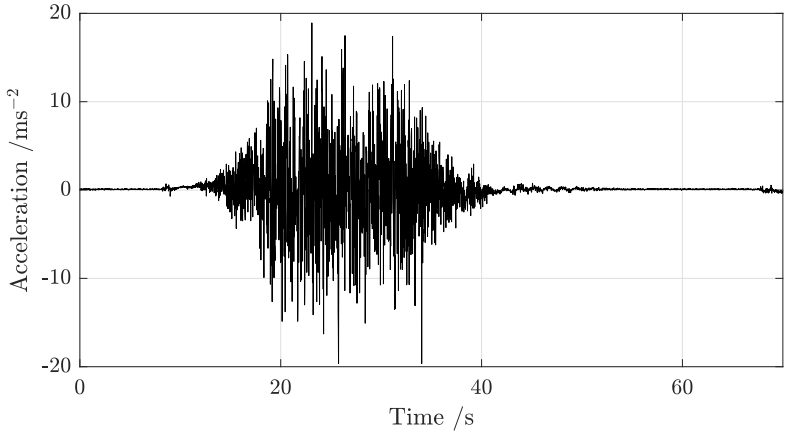


(b) Data retrieved from S2.

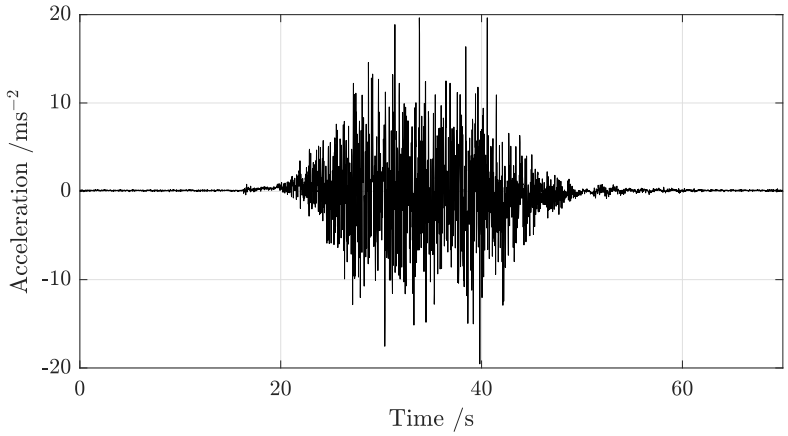


(c) Data retrieved from S3.

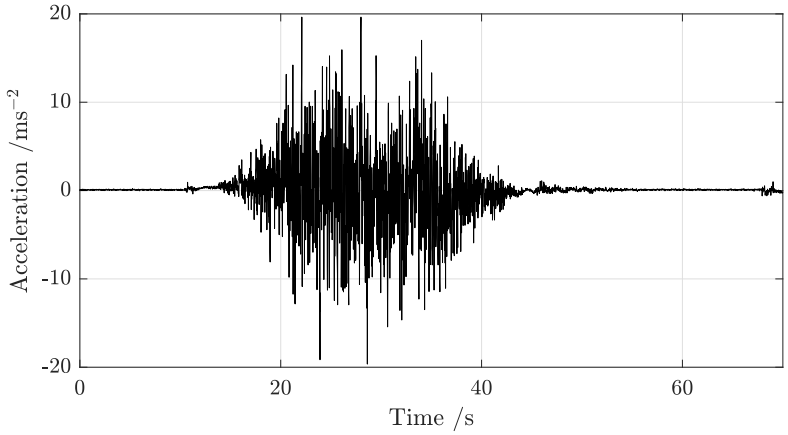
Figure 6.8: Extracted acceleration versus time curves from the DAS for the forward motion of the stacker crane, lifting carriage at Y9, 1st measurement.



(a) 2nd measurement.



(b) 3rd measurement.



(c) 4th measurement.

Figure 6.9: Extracted S3 acceleration versus time curves from the DAS, lifting carriage at Y9, 2nd, 3rd and 4th measurements.

Fast Fourier Transform

For a given function of time, $g(t)$, its forward Fourier transform, $G(f)$, is defined as being [54]

$$G(f) = \int_{-\infty}^{\infty} g(t) e^{-j2\pi ft} \mathrm{d}t \ , \tag{6.1}$$

where f is the frequency in Hz and $j = \sqrt{-1}$.

If $g(t)$ is sampled in the time domain so that N time samples were obtained, each containing the value g_k of function $g(t)$ at $k = 1, \ldots, N$, the forward Discrete Fourier Transform (DFT) of the sampled signal, G_k $k = 1, \ldots, N$, can be computed by replacing the integral of equation (6.1) by finite sums [55]:

$$G_k = \frac{1}{N} \sum_{n=0}^{N-1} g_n e^{-j\frac{2\pi kn}{N}} \ . \tag{6.2}$$

From the previous equation, it can be seen that in order to obtain N frequency components from N time samples, N^2 complex multiplications are required. The FFT algorithm obtains the same result with a number of complex multiplication of the order of $N \log_2 N$ [55].

To prevent misinterpretation of frequencies above half the sampling frequency, $f_s/2$, designated as the Nyquist frequency, a practical limitation is imposed on the frequency content of the discrete signal. Therefore, the analysed frequencies range from 0 Hz to $f_s/2$ [55]. Moreover, the frequency resolution, Δf is given by

$$\Delta f = \frac{f_s}{N} \ . \tag{6.3}$$

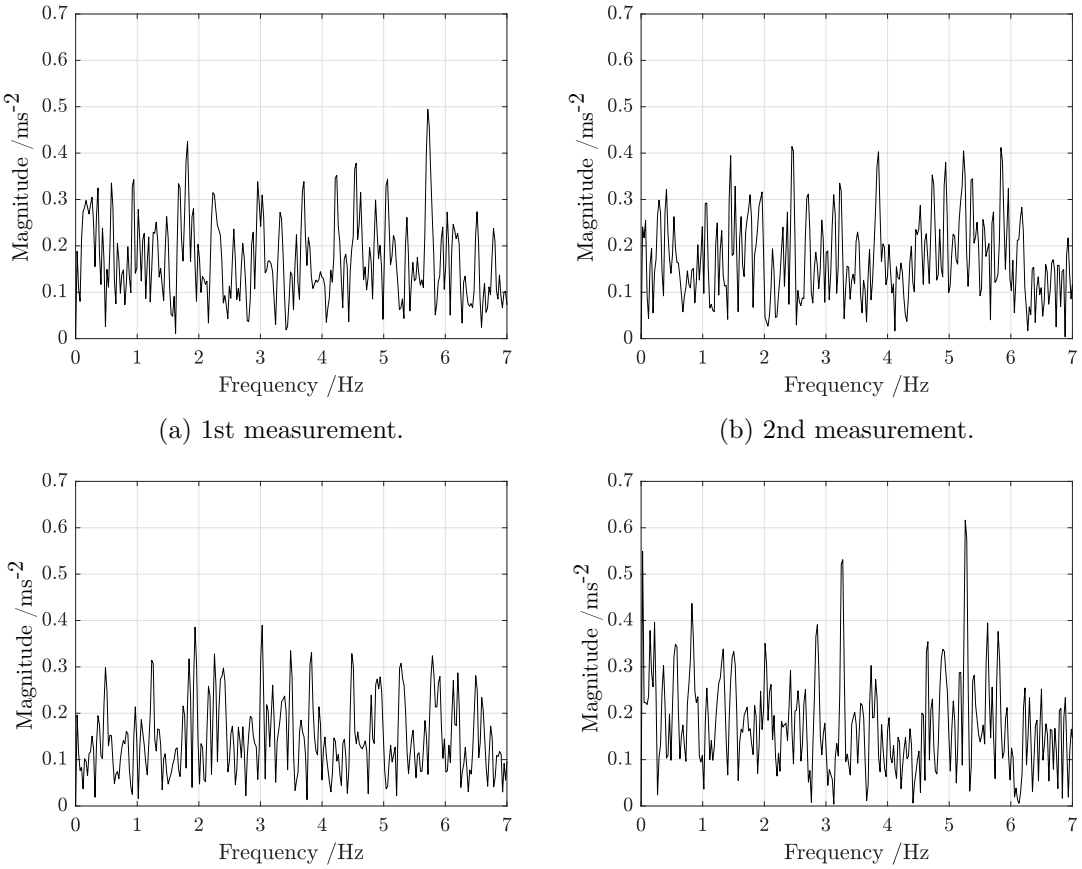
Computed FFTs

From the modal analysis of a 30 m mast STK-21-C (section 4.3.1), the first three natural frequencies of vibration due to bending in the travel plane are expected to lie below the 7 Hz range. As such, a 6th order Butterworth low-pass filter was applied with a cut-off frequency of 7 Hz as to filter higher frequency content, using VDATA. The FFTs of the filtered signal were then computed. On Figure 6.10, the FFTs of the acceleration data shown in Figures 6.8c and 6.9 are presented.

The natural frequencies of the stacker crane aren't clear from the computed FFTs not only due to incoherence in the location of the frequency response peaks of the different measurements but also due to their rich frequency content. Some reasons can be appointed for this:

- as the stacker crane is undergoing what is effectively a transient loading condition due to a variety of reasons, e.g., misalignments in rails or the fact that the gear motor is actively trying to make the crane follow an imposed velocity curve, the frequencies of the system's response vary with time;

- relating to the previous point: it was shown on section 4.3.1 that the boundary conditions have a significant influence on the first and third travel plane bending modes which, transfering this knowledge to the experiments, can mean a very different frequency response between, for example, the interval of time where the crane travels at its rated speed and the interval after coming to a stop, where free vibration of the structure still occurs but the bottom carriage is stopped.



(a) 1st measurement.

(b) 2nd measurement.

(c) 3rd measurement.

(d) 4th measurement.

Figure 6.10: Computed FFTs from the filtered S3 data, lifting carriage at Y9.

– the observed peaks can come from other elements of the warehouse like the rack or on-board elements of the stacker crane and not the vibration of the structure itself;

– the remaining stacker cranes of the warehouse were kept functioning during the experiments as it was only allowed to stop one. In turn, this may have provoked additional noise in the signal due to the induced vibrations on the warehouse's rack and building;

Nevertheless, peaks of response can be found for measurements 1, 3 and 4 for frequencies near 2 Hz and 3 Hz which show some consistency.

The attention was then shifted towards acquiring the FFTs on smaller time intervals. The acceleration, constant velocity, deceleration, and post-stop phases were analysed. Particularly interesting results can be found on this last case. Figure 6.11 shows and example of the retrieved S3 data during the die-down vibration phase when the crane comes to a stop as well as the obtained signal after applying a low pass 7 Hz filter. The computed FFTs for this time interval and analogous ones on other measurements show a predominant frequency response of the crane for 0.68 Hz as seen in Figure 6.12 ("M" stands for measurement). This corresponds to the first natural frequency of vibration. The response peak observed in measurement 4 between the 5 and 6 Hz range might be due to vibrations caused by other effects other than the excitation of the structure's modes such as the ones discussed earlier.

Following the same procedure for the retrieved data from the Y1 and Y5 tests, Figures 6.13 and 6.14 show the computed FFTs for these cases. Note that the first natural frequency tends to increase as the lifting carriage is positioned lower, as expected. Note, also, on Figure 6.13 that peaks of response at 2.42 Hz and 4.07 Hz are identified which could correspond to the 2nd and 3rd bending modes of vibration in the travel plane when the lifting carriage is positioned in the middle of the mast. The reason why these appear only for Y5 is due to the fact that these natural modes have their minimum frequencies when the lifting carriage is near the middle of the masts as was seen in section 4.3.1, which is also where the highest free vibration amplitudes are found, therefore being easier to excite these higher modes in this particular case.

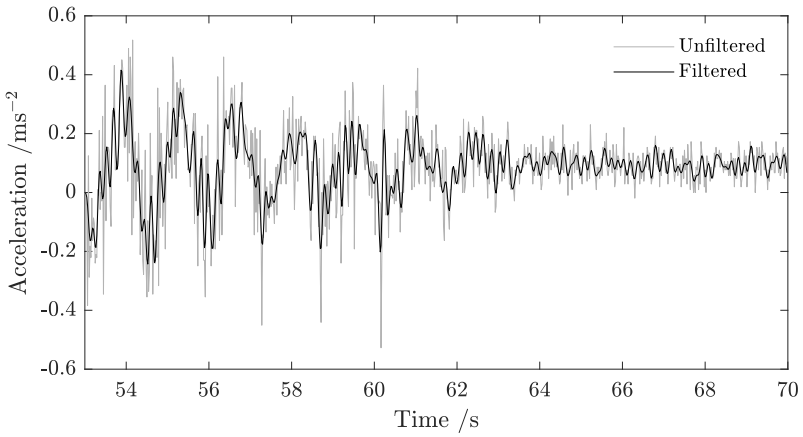


Figure 6.11: Filtered and unfiltered post stop-phase S3 data, lifting carriage at Y9, 1st measurement.

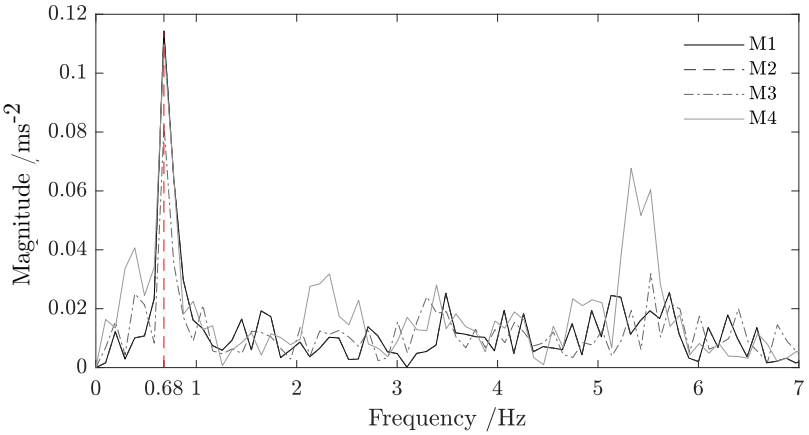


Figure 6.12: Computed FFTs from S3 data for the post-stop phase, lifting carriage at Y9.

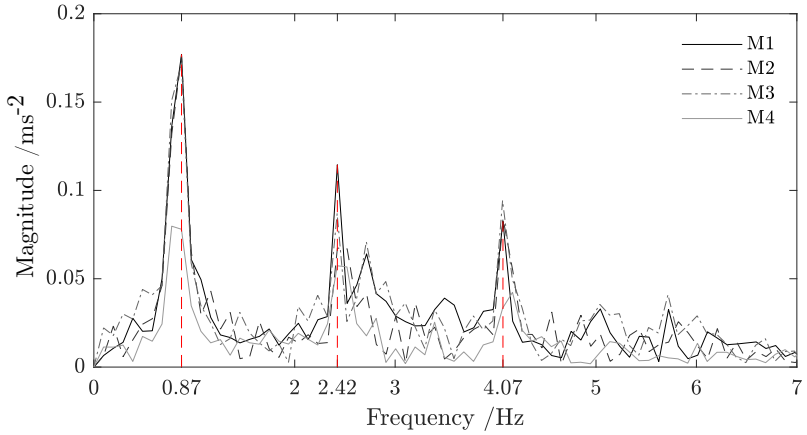


Figure 6.13: Computed FFTs from S3 data for the post-stop phase, lifting carriage at Y5.

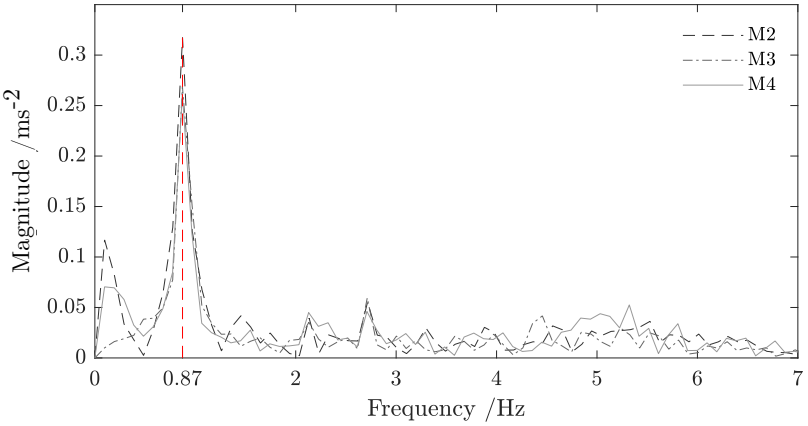


Figure 6.14: Computed FFTs from S3 data for the post-stop phase, lifting carriage at Y1.

Comparison with numerical results

Numerical models were developed using the process outlined in Chapter 4, adapting it to the tested stacker crane's specifications. The mass of the additional components was considered from the real values, as reported in Table 6.1, and the total model's mass is 33611 kg. For the mesh properties, Table 6.4 can be consulted.

Table 6.4: Mesh properties of the tested STK-21-C model.

Num. elements	Num. nodes	Num. DOFs
168705	108711	651604

The identified first natural frequencies for each position of the lifting carriage were compared with two numerical models. In one of them (designated as "One side"), the crane's movement was fixed on the wheels from one side as to represent the locking of the wheels after coming to a stop while in the other (designated as "Free"), the stacker crane was free to move in the travel direction. The first natural frequency results from the modal simulations carried and their corresponding error relative to the values retrieved from the identification procedure in Figures 6.12 to 6.14 can be seen in Table 6.5. Figure 6.15

also illustrates the differences between the computed and identified values where h_r is the relative position throughout the carriage's course following the notation of section 4.3.1.

Table 6.5: Computed versus experimentally identified 1st natural frequency for tested lifting carriage's positions.

Position	Identified /Hz	"One side"		"Free"	
		Computed /Hz	Error /%	Computed /Hz	Error /%
Y1	0.87	1.08	24.1	1.39	59.8
Y5	0.87	0.97	11.5	1.43	64.4
Y9	0.68	0.81	19.1	1.18	73.5

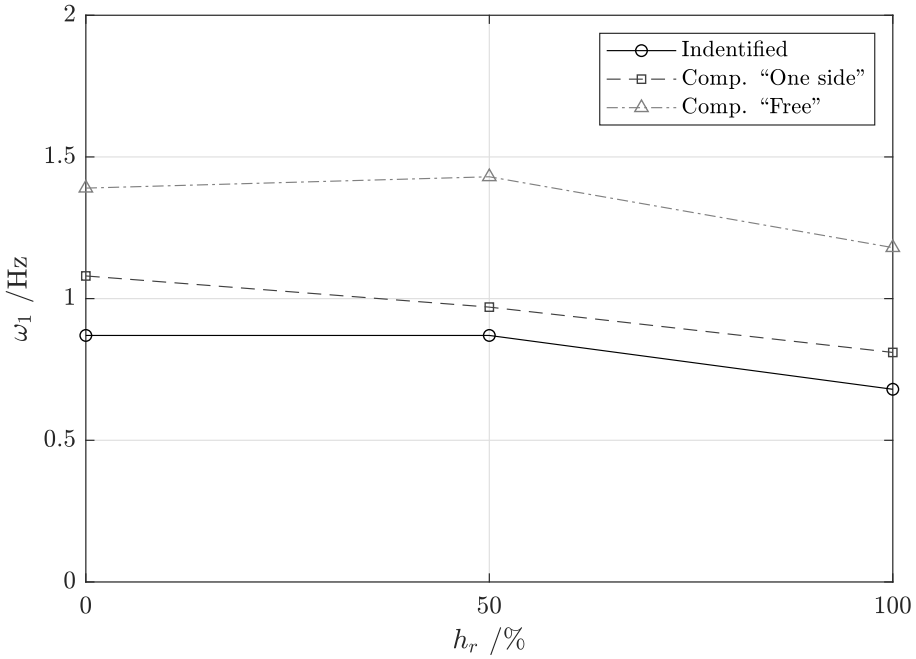


Figure 6.15: Experimental and computed values for the first natural frequency of the tested STK-21-C as a function of the lifting carriage's position.

For both models, the error was significant, especially for the "Free" case where all frequencies were offset by about 0.5 Hz. Although containing larger error, this model follows a variation more similar to the identified frequencies than the "One side" model which was expected to be a closer approximation of the real conditions the crane is subject to.

It must be remembered that the experimental procedure had several limitations as explained before. Moreover, due to the already reported error in the time stamps of the DAS, the intervals analysed to achieve the results in Figures 6.12 to 6.14 were selected by analysis of each set of data individually instead of looking at the interval of time corresponding to the same portion of the PLC's velocity versus time curve. Such variation in the procedure is prone to introduce error in the identified frequencies.

In any case, it may be argued that the ignored mass when creating the models is one of the reasons for the disparity of the numerical and the identification procedure results as the model weights 1.8% less than the real stacker crane. The consideration of the mass of

components such as sheaves and maintenance platforms in the higher regions of the crane might be particularly impactful on the model's dynamic behaviour.

Chapter 7

Conclusion

7.1 Conclusions

Automated storage and retrieval systems are adequate solutions when a high volume of loads has to be moved into and out of storage. The need for increased storage density and faster material handling serve as motivation for the construction of faster and higher stacker cranes but the elevated cost associated with such systems is an incentive for their optimization to a given range of standard applications.

The main goal of the present work was thus to study the possibility of decreasing the stroke of the system's shock absorber and therefore increase the aisle's useful space. Such reduction requires larger magnitudes of deceleration in the stacker crane's structure which must comply with the applied standards.

Chapter 2 allowed for the introduction to the topic of AS/RS systems and the various systems which are part of a stacker crane. Particular attention was given to the design and selection of hydraulic shock absorbers as well as the applied standards to the design of S/R machines, such as FEM 9.311 and EN 528:2008. The chapter ends with the presentation of Consoveyo, S.A.'s product lineup and a benchmarking with competitors from which the following conclusions were gathered:

- most current stacker crane manufacturers provide solutions up to a height of 45 m and payloads of up to 6 t;
- Consoveyo, S.A.'s current range of products is able to satisfy most applications;
- improvements should be done to the current product lineup in order to achieve higher vertical velocities.

From the development of a multi degree of freedom model based on the Assumed-modes Method of a beam-mass-carriage system on Chapter 3, it was found that:

- the influence of the lumped mass on the beam's free bending vibration is highly reliant on its vertical position;
- as the lumped mass' position approaches the vibration nodes of the system without lumped mass, the correspondent natural mode of vibration (shape and frequency) becomes independent of the lumped mass and the natural frequency achieves its highest value;
- the impact of the intermediate mass on the frequency and mode shapes relies on its ratio to the carriage's mass, being the most noticeable for low (< 0.10) values of such ratio.

In Chapter 4, the development of FEM models mainly based on shell elements for the study of the free vibration of the structure of stacker cranes was presented. Both a double (STK-21-C) and single (STK-25) mast stacker crane were studied which allows for the application of the proposed modelling procedure to the remaining portfolio of cranes. Being the first to be studied, the double mast stacker crane was also subject to a more in-depth parametric study which issued that:

- its first six natural mode shapes comprise the bending vibration of the masts in the planes normal to and containing the travel direction;
- the variation of the payload's position has a similar impact on the modes of vibration as the one depicted by the beam-mass-carriage system, even though the last one is more applicable to single mast stacker cranes;
- for the carriage at its highest position, the payload's mass has the highest impact on the first bending mode of vibration in the travel plane which, even then, isn't considerable in the practical payload range;
- the allowance or restriction of the crane's horizontal motion has a considerable impact on its free vibration.

Additionally, the study of the single mast free vibrational behaviour with shell and beam FEM models raised awareness for the fact that, for lower mast heights:

- the offset of the COG of components such as the lifting carriage induces torsion vibration in the mast adding to the bending observed at larger heights;
- the bending vibration of the bottom carriage also contributes to the torsional vibration of the mast.

It's on Chapter 5 that the main topic of this dissertation is addressed. Using the Transient Structural module of ANSYS© WB Mechanical, the effect of the decelerations imposed by the shock absorber on the crane's structure is studied by analysing the output displacements, nodal forces and stresses predicted by the FEM models. The effect of the weight of the structure and the working loads is also accounted for. In terms of displacements, the analysis of the results led to the following conclusions:

- the displacement response of the structure is mainly governed by the first mode of vibration in the travel direction which implies that, for stopping times higher than a certain value on the order of half the fundamental period of the crane, the maximum relative displacement of the upper crossbeam will occur before the bottom carriage comes to a stop;
- values of the order of 1000 mm for the maximum displacement of the mast's top to the bottom carriage were achieved which have to be accounted for when designing the warehouse as to prevent collisions of the crane with other warehouse equipment.

From the wheel loads predicted by the model, it can be seen that tipping of the machine is extremely likely in a situation where the stacker crane is stopped by the shock absorber. Such tipping behaviour isn't predicted by current models.

As for the stresses, in double mast stacker cranes:

- the local rigidity added by the reinforcements of the masts in the lower region provoke higher stress values immediately above said reinforcements than below;

- the effect of the upper crossbeam on the masts provokes the highest stress values found on these components on the upper region instead of the initially expected lower region;
- maximum overall stress values were found in the upper crossbeam which was the limiting factor in all studied cases.

And, for single mast stacker cranes:

- maximum stresses are found, as expected, in the flanges of the I-beams in the 1st mast level;
- the inclusion of contact elements with the *bonded* behaviour induces numerical stress singularities in the critical regions of the elements mentioned in the previous point. Therefore, criteria had to be established to determine the maximum allowable accelerations.

In regards to the obtained acceleration values and their impact on the aisle's useful length:

- for the double mast stacker crane model, the results propose reductions of useful aisle length for several cases, as high as 2300 mm. Only the studied lowest height/payload combination allows for an increase in aisle useful length, of 240 mm;
- in its turn, for the studied single mast stacker crane model, increases in aisle useful length up to 800 mm are possible, corresponding to an increase in deceleration magnitude from 6 to 8 m/s^2.

As a final note regarding Chapter 5, the conservative options taken throughout the development of the models may have led to overly conservative results. Also, the lifting carriage and LHD's mass are based upon each particular project specifications which should be taken into account when considering the presented results.

Finally, Chapter 6 aimed at comparing data gathered with accelerometers from an operational stacker crane to the computed results of the numerical models. Due to external limitations, the impact conditions couldn't be tested so the data was gathered from the motion of the crane between two positions. The main important points from this chapter are:

- the influence of external vibration sources as well as possible changes to the crane structure's vibrational behaviour during the different phases of the movement, from one position to the other, provided an high frequency content in the range of interest;
- analysis of smaller sets of data, particularly the ones that are thought to have been recorded right after the bottom carriage stops when the vibrations due to the travel motion die down, reveals what is thought to be the first natural frequency of the crane's structure;
- comparison of the identified fundamental frequency with numerical results reveal errors ranging from 11.5% to 73.5% depending on the set of boundary conditions applied. The model which failed the identified frequencies by a larger margin was, however, the one that better represented the variation of the identified frequencies with the lifting carriage's position.

7.2 Future Work

Since the main objective towards which this dissertation was proposed wasn't fulfilled, the first step would be to use the presented modelling procedures to study the remaining models of Consoveyo, S.A.'s line up as to obtain similar information to the one presented for the STK-21-C and STK-25.

Additionaly, the following studies are suggested:

- the repetition of the experimental procedure in a more favourable and reproducible environment;
- further studies into "Operational Modal Analysis" techniques as to retrieve the natural vibration modes of the structure;
- model calibration using the information gathered from the previous two points, possibly, by adding the components on the upper regions of the crane as lumped masses;
- the development of FEM sub-models [45] of the connection of the mast to the bottom carriage in single mast stacker cranes as to accurately model the stresses in this regions and thus minimize numerical singularities;
- the implementation of velocity curves which are closer to the shock absorber manufacturer's specifications;
- the inclusion of the interaction between the wheels and the lower rail in the FEM models;
- to use the experimental information gathered in order to include damping in the numerical model.

References

[1] Consoveyo, S.A. `https://www.consoveyo.com`, . Accessed: 2019-03-01.

[2] Körber AG. Of humans and machines: The history of Körber. `https://www.koerber.com/en/we/of-humans-and-machines-the-history-of-koerber/`, . Accessed: 2019-03-01.

[3] EN 528:2008. Rail dependent storage and retrieval equipment - Safety requirements. Standard, European commitee for standardization, Brussels, BE, 2008.

[4] Daniel Gorges, Jens Kroneis, and Steven Liu. Active vibration control of storage and retrieval machines. In *ASME 2008 International Design Engineering Technical Conferences and Computers and Information in Engineering Conference*, pages 1037–1046. American Society of Mechanical Engineers, 2008.

[5] Sándor Hajdu and Péter Gáspár. Distributed parameter modeling of single-mast stacker crane structures. *Periodica Polytechnica Transportation Engineering*, 42(1): 1–9, 2014.

[6] Sándor Hajdu and Péter Gáspár. Investigation of the influence of lifted load on dynamical behavior of stacker cranes through unstructured uncertainties. In *2013 IEEE 14th International Symposium on Computational Intelligence and Informatics (CINTI)*, pages 179–184. IEEE, 2013.

[7] Sándor Hajdu and Péter Gáspár. Multi-body modelling of single-mast stacker cranes. *International Journal of Engineering Systems Modelling and Simulation*, 8(3):218–226, 2016.

[8] Sándor Hajdu and Péter Gáspár. Reducing the mast vibration of single-mast stacker cranes by gain-scheduled control. *International Journal of Applied Mathematics and Computer Science*, 26(4):791–802, 2016.

[9] Sándor Hajdu and Péter Gáspár. From modeling to robust control design of single-mast stacker cranes. *Acta Polytechnica Hungarica*, 11(10):135–149, 2014.

[10] Mathias Bachmayer, M Schipplick, T Thümmel, S Kessler, W Günthner, and H Ulbrich. Nachschwingungsfreie Positionierung elastischer Roboter durch numerische und analytische Trajektorienplanung am Beispiel Regalbediengerät [Non-vibrational positioning of elastic robots through numerical and analytical trajectory planning using the example of a stacker crane]. *VDE/VDI-Tagung: Elektrischmechanische Antriebssysteme–Innovationen–Trends–Mechatronik, Böblingen*, 2008.

[11] Tobias Loose. Benchmark-Anwendung zur Schwingungsanalyse und-dämpfung von Regalbediengeräten am Beispiel eines Labormodells [Benchmark - Application for

vibration analysis and damping of storage and retrieval machines using the example of a laboratory model]. *F. Hoffmann; E. Hüllermeier, editor*, 25:127–144, 2015.

[12] S Park, WK Chung, Y Youm, and JW Lee. Natural frequencies and open-loop responses of an elastic beam fixed on a moving cart and carrying an intermediate lumped mass. *Journal of Sound and Vibration*, 230(3):591–615, 2000.

[13] S Park and Y Youm. Motion of a moving elastic beam carrying a moving mass—analysis and experimental verification. *Journal of Sound and Vibration*, 240 (1):131–157, 2001.

[14] Trevor Neville Haas. *Numerical (FEA) evaluation of crane end buffer impact forces*. PhD thesis, Stellenbosch: University of Stellenbosch, 2007.

[15] Cyril Feau, Ioannis Politopoulos, George S Kamaris, Charlie Mathey, Thierry Chaudat, and Georges Nahas. Experimental and numerical investigation of the earthquake response of crane bridges. *Engineering Structures*, 84:89–101, 2015.

[16] Andrea Arena, Arnaldo Casalotti, Walter Lacarbonara, and Matthew P Cartmell. Dynamics of container cranes: three-dimensional modeling, full-scale experiments, and identification. *International Journal of Mechanical Sciences*, 93:8–21, 2015.

[17] FEM 9.311. Rules for the design of storage and retrieval machines - Structures. Standard, European materials handling federation, Brussels, BE, 1978.

[18] Alan Rushton, Phil Croucher, and Peter Baker. *The handbook of logistics and distribution management: Understanding the supply chain*. Kogan Page Publishers, 2014.

[19] Hannan Sadjady. Physical flows. *Logistics operations and management: concepts and models*, pages 11–42, 2011.

[20] Consoveyo, S.A. Stacker Cranes. `https://www.consoveyo.com/en/products/stacker-cranes.html`, . Accessed: 2019-02-25.

[21] FEM 1.001. Rules for the design of hoisting appliances. Standard, European materials handling federation, Brussels, BE, 1978.

[22] Mecalux, S.A. Stacker Cranes for Pallets. `https://www.mecalux.co.uk/automated-warehouse-pallets/stacker-cranes-pallets`. Accessed: 2019-03-11.

[23] Eurofork S.p.A. Handling Devices Catalogue. `https://www.eurofork.com/sites/default/files/download/eurofork-load-handling-devices.pdf`. Accessed: 2019-02-19.

[24] DAMBACH Lagersysteme GmbH & Co. KG. Compact Shuttle. `https://www.dambach-lagersysteme.de/en/products/load-handling-devices/compact-shuttle.html`, . Accessed: 2019-02-19.

[25] Buffer Dynamics. `http://www.open.edu/openlearncreate/mod/oucontent/view.php?id=13463&section=1.2.9`. Accessed: 2019-02-15.

[26] Weforma Dämpfungstechnik GmbH. Heavy-Duty Shock Absorbers Catalogue. `http://www.weforma.com/fileadmin/pdf/Kataloge/2017/Weforma_17_LDS.pdf`, . Accessed: 2019-02-15.

[27] LEBEN & Co. GmbH. http://www.compenser.de/index.php?Leben-und-Co-GmbH-EN, . Accessed: 2019-02-15.

[28] Weforma Dämpfungstechnik GmbH. http://www.weforma.com/en/home.html, . Accessed: 2019-02-15.

[29] FEM 9.832. Basis of calculations for storage and retrieval machines – Tolerances, deformations and clearances in the storage system Part 1: General, Single deep and Double deep Beam Pallet racking. Standard, European materials handling federation, Brussels, BE, 2012.

[30] EPAL. EPAL Euro pallet. https://www.epal-pallets.org/eu-en/load-carriers/epal-euro-pallet/. Accessed: 2019-03-01.

[31] Automha S.p.A. SRM. https://www.automha.it/en/srm-autostore/. Accessed: 2019-03-11.

[32] Cassioli Srl. Automated warehouses. https://www.cassioli.com/products/automated-warehouse/. Accessed: 2019-03-11.

[33] Daifuku Co., Ltd. Unit-load AS/RS. https://www.daifuku-logisticssolutions.com/en/product/asrs/unitload.html. Accessed: 2019-03-11.

[34] Duro Felguera, S.A. Logistics Systems. http://www.dfdurofelguera.com/index.asp?MP=9&MS=34&TR=C&IDR=650. Accessed: 2019-03-11.

[35] GEBHARDT Fördertechnik GmbH. Storage systems. https://www.gebhardt-foerdertechnik.de/en/solutions/storage-systems/. Accessed: 2019-03-11.

[36] MLOG Logistics GmbH. Storage and retrieval machines. https://www.kardex-mlog.com/en/products-mlog/storage-and-retrieval-machines.html, . Accessed: 2019-03-11.

[37] LTW Intralogistics GmbH. Solutions. https://ltwusa.com/index.php/en/solutions.html, . Accessed: 2019-03-11.

[38] SSI Schaefer Ltd. EXYZ storage-retrieval machine. https://www.ssi-schaefer.com/en-gb/products/storage/pallet-rack-systems/exyz-storage-retrieval-machine-28328. Accessed: 2019-03-11.

[39] Swisslog Holding AG. Automated pallet warehouse AS/RS. https://www.swisslog.com/en-us/warehouse-logistics-distribution-center-automation/products-systems-solutions/asrs-automated-storage-,-a-,-retrieval-systems/pallets-heavy-loads, . Accessed: 2019-03-11.

[40] System Logistics S.p.A. Stacker cranes. http://www.systemlogistics.com/eng/products/asrs/stacker-cranes. Accessed: 2019-03-11.

[41] DAMBACH Lagersysteme GmbH & Co. KG. Storage and Retrieval Machines. https://www.dambach-lagersysteme.de/en/products/automated-storage-systems/storage-retrieval-machines.html, . Accessed: 2019-03-11.

[42] Dematic. Unit Load AS/RS. https://www.dematic.com/en-us/products/products-overview/storage-systems/unit-load-asrs. Accessed: 2019-03-11.

[43] J. Dias Rodrigues. *Apontamentos de Vibrações de Sistemas Mecânicos [Notes on Vibration of Mechanical Systems]*. Faculdade de Engenharia da U.PORTO, PORTO, 2017 edition, 2017.

[44] EN 10025-2:2004. Hot rolled products of structural steels - Part 2: Technical delivery conditions for non-alloy structural steels. Standard, European commitee for standardization, Brussels, BE, 2004.

[45] ANSYS® Mechanical Enterprise, Release 2019 R1. Help System. ANSYS, Inc.

[46] Eugenio Oñate. *Structural analysis with the finite element method. Linear statics: volume 1: basis and solids*. Springer Science & Business Media, 2009.

[47] J. F. Silva Gomes. *Mecânica dos sólidos e resistência dos materiais [Solid Mechanics and Strength of Materials]*. Edições INEGI, 2004.

[48] LEBEN & Co. GmbH. C-Series. `https://www.compenser.de/index.php?C-Series`, . Accessed: 2019-05-24.

[49] NXP Semiconducters. `https://www.nxp.com/`. Accessed: 2019-06-24.

[50] NXP Semiconducters. MMA8451Q 3-Axis, 14-bit/8-bit Digital Accelerometer, Data sheet. `https://www.nxp.com/docs/en/data-sheet/MMA8451Q.pdf`. Accessed: 2019-06-24.

[51] Adafruit Industries. Overview - Adafruit MMA8451 Accelerometer Breakout - Adafruit Learning System. `https://learn.adafruit.com/adafruit-mma8451-accelerometer-breakout/overview`. Accessed: 2019-06-24.

[52] Stephen Hanley. *Shock & Vibration Overview Handbook*. Mide Technology, 2016.

[53] Tom Irvine. Vibrationdata - Shock & Vibration Software & Tutorials. `https://vibrationdata.wordpress.com/`. Accessed: 2019-06-24.

[54] Zhi-Fang Fu and Jimin He. *Modal analysis*. Elsevier, 2001.

[55] Randolph B. Randall. *Frequency analysis*. Brüel & Kjær, 1987.

Appendix A

Proof of equations (3.14) and (3.18)

Integration by parts in respect to time of each term in equation (3.13) provides

$$\begin{aligned}\int_{t_1}^{t_2} \delta T \mathrm{d}t = &\left[M\dot{x}_b(t)\delta x_b(t)\right]\Big|_{t_1}^{t_2} - \int_{t_1}^{t_2} M\ddot{x}_b(t)\delta x_b(t)\mathrm{d}t \\ &+ \int_0^l \left[\rho(y)\left[\dot{x}_b(t)+\dot{w}(t)\right]\left[\delta x_b(t)+\delta w(y,t)\right]\right]\Big|_{t_1}^{t_2}\mathrm{d}y \\ &- \int_0^l \int_{t_1}^{t_2} \rho(y)\left[\delta x_b(t)+\delta w(y,t)\right]\left[\ddot{x}_b(t)+\ddot{w}(y,t)\right]\mathrm{d}t\mathrm{d}y \ ,\end{aligned} \tag{A.1}$$

Since, by definition, the variations $\delta w(y,t)$ and $\delta x_b(t)$ are null for arbitrary $t = t_1 = t_2$ it results that

$$\begin{aligned}\int_{t_1}^{t_2} \delta T \mathrm{d}t = &- \int_{t_1}^{t_2} M\ddot{x}_b(t)\delta x_b(t)\mathrm{d}t \\ &- \int_{t_1}^{t_2} \left\{ \int_0^l \rho(y)\left[\delta x_b(t)+\delta w(y,t)\right]\left[\ddot{x}_b(t)+\ddot{w}(y,t)\right]\mathrm{d}y \right\}\mathrm{d}t \ .\end{aligned} \tag{A.2}$$

For the variation of potential energy, a double integration by parts in respect to y of equation (3.17) results in

$$\begin{aligned}\int_{t_1}^{t_2} \delta V \mathrm{d}t &= \int_{t_1}^{t_2} \left\{ \left[EIw''(y,t)\frac{\partial}{\partial y}\left(\delta w(y,t)\right)\right]\Big|_0^l \right. \\ &\quad \left. - \int_0^l \frac{\partial}{\partial y}\left[EIw''(y,t)\right]\frac{\partial}{\partial y}\left(\delta w(y,t)\right)\mathrm{d}y \right\}\mathrm{d}t \\ &= \int_{t_1}^{t_2} \left\{ \left[EIw''(y,t)\frac{\partial}{\partial y}\left(\delta w(y,t)\right)\right]\Big|_0^l \right. \\ &\quad \left. - \left[\frac{\partial}{\partial y}\left(EIw''(y,t)\right)\delta w(y,t)\right]\Big|_0^l \right\}\mathrm{d}t \\ &\quad + \int_{t_1}^{t_2} \left\{ \int_0^l \frac{\partial^2}{\partial y^2}\left[EIw''(y,t)\right]\delta w(y,t)\mathrm{d}y \right\}\mathrm{d}t \ .\end{aligned} \tag{A.3}$$

Appendix B

Finite element reference

SHELL181: 4-Node Shell

The SHELL181 element, whose geometry is shown in Figure B.1, is a 4-node linear shell element based on the Mindlin-Reissner shell theory and thus suitable for analysing thin to moderately-thick shell structures. Each node has six degrees of freedom: three translations in the x, y and z directions and rotations about these axes [45].

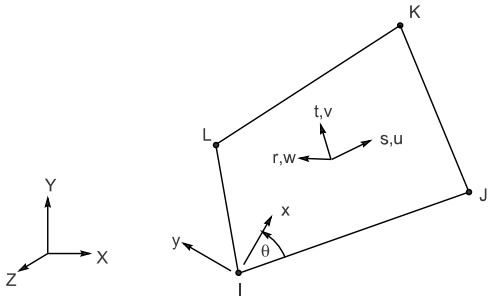


Figure B.1: SHELL181 finite element [45].

BEAM188: 3D 2-Node Beam

The BEAM188 element of Figure B.2 is a three-dimensional 2-node beam element based on the Timoshenko beam theory suitable for the analysis of slender to moderately thick beam structures. Each node has six degrees of freedom: three translations in the x, y and z directions and rotations about these same axes [45].

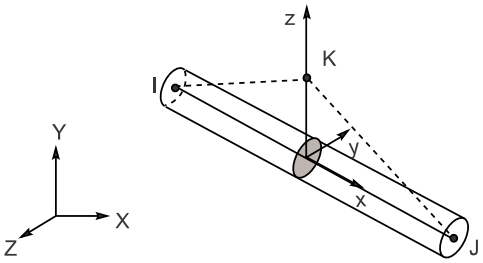


Figure B.2: BEAM188 finite element [45].

SOLID185: 3D 8-Node Solid

The SOLID185 element (Figure B.3) is a three-dimensional 8-node solid element. Each node has three degrees of freedom: translations in the nodal x, y and z directions [45].

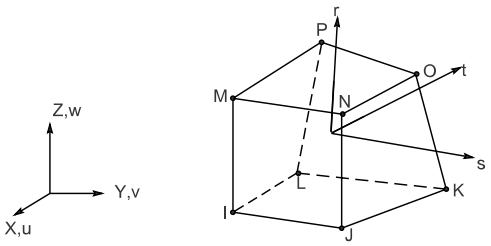


Figure B.3: SOLID185 finite element [45].

CONTA174: 3D 8-Node Surface-to-Surface Contact

The definition of surface-to-surface contact uses elements CONTA174 and TARGE170 (Figure B.4). The CONTA174 elements overlays the elements to which they are connected, thus adopting its geometric characteristics (see Figure B.5) with contact occurring when the element surface penetrates an associated target surface overlaid by TARGE170 segments. The mid-side nodes of a contact element are dropped if the underlying element doesn't have mid-side nodes [45].

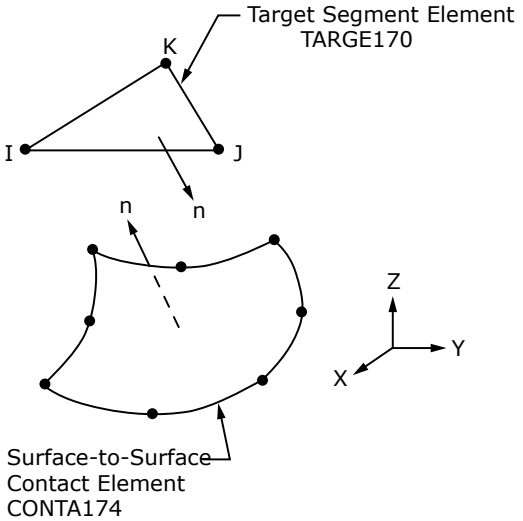


Figure B.4: CONTA174 and TARGE170 finite elements [45].

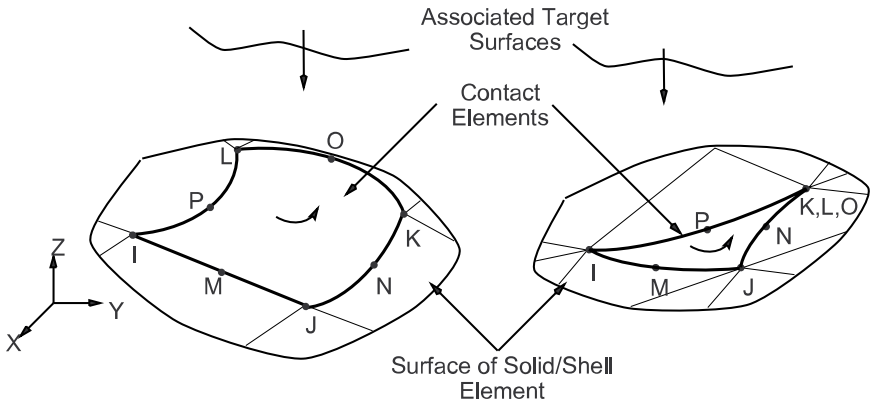


Figure B.5: Contact elements definition [45].

Appendix C

STK-21-C numerical simulation results

C.1 Maximum relative displacement of the upper crossbeam

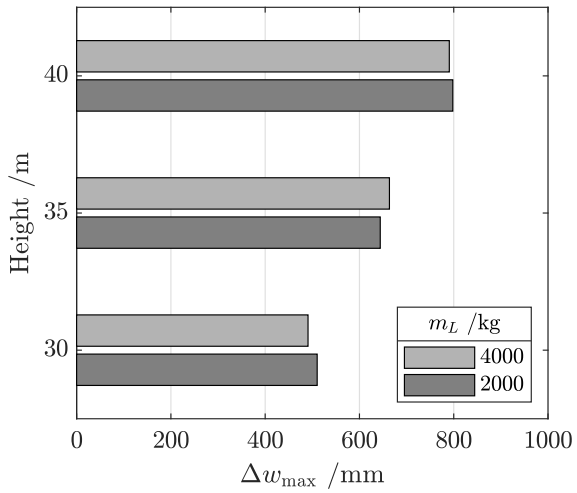
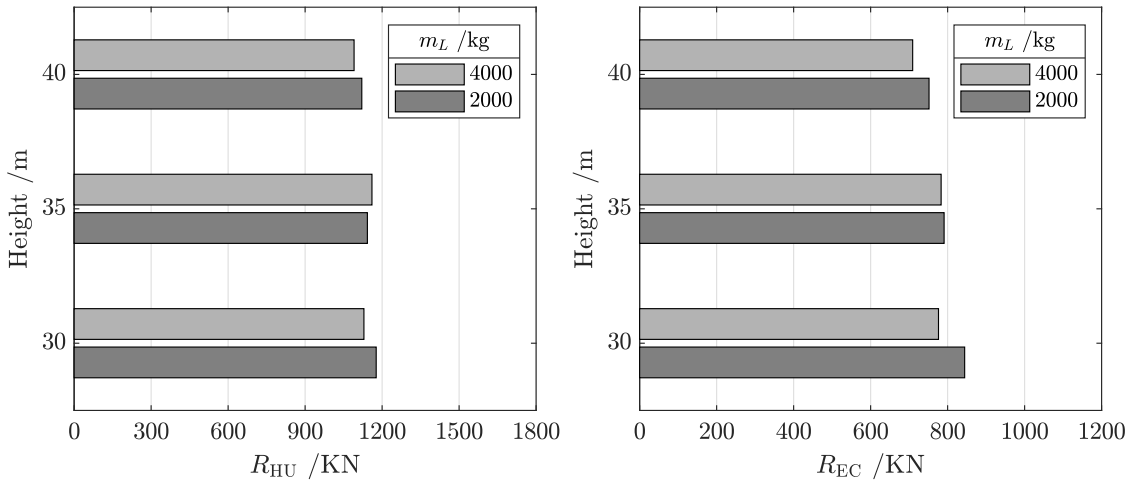


Figure C.1: Maximum relative displacement of the upper crossbeam for the conditions of Figure 5.41.

C.2 Maximum wheel loads



(a) HU's side. (b) EC assembly's side.

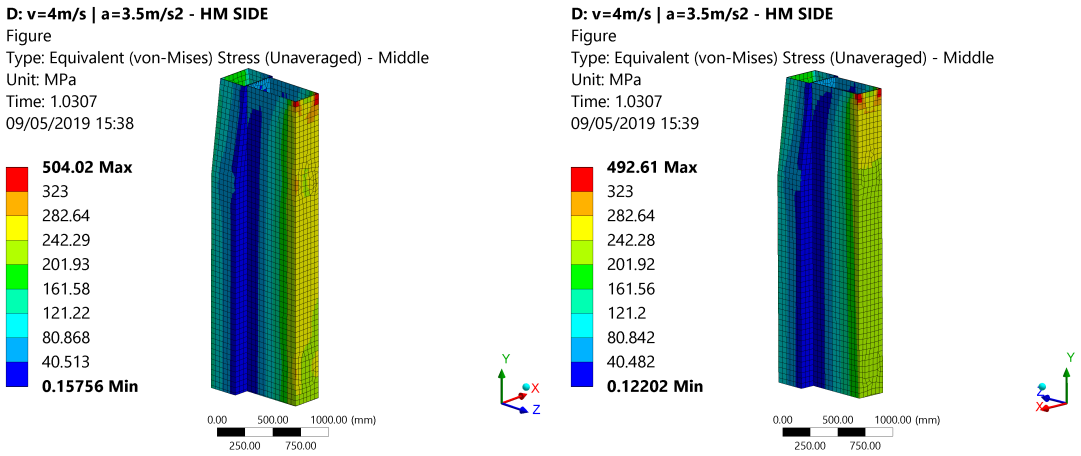
Figure C.2: Maximum wheel reactions for the conditions of Figure 5.41.

C.3 Stresses

The following results are for the corresponding maximum deceleration case only.

C.3.1 Masts' height: 40 m

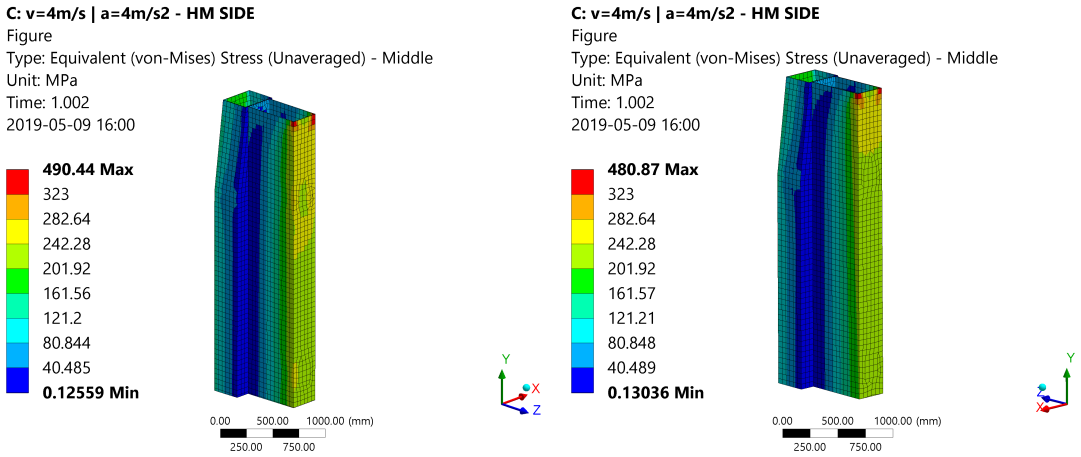
$m_L = 4000$ kg



(a) HU's side. (b) ECs' assembly side.

Figure C.3: Contour plots of σ_{eq} on the upper region of the mast at $t = 1.0287$ s for $\Delta t_{\text{stop}} = 1.14$ s and $m_L = 4000$ kg.

$m_L = 2000$ kg



(a) HU's side. (b) ECs' assembly side.

Figure C.4: Contour plots of σ_{eq} on the upper region of the mast at $t = 1.00$ s for $\Delta t_{\text{stop}} = 1.00$ s and $m_L = 2000$ kg.

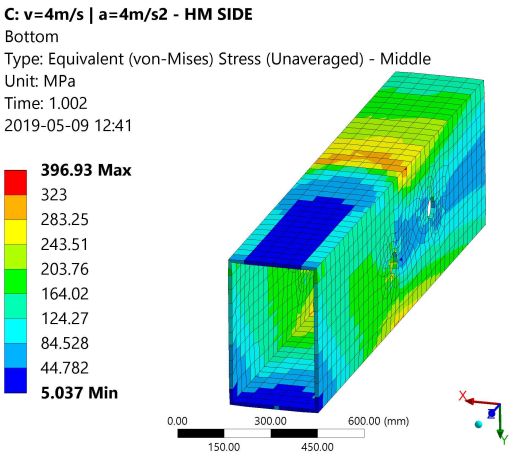
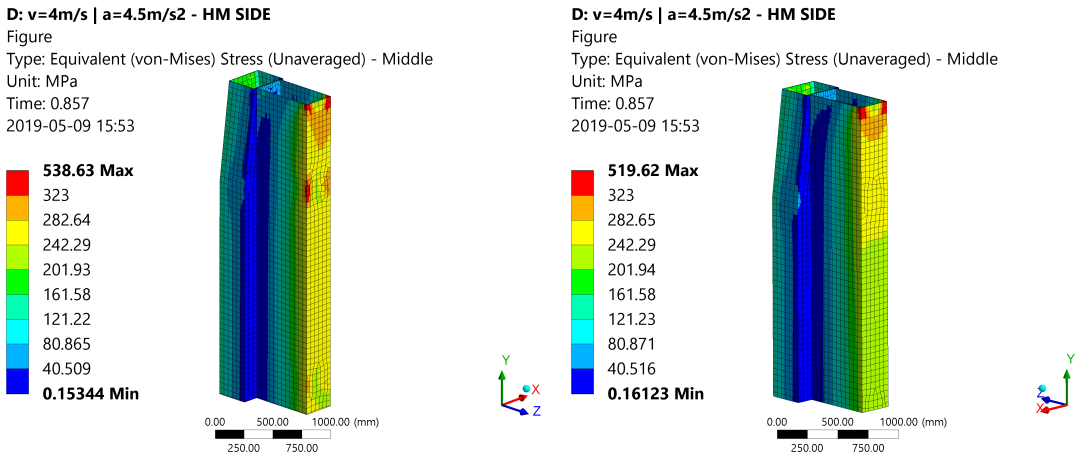


Figure C.5: Detail of σ_{eq} on the downward face of the upper crossbeam at $t = 1.00$ s for $\Delta t_{\text{stop}} = 1.00$ s and $m_L = 2000$ kg.

C.3.2 Masts' height: 35 m

$m_L = 4000$ kg



(a) HU's side. (b) ECs' assembly side.

Figure C.6: Contour plots of σ_{eq} on the upper region of the mast at $t = 0.855$ s for $\Delta t_{\text{stop}} = 0.88$ s and $m_L = 4000$ kg.

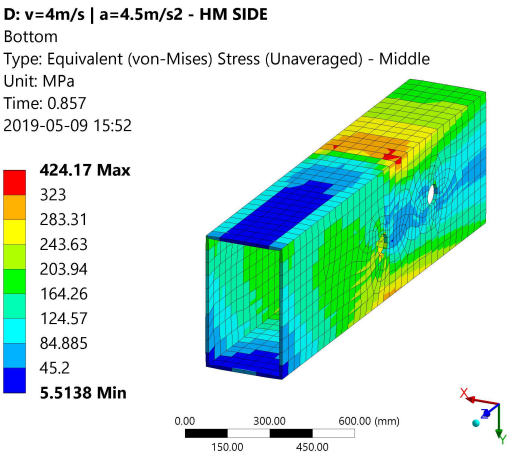
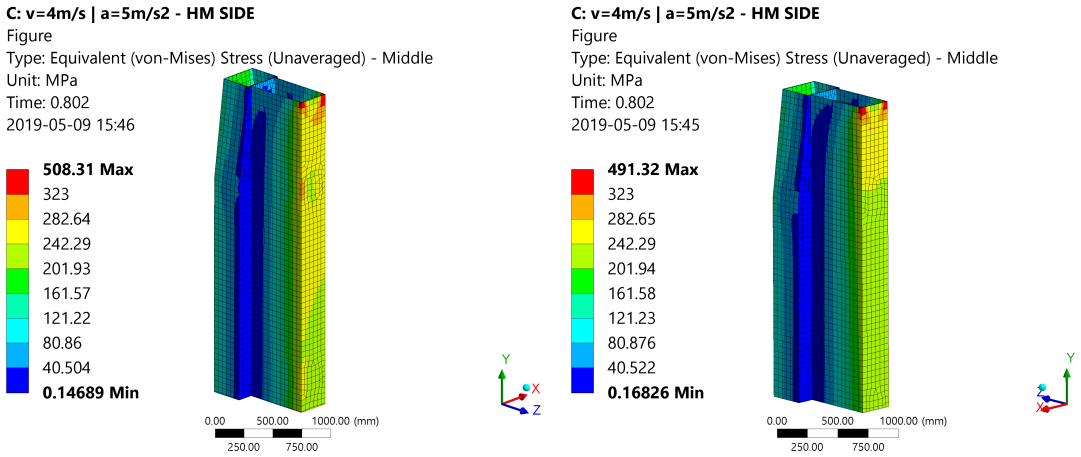


Figure C.7: Detail of σ_{eq} on the downward face of the upper crossbeam at $t = 0.855$ s for $\Delta t_{\text{stop}} = 0.88$ s and $m_L = 4000$ kg.

$m_L = 2000$ kg



(a) HU's side. (b) ECs' assembly side.

Figure C.8: Contour plots of σ_{eq} on the upper region of the mast at $t = 0.80$ s for $\Delta t_{\text{stop}} = 0.80$ s and $m_L = 2000$ kg.

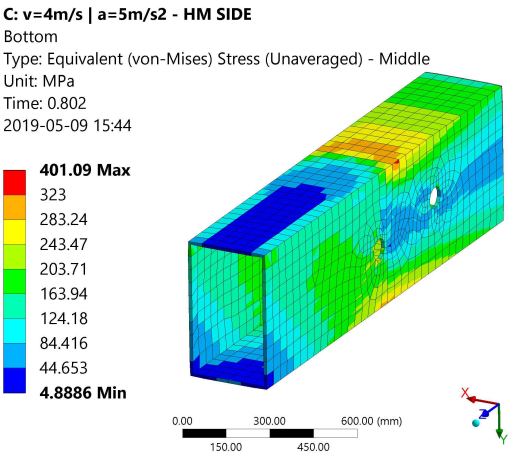
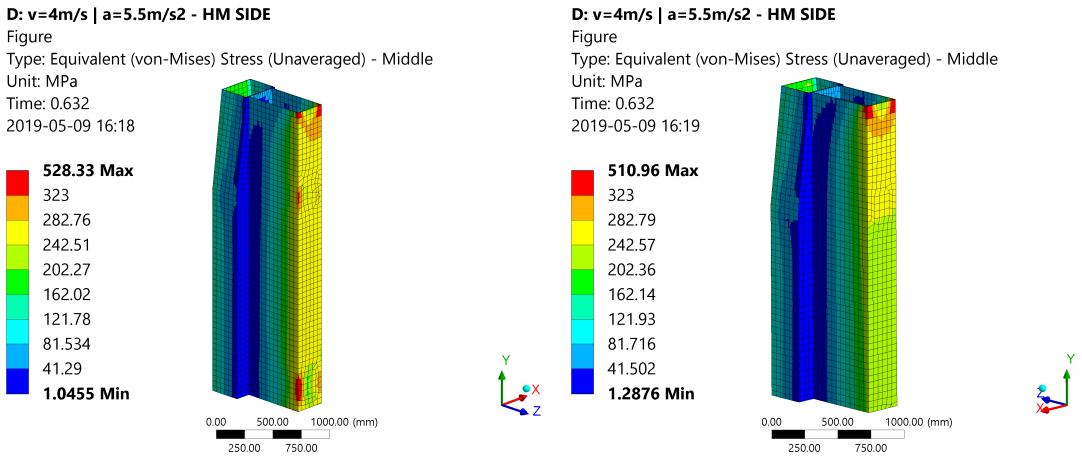


Figure C.9: Detail of σ_{eq} on the downward face of the upper crossbeam at $t = 0.80$ s for $\Delta t_{\text{stop}} = 0.80$ s and $m_L = 2000$ kg.

C.3.3 Masts' height: 30 m

$m_L = 4000$ kg



(a) HU's side. (b) ECs' assembly side.

Figure C.10: Contour plots of σ_{eq} on the upper region of the mast at $t_{\text{sim}} = 0.630$ s for $\Delta t_{\text{stop}} = 0.72$ s and $m_L = 4000$ kg.

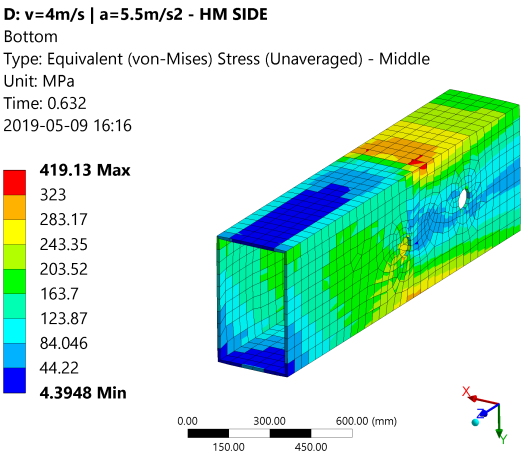
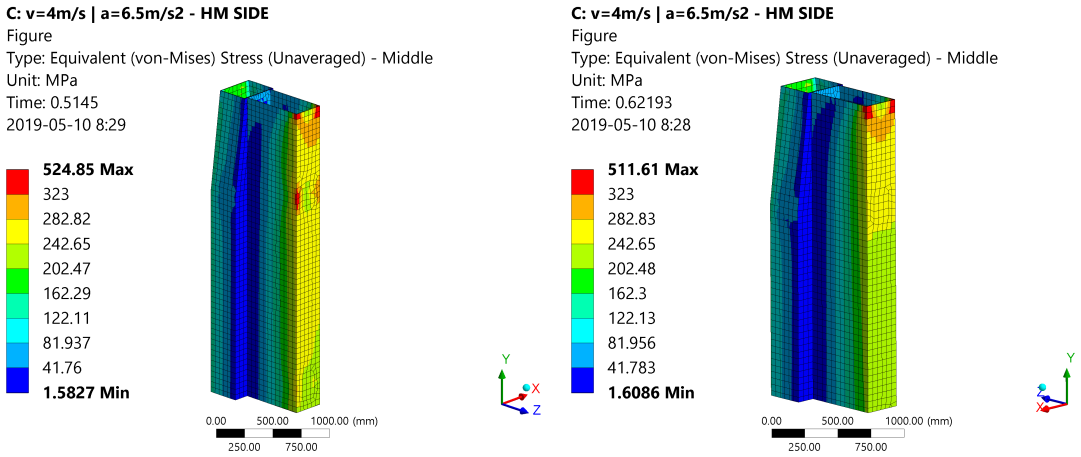


Figure C.11: Detail of σ_{eq} on the downward face of the upper crossbeam at $t = 0.630$ s for $\Delta t_{\text{stop}} = 0.72$ s and $m_L = 4000$ kg.

$m_L = 2000$ kg



(a) HU's side at $t_{\text{sim}} = 0.5145$ s. (b) ECs' assembly side at $t_{\text{sim}} = 0.6219$ s.

Figure C.12: Contour plots of σ_{eq} on the upper region of the mast for $\Delta t_{\text{stop}} = 0.61$ s and $m_L = 2000$ kg.

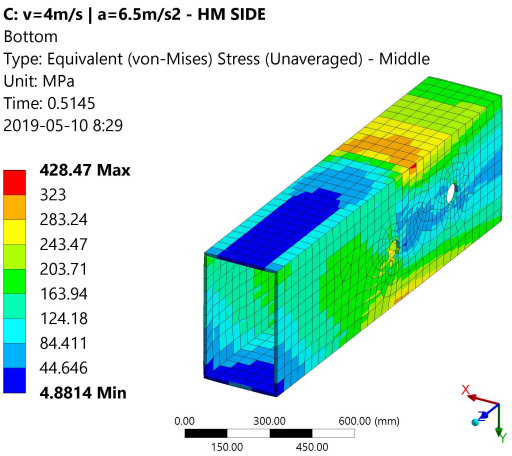


Figure C.13: Detail of σ_{eq} on the downward face of the upper crossbeam at $t_{\text{sim}} = 0.5145$ s for $\Delta t_{\text{stop}} = 0.61$ s and $m_L = 2000$ kg.

Appendix D

STK-25 numerical simulation results

D.1 Model details

The following Tables D.1 and D.2 provide details on the mass and mesh properties, respectively, of the STK-25 numerical models for the transient analyses. The machine's wheelbase is 6300 mm.

Table D.1: Total mass of the STK-25 structure model per height.

Height /m	Total mass /kg
45	17615
40	16444
35	14869
30	13557

Table D.2: Mesh properties of the STK-25 models per height.

Height /m	Num. elements	Num. nodes	Num. DOFs
45	256648	248971	1478242
40	236977	229683	1362586
35	212586	206977	1230094
30	191312	185873	1103470

D.2 Maximum relative displacement of the upper crossbeam

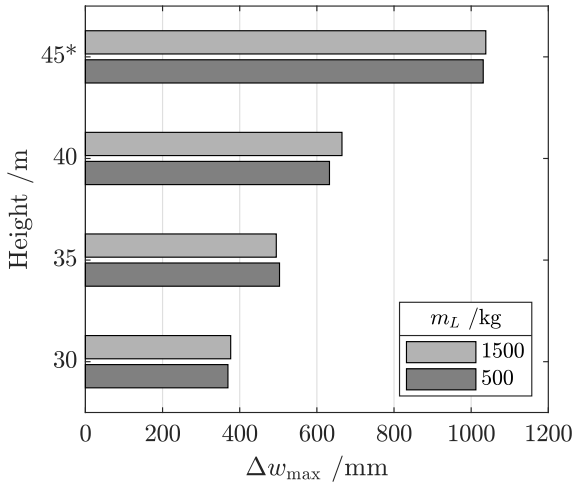
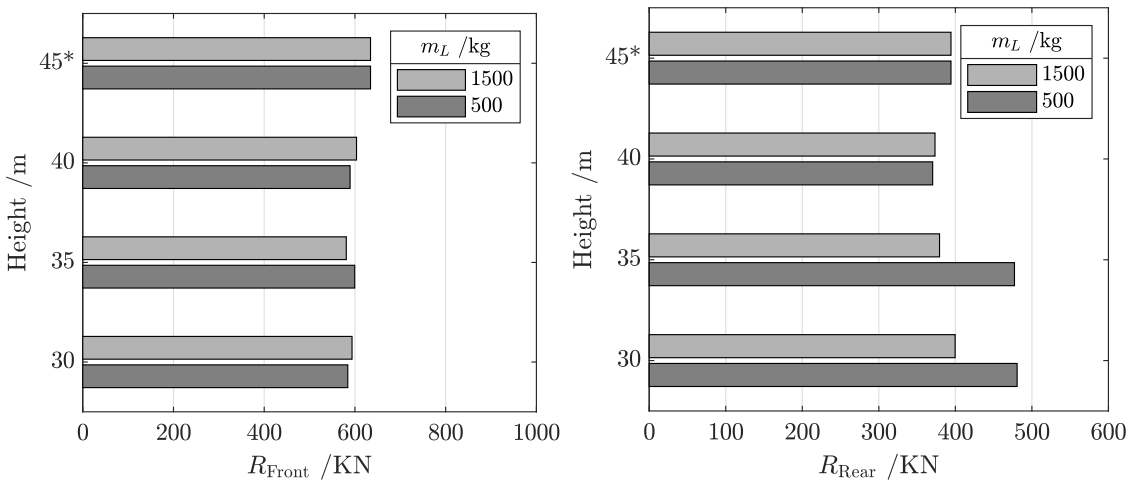


Figure D.1: Maximum relative displacement of the upper crossbeam for the conditions of Figure 5.47a.

D.3 Maximum wheel loads



(a) Front.

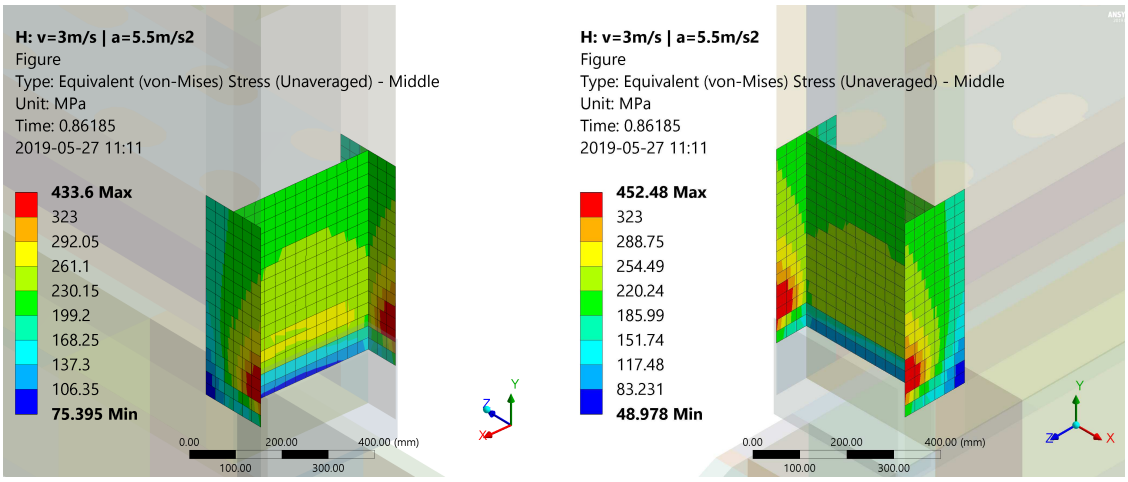
(b) Rear.

Figure D.2: Maximum wheel reactions for the conditions of Figure 5.47a.

D.4 Stresses

D.4.1 Mast's height: 45 m

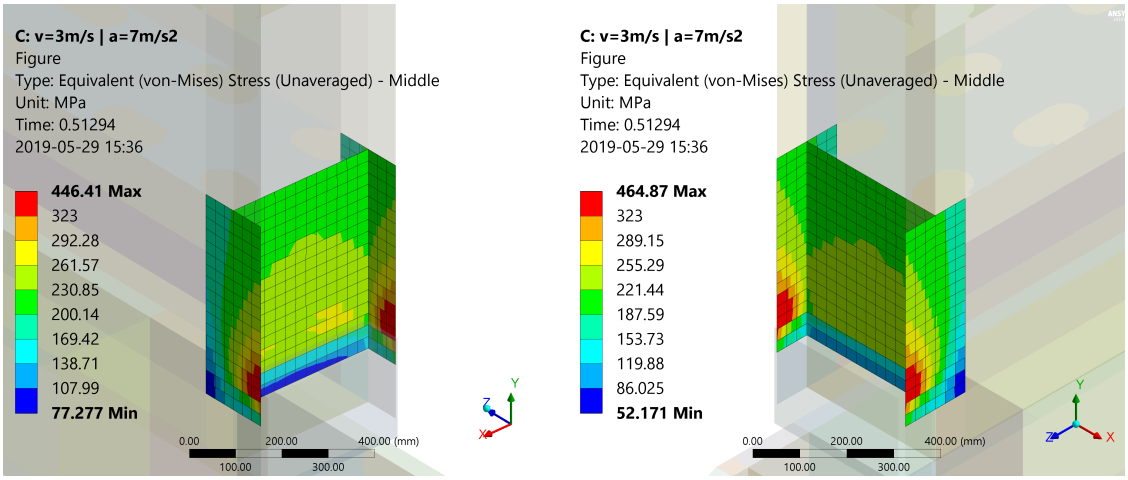
$m_L = 1500$ kg



(a) Front of the mast. (b) Back of the mast.

Figure D.3: Contour plots of σ_{eq} on the lower region of the 45 m STK-25 ($v_i = 3$ m/s; $\Delta t_{\text{stop}} = 0.54$ s; $t = 0.85985$ s).

$m_L = 500$ kg

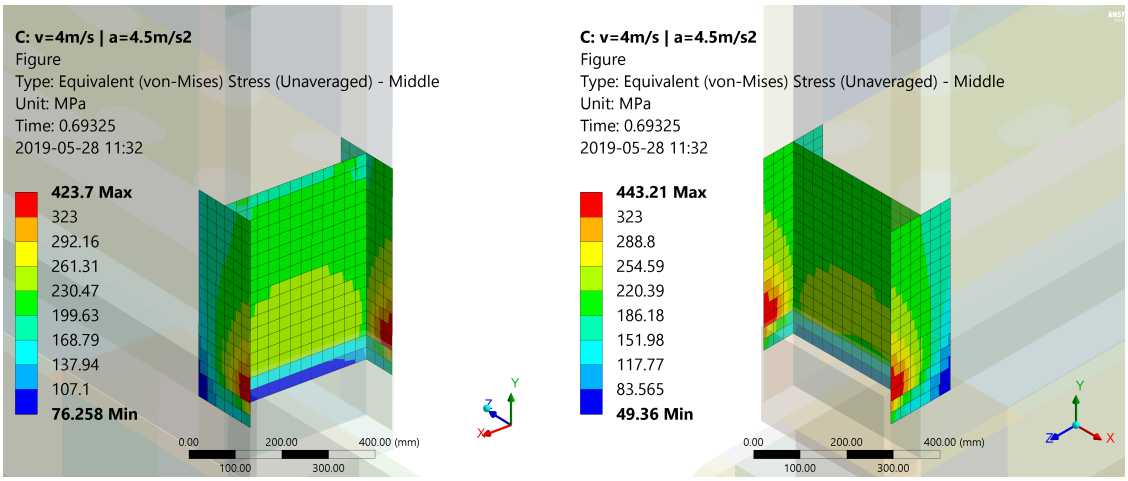


(a) Front of the mast. (b) Back of the mast.

Figure D.4: Contour plots of σ_{eq} on the lower region of the 45 m STK-25 ($v_i = 3$ m/s; $\Delta t_{\text{stop}} = 0.42$ s; $t_{\text{sim}} = 0.51094$ s).

D.4.2 Mast's height: 40 m

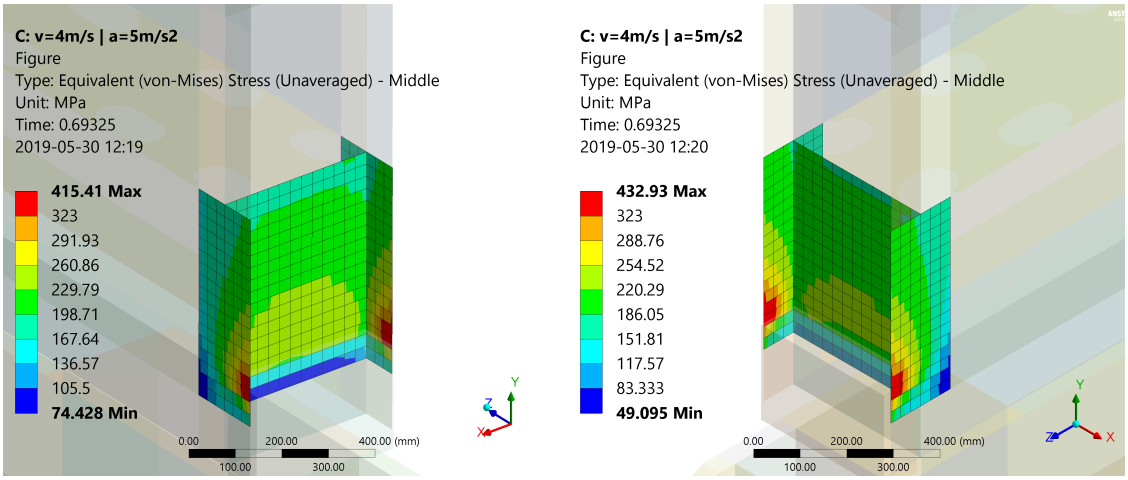
$m_L = 1500$ kg



(a) Front of the mast. (b) Back of the mast.

Figure D.5: Contour plots of σ_{eq} on the lower region of the 40 m STK-25 ($v_i = 4$ m/s; $\Delta t_{\text{stop}} = 0.88$ s; $t = 0.69125$ s).

$m_L = 500$ kg

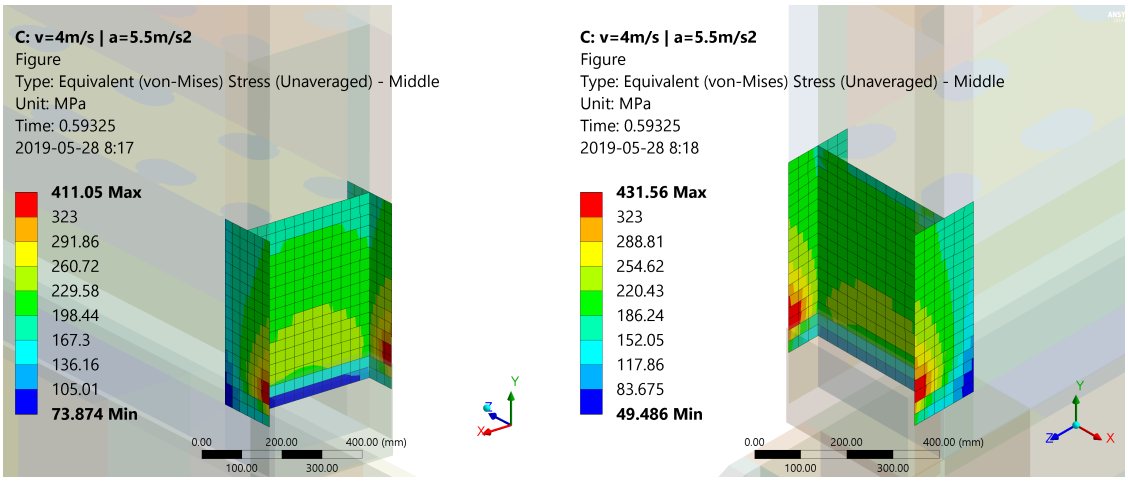


(a) Front of the mast. (b) Back of the mast.

Figure D.6: Contour plots of σ_{eq} on the lower region of the 40 m STK-25 ($v_i = 4$ m/s; $\Delta t_{\text{stop}} = 0.80$ s; $t = 0.69125$ s).

D.4.3 Mast's height: 35 m

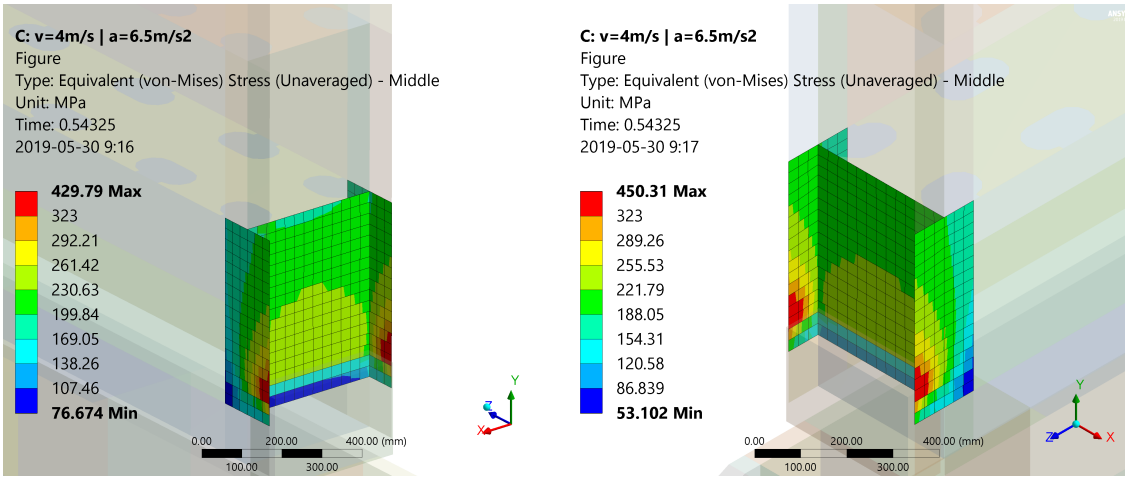
$m_L = 1500$ kg



(a) Front of the mast. (b) Back of the mast.

Figure D.7: Contour plots of σ_{eq} on the lower region of the 35 m STK-25 ($v_i = 4$ m/s; $\Delta t_{\text{stop}} = 0.72$ s; $t = 0.59125$ s).

$m_L = 500$ kg

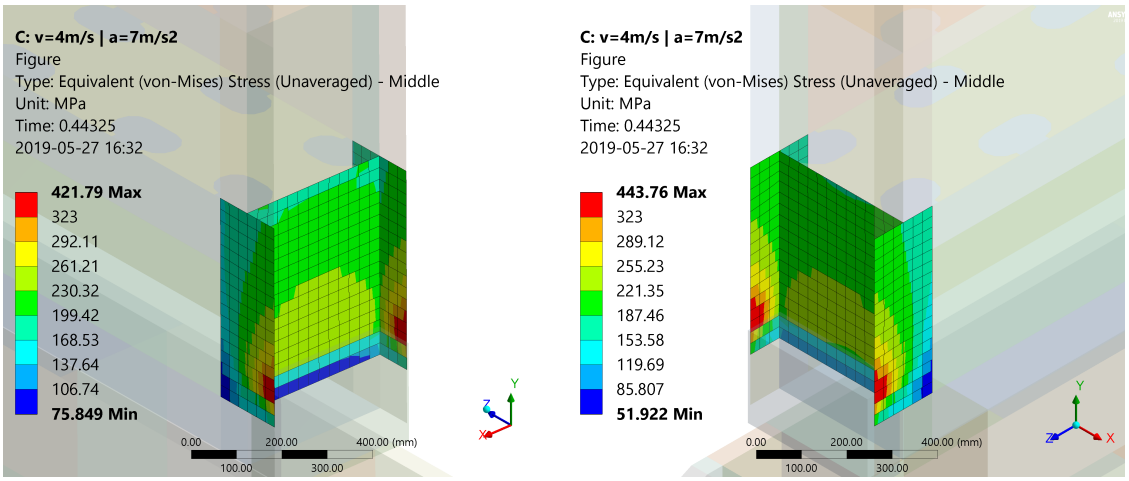


(a) Front of the mast. (b) Back of the mast.

Figure D.8: Contour plots of σ_{eq} on the lower region of the 35 m STK-25 ($v_i = 4$ m/s; $\Delta t_{\text{stop}} = 0.61$ s; $t = 0.54125$ s).

D.4.4 Mast's height: 30 m

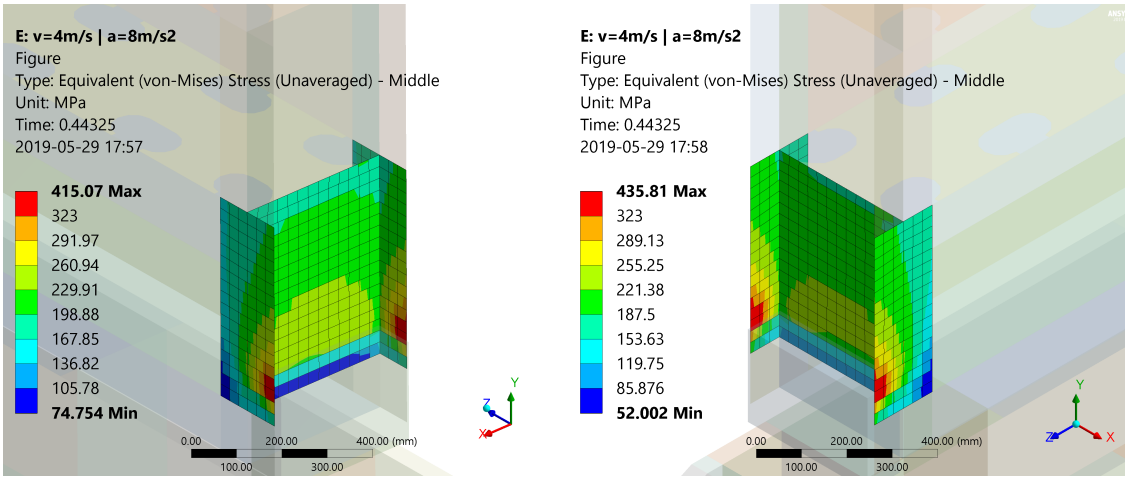
$m_L = 1500$ kg



(a) Front of the mast. (b) Back of the mast.

Figure D.9: Contour plots of σ_{eq} on the lower region of the 30 m STK-25 ($v_i = 4$ m/s; $\Delta t_{\text{stop}} = 0.57$ s; $t = 0.44125$ s).

$m_L = 500$ kg



(a) Front of the mast. (b) Back of the mast.

Figure D.10: Contour plots of σ_{eq} on the lower region of the 30 m STK-25 ($v_i = 4$ m/s; $\Delta t_{\text{stop}} = 0.50$ s; $t = 0.44125$ s).

Appendix E

NXP® MMA8451Q capacitive accelerometer data sheet [50]

NXP Semiconductors
Data sheet: Technical data

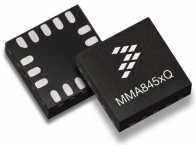
Document Number: MMA8451Q
Rev. 10.3, 02/2017

MMA8451Q, 3-axis, 14-bit/8-bit digital accelerometer

MMA8451Q

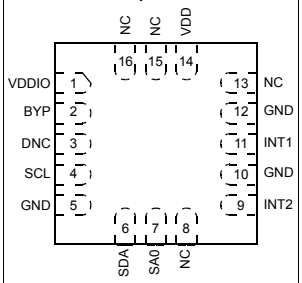
The MMA8451Q is a smart, low-power, three-axis, capacitive, micromachined accelerometer with 14 bits of resolution. This accelerometer is packed with embedded functions with flexible user programmable options, configurable to two interrupt pins. Embedded interrupt functions allow for overall power savings relieving the host processor from continuously polling data. There is access to both low-pass filtered data as well as high-pass filtered data, which minimizes the data analysis required for jolt detection and faster transitions. The device can be configured to generate inertial wakeup interrupt signals from any combination of the configurable embedded functions allowing the MMA8451Q to monitor events and remain in a low-power mode during periods of inactivity. The MMA8451Q is available in a 16-pin QFN, 3 mm x 3 mm x 1 mm package.

Top and bottom view



16-pin QFN
3 mm x 3 mm x 1 mm

Top view



Pin connections

Features

- 1.95 V to 3.6 V supply voltage
- 1.6 V to 3.6 V interface voltage
- ±2 *g*/±4 *g*/±8 *g* dynamically selectable full scale
- Output data rates (ODR) from 1.56 Hz to 800 Hz
- 99 µg/√Hz noise
- 14-bit and 8-bit digital output
- I^2C digital output interface
- Two programmable interrupt pins for seven interrupt sources
- Three embedded channels of motion detection
  - Freefall or motion detection: one channel
  - Pulse detection: one channel
  - Jolt detection: one channel
- Orientation (portrait/landscape) detection with programmable hysteresis
- Automatic ODR change for auto-wake and return to sleep
- 32-sample FIFO
- High-pass filter data available per sample and through the FIFO
- Self-test
- Current consumption: 6 µA to 165 µA

Typical Applications

- E-compass applications
- Static orientation detection (portrait/landscape, up/down, left/right, back/front position identification)
- Notebook, e-reader, and laptop tumble and freefall detection
- Real-time orientation detection (virtual reality and gaming 3D user position feedback)
- Real-time activity analysis (pedometer step counting, freefall drop detection for HDD, dead-reckoning GPS backup)
- Motion detection for portable product power saving (auto-sleep and auto-wake for cell phone, PDA, GPS, gaming)
- Shock and vibration monitoring (mechatronic compensation, shipping and warranty usage logging)
- User interface (menu scrolling by orientation change, tap detection for button replacement)

Ordering information			
Part number	**Temperature range**	**Package description**	**Shipping**
MMA8451QT	–40 °C to +85 °C	QFN-16	Tray
MMA8451QR1	–40 °C to +85 °C	QFN-16	Tape and Reel

© NXP Semiconductors N.V. 2017